UNIVERSIDADE FEDERAL DE MINAS GERAIS

INSTITUTO DE CIÊNCIAS BIOLÓGICAS

DEPARTAMENTO DE MORFOLOGIA

Bruna Araújo David

Estudo da origem, localização e função de fagócitos durante o repovoamento hepático

Belo Horizonte

2016

Bruna Araújo David

Estudo da origem, localização e função de fagócitos durante o repovoamento hepático

Texto apresentado ao Programa de Pós-Graduação em Biologia Celular do Departamento de Morfologia do Instituto de Ciências Biológicas da Universidade Federal de Minas Gerais como requisito para defesa de tese de doutorado.

Orientador: Prof. Dr. Gustavo Batista de Menezes

Belo Horizonte

2016

Universidade Federal de Minas Gerais - Instituto de Ciências Biológicas
Programa de Pós-Graduação em Biologia Celular

ATA DA DEFESA DE TESE DE DOUTORADO DE

BRUNA ARAUJO DAVID

165/2016
Entrada
2°/2015
2015744333

Às **nove horas** do dia **25 de novembro de 2016**, reuniu-se, no Instituto de Ciências Biológicas da UFMG, a Comissão Examinadora da Tese, indicada pelo Colegiado do Programa, para julgar, em exame final, o trabalho final intitulado: **"ESTUDO DA ORIGEM, LOCALIZAÇÃO E FUNÇÃO DE FAGÓCITOS DURANTE O REPOVOAMENTO HEPÁTICO"**, requisito final para obtenção do grau de Doutora em Biologia Celular. Abrindo a sessão, o Presidente da Comissão, **Dr. Gustavo Batista de Menezes**, após dar a conhecer aos presentes o teor das Normas Regulamentares do Trabalho Final, passou a palavra à candidata, para apresentação de seu trabalho. Seguiu-se a arguição pelos examinadores, com a respectiva defesa da candidata. Logo após, a Comissão se reuniu, sem a presença da candidata e do público, para julgamento e expedição de resultado final. Foram atribuídas as seguintes indicações:

Prof./Pesq.	Instituição	Indicação
Dr. Gustavo Batista de Menezes	UFMG	APROVADA
Dr. Caio Tavares Fagundes	UFMG	APROVADA
Dr. Flávio Almeida Amaral	UFMG	APROVADA
Dra. Silvia Dantas Cangussu	UFOP	aprovada
Dra. Andrea Teixeira de Carvalho	CPqRR	APROVADA

Pelas indicações, a candidata foi considerada: APROVADA

O resultado final foi comunicado publicamente à candidata pelo Presidente da Comissão. Nada mais havendo a tratar, o Presidente encerrou a reunião e lavrou a presente ATA, que será assinada por todos os membros participantes da Comissão Examinadora. **Belo Horizonte, 25 de novembro de 2016.**

Dr. Gustavo Batista de Menezes (Orientador) ____________

Dr. Caio Tavares Fagundes Caio Tavares Fagundes

Dr. Flávio Almeida Amaral Flávio Almeida Amaral

Drª. Silvia Dantas Cangussu Cangussu

Drª. Andrea Teixeira de Carvalho ATCarvalho.

Profa. Luciana de Oliveira Andrade
COORDENADORA DO PROGRAMA DE
PÓS GRADUAÇÃO EM BIOLOGIA CELULAR ICB/UFMG

Obs: Este documento não terá validade sem a assinatura e carimbo do Coordenador.

Este trabalho foi realizado no Centro de Biologia Gastrointestinal, do Departamento de Morfologia, localizado no Instituto de Ciências Biológicas da Universidade Federal de Minas Gerais (UFMG) em parceria com a Escola Médica de Harvard (EUA) e a Universidade de Calgary (Canadá). Também foi utilizado o laboratório de Imunofarmacologia do Departamento de Bioquímica e Imunologia (ICB-UFMG). Contamos com o apoio financeiro das agências CAPES, FAPEMIG e CNPq.

"Todo ser carrega em si o dom de ser capaz..."

(Almir Sater e Renato Teixeira, 1991)

AGRADECIMENTOS

À Deus, pelo dom da vida e por todos os acontecimentos que me trouxeram até aqui e me tornaram quem eu sou hoje. Por todas as oportunidades e pessoas pelo caminho.

À minha família, em especial meu pai, minha mãe e minha irmã Nicole, pelo amor, apoio e incentivo. Às minhas tias(os) e primas(os), muitíssimo obrigada por tudo que já fizeram por mim. Pelo estabelecimento de laços que jamais serão desfeitos, por serem a melhor e mais encantadora e feliz referência de família, pelo cuidado e afeto, por todos os abraços apertados capazes de fazer o mundo girar mais devagar e tirar o peso de uma vida inteira, pelo aconchego de um lar em todas as visitas, mesmo as mais demoradas. Pela compreensão, risadas, alegrias, festas, brincadeiras, amizade, gordices e fofuras, bom humor, paz, confiança, sabedoria, força, sinceridade, inspiração, liberdade... Obrigada por manterem vivos em mim a esperança e o otimismo que me fizeram nutrir a certeza inabalável de que o impossível é só questão de opinião. Por nunca me deixarem esquecer valores como dignidade, respeito, generosidade, humildade e tudo mais que me permite olhar minha história e sentir orgulho do que enxergo, pois tenho simpatia pela pessoa que o tempo me fez e vocês são responsáveis por isso.

À Eloá, Gau, Lud e Carol, pela amizade, amor e paciência incondicional. Pelo companheirismo, lealdade e incentivo. Tão essenciais quanto o coração que bate dentro de mim.

À Miroca, Vitão, Phil e Fabikinho, a gratidão que sinto vai além do imaginável pela família que e foi permitido escolher, pois não se trata apenas de um ano ou dois e sim de toda uma vida. Muito obrigada pela atenção, generosidade, companheirismo, amizade, conselhos, alegrias, respeito, farras, carinho, incentivo...

Aos membros do NEI pelo dia-a-dia alegre e descontraído. Pela generosidade e companheirismo.

Às vezes me pego pensando sobre os desígnios que nos são dados através do tempo e na maneira com a qual lidamos com cada oportunidade. Nessas horas volto a pensar sobre o poder de nossas escolhas. Da grandiosidade de uma fração de segundo que modifica por inteiro esse caminho antes predefinido. Da força de um sorriso, de um olhar, de um carinho. Sendo assim, torna-se impossível não crer na graça divina que é o fato de termos nos encontrado. Torna-se impossível deixar de agradecer pela existência de cada um de vocês.

Impossível deixar de agradecer pelos milhões de milésimos de segundos que me fizeram estar aqui. Um agradecimento repleto da mais sincera gratidão aos meus amigos Maísa, Rafa, Pedro, Riri, Sarah (fumo do meu coração), Débora, Brenda, Maria Alice (a IC mais fofa do mundo!), Alan, André e Mônica, acima de tudo pela GENEROSIDADE.

Ao meu orientador, Gustavo Menezes, por acreditar e caminhar comigo. Por me ensinar a navegar em qualquer tempo, qualquer mar. Que o céu é o limite e nós somos imbatíveis. Por me ensinar, não com palavras, mas com exemplos diários a exercer com maestria a profissão que escolhi me dedicar. Pela amizade, companheirismo e fé depositada em mim como pessoa. Por insistir que não existe impossível para quem escolheu procurar e encontrar o lado bom de tudo.

Aos funcionários do biotério, Hermes e Pedro, pelo carinho, atenção e compreensão.

A todos os colegas e professores do Programa de Pós-graduação em Biologia Celular pelo convívio e aprendizado.

Aos membros da banca por aceitar meu convite e contribuir de forma tão positiva e construtiva para meu trabalho.

SUMÁRIO

LISTA DE ABREVIATURAS 9

LISTA DE ILUSTRAÇÕES 12

LISTA DE FIGURAS 13

RESUMO 14

ABSTRACT 15

1. INTRODUÇÃO 16

2. OBJETIVOS 25

  2.1. Objetivo principal 25

  2.2. Objetivos específicos 25

3. METODOLOGIA 26

  3.1. Animais 26

  3.2. Microscopia confocal e imunohistoquímica 26

  3.3. Células hepáticas não-parenquimais (*liver non-parenchimal cells* - LNPCs) 27

  3.4. Animais quimera - medula óssea GFP 28

  3.5 Microcirculação hepática 28

  3.6. Modelo de depleção com clodronato (CLL) 28

  3.7. Tratamento com toxina diftérica 29

  3.8. Modelo de lesão hepática 29

  3.9. Medida de função hepática por depuração de verde de indocianina (ICG - *indocyanine green*) 29

  3.10. Avaliação histológica do fígado 30

  3.11. Injeção sistêmica de *E. coli* 30

  3. 12. Dosagem de citocinas por Multiplex 30

  3.13. Análise dos dados de expressão gênica 31

  3.14. Análise estatística 31

4. RESULTADOS 32

  4.1. High dimensional identification of liver phagocytes 32

  4.2. Emergency repopulation dynamics following sudden phagocyte depletion 44

  4.3. A CXC3CL1 gradient drives extravascular DC reestablishment 49

  4.4. Phagocyte depletion and replenishment imprints a temporary altered response to injury 53

  4.5. Phagocytic instruction of BM-derived KCs during replenishment 56

4.7. Legends for Supplementary Movies (CD em anexo) 59
5. DISCUSSÃO 60
6. REFERÊNCIAS BIBLIOGRÁFICAS 63
PRODUÇÃO CIENTIFICA 69
DIVULGAÇÃO CIENTIFICA 127
PRÊMIOS 133
ORIENTAÇÕES 136
ATIVIDADE EXTRA-CURRICULAR 138

LISTA DE ABREVIATURAS

µm - micrômetros

ACTb - beta actina

ALT - alanina aminotransferase

ANOVA - analysis of variance

APAP - a*cetaminophen* ou N-acetyl-p-aminophenol ou paracetamol

b-CD - células dendríticas do baço

BM - *bone marrow*; medula óssea

BV - b*rilhant violet*; violeta brilhante

CCL2 - *C-C chemokine ligand type 2*

CCR2 - *C-C chemokine receptor type 2*

CDs - células dendríticas

CEBIO - centro de bioterismo da UFMG

CETEA - comitê de ética em experimentação animal da UFMG

CKs - células de kupffer

CLL - clodronato

CX3CL1 - *CX3C chemokine ligand* ou fraquitalquina

CX3CR1 - *CX3C chemokine receptor*

CyTOF - *time of flight mass cytometry*

DAPI - 4′,6-diamidino-2-phenylindole dihydrochloride

DCs - *dendritic cells*

DNA - *deoxyribonucleic acid*; ácido desoxirribonucleico - ADN

DTR - *diphtheria toxin receptor;* receptor de toxina diftérica

EYFP - *enhanced* yellow *fluorescent protein*; proteína amarelo fluorescente

FACS - *fluorescence-activated cell sorting*; separação celular por fluorrescência

Fig. - Figura

FITC - *fluorescein isothiocyanate;* isotiocianato de fluoresceína

GFP - g*reen fluorescent protein*; proteína verde fluorescente

H&E - hematoxilina e eosina

HSCs - *hepatic stellate cells*; células estreladas hepáticas ou células de Ito

HVO - *hepatic vascular oclusion*; oclusão vascular hepática

ICG - *indocyanine green*; verde de indocianina

IFNγ - interferon gama

IL - interleucina

KCs - *Kupffer cells*

kg - *kilogram*; quilograma

LB - Luria Bertani

LNPCs - *liver non-parenchimal cells*; células hepáticas não-parenquimais

LPS - lipopolissacarídeo

LysM - lisosima M

mg - miligrama

MHC - *major histocompatibility complex*; complexo de histocompatibilidade principal

MIP - m*acrophage inflammatory protein*; proteína inflamatória de macrófagos

MIV - microscopia intravital

MOMs - macrófagos originados de monócitos

NK - *natural killer*

NKT - linfócitos T *natural killer*

nm - nanômetros

PBS - *phosphate buffered saline*; salina tamponada com fosfato

PCoA - *principal coordinates analysis*; análise de coordenada principal

pDCs - *plasmacytoid dendritic cells*; células dendríticas plasmacitóides

PE - *phycoerythrin*; ficoeritrina

p-MØ - macrófago peritonial

RFP - r*ed fluorescent protein*; proteína vermelho fluorescente

rpm - rotações por minuto

RPMI - r*oswell park memorial institute*

RT-PCR - *reverse transcription polymerase chain reaction*; reação da transcriptase reversa

s-DC - *spleen dendritic cells*; células dendríticas do baço

SMF - sistema mononuclear fagocítico

TD - toxina diftérica

TGFβ - t*ransforming growth factor*; fator de transformação de crescimento

T_H - célula T *helper*

TNF α - fator de necrose tumoral alfa

LISTA DE ILUSTRAÇÕES

Ilustração 1: Macrófagos residentes apresentam três possíveis origens..................................17

Ilustração 2: Monócitos são recrutados para os tecidos a fim de repor a população de macrófagos residentes originais em quantidade diretamente proporcional á extensão do insulto..20

Ilustração 3: Heterogeneidade na ontogenia de macrófagos residentes durante a homeostase em tecidos de indivíduos adultos..22

LISTA DE FIGURAS

Figure 1: Identification of liver phagocytes by CyTOF and intravital microscopy...............33

Figure 2: Additional CyTOF analysis and NK frequency in LNPCs......................................34

Figure 3: Identification of main hepatic vascular arrangements..36

Figure 4: Expression of different cell surface markers in liver phagocytes............................37

Figure 5: Liver dendritic cells are located in the subcapsular compartment and are CD11^{+}……………………………………………………………………………………39

Figure 6: Characterization of different cell surface markers and CCR2 role in phagocytes..40

Figure 7: Genetic profiles of different liver phagocytes...42

Figure 8: Emergency repopulation dynamics of liver phagocytes..44

Figure 9: Additional dot plots from CyTOF analysis from mice 7 and 17 days after phagocyte depletion..46

Figure 10: Differential repopulation kinetics of dendritic and Kupffer cells..........................47

Figure 11: CX3CR1 guides bone marrow precursors to repopulate the liver........................49

Figure 12: Replenishment by bone marrow monocytes and drug induced liver injury...........51

Figure 13: Substitution of phagocytes imprints a temporary altered response to injury and infection..53

Figure 14: Reestablishment of liver function after phagocyte educational period is dependent on hepatic environment rather than bacterial clues...54

RESUMO

Macrófagos e células dendríticas são fagócitos presentes em quase todos os tecidos em mamíferos e desempenham um importante papel para a homeostase corporal e na orquestração de respostas imune. Fagócitos hepáticos desempenham um papel fundamental na resposta imune do organismo e diferentes mecanismos são necessários para controlar a densidade e a localização dessas células nos diferentes compartimentos do fígado. No entanto, em eventos que perturbam o equilíbrio tecidual, incluindo lesões de diferentes graus, infecções ou intoxicação por medicamentos, uma considerável parte destes fagócitos residentes no fígado podem morrer, o que deixa grandes áreas desprovidas dessas células. Tal evento pode, por exemplo, modificar as importantes funções que o fígado desempenha. Para entender melhor o papel destas células, nós utilizamos uma combinação inédita de citometria associada à espectrometria de massa (CyTOF), expressão gênica e microscopia intravital hepática, e isso nos permitiu determinar precisamente as populações fagocíticas no fígado e as consequências funcionais de sua substituição por precursores mielóides após diferentes estímulos hepáticos. Enquanto os macrófagos hepáticos (células de Kupffer) estão localizados exclusivamente no interior do lúmen microvascular hepático, nós caracterizamos, pela primeira vez, uma nova população de células dendríticas que estão localizadas principalmente debaixo da fina cápsula que envolve o fígado. Após a completa depleção das células dendríticas e células de Kupffer, um modelo que mimetiza diversas doenças em humanos, precursores da medula óssea migram pela via intravascular para repopular o fígado lesado, e estas células, de maneira interessante, ocupam a mesma localização, densidade e função das células originalmente depletadas. No entanto, fígados em estágio inicial de repovoamento apresentam uma severa deficiência na capacidade de responder a lesões tóxicas e especialmente na eficiência em remover as bactérias que se espalham pelo sangue durante pelo menos 30 dias. Após este "período educacional", os novos fagócitos retornam à resposta normal à lesão e reassumem a capacidade de remover bactérias da corrente sanguínea. Desta forma, nossos dados ajudam a expandir nosso entendimento sobre a capacidade do fígado de "educar" novos fagócitos originados da medula óssea que são recrutados durante o processo de regeneração hepática. Ainda, descrevemos como o fígado molda e matura duas populações celulares vastamente diferentes e localizadas em dois compartimentos teciduais opostos. Nossos achados, especialmente no que tange à transitória janela de susceptibilidade durante a regeneração, podem ter um impacto profundo na maneira pela qual pacientes com lesão hepática são atualmente tratados na clínica.

ABSTRACT

Macrophages and dendritic cells are phagocytes present in almost all tissues in mammals and play a pivotal role for tissue homeostasis and during immune responses. Liver phagocytes play a vital role in host immune responses and exquisite mechanisms are necessary to govern the density and the location of the different hepatic leukocytes. However in catastrophic events including trauma, infections or toxin ingestion, many of the liver phagocytes can be wiped out leaving large areas devoid of these cells. Here we used a unique combination of mass cytometry (*Time of flight mass cytometry* - CyTOF), gene expression and liver intravital approaches to precisely determine phagocytic populations within the liver and the functional consequences of their replenishment by myeloid precursors. While Kupffer cells were exclusively located in the sinusoidal lumen, we identified a previously unknown population of dendritic cells that was mainly located under the liver capsule. After full depletion of dendritic and Kupffer cells, intravascular myeloid precursors replenished location, density and function of both populations. However, we also discovered that these emergency repopulated livers were dysfunctional in their ability to respond to injury and to clear bacteria for at least 30 days, which might have a huge impact in how hepatitis patients are treated. After this “educational period”, these new phagocytes returned to normal response to injury and bacterial trapping. Conclusions: Our data shed light on the liver’s ability to locally shape phagocyte precursors into two vastly different immune cells localized to two fundamentally different tissue compartments, and opened new perspectives in the relevance of the immune-based approach in gastroenterology practice regarding to liver injured patients.

1. INTRODUÇÃO

Os primeiros fagócitos foram identificados em organismos marinhos e descritos por Elie Metchnikoff, no século XIX, em virtude da sua natureza fagocítica (Gordon, 2008; 2016). Nos mamíferos, são encontrados em praticamente todos os tecidos, onde exibem grande diversidade anatômica e funcional (Perdiguero and Geissmann, 2016). Têm papéis em inúmeros aspectos da biologia de um organismo; desde desenvolvimento, homeostase e reparo, até respostas imunes a agentes patogênicos (Heymann and Tacke, 2016).

Devido à sua capacidade fagocítica, macrófagos foram primeiramente classificados como membros do Sistema Mononuclear Fagocitário (SMF) onde eram consideradas células finais de linhagens com progenitores da medula óssea (Geissmann *et al*., 2010). Entretanto, estudos recentes têm mostrado que a maioria dos macrófagos são derivados de progenitores embrionários (Naito *et al.*, 1997; Schulz *et al.*, 2012; Yona *et al.*, 2013; Ginhoux and Jung, 2014; Zigmond *et al.*, 2014) e o rastreamento de progenitores e linhagens de macrófagos residentes indicam que pelo menos três linhagens de macrófagos se diferenciam em camundongos em diferentes estágios do desenvolvimento, persistindo até a idade adulta. São elas: saco vitelínico, fígado fetal e medula óssea (Ginhoux *et al.*, 2010; Hoeffel *et al.*, 2012; Schulz *et al.*, 2012), como mostrado na Ilustração 1.

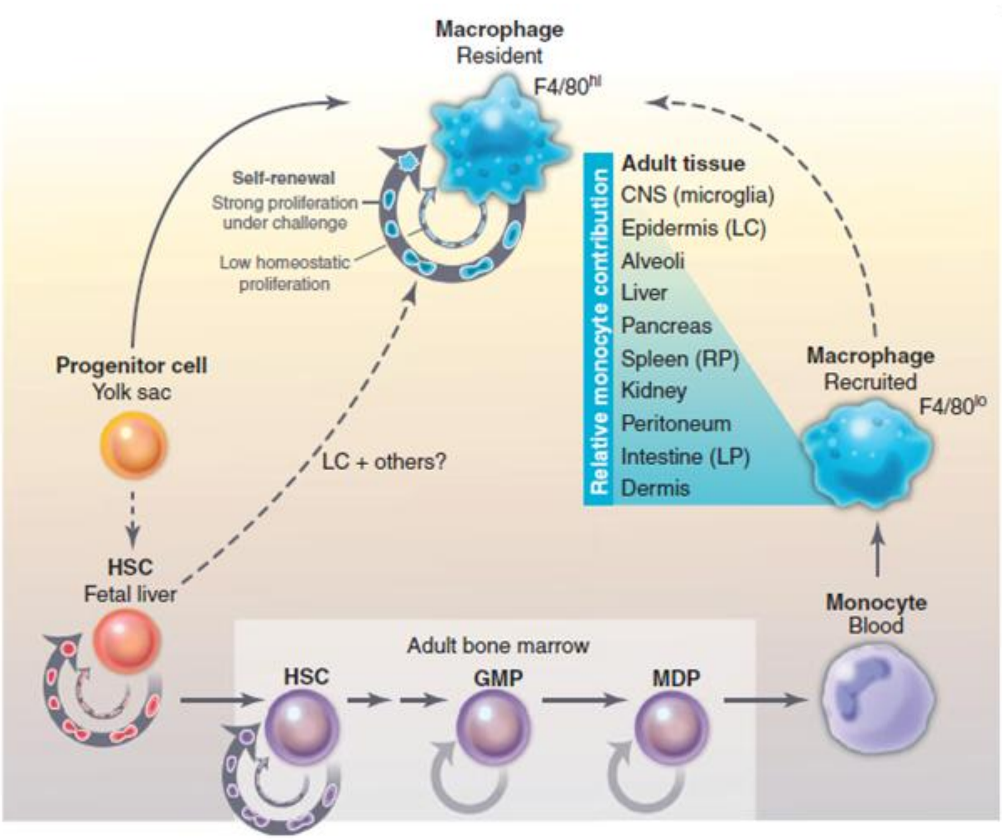
Macrophage
Resident
F4/80hi
Self-renewal
Strong proliferation under challenge
Low homeostatic proliferation
Adult tissue
CNS (microglia)
Epidermis (LC)
Alveoli
Liver
Pancreas
Spleen (RP)
Kidney
Peritoneum
Intestine (LP)
Dermis
Relative monocyte contribution
Progenitor cell
Yolk sac
LC + others?
Macrophage
Recruited
F4/80lo
HSC
Fetal liver
Monocyte
Blood
Adult bone marrow
HSC
GMP
MDP

Sieweke and Allen. *Science*, 2013

Ilustração 1: Macrófagos residentes apresentam três possíveis origens. Os macrófagos podem ser originados de progenitores do saco vitelino no início do desenvolvimento embrionário, de progenitores do fígado fetal e, finalmente, precursores da medula óssea. Uma vez estabelecidas, estas populações são mantidas por proliferação local ou recrutamento de monócitos, ou ambos. Em condições de homeostase, a contribuição relativa dos monócitos para a manutenção dos macrófagos residentes varia de acordo com o tecido.

Macrófagos residentes regulam a homeostase do tecido atuando como sentinelas e respondendo a alterações fisiológicas e a insultos externos. Durante as adaptações para manter a homeostase, macrófagos de diferentes fenótipos podem também ser recrutados de reservatórios como sangue, baço e medula óssea (Geissmann *et al*., 2010), e também a partir de progenitores presentes nos tecidos ou através de proliferação local (Jenkins *et al.*, 2011; Schulz *et al.*, 2012). Assim, macrófagos são um conjunto diversificado de células que mudam constantemente seu estado funcional para novos estados em resposta a alterações na fisiologia do tecido ou desafios do ambiente onde se encontram (Ginhoux *et al*., 2016). Portanto, macrófagos não deveriam ser agrupados em um único tipo celular, e sim subdivididos em diferentes subconjuntos funcionais de acordo com suas diferentes origens. Além disso, o estabelecimento dos perfis de transcrição de macrófagos residentes pelo Projeto Genoma mostrou que essas populações apresentam alta diversidade de transcrição com um mínimo de sobreposição, sugerindo que existem muitas classes únicas de macrófagos (Gautier *et al*., 2012).

Quando os tecidos são danificados por uma infecção, lesão ou inflamação, monócitos circulantes são recrutados e se diferenciam em macrófagos à medida que migram para o tecido afetado (Geissmann *et al.*, 2010; Lee *et al.*, 2010; Dal-Secco *et al.*, 2015). Estes macrófagos recrutados apresentam um fenótipo pró-inflamatório nas fases iniciais e secretam uma variedade de mediadores inflamatórios, incluindo o TNF-α, IL-1 e óxido nítrico, que ativam mecanismos de defesa antimicrobianos, incluindo processos oxidativos que contribuem para a eliminação de organismos invasores (Murray and Wynn, 2011). Também produzem IL-12 e IL-23, que promovem a diferenciação e expansão de células T_H1 e T_H17 (células T auxiliares que expressam o IFN-γ e IL-17), ajudando a guiar respostas inflamatórias. Embora estes macrófagos pró-inflamatórios sejam inicialmente benéficos por facilitarem o reconhecimento de organismos invasores, eles também desencadeiam dano tecidual (Nathan and Ding, 2010). Se a resposta inflamatória não é regulada devidamente, ela pode se tornar patogênica e contribuir para a progressão da doença, como é visto em muitas doenças inflamatórias e autoimunes (Krausgruber *et al.*, 2011). Em contrapartida, macrófagos apoptóticos, bem como aqueles que apresentam fenótipo anti-inflamatório ou resolutivo, atenuam a resposta inflamatória e ao mesmo tempo promovem o reparo tecidual (Murray and Wynn, 2011).

CÉLULAS DE KUPFFER

As células de Kupffer, macrófagos residentes no tecido hepático, foram identificadas por von Kupffer em 1876 e constituem a maior população de macrófagos residentes do organismo . Estão envolvidas no metabolismo de vários compostos, respostas imunológicas e reações inflamatórias (Decker, 1998; Arii and Imamura, 2000; Bottcher *et al.*, 2011; Heymann *et al.*, 2015). Encontram-se sobre as células endoteliais dentro dos sinusóides, o que as deixa completamente expostas ao conteúdo sanguíneo, e permite que fagocitem material diretamente da microcirculação hepática (Sleyster and Knook, 1982). As CKs em conjunto com as células endoteliais dos sinusóides hepáticos formam o maior sistema reticuloendotelial do corpo, que basicamente tem a função de capturar antígenos, microrganismos e células senescentes, e eliminá-los do sangue (Toth and Thomas, 1992; Seki *et al.*, 2000). Esta função de filtro impede que grandes quantidades de lipopolissacarídeo (LPS), restos celulares e microrganismos atinjam a circulação sistêmica, prevenindo a disseminação de patógenos em condições homeostáticas e patológicas (Toth and Thomas, 1992; Seki *et al.*, 2000; Thomson and Knolle, 2010). Ademais, são cruciais na defesa do hospedeiro contra bacteremia, uma vez que são responsáveis pela eliminação de 70-80% das bactérias que entram na corrente sanguínea.

Embora o tecido hepático seja uniforme a nível histológico, este é heterogêneo em relação à morfometria e histoquímica. CKs localizadas nas regiões periportais (Zonas Sinusoidais) diferem das células das regiões centrolobulares (Zonas Pericentrais) em várias enzimas, receptores e estruturas subcelulares. São cerca de duas vezes mais abundantes nas regiões periportais se comparadas às regiões centrolobulares (Sleyster and Knook, 1982; Decker, 1998; Arii and Imamura, 2000; Laskin *et al.*, 2001). As células das regiões periportais são maiores, possuem maior atividade de enzimas lisossomais, apresentam maior capacidade fagocítica e produzem menos ânion superóxido (Sleyster and Knook, 1982). Por outro lado, células das regiões centrolobulares são mais reativas a processos inflamatórios. Assim, a heterogeneidade funcional e o tamanho das CKs estão relacionados à sua localização nos lóbulos hepáticos (Sleyster and Knook, 1982).

Apesar da perspectiva de que CKs são macrófagos fixos no tecido, há evidências de que elas têm a capacidade de migrar ao longo das paredes sinusoidais com uma velocidade média de ~ 4,6 micrômetros/minuto (Macphee *et al.*, 1992). Macrófagos hepáticos estão envolvidos ainda na patogênese de lesões hepáticas mediadas por substâncias químicas, toxinas e agentes farmacológicos (Gregory and Wing, 2002; Su, 2002), como tetracloreto de carbono (CCl4), endotoxinas, galactosamina e paracetamol (APAP) através da liberação de substâncias biologicamente ativas que promovem o processo inflamatório (Su, 2002). Em lesões hepáticas e necrose hepatocelular, CKs ativadas são uma importante fonte de mediadores inflamatórios incluindo citocinas, superóxido, óxido nítrico, enzimas lisossomais e proteolíticas e demonstram aumento de citotoxicidade e quimiotaxia.

Macrófagos infiltrados e residentes desempenham um papel fundamental no reparo da vasculatura hepática e na recuperação global do tecido (Arii and Imamura, 2000). Macrófagos residentes produzem fatores angiogênicos que promovem a proliferação e migração de células do endotélio dos sinusóides (You *et al.*, 2013). Além disso, a produção de quimiocinas tais como a proteína inflamatória de macrófagos (*macrophage inflammatory protein* - MIP-2), que induz a proliferação de hepatócitos, também tem uma função protetora em modelos de lesão induzida por APAP (Hogaboam, Bone-Larson, *et al.*, 1999; Hogaboam, Simpson, *et al.*, 1999; Bone-Larson *et al.*, 2000). Esta proteção também é mediada, possivelmente, pela produção de

IL-10 e IL-18, uma vez que a depleção dessas células aumenta a susceptibilidade do fígado murino ao APAP (Ju *et al*., 2002).

Os macrófagos residentes "originais" presentes no fígado após o nascimento são originados no início do desenvolvimento embrionário, a partir de precursores do saco vitelínico (Gomez Perdiguero *et al*., 2015). Após semearem o fígado fetal, são mantidos por proliferação local com pouca ou nenhuma contribuição relativa de monócitos ao longo da vida adulta (Sieweke and Allen, 2013; Yona *et al.*, 2013). Porém, esse padrão é alterado quando há dano tecidual. Em situações de desequilíbrio, monócitos são recrutados para o fígado em quantidade diretamente proporcional á extensão do insulto como mostrado na Ilustração 2 (Ginhoux and Jung, 2014). Esses monócitos podem, então, atuar na resolução/restauração tecidual e, em seguida, serem eliminados ou se diferenciarem em macrófagos (MOMs) e permanecerem no tecido (Ginhoux and Jung, 2014). Embora muitos estudos sejam voltados para tal fim, pouco se sabe das possíveis consequências da substituição parcial e gradativa de CKs por MOMs uma vez que ainda não está claro se monócitos infiltrados se diferenciam de forma plena em macrófagos residentes originais.

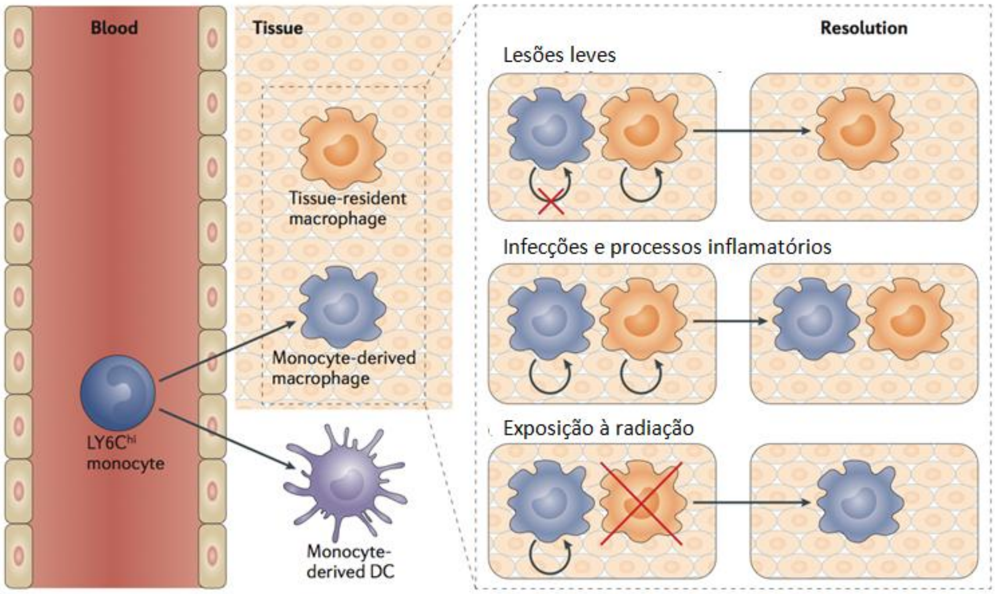

Ginhoux and Jung. *Nature*, 2014

Ilustração 2: Monócitos são recrutados para os tecidos a fim de repor a população de macrófagos residentes originais em quantidade diretamente proporcional á extensão do insulto. Em lesões leves que levam a moderada ou nenhuma perda de macrófagos residentes, ou quando poucos ou nenhum monócito sanguíneo é recrutado, o repovoamento, caso necessário, ocorre exclusivamente a partir da população endógena, por proliferação local. Em infecções e processos inflamatórios ocorre repovoamento a partir de monócitos derivados do sangue e também por proliferação local, o que conduz a uma situação de 'macrófagos quimera' com compartimentos de macrófagos que são misturadas, tanto de origem embrionária e quanto mielóide. No entanto, não se compreende ainda plenamente se estes macrófagos derivados de monócitos persistem e tornam-se totalmente integrados aos macrófagos originais, ou se eles são um complemento temporário para a população endógena. No caso de lesões inflamatórias graves que conduzem a uma grande perda de macrófagos residentes ou a supressão parcial da sua capacidade de auto-renovação, tais como o transplante de medula óssea e exposição à radiação, ocorre repovoamento a partir de monócitos do sangue.

CÉLULAS DENDRÍTICAS

No início de 1970, Ralph Steinman e Zanvil Cohn identificaram uma população de células hematopoiéticas no baço de ratos que se destacaram por sua capacidade de apresentação de antígenos e estimulação de células T, denominadas células dendríticas (CDs) (Steinman and Cohn, 1973). Similar a algumas populações de macrófagos, CDs derivam de progenitores hematopoiéticos e são encontradas em tecidos linfoides e não linfóides (Haniffa *et al.*, 2013). Inicialmente acreditou-se que tais células apresentavam baixa capacidade fagocítica. Porém, existem evidências que CDs possuem grande atividade fagocítica que é em grande parte dedicada a informar o sistema imunológico adaptativo sobre alterações em tecidos periféricos. Após fagocitar antígenos presentes nos tecidos essas células migram para os nódulos linfáticos onde apresentam tais antígenos e ativam células T (Mellman and Steinman, 2001).

CDs são classificados em dois subconjuntos principais que incluem CDs clássicas e plasmocitóides (Heath and Carbone, 2009). Em condições de repouso em tecido não-linfóides, as células dendríticas plasmocitóides têm sua capacidade fagocítica e de apresentação de antígenos limitadas (Villadangos and Young, 2008). CDs clássicas formam uma população heterogênea de células hematopoiéticas. Um dos maiores desafios para compreender os mecanismos moleculares que controlam as funções atribuídas às CDs tem sido a falta de marcadores específicos para definir suas linhagens. Por esse motivo, CDs continuam a serem definidas como células hematopoiéticas que expressam quantidades elevadas de MHC de classe II (partilhada por células B ativadas e macrófagos) e da integrina CD11c (também expressa por algumas populações de macrófagos, células T ativadas, células B e células NK) (Hashimoto *et al.*, 2011).

Os monócitos podem ser facilmente diferenciados em CDs *in vitro* (Sallusto and Lanzavecchia, 1994), mas a contribuição exata de monócitos para o *pool* de CDs em condições de repouso permanece obscura. Em contraste com estados de repouso, a diferenciação de monócitos em CDs aumenta dramaticamente nos tecidos inflamados.

RELEVÂNCIA DE ESTUDOS DE FAGÓCITOS MONONUCLEARES *IN VIVO*

O programa de transcrição que controla a diferenciação de monócitos em macrófagos foi recentemente revisto (Auffray *et al.*, 2009; Geissmann *et al.*, 2010). Contudo, a maioria dos estudos sobre a regulação da transcrição da diferenciação de macrófagos foram feitos *in vitro* com enriquecimento de populações de progenitores. Ainda, a maior parte dos estudos que caracterizaram e definiram populações e fenótipos de macrófagos foram feitos com purificação e isolamento de células (por exemplo, por digestão) e imunofenotipagem por citometria de fluxo. Embora esses estudos tenham vantagens em termos de segregação populacional por ocorrência simultânea ou ausência de marcadores celulares de interesse, tais métodos tem como limitante inerente a perda da localização original e a morfologia das células no órgão de interesse. De fato, nestes estudos as células são analisadas fora do seu contexto natural. Logo, o papel exato desses fatores de transcrição na condução do processo de diferenciação de monócitos em subconjuntos distintos de macrófagos *in vivo* ainda necessita de mais esclarecimentos. Isto é particularmente importante dado que a especialização funcional de macrófagos seja, provavelmente, regulada a nível tecidual (Van De Laar *et al.*, 2016).

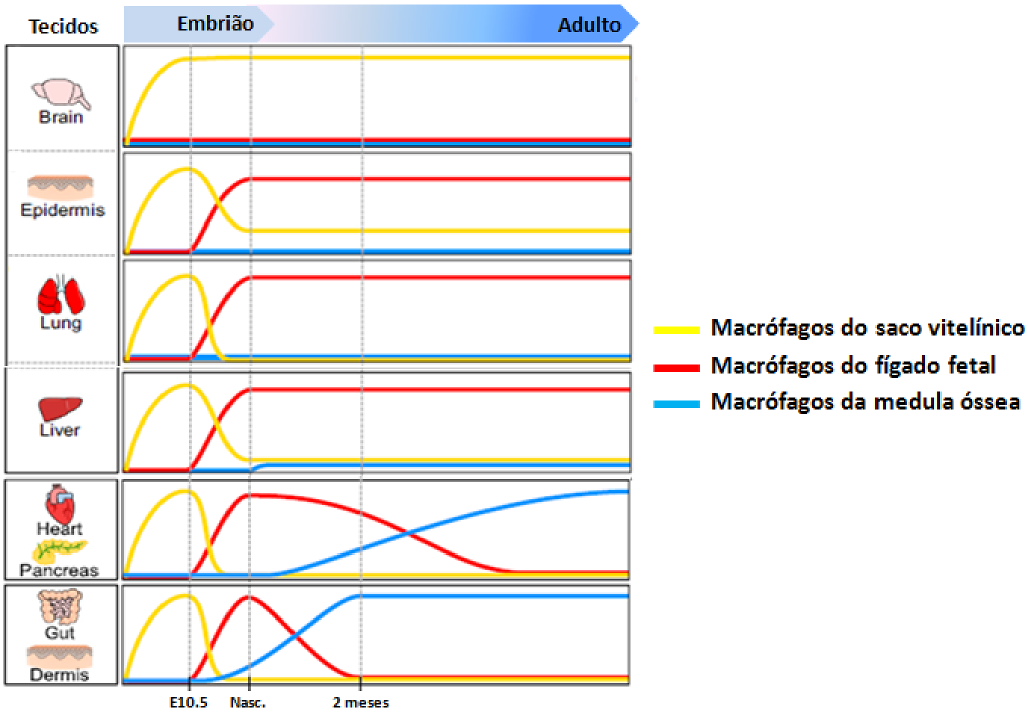

Guinhoux and Guilliams, *Immunity*, 2016

Ilustração 3: Heterogeneidade na ontogenia de macrófagos residentes durante a homeostase em tecidos de indivíduos adultos. No cérebro, os macrófagos presentes no tecido adulto (microglia) são originados de precursores do saco vitelínico e não há contribuição de monócitos para manutenção da população endógena em condições normais. Na epiderme, a população de macrófagos residentes (células de Langerhans) é mista, com células originadas no saco vitelínico e no fígado fetal. Os macrófagos alveolares presentes no pulmão de indivíduos adultos por sua vez, têm origem no saco vitelínico, mas são substituídos por precursores do fígado fetal no fim do período embrionário. Isso também acontece no fígado. Entretanto, a população de macrófagos hepáticos (células de Kupffer) recebe uma pequena contribuição de monócitos da medula óssea após o nascimento. Órgãos como coração, pâncreas, intestino e derme têm seus macrófagos do saco vitelínico substituídos por progenitores do fígado fetal que, por sua vez, são substituídos por monócitos originados na medula óssea ao longo da vida.

JUSTIFICATIVA DO TRABALHO

O fígado é um órgão-chave para a maturação de células imunes durante a embriogênese (Epelman *et al*., 2014, Ginhoux e Jung, 2014) e também desempenha um papel essencial na vigilância imunológica ao longo da vida (Lee *et al*., 1999). O ambiente hepático compreende uma vasta população de células imunes, incluindo células *natural killer* (NK) (Wisse *et al*., 1976) e NKT (Bendelac *et al*., 2007), células dendríticas (CDs) (Thomson *et al*., 2002) e macrófagos (Células de Kupffer - CKs) (Jenne e Kubes, 2013). Para realizar importantes funções imunes, os fagócitos hepáticos estão estrategicamente posicionadas em diferente compartimentos hepáticos. As células de Kupffer estão localizadas especificamente no lúmen sinusoidal, onde estão constantemente expostas ao conteúdo sanguíneo, ingerindo eritrócitos evelhecidos (Lee *et al*., 2011; Terpstra e van Berkel, 2000) e capturando patógenos que possam se espalhar pela corrente sanguínea levando a infecção sistêmica (Balmer *et al*., 2014; Wong *et al*., 2013). Estudos recentes demonstraram que os macrófagos povoam o fígado durante a embriogênese advindos de progenitores do fígado fetal e este conjunto de células residentes é mantido na idade adulta principalmente por proliferação local e, em menor grau, via recrutamento de progenitores derivados da medula óssea como mostrado na Ilustração 3 (Ginhoux and Guilliams, 2016). De fato, existem evidências crescentes de que a população de células de Kupffer é composta principalmente por células que se assemelham aos precursores embrionários, e diferente de células hematopoiéticas (Schulz *et al*., 2012; Yona *et al*., 2013). Contudo, monócitos circulantes migram para um fígado desprovido de células de Kupffer (por exemplo, pós lesão hepática) e dão origem a macrófagos que se assemelhem geneticamente à células de Kupffer originais ao longo do tempo (Scott *et al*., 2016).

De maneira interessante, as células dendríticas, que também povoam o ambiente hepático, desenvolvem-se a partir de células-tronco hematopoiéticas derivadas da medula óssea, mas precursores de monócitos circulantes também podem contribuir para a população de células dendríticas residentes (Liu e Nussenzweig, 2010). Uma pequena população de células dendríticas hepáticas foi previamente descrita (Matsuno *et al*., 1996, Sato *et al*., 1998, Woo *et al*., 1994). No entanto, ainda são necessários estudos *in vivo* direcionados a definir precisamente a localização e a densidade real destas células no fígado, bem como a sua relação com outras células hepáticas. Além disso, apesar de serem descritos como fagócitos, a capacidade de células dendríticas de fagocitar e destruir patógenos continua elusiva (Waite *et al*., 2011).

As populações de células de Kupffer e dendríticas hepáticas na idade adulta são, portanto, uma combinação de precursores derivados da fase embrionária e de células derivadas de monócitos da medula óssea. Ainda, é muito provável que múltiplos fatores definam a extensão da contribuição diferencial dessas duas fontes de células (Ginhoux e Jung, 2014). No entanto, durante o "repovoamento emergencial" - um termo que cunhamos neste trabalho para explicar uma situação onde há perda súbita de fagócitos hepáticos devido a ingestão de toxinas, patógenos (por exemplo, *Listeria*) ou trauma - a auto-replicação de precursores não é mais uma opção. Sob condições fisiológicas, as citocinas secretadas pelos fagócitos hepáticos contribuem para regular o *millieu* hepático, induzindo tolerância hepática a produtos bacterianos oriundos do intestino que normalmente chegam via circulação portal (Knolle *et al*., 1995). Além disso, estas citocinas podem conferir um certo grau de tolerogenicidade às células dendríticas hepáticas, inibindo a sua completa maturação e sua capacidade de estimular linfócitos T (Lau e Thomson, 2003). De fato, a depleção de fagócitos hepáticos, ou a redução parcial da sua densidade, está associada com a quebra de tolerância contra antígenos (Heymann *et al*., 2015), bem à uma resposta imune exacerbada à lesão hepática induzida por fármacos (Holt *et al*., 2010) e ainda durante a fibrose (Connolly *et al*., 2011, Connolly *et al*., 2009). Neste trabalho nós utilisamos uma combinação de imunofetipagem de alta-dimensão com abordagens de imagem *in vivo* para determinar precisamente as populações fagocíticas hepáticas e as consequências funcionais da sua remoção química seguida da substituição das células originais por células advindas da medula óssea.

2. OBJETIVOS

2.1. Objetivo principal

Elucidar a dinâmica de repovoamento de fagócitos hepáticos e as consequências da substituição dos mesmos.

2.2. Objetivos específicos

a) Determinar as populações de células não-parenquimais presentes no fígado na homeostase;

b) Analisar a dinâmica de repovoamento de fagócitos hepáticos após um modelo de depleção total dessas células;

c) Estabelecer possíveis alterações no ambiente hepático em decorrência da ausência e substituição dos fagócitos residentes;

d) Investigar as consequências funcionais para o órgão na ausência dessas células e durante o processo de repovoamento.

3. METODOLOGIA

3.1. Animais

Camundongos C57BL/6 *wild type*, LysM-EGFP (Lyz2$^{\text{tm1.1Graf}}$), B6 ACTb-EGFP (C57BL/6$^{\text{Tg(CAG-EGFP)1Osb/J}}$, beta-actina de galinha), CCR2$^{-/-}$ (B6.129S4-CCR2$^{\text{tm1Ifc}}$/Jand), CD11c-EYFP (NOD.$^{\text{Cg-Tg(Itgax-Venus)1Mnz/QtngJ}}$) foram obtidos do Centro de Bioterismo da Universidade Federal de Minas Gerais (CEBIO - UFMG, Brasil). Os camundongos Swiss/NIH *germ-free* foram derivados de um núcleo livre de germes (Taconic Farms). CD11c-EYFP-DTR, CX3CR1$^{\text{gfp/gfp}}$ e CX3CR1$^{\text{gpf/wt}}$ (B6.129P-$^{\text{Cx3cr1tm1Litt/J}}$) foram cedidos pela *facility* da Universidade de Calgary (Alberta, Canadá). Os camundongos CX3CR1-DTR-EYFP (B6.129P2$^{\text{(Cg)-Cx3cr1tm2.1(cre/ ERT2) Litt/WganJ}}$) foram cedidos pela *facility* do Instituto de Medicina de Harvard (Boston, MA, EUA). Além desses, geramos em nosso laboratório, o animal CCR2$^{\text{rfp/wt}}$ CX3CR1$^{\text{gpf/wt}}$CD11c-EYFP com tripla fluorescência através do cruzamento do animal duplo *knockout* CCR2$^{\text{rfp/rfp}}$CX3CR1$^{\text{gfp/gfp}}$ com o animal CD11c-EYFP. Os camundongos que expressam o receptor da toxina diftérica (TD) receberam tamoxifeno (10 mg por camundongo, diluído em óleo de amendoim, i.p.) durante 5 dias consecutivos e tratados com TD (500 ng por camundongo, diluído em PBS estéril, i.p.) durante 2 dias consecutivos para depleção seletiva de células previamente aos experimentos. Os animais foram acondicionados em grupos de cinco por gaiola, com ração (Labina) e água *ad libitum*, em condições controladas de temperatura (25ºC) e luminosidade (ciclo claro/escuro de 12/12h). Os procedimentos experimentais realizados estão de acordo com as normas dos Comitês Permanentes de Animais em todas as instituições e do Comitê de Ética em Experimentação Animal da UFMG (CETEA protocolo 051/11).

3.2. Microscopia confocal e imunohistoquímica

Os procedimentos para microscopia intravital confocal foram realizadas como descrito por MARQUES *et al*., 2015. Anteriormente à cirurgia, os camundongos receberam uma dose única ou uma mistura dos seguintes anticorpos ou sondas fluorescentes: anti-F4/80 PE (4 µg, clone BM8, eBiosciences, EUA) CD31 BV-421 (4 µg, clone MEC 13.3, BD Horizon, EUA), anti-CX3CL1 PE (60 µl por camundongo, eBiosciences, EUA), DAPI (0,1 ml a 1 mM, Sigma, EUA), albumina FITC (0,1 ml a 5 mg por ml). Os fragmentos de fígado também foram corados com anti-podoplanina PE (solução 1:50, Biolegend, EUA), anti-GFP (solução 1:50, Santa Cruz, EUA) ou anti-desmina (1:50, Dako, EUA) para imagens *ex vivo*. Utilizou-se goat anti-mouse conjugado com Alexa Fluor 586 como anticorpo secundário para os experimentos com anti-desmina (1:50, Thermo Fisher Scientific, EUA). A autofluorescência de vitamina A foi visualizada utilizando um laser a 405 nm. Os camundongos foram fotografados utilizando microscópio confocal Nikon Eclipse T*i*. A densidade celular, localização e reconstrução 3D foram feitas usando Volocity (6.3) Perkin Elmer, EUA.

3.3. Células hepáticas não-parenquimais (*liver non-parenchimal cells* - LNPCs)

As células hepáticas não-parenquimais foram isoladas como descrito por DAVID *et al*., 2016. Os fígados foram digeridos com solução de colagenase (10 mg/ml) e as células foram separadas por centrifugação diferencial. Para os experimentos de CyTOF, 1x10^6 células foram coradas com anticorpos conjugados com diferentes isótopos como descrito previamente (David, Rubino, *et al.*, 2016). Os eventos foram analisados dentro de células CD45$^+$, e células T e B, hemácias e *hepatic stellate cells* (HSCs) foram excluídas da análise. A frequência das células NK (CD3$^-$NKp46$^+$NK1.1$^+$) foi investigada por citometria de fluxo. A ausência de HSCs nestas amostras foi também verificada por RT-PCR. A lista completa do painel de anticorpos e genes utilizados em RT-PCR (sondas Taqman) pode ser encontrada nas Tabelas 1 e 2, respectivamente. As amostras foram adquiridas no equipamento *Helios Mass Cytometer* (Fluidigm) e os dados foram plotados utilizando a análise viSNE.

Para os experimentos de *Nanostring*, LNPCs foram isoladas de camundongos CX3CR1$^{gfp/wt}$ e corados com anti-F4/80 APC (1: 100, clone BM8, eBiosciences, EUA). As amostras foram adquiridas utilizando o separador de células FACSAriaTMIII e os *gates* foram feitos em F4/80$^+$CX3CR1$^-$ para células intravasculares e F4/80$^-$CX3CR1$^+$ para células extravasculares. Como controle externo, foram utilizados macrófagos peritoniais recolhidos da cavidade peritonial três dias após injeção i.p. de 1 ml de tioglicolato 4% e células dendríticas do baço F4/80$^-$CD11c$^+$ também separadas por utilizando o FACSAriaTMIII. Aproximadamente 1x10^5 de cada tipo de celular foi separado, e cada amostra consistiu num pool de 2 camundongos, e 3 amostras foram analisadas independentemente.

3.4. Animais quimera - medula óssea GFP

Camundongos C57BL/6 *wild type* foram previamente expostos a uma dose subletal (9 grays) de radiação ionizante dividida em duas doses consecutivas de 4 + 5 grays, com intervalo de três horas entre elas. Para reconstituir a medula desses animais, cada um deles recebeu, por via endovenosa, $1x10^7$ células retiradas da medula óssea de camundongos B6 ACTb-EGFP (β-actina GFP).

Para a retirada de células da medula camundongos B6 ACTb-EGFP (β-actina GFP) foram previamente anestesiados e tiveram os ossos dos membros posteriores (fêmur e tíbia) retirados para extração da medula óssea. As células da medula foram removidas utilizando uma agulha e meio de cultura RPMI (*Roswell Park Memorial Institute medium*) gelado para lavar o interior dos ossos. Após a retirada, as células foram contadas e mantidas em meio de cultura gelado até o momento da transferência para os animais irradiados.

3.5 Microcirculação hepática

Para elucidar as estruturas e o arranjo dos componentes da vasculatura hepática, realizamos o procedimento para microscopia intravital e após posicionar o camundongo no microscópio injetamos 100 µl de FITC albumina (5mg/ml) filmando sem intervalos os 10 minutos subsequentes. O vídeo mostra o sentido do fluxo sanguíneo no tecido e nos permitiu, consequentemente, determinar as regiões de espaço porta (entrada do sangue) e veias centrolobulares (saída do sangue).

3.6. Modelo de depleção com clodronato (CLL)

Para depleção de macrófagos e células dendríticas hepáticos, camundongos foram tratados com 200 µl i.v. de clodronato (CLL) encapsulado em lipossomos em uma solução a 5mg/ml em suspensão. A depleção foi observada, em média, 48 horas após o tratamento e confirmada por microscopia intravital.

3.7. Tratamento com toxina diftérica

Os camundongos CD11c-DTR e CX3CR1-DTR, e seus respectivos controles, receberam um volume final de 100 µl de solução i.p. contendo 1µg de toxina diftérica (Diphtheria Toxin from *Corynebacterium diphtheriae*, Sigma) diluídos em PBS 1x.

3.8. Modelo de lesão hepática

Os camundongos foram submetidos a um jejum de 15 horas na noite anterior ao experimento e então tratados com paracetamol (APAP), por via oral, dissolvido em salina estéril aquecida (600 mg/kg). Animais controle receberam apenas o veículo aquecido. Para a coleta de amostras, os animais foram anestesiados com uma injeção i.p. de ketamina e xilazina e submetidos a uma laparotomia. O sangue foi coletado para obtenção do soro e o fígado foi retirado e dividido em fragmentos para a realização de histologia (H&E) e ensaios bioquímicos.

Para determinar a atividade de alanina aminotransferase (Jagger *et al.*) no soro utilizamos o kit transaminase ALT cinético (Bioclin). O ensaio cinético é o método recomendado pela *International Federation of Clinical Chemistry*.

3.9. Medida de função hepática por depuração de verde de indocianina (ICG - *indocyanine green*)

Os camundongos receberam, por via endovenosa, 20 mg/kg de verde de indocianina diluída em água de injeção. Exatos vinte minutos após a injeção, os animais foram anestesiados por via endovenosa e submetidos a uma laparotomia para retirada do sangue. O sangue foi centrifugado a 7000 rpm por 15 minutos para obtenção do soro. Em placas de 96 poços, plaqueamos 240 µl de soro puro por poço, e nas diluições de 1:5 e 1:10 . Foi feita uma curva padrão de oito pontos com diluições seriadas de 1:2, sendo o primeiro ponto a 100 µg/ml. A leitura foi realizada em 800 nm. Os valores obtidos equivalem à quantidade de corante não depurado em µg por ml de sangue.

3.10. Avaliação histológica do fígado

Os fígados foram lavados com salina e seu lobo inferior foi fixado em formol 4% tamponado. Posteriormente, as amostras foram desidratadas em soluções de álcool etílico, banhadas em xilol e incluídas em blocos de parafina histológica. Cortes teciduais de 6 µm de espessura foram obtidos utilizando um micrótomo e corados com hematoxilina & eosina (H&E). A visualização dos cortes foi feita em um microscópio óptico BX41 (Olympus) e as imagens obtidas utilizando uma câmera Moticam 2500 (Motic) e o *software* Motic Image Plus 2.0ML.

3.11. Injeção sistêmica de *E. coli*

Escherichia coli GFP (ATCC® 25922GFP) foram cultivadas em meio LB (MP Biomedicals). Para experimentos de citometria de fluxo, os camundongos receberam $5x10^6$ *E. coli* por via intravenosa e recolheu-se sangue após 5 minutos. As amostras de sangue foram imediatamente diluídas em PBS (*phosphate buffer solution*) 1x (1:20) e lidas no citômetro. Para imagens *in vivo* da captura de *E. coli*, os camundongos receberam por via intravenosa $5x10^7$ bactérias e foram filmados em microscópio confocal durante 10 minutos.

3. 12. Dosagem de citocinas por Multiplex

Amostras de fígado foram pesadas (50 mg de tecido do lobo esquerdo) e homogeneizadas com 450 µl de solução (PBS 1x, 0,2% Triton e 1:25 de inibidor de protease). Em seguida, as amostras foram centrifugadas a 12.000 rpm por 10 minutos a 4°C e o sobrenadante recolhido e utilizado para dosagem das citocinas. A concentração de citocinas no sobrenadante foi quantificada seguindo as instruções do fabricante (Milliplex MCYTOMAG-0K-32. Kit de Citoquina MAGNETICA de camundongo).

3.13. Análise dos dados de expressão gênica

A abundância na expressão gênica foi obtida por *Nanostring nCounter mouse Immunology Assay*. A correlação de expressão gênica entre os diferentes tipos de células foi calculada e plotada como *heatmap* usando a plataforma R. Os genes expressos diferencialmente foram identificados pelo *DESeq2 R Package*. Os resultados estaticamente relevantes consistem em valores de p <0,05 e uma variação de pelo menos 50% superior ou inferior. A classificação funcional foi realizada por associação cruzada utilizando as bases de dados *KEGG Pathways e KEGG Brite*.

3.14. Análise estatística

A comparação entre dois grupos foi feita pelo teste T de Student. No caso de três ou mais grupos, o teste foi one-way ANOVA, com pós-teste de Tukey. No caso de os dados não possuírem distribuição normal, o teste de Mann-Whitney (para dois grupos) ou Kruskal-Wallis (para três ou mais) seguido do pós-teste de Dunn foram aplicados. Todos os resultados foram apresentados como a média ± erro padrão da média (epm), e são referentes a pelo menos dois experimentos independentes, contendo no mínimo 3 replicatas. O nível de significância foi definido como p<0.05. Os gráficos e estatística foram feitos com o auxílio do programa GraphPad Prism 6.

4. RESULTADOS

* Os resultados a seguir foram publicados na revista *Gastroenterology* (fator de impacto 18.2) em 2016 como resultado da presente tese de doutorado. Artigo completo em anexo.

4.1. High dimensional identification of liver phagocytes

To better characterize the resident phagocytic populations, we purified liver non-parenchymal cells ($CD45^+$ LNPCs) and performed time-of-flight mass cytometry (CyTOF) analysis. CyTOF allows for simultaneous staining with multiple combinations of cell markers, and can reveal new immune cell populations that would not otherwise be uncovered by conventional flow cytometry. In these experiments, we gated on $CD45^+$ cells and excluded red blood cells, Ito cells and B and T cells during analysis. Using an unbiased viSNE analysis to map high-dimensional cytometry data, we identified twelve clusters of LNPCs (**Fig. 1A**). The majority of cells mapped to either F4/80 (clusters 1-4) or CD11c (clusters 5-8) (**Fig. 1A and B**). Cluster 1 was defined as mature granulocytes due to intermediate expression level of Ly6G (**Fig. 1A and B**) and high expression of CD24 (**Fig. 2A**). Based on the expression of F4/80, MHCII and CD11b (**Fig. 1A and B**), we defined two different populations of Kupffer cells (clusters 2 and 3). KC cluster 2 expressed CD206, CD317 and CD1d whereas cluster 3 was negative for CD206, CD317 and CD1d, but expressed CD11c (**Fig. 1A** and **Fig. 2A**). Cluster 4 and 5 were characterized as infiltrating monocytes, since they were $CD11b^+Ly6C^+MHC\text{-}I^{int}MHC\text{-}II^{lo}$, but cluster 5 was $F4/80^-$ and $CD11c^{lo}$ (**Fig. 1A and B**). Clusters 6-8 and 11 were categorized as DCs, since they were $CD11c^+CD11b^{int/hi}F4/80^-Ly6G^-MHC\text{-}I^+MHC\text{-}II^{+/lo}$. Cluster 8 was defined as plasmacytoid dendritic cells (pDCs) due to their high expression of the pDC marker CD317 (**Fig. 1A and B**). Cluster 9 was also defined as granulocytes according to their high expression of Ly6G, CD11b and Gr1 as well as intermediate expression of CD24 and Ly6C (**Fig. 1A and 1B** and **Fig. 2A**). Finally, cells that expressed the high affinity IgE receptor (FcεRI), together with CD44 and CD11b, were clustered as basophils (cluster 10) (**Fig. 1A and B** and **Fig. 2A**). Cluster 11 may represent a population of conventional DCs due to the expression of CD11c, CD11b, CD8a and CD103 (**Fig. 1A and B** and **Fig. 2A**). $CD11c^+$ NK cells (NK1.1 and NKp46) comprised an insignificant population in this setup (<0.2%) and were not considered during analysis (**Fig.

2B). Cluster 12 could not be categorized using the markers chosen for this experiment. A schematic clustering explanation is depicted in **Fig. 1A.**

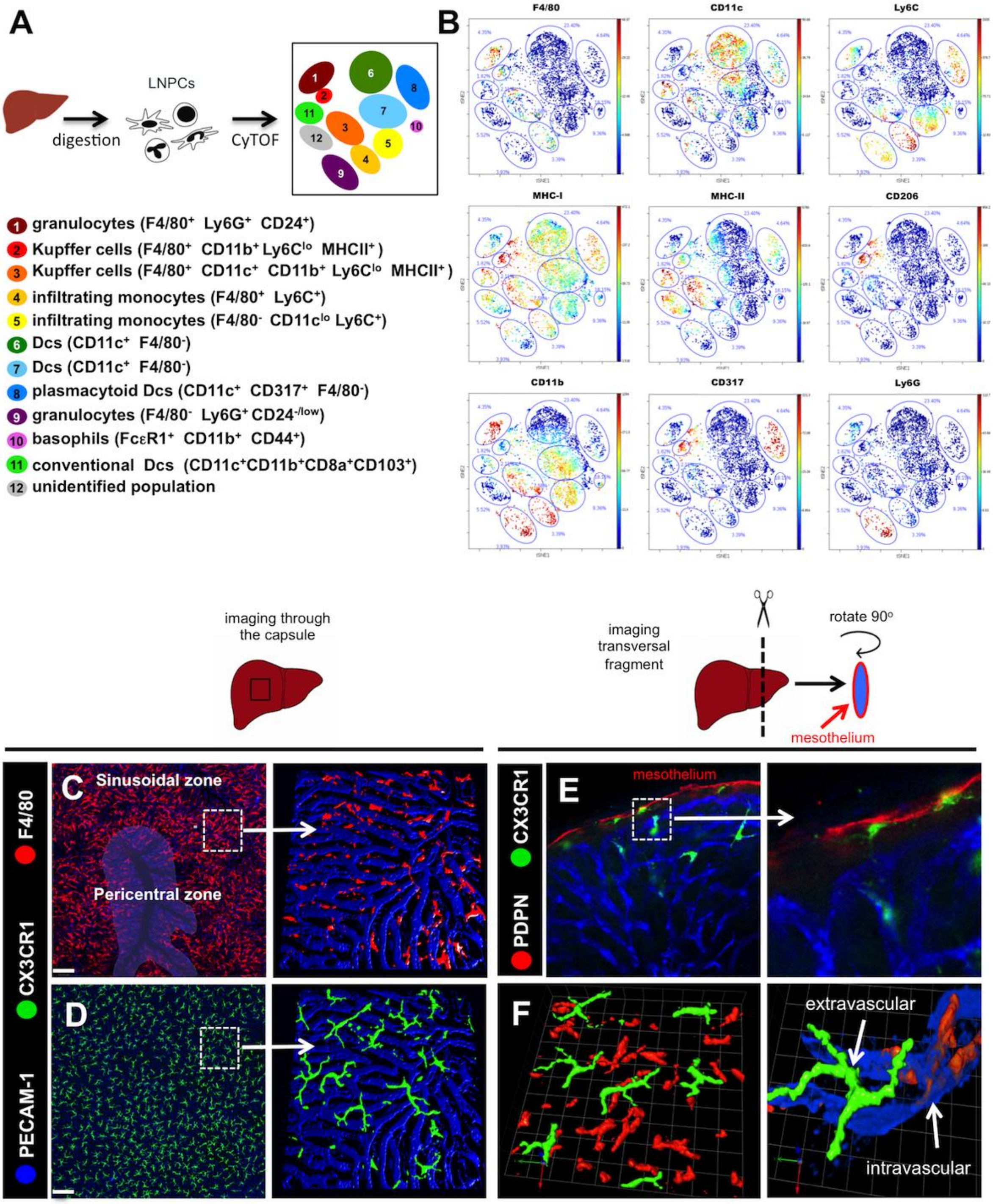
A
LNPCs
digestion
CyTOF
1
2
3
4
5
6
7
8
9
10
11
12
1 granulocytes (F4/80+ Ly6G+ CD24+)
2 Kupffer cells (F4/80+ CD11b+ Ly6Clo MHCII+)
3 Kupffer cells (F4/80+ CD11c+ CD11b+ Ly6Clo MHCII+)
4 infiltrating monocytes (F4/80+ Ly6C+)
5 infiltrating monocytes (F4/80- CD11clo Ly6C+)
6 Dcs (CD11c+ F4/80-)
7 Dcs (CD11c+ F4/80-)
8 plasmacytoid Dcs (CD11c+ CD317+ F4/80-)
9 granulocytes (F4/80- Ly6G+ CD24-/low)
10 basophils (FcεR1+ CD11b+ CD44+)
11 conventional Dcs (CD11c+CD11b+CD8a+CD103+)
12 unidentified population
B
F4/80
CD11c
Ly6C
MHC-I
MHC-II
CD206
CD11b
CD317
Ly6G
imaging through the capsule
imaging transversal fragment
rotate 90°
mesothelium
F4/80
CX3CR1
PECAM-1
C
Sinusoidal zone
Pericentral zone
D
CX3CR1
PDPN
E
mesothelium
F
extravascular
intravascular

Figure 1: Identification of liver phagocytes by CyTOF and intravital microscopy. (**A**) Schematic representation of isolation liver non-parenchymal cells (LNPC) and clustering after CyTOF analysis. (**B**) Dot plot representation of viSNE analysis showing different clusters and the expression of several different surface markers that enable the distinction of immune populations. (**C**) Liver confocal intravital microscopy imaging through the capsule evidencing the distribution of F4/80$^+$ cells (Kupffer cells; in red; anti-F4/80) in different liver regions. (**D**) Same as **C** but for CX3CR1$^+$ cells (CX3CR1$^{gfp/wt}$ mice). (**E**) *Ex vivo* imaging of liver fragment revealed that DCs (CX3CR1$^+$ cells) are mainly located under the mesothelium (stained with anti-podoplanin). (**F**) 3D rendering of F4/80$^+$ (intravascular) and CX3CR1$^+$ cells (extravascular) showing their different spatial location. Scale bars, 120 µm. Error bars indicate the mean (± s.e.m.). *$P < 0.05$ (unpaired *t*-test). N=5/group.

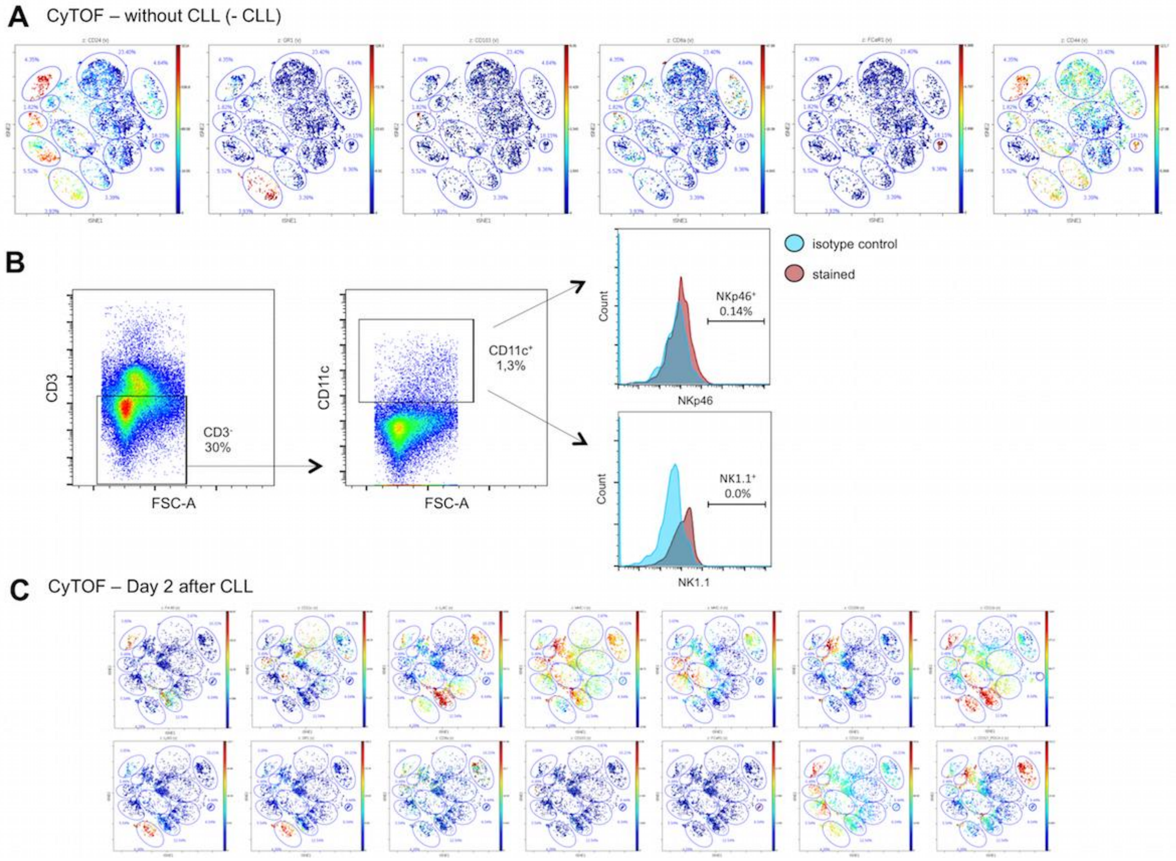

Figure 2: Additional CyTOF analysis and NK frequency in LNPCs. (A) Additional dot plots from CyTOF analysis from untreated group. (**B**) Gating strategy for assessment of CD11c^{+} NK cells frequency in liver non-parenchymal cells samples. CD11c^{+} NK cells were defined as CD3^{-}CD11c^{+}NKp46^{+}NK1.1^{+} events. (**C**) Additional dot plots from CyTOF analysis from mice 2 days after CLL treatment.

To spatially resolve the location and the relationship between the main F4/80$^+$ and CD11c$^+$ populations, we imaged the liver by confocal intravital microscopy (Marques *et al.*, 2015). We first identified the main vascular arrangements that could constitute points of reference for the location of different liver immune cells (**Fig. 3** and **Supplementary Movie 1**). Based on *in vivo* blood flow tracking, two main vascular regions were defined: the area surrounding a centrilobular vein was termed the pericentral zone, and the remaining areas in between were referred to as the sinusoidal zone (**Fig. 1C**). In an expanded field of view, we observed that F4/80$^+$ cells were not homogeneously distributed within the liver, as they accumulated preferentially in the sinusoidal zone rather than in pericentral areas (**Fig. 1C**). Three-dimensional reconstruction showed that these cells exclusively and specifically inhabited the intravascular compartment (**Fig. 1C** and **Supplementary Movie 2**). Consistent with this, all F4/80$^+$ cells were also positive for lysozyme M, a marker for macrophages (LysM-EGFP mice; **Fig. 4A**), confirming that all of these cells were KCs and none were ever seen in the parenchyma.

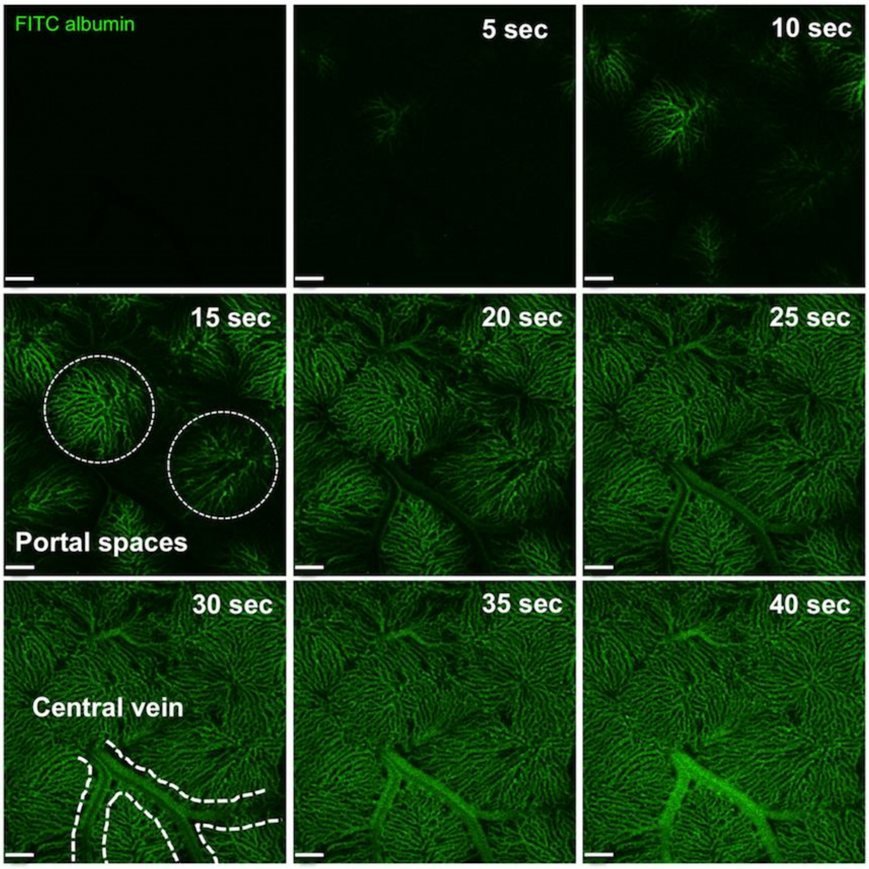
FITC albumin
5 sec
10 sec
15 sec
Portal spaces
20 sec
25 sec
30 sec
Central vein
35 sec
40 sec

Figure 3: Identification of main hepatic vascular arrangements. Snapshots of chronological distribution of FITC-albumin within the liver (5mg/Kg). Portal spaces were identified as the first vascular region evidenced by fluorescence, and central vein were defined as the secondary draining vessels. Scale bars, 120 µm.

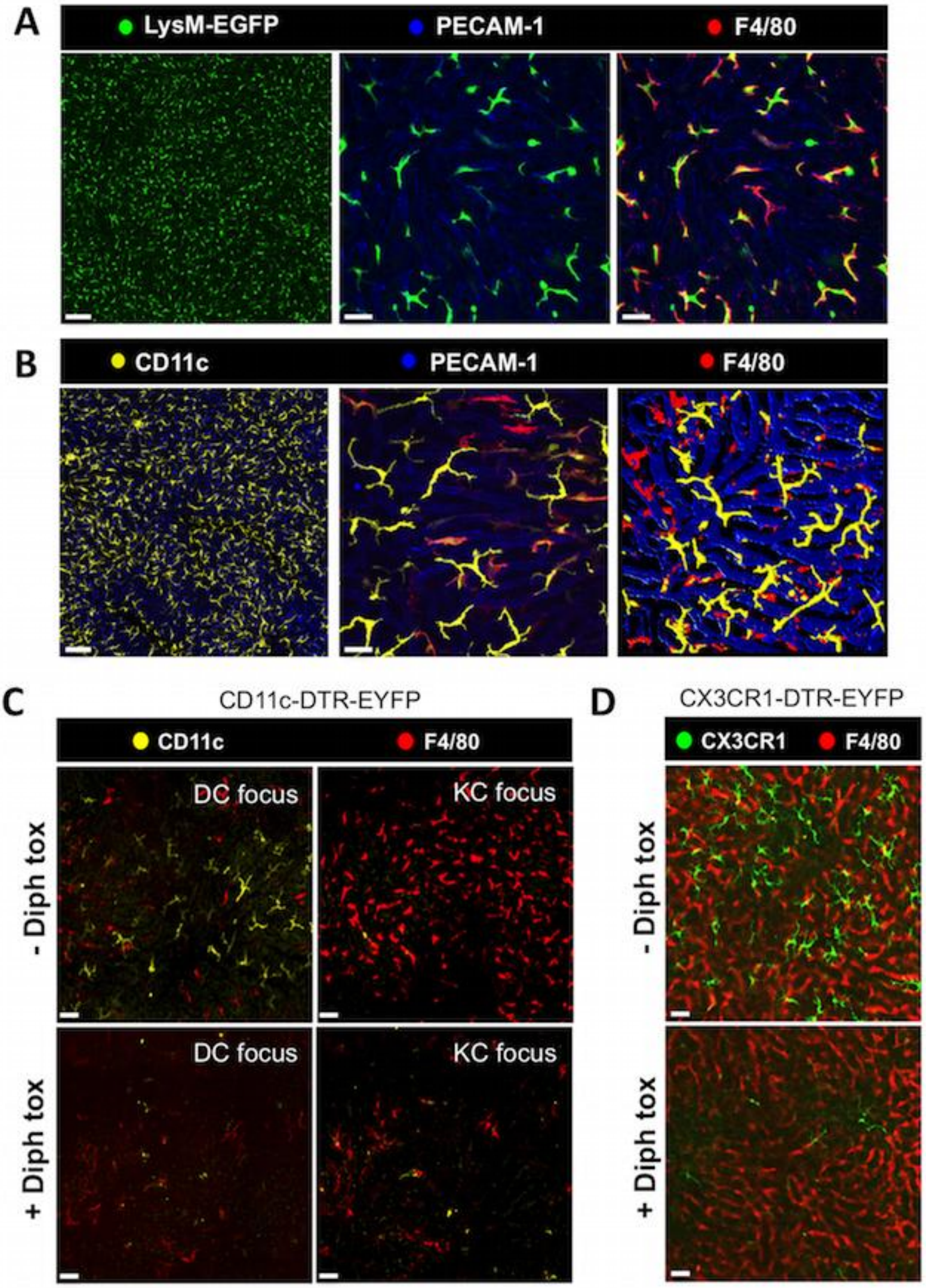
A
LysM-EGFP
PECAM-1
F4/80
B
CD11c
PECAM-1
F4/80
C
CD11c-DTR-EYFP
CD11c
F4/80
DC focus
KC focus
- Diph tox
+ Diph tox
DC focus
KC focus
D
CX3CR1-DTR-EYFP
CX3CR1
F4/80
- Diph tox
+ Diph tox

Figure 4: Expression of different cell surface markers in liver phagocytes. (A) Liver macrophage expression of lysozyme M (LysM-EGFP mice) and F4/80. (B) Same for A, but for CD11c (CD11c-EYFP mice). (C) Depletion of both intravascular CD11c$^+$F4/80$^+$ and extravascular CD11c$^+$ cells upon diphtheria toxin (DT) treatment in CD11c-DTR-EYFP mice. (D) Expression of EYFP and DTR under control of CX3CR1 in liver dendritic cells and selective depletion following diphtheria toxin administration. Note that only CX3CR1$^+$ cells are depleted after DT treatment, with no effect on intravascular F4/80$^+$ cells. Scale bars, 120 µm. Illustrative images from different experiments (N>5).

Intravital imaging also revealed a large hepatic population of CD11c$^+$ cells with differential spatial distribution (CD11c-EYFP reporter mice; **Fig. 4B**). The CD11c$^+$F4/80$^-$ population was larger in size, displayed numerous dendrites on their surface and inhabited the extravascular space, suggestive of a population of DCs (**Supplementary Movie 3**). However, as mentioned above, CD11c$^+$F4/80$^+$ cells were also observed lining the intravascular area, and resembled KC morphology validating two different Kupffer cell populations from CyTOF (**Fig. 1B**, **Fig. 4B** and **Supplementary Movie 3**). CD11c expression in both intravascular and extravascular populations was confirmed by CD11c-targeted depletion (CD11c-DTR-EYFP mice), which caused full depletion of extravascular CD11c$^+$ cells and also a significant decrease (~50%) in intravascular CD11c$^+$F4/80$^+$ cells (**Fig. 4C**).

To image just the extravascular cells, we used CX3CR1$^{gfp/wt}$ reporter mice because CX3CR1 is expressed on DCs (Ginhoux *et al*., 2009) but not on mature KCs under homeostatic conditions (Yona *et al*., 2013). We found an exclusively extravascular population of CX3CR1$^+$ cells (**Fig. 1D** and **Supplementary Movie 4**), which were similar in shape and number to an extravascular CD11c$^+$F4/80$^-$ population (**Fig. 4B**). Intravital images through the liver surface showed that CX3CR1$^+$ cells are abundant and uniformly distributed in the field of view; however, *ex vivo* imaging of liver fragments using transversal slices revealed that such spider-like CX3CR1$^+$ cells were found mainly under a thin layer of mesothelium that covers the liver (**Fig. 1E**), and were not distributed throughout the sinusoids as KCs. Also, CX3CR1$^+$ cells were CD11c$^+$ (**Fig. 5A**), but negative for desmin (**Fig. 6A**), excluding them as population of hepatic stellate cells (HSCs). Of note, CD11c$^+$ cells were also negative for desmin (**Fig. 6A**). Deeper imaging within the liver showed that some CX3CR1$^+$ cells were also found surrounding larger hepatic vessels (**Fig. 5B and C**). As seen in higher magnification of 3D reconstructions, there is an intimate contact of some F4/80$^+$ intravascular and CX3CR1$^+$ extravascular cells, and the latter emit protrusions to reach the vessel lumen (**Fig. 1F**). To confirm that extravascular, and not intravascular cells, specifically expressed CX3CR1, we used a mouse strain that has both DTR and EYFP expression under control of CX3CR1 (CX3CR1 (CreER)-DTR-EYFP). Treatment with DT led to 95% depletion of extravascular CX3CR1$^+$ cells, with no detectable effects on intravascular F4/80$^+$ cells, validating CX3CR1 as a selective marker for extravascular cells under homeostatic conditions (monitored by intravital microscopy; **Fig. 4D**).

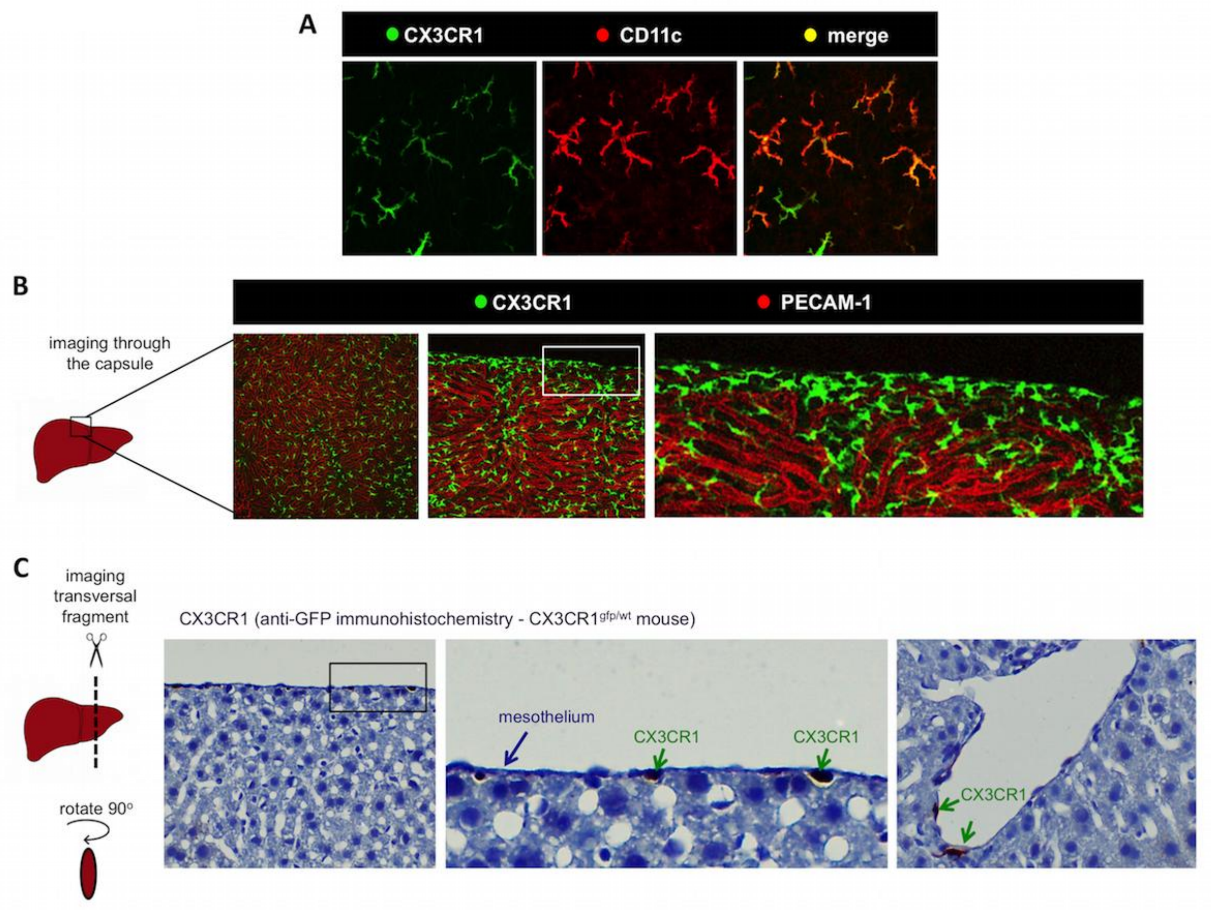
A
CX3CR1
CD11c
merge
B
CX3CR1
PECAM-1
imaging through the capsule
C
imaging transversal fragment
rotate 90°
CX3CR1 (anti-GFP immunohistochemistry - CX3CR1gfp/wt mouse)
mesothelium
CX3CR1
CX3CR1
CX3CR1

Figure 5: Liver dendritic cells are located in the subcapsular compartment and are CD11c^{+}. (A) Liver intravital microscopy of CX3CR1$^{gfp/wt}$ mouse showing the distribution of CD11c^{+} dendritic (anti-CD11) cells and **(B,C)** confirmation of sub-mesothelial location of CX3CR1^{+} cells by intravital microscopy **(B)** immunohistochemistry **(C).** Illustrative images from different experiments (N>5).

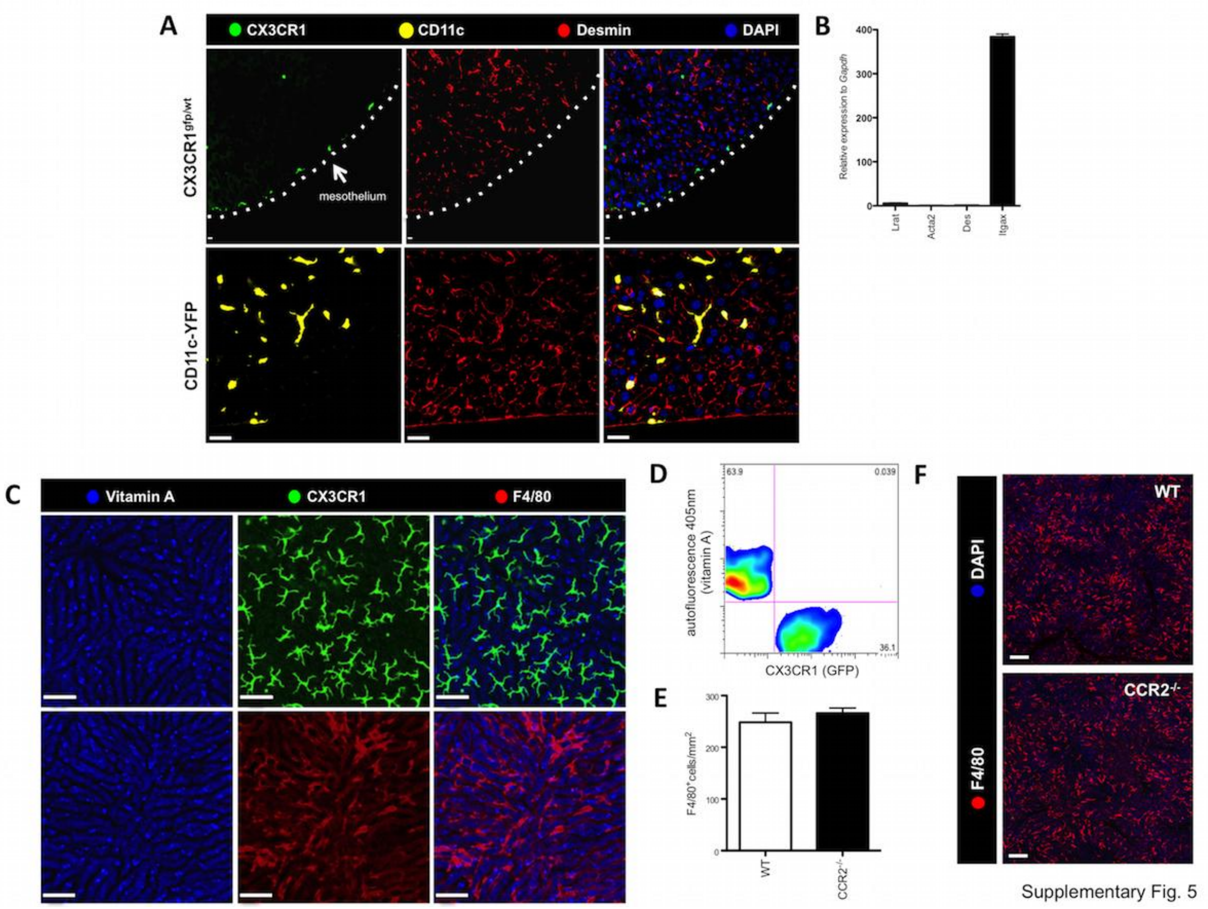
A
CX3CR1
CD11c
Desmin
DAPI
CX3CR1gfp/wt
mesothelium
CD11c-YFP
B
Relative expression to Gapdh
400
300
200
100
0
Lrat
Acta2
Des
Itgax
C
Vitamin A
CX3CR1
F4/80
D
autofluorescence 405nm (vitamin A)
63.9
0.039
36.1
CX3CR1 (GFP)
E
F4/80+cells/mm2
300
200
100
0
WT
CCR2-/-
F
DAPI
F4/80
WT
CCR2-/-
Supplementary Fig. 5

Figure 6: Characterization of different cell surface markers and CCR2 role in phagocytes. (A) Liver *ex vivo* transversal fragment showing that subcapsular neither CX3CR1$^+$ nor CD11c$^+$ cells are positive for desmin (anti-desmin antibody), excluding this population as hepatic stellate cells. **(B)** Real-time PCR from isolated macrophages and dendritic cells showing that hepatic stellate cells (HSCs) did not contaminate samples. The following HSCs genes were measured: lecithin retinol acyltransferase (*Lrat*), desmin (David, Rezende, *et al.*) and alpha-actin-2 (*Acta2*). Data were normalized by a constitutive gene (*Gapdh*) and *Itgax* (CD11c) was used as positive control. **(C)** Liver intravital microscopy showing that neither CX3CR1$^+$ cells nor F4/80$^+$ have vitamin A granules (auto-fluorescence in 405nm laser). (**D)** Flow cytometry investigation of the absence of vitamin A in CX3CR1$^+$ population (auto-fluorescence in 405nm laser). **(E)** CCR2$^{-/-}$ mouse have normal KC density (anti-F4/80) and **(F)** location. Scale bars in A, 10 µm; B, 65µm and E, 120µm.

Next, we isolated extravascular CX3CR1$^+$F4/80$^-$ and intravascular CX3CR1$^-$F4/80$^+$ cells by sorting (**Fig. 7A**) and dissected their phenotypic identities by measuring gene expression using the Nanostring nCounter mouse immunology assay, a multiplexed mRNA hybridization approach. We excluded the presence of HSCs in these samples since after our isolation procedure we did not detect the expression of HSCs common genes (**Fig. 6B)**. Also, we did not detect vitamin A granules by either intravital microscopy (**Fig. 6C)** or FACS **(Fig. 6D)**. Both liver-isolated populations clustered together when compared to a liver-unrelated cell (activated peritoneal macrophage; **Fig. 7B and C**). This approach suggests that the extravascular CX3CR1$^+$F4/80$^-$ and intravascular CX3CR1$^-$F4/80$^+$ cells have a similar source and/or environment dictating their clustered genotype.

However, functional category analysis showed that intra and extravascular cells had differential expression of genes belonging to C and I-type lectins, glycosaminoglycan-binding proteins, cytokines and various other molecules (**Fig. 7C** and GEO accession number: **GSE81645**). Phagocytosis-promoting receptors were significantly enriched on the CX3CR1$^-$F4/80$^+$ population (**Fig. 7E**), suggesting an active role in recognition and clearance of bacteria or antigens from the circulation. In line with this, CX3CR1$^-$F4/80$^+$ cells had significantly higher expression of macrophage-related genes, such as *Marco*, *Cd163* and *Mrs1* (**Fig. 7F**). By contrast, CX3CR1$^+$F4/80$^-$ cells had enriched pathways involved in antigen processing and presentation (**Fig. 7E**), with higher expression of DC common genes, including *Cx3cr1*, *Prf1*, and *Itgax* (**Fig. 7F**). In fact, hierarchical clustering (**Fig. 7B**) and principal coordinate analysis (PCoA) (**Fig. 7C**) confirmed that the genetic profile of CX3CR1$^+$F4/80$^-$ cells was closely related to a classic DC isolated from the spleen. Taking together the expression of surface markers, cell morphology and genetic profile, we established that extravascular CX3CR1$^+$F4/80$^-$ cells are a population of liver DCs that are mainly located in the submesothelial space, while intravascular CX3CR1$^-$F4/80$^+$ cells comprised the hepatic resident macrophages, or KCs.

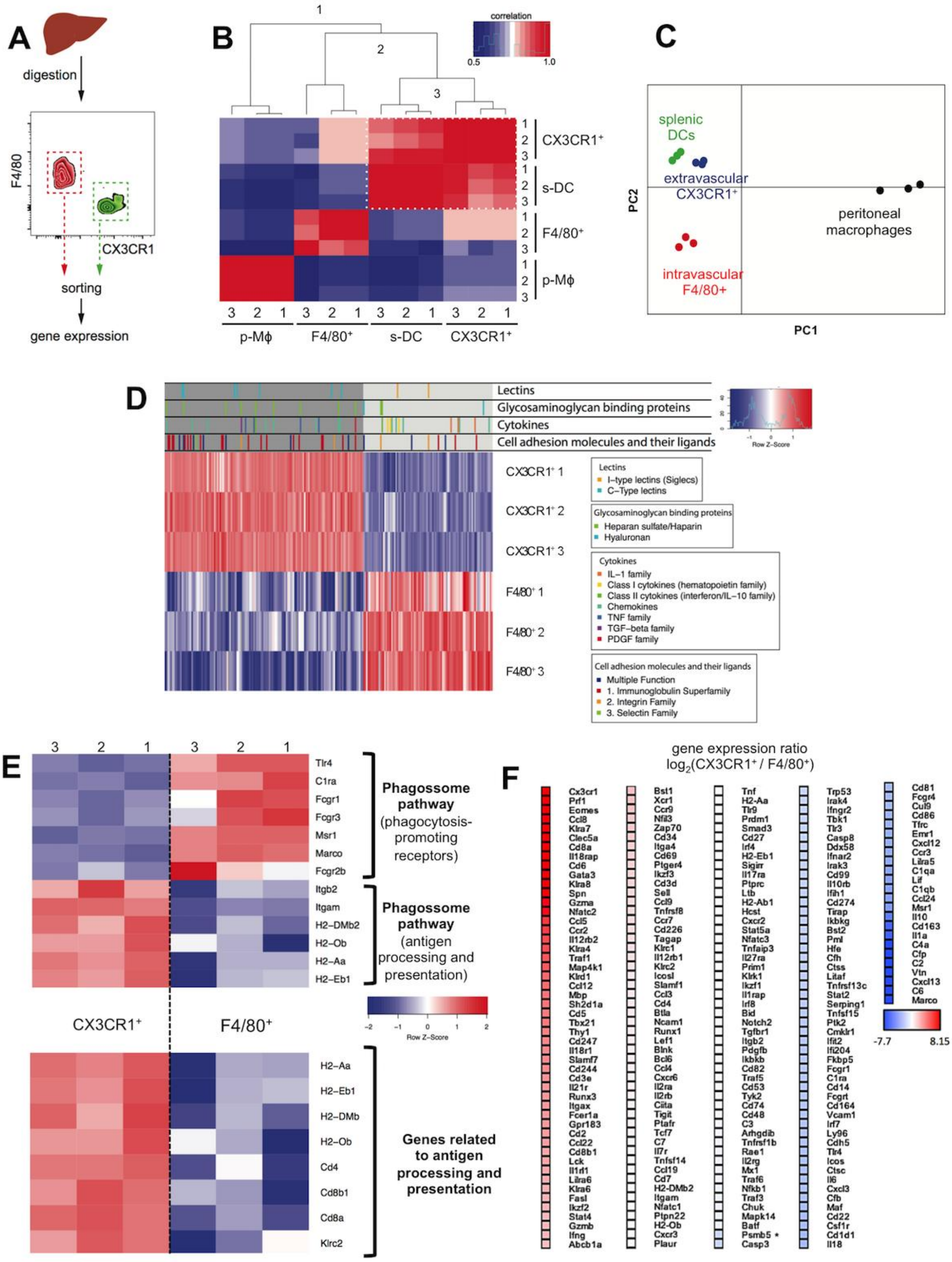

Figure 7: Genetic profiles of different liver phagocytes. (**A**) Schematic representation of isolation and sorting of CX3CR1$^+$ and F4/80$^+$ cells. Total RNA was extracted to further gene analysis. (**B**) Heatmap showing gene expression correlation between liver CX3CR1$^+$ and F4/80$^+$ cells, splenic dendritic cells (s-DC) and peritoneal macrophages (p-Mϕ). White dotted square highlights the genetic proximity between liver CX3CR1$^+$ cells and splenic DCs (correlation ~1). (**C**) Principal coordinates analysis (PCoA) of different isolated cells showing how extravascular CX3CR1$^+$ cells genetically correlate with splenic DCs. (**D**) Functional category analysis based on the gene expression ratio between liver CX3CR1$^+$ and F4/80$^+$ cells evidencing their putative different functions within the liver. (**E**) Same as **D**, but grouped as functional pathways based on gene ontology. (**F**) Statistically different genes ranked as expression ration of CX3CR1$^+$/F4/80$^+$. N=3/group.

4.2. Emergency repopulation dynamics following sudden phagocyte depletion

To better understand how these two populations are maintained within the liver, we removed liver phagocytes with clodronate-loaded liposomes (CLL), a commonly used method to deplete tissue macrophages, and monitored their replenishment dynamics. Focusing on F4/80-gated clusters (**Fig. 8A**), CyTOF analysis showed that the majority of KCs (clusters 2-3) were depleted 2 days after CLL treatment (**Fig. 8A** and **Fig. 2C**). The frequency of infiltrating monocytes was increased (cluster 4), suggesting that these cells may consist in a source of monocyte-derived macrophages. Gating on CD11c^{+} events (**Fig. 8B**), we observed that DC clusters (6, 7 and 11) were also reduced, demonstrating that CLL treatment depletes not only KCs, but also DCs (**Fig. 8B**). Intravital imaging confirmed full depletion of KCs (**Fig. 8C**) and ~95% reduction in DC numbers (**Fig. 8D**) after CLL. Of note, the remaining DCs after CLL treatment were mainly the pDCs (cluster 8), which were not affected by CLL **(Fig. 8B)**. At this time point, F4/80^{+}Ly6C^{+} infiltrating monocytes belonging to cluster 4 were highly increased (20.11% in non-depleted group to 56.70% in CLL day 2 group; **Fig. 8A**).

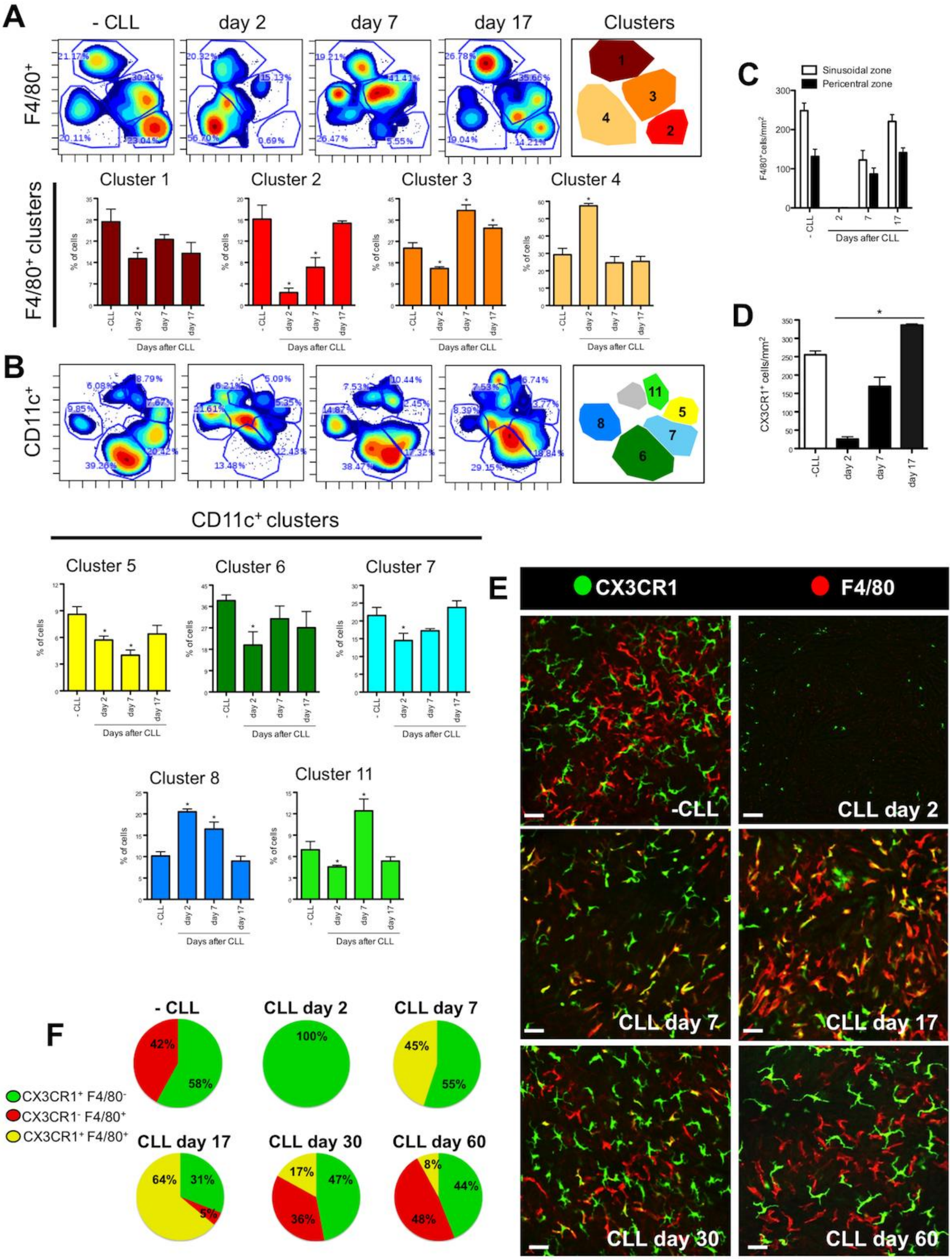

Figure 8: Emergency repopulation dynamics of liver phagocytes. (**A**) Density dot plot from CyTOF showing clustered populations based on F4/80 expression during phagocyte replenishment period and percentage of cells in the different F4/80$^+$ clusters during phagocyte replenishment period. Mice were treated with clodronate liposomes (CLL; 200µL) at day zero, and evaluated in different timepoints. (**B**) Same as **A**, but for CD11c expression. (**C**) Quantification of F4/80$^+$ cells in different liver zones showing their heterogeneous distribution and their recovery to normal number and location after 17 days. (**D**) Same as **C**, but for CX3CR1$^+$ cells (CX3CR1$^{gfp/wt}$ mice). (**E**) Liver intravital microscopy throughout phagocyte repopulating period. (**F**) Quantification of CX3CR1$^+$, F4/80$^+$ or double positive cells from intravital microscopy. Scale bars, 40 µm. Error bars indicate the mean (± s.e.m.). *$P < 0.05$ (unpaired *t*-test), in comparison to –CLL group. CLL = clodronate liposomes. N=5/group

One week following depletion, CLL-depleted clusters began to replenish the liver (**Fig. 8A and B** and **Fig. 9A**) and infiltrating monocytes (cluster 4) returned to baseline frequency. *In vivo* imaging showed that the majority of the two populations of replenished cells were CX3CR1$^+$ and inhabited the intravascular compartment at the 7th day post depletion (**Fig. 8E**). These cells were homogeneously distributed throughout the liver (**Fig.8E**) and F4/80 expression was now (but not at day 2) detected on half of the population of CX3CR1$^+$ cells (**Fig. 8F**). Seventeen days after CLL treatment, normal frequencies and numbers of both KC and DC clusters were observed as determined by CyTOF analysis (**Fig. 8A and B** and **Fig. 9B**). Almost all cells remained CX3CR1$^+$ whereas F4/80 expression was found on 64% of these cells and a small population of F4/80$^+$ cells (5%) has lost their CX3CR1 expression (**Fig. 8E and F**). By day 30, 36% of cells were F4/80$^+$CX3CR1$^-$ with only 17% double positive cells. After 60 days, cells returned to near baseline distribution with only 8% remaining F4/80$^+$CX3CR1$^+$ (**Fig. 8F**). Noteworthy is that at day 7 all of the CX3CR1$^+$ cells (half F4/80 positive half negative) were still inside the vasculature suggesting that their early differentiation occurs in the sinusoids. KC distribution recovered 80% of the baseline values at day 17 after depletion (**Fig. 10 A and B**) while the DC density was still reduced at the same timepoint, suggesting that DCs have slower repopulation kinetics in comparison to KCs. Normal cell numbers were observed at day 30 for both cell types (**Fig. 10A and B**). Normalized absolute event numbers corroborated frequency data from all CyTOF experiments.

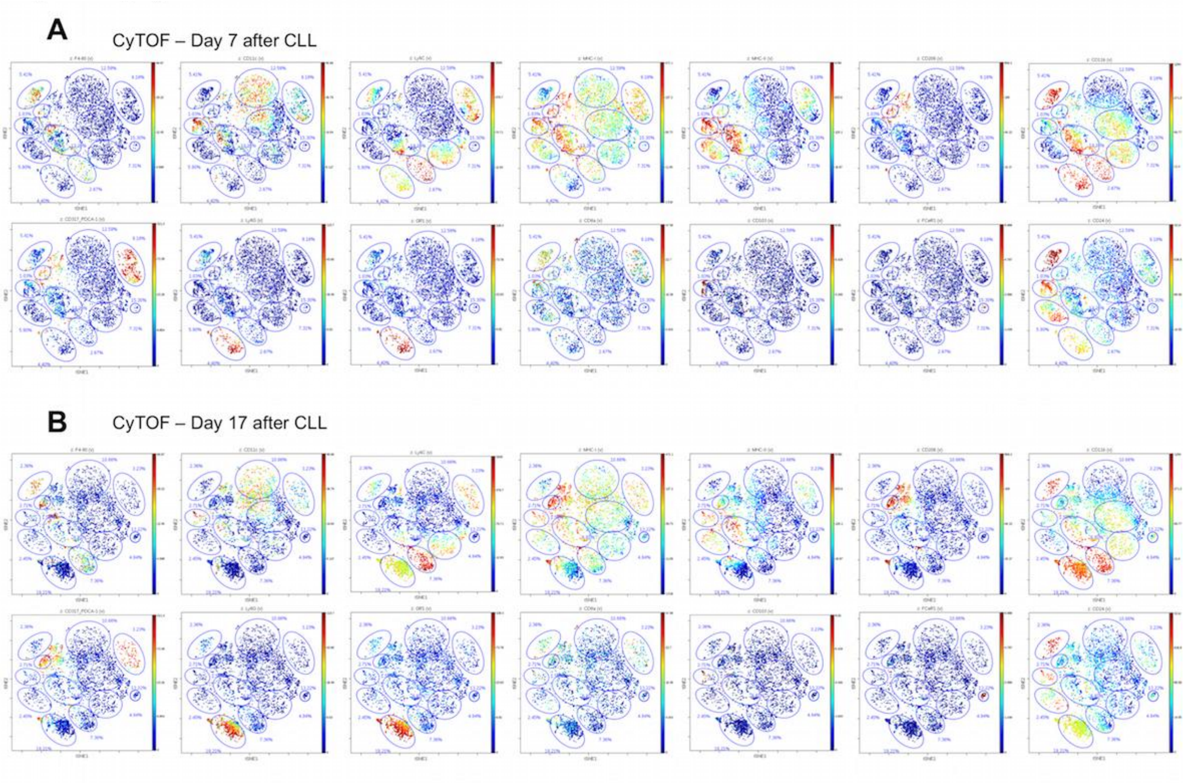

Figure 9: Additional dot plots from CyTOF analysis from mice 7 and 17 days after phagocyte depletion. Expression of cell surface markers in liver non-parenchymal cells clodronate depleted mice after 7 days **(A)** and after 17 days **(B)**. CyTOF was performed and events were clustered as described in Methods and Results.

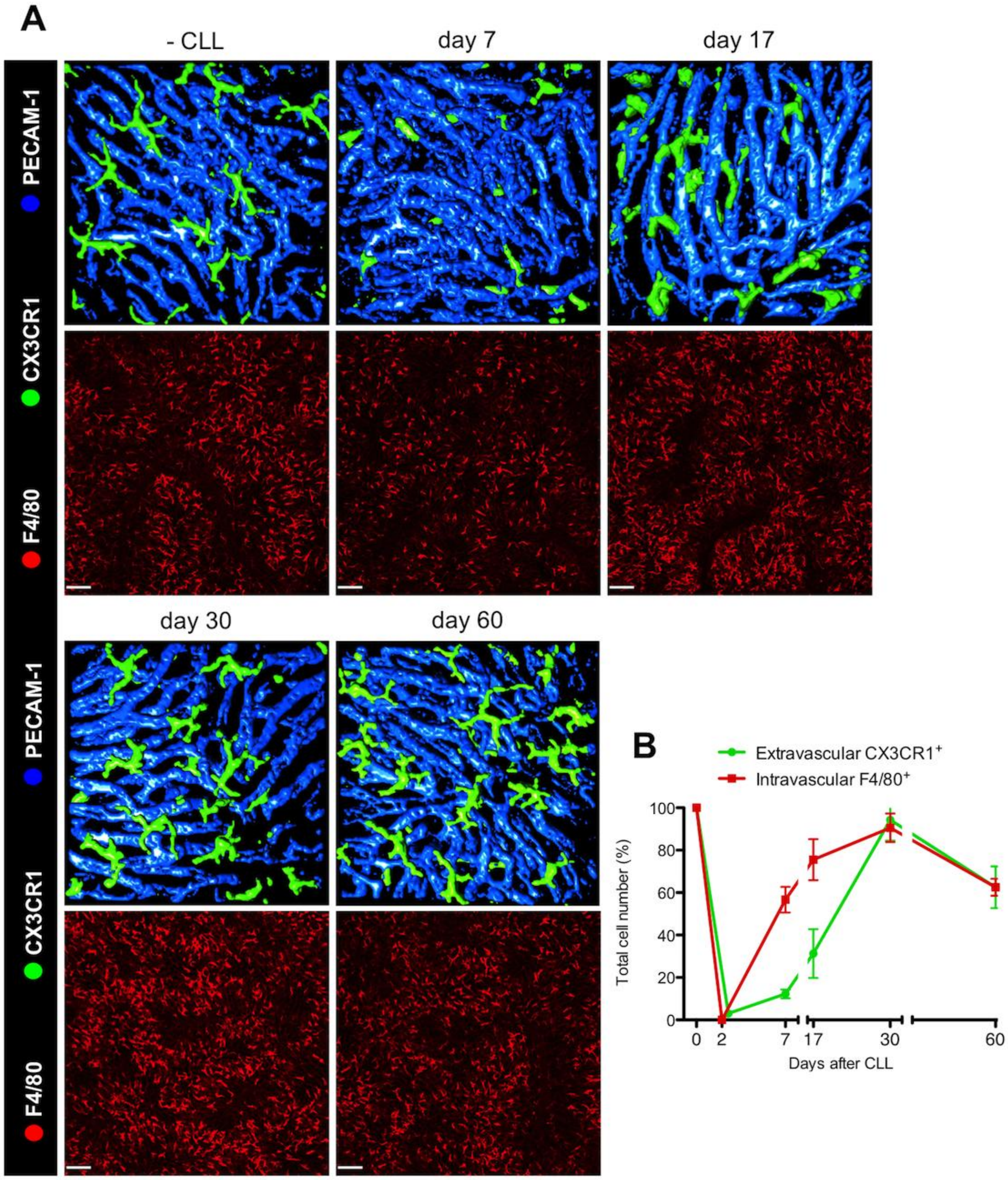
A
- CLL
day 7
day 17
day 30
day 60
● PECAM-1
● CX3CR1
● F4/80
B
Extravascular CX3CR1⁺
Intravascular F4/80⁺
Total cell number (%)
100
80
60
40
20
0
0
2
7
17
30
60
Days after CLL

Figure 10: Differential repopulation kinetics of dendritic and Kupffer cells. **(A)** Liver intravital microscopy images from different timepoints after clodronate injection. Upper panel shows extravascular CX3CR1$^+$ cells (in green, 3D rendering; CX3CR1$^{gfp/wt}$ mice). Sinusoids were evidenced in blue (anti-PECAM-1 antibody). Kupffer cells (intravascular F4/80$^+$ cells stained with anti-F4/80 antibody) are depicted in lower panels. (**B**) Quantification of cell numbers over the repopulation period in comparison to baseline values (adjusted to 100% as control). Scale bars, 120 µm.

4.3. A CXC3CL1 gradient drives extravascular DC reestablishment

Since CX3CR1 expression was prevalent early in the repopulation period, we hypothesized that a gradient of its ligand, CX3CL1, would guide CX3CR1$^+$ phagocyte precursors initially to the sinusoids and facilitated their differentiation into mature KCs and DCs. *In vivo* staining revealed that CX3CL1 was constitutively found in the liver microvasculature (**Fig. 11A and B**) and its expression was increased following depletion and during the first time points of the replenishment phase (2nd and 7th day after CLL; **Fig. 11A and B**). CX3CL1 was also increased in the extravascular compartment (arrow heads on **Fig. 11A**) and, following 17 days post CLL treatment, baseline expression of CX3CL1 was re-established (**Fig. 11A**). This suggests that CX3CL1 production precedes DC extravasation to extravascular spaces. To confirm the role of CX3CL1 on both cell recruitment and distribution, we used CX3CR1$^{gfp/gfp}$ (deficient) mice and found ~50% less liver DCs under basal conditions in comparison to the heterozygote strain (CX3CR1$^{gfp/wt}$; **Fig. 11C and D**). This 50% relative reduction in DC density in CX3CR1 deficient mouse was seen throughout the emergency repopulation period (**Fig. 11D**). Interestingly, CX3CR1 deficient mice had about 20-30% more KCs under basal conditions (**Fig. 11E and F**), and this small density increase was observed throughout the experimental time (**Fig. 11F**). This suggests that CX3CR1 was not required for progenitor cell recruitment and KC development, but was crucial for DC extravasation and survival in the extravascular space. Because CCL2/CCR2 interaction mediates monocyte egress from bone marrow and their further recruitment into tissues, we also investigated the contribution of CCR2 to phagocyte seeding within the liver. In sharp contrast to the absence of CX3CR1, CCR2$^{-/-}$ mice have normal KC/DC distribution and density (**Fig. 6E and F**). In addition, CCR2 seems to not contribute to further DC emigration and maturation within the extravascular compartment.

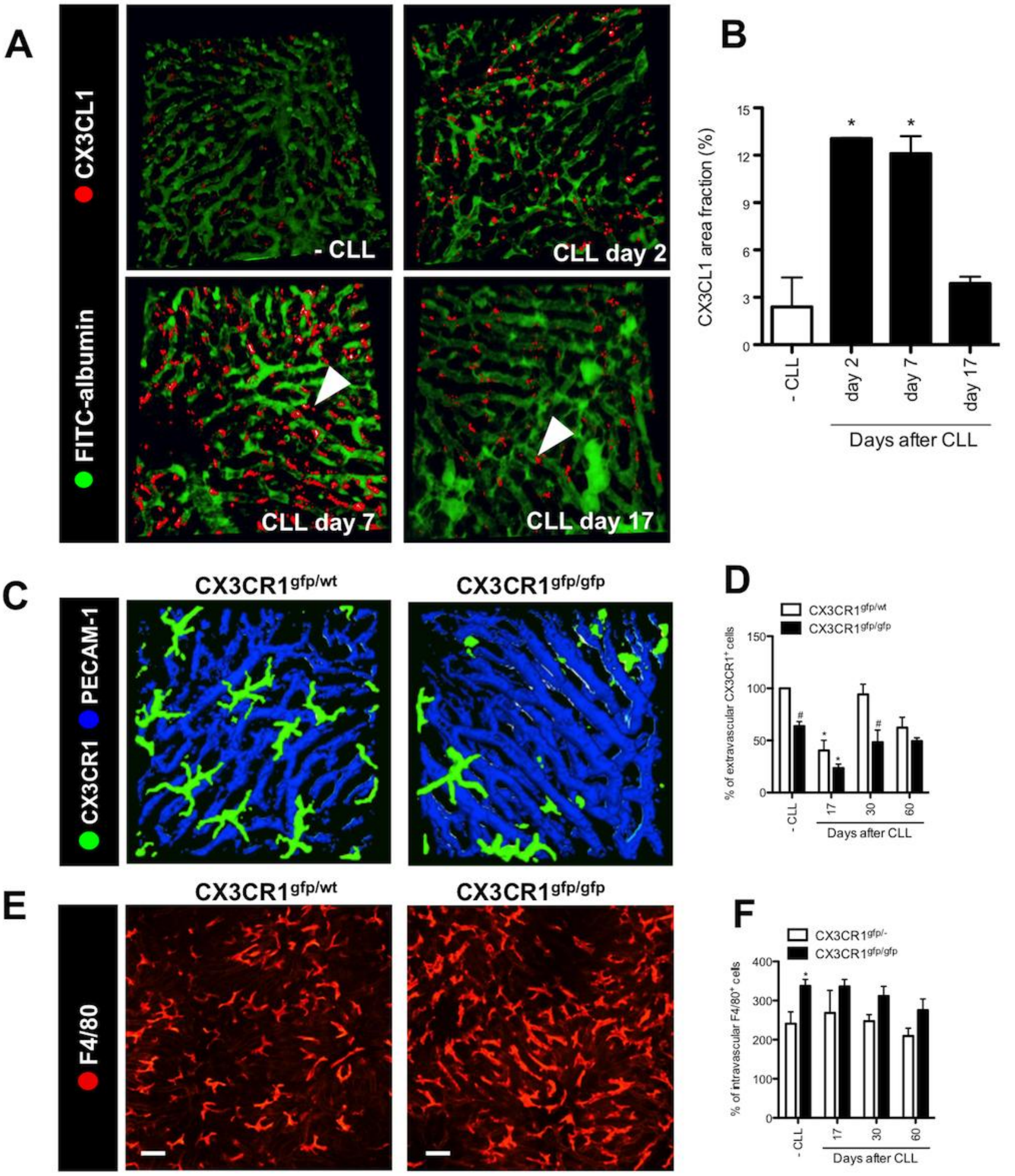
A
● CX3CL1
● FITC-albumin
- CLL
CLL day 2
CLL day 7
CLL day 17
B
CX3CL1 area fraction (%)
0
3
6
9
12
15
*
*
- CLL
day 2
day 7
day 17
Days after CLL
C
● CX3CR1 ● PECAM-1
CX3CR1gfp/wt
CX3CR1gfp/gfp
D
CX3CR1gfp/wt
CX3CR1gfp/gfp
% of extravascular CX3CR1+ cells
0
50
100
150
#
*
*
#
- CLL
17
30
60
Days after CLL
E
● F4/80
CX3CR1gfp/wt
CX3CR1gfp/gfp
F
CX3CR1gfp/-
CX3CR1gfp/gfp
% of intravascular F4/80+ cells
0
100
200
300
400
*
- CLL
17
30
60
Days after CLL

Figure 11: CX3CR1 guides bone marrow precursors to repopulate the liver. (**A**) Liver intravital microscopy showing the expression and distribution of CX3CL1 (in red; anti-CX3CL1) and **(B)** digital quantification of CX3CL1 distribution within the liver. Vessels were stained by intravenous injection of FITC-albumin (5mg/Kg). (**C**) Liver intravital microscopy from CX3CR1$^{gfp/wt}$ and CX3CR1$^{gfp/gfp}$ (deficient) mice showing the reduced number of extravascular DCs in deficient mice. (**D**) Quantification of extravascular CX3CR1^{+} cells during repopulation period. (**E**) Same as **C**, but for intravascular F4/80^{+} cells. (**F**) Same as **D**, but for intravascular F4/80^{+} cells. Scale bars, 40 µm. **P* < 0.05, in comparison to vehicle-treated group and $^{\#}$*P* < 0.05 in comparison to – CLL group of the respective timepoint (one way ANOVA test). CLL = clodronate liposomes. N=5/group.

To test whether the bone marrow is the major source of intravascular precursors that replenish the liver, we transplanted GFP-expressing BM precursors to gamma ray-irradiated mice. Intravital imaging confirmed that ~99% of liver KCs and also extravascular DCs were derived from the BM (**Fig. 12A**). Altogether, we demonstrated that both KC and DC replenishment occurs initially via myeloid precursors that accumulate within the sinusoids after depletion. Cells that sustain CX3CR1 expression emigrate towards the extravascular compartment by following a CX3CL1 gradient, thus re-establishing the DC population.

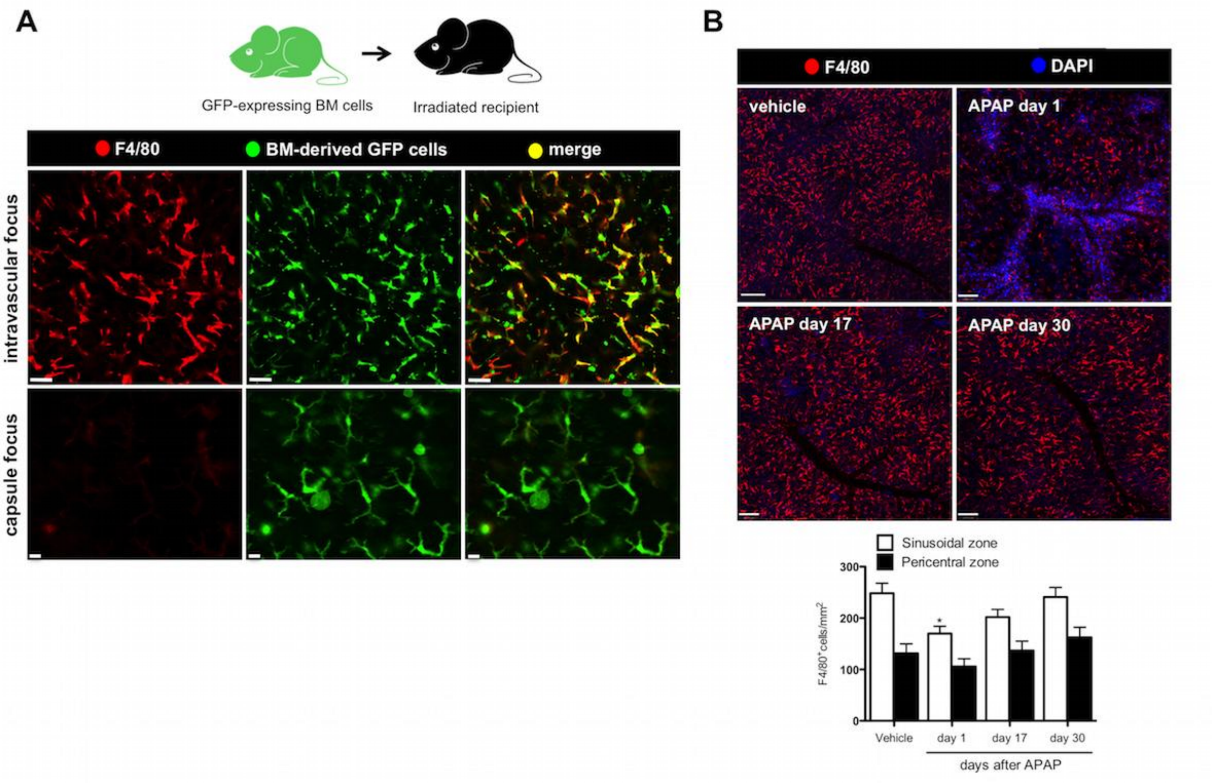
A
GFP-expressing BM cells
Irradiated recipient
F4/80
BM-derived GFP cells
merge
intravascular focus
capsule focus
B
F4/80
DAPI
vehicle
APAP day 1
APAP day 17
APAP day 30
Sinusoidal zone
Pericentral zone
F4/80+cells/mm2
300
200
100
0
*
Vehicle
day 1
day 17
day 30
days after APAP

Figure 12: Replenishment by bone marrow monocytes and drug induced liver injury. (A) Replenishment of liver phagocytes is driven by a bone marrow-derived precursor. Different focal planes imaged by intravital confocal microscopy from GFP-expressing bone marrow chimeras showing that all Kupffer cells (F4/80$^+$GFP$^+$ cells in intravascular focus) and dendritic cells (GFP$^+$ cells in capsule focus) were derived from the bone marrow. (**B**) Acetaminophen (APAP) treatment caused a significant depletion of KCs (F4/80$^+$ cells) and normal cell density and location were restored after 17-30 days. Scale bars in KC focus, 35 µm, in DC focus, 20 µm and in APAP-treated group 120 µm. *$P < 0.05$ (unpaired *t*-test) in comparison to vehicle.

4.4. Phagocyte depletion and replenishment imprints a temporary altered response to injury

Acute liver failure is a worldwide medical concern, and it is becoming increasingly clear that liver immune cells play a key role in the pathogenesis. In these situations, the local milieu of immune cells is thought to be set towards a regulatory phenotype that minimizes liver injury following toxicity and other pathogenic events. Thus, we investigated the impact of the absence of hepatic phagocytes in a model of acetaminophen-induced sterile liver injury. To better define the clinical impact of our procedures, we directly assessed liver metabolic function by monitoring the hepatic clearance rate of indocyanine green (ICG), an excellent index of liver function. Phagocyte depletion by CLL led to overt liver dysfunction following acetaminophen administration in comparison to non-depleted mice (**Fig. 13A**). Moreover, absence of phagocytes delayed recovery to normal function after acetaminophen challenge (**Fig. 13A**). Of note, APAP administration alone also caused significant reduction in KC numbers (~40% reduction; **Fig. 12B).**

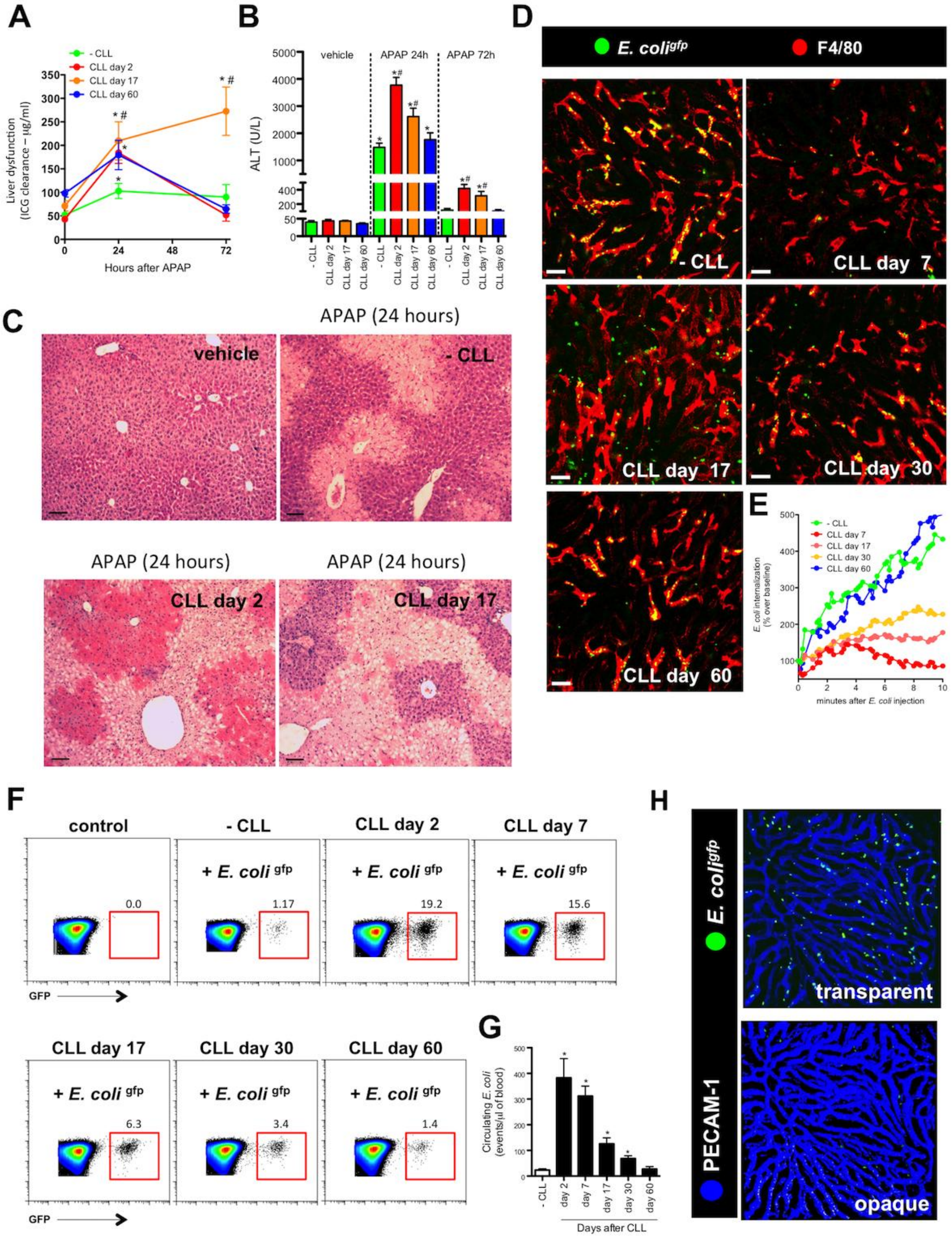

Figure 13: Substitution of phagocytes imprints a temporary altered response to injury and infection. Assessment of liver function (**A**) and (B) injury during different times of repopulation period. Mice received a single dose of indocyanine green (ICG) (20mg/Kg) and its clearance from the circulation was measured over the time. (**C**) Liver histopathology analysis from mice treated with acetaminophen (APAP; 500mg/Kg) after different periods of repopulation confirming overt injury in repopulated mice. (**D**) *In vivo* imaging of *E. coli*^{gfp} capture by Kupffer cells (F4/80^{+}) in control mice and at different timepoints after phagocyte depletion. (**E**) Digital quantification of *E. coli*^{gfp} accumulation inside Kupffer cells expressed as increased over the baseline (set as 100% as the first frame after injection. (**F**) Quantification of free flowing *E. coli*^{gfp} by FACS in the blood during repopulation period. Numbers in the gates are GFP^{+} events/µl. (**G**) Serum *E. coli*^{gfp} concentration normalized by blood volume. Data collected from FACS. **(H)** Liver intravital microscopy evidencing the exclusive intravascular location of GFP-expressing *E. coli*. Scale bars in (**C**), 100 µm, and in (**D and F**), 65 µm. Error bars indicate the mean (± s.e.m.). *$P < 0.05$, in comparison to vehicle-treated group and $^{\#}P < 0.05$ in comparison to – CLL group of the respective timepoint (one way ANOVA test). CLL = clodronate liposomes; ICG: indocyanine green. N=5/group.

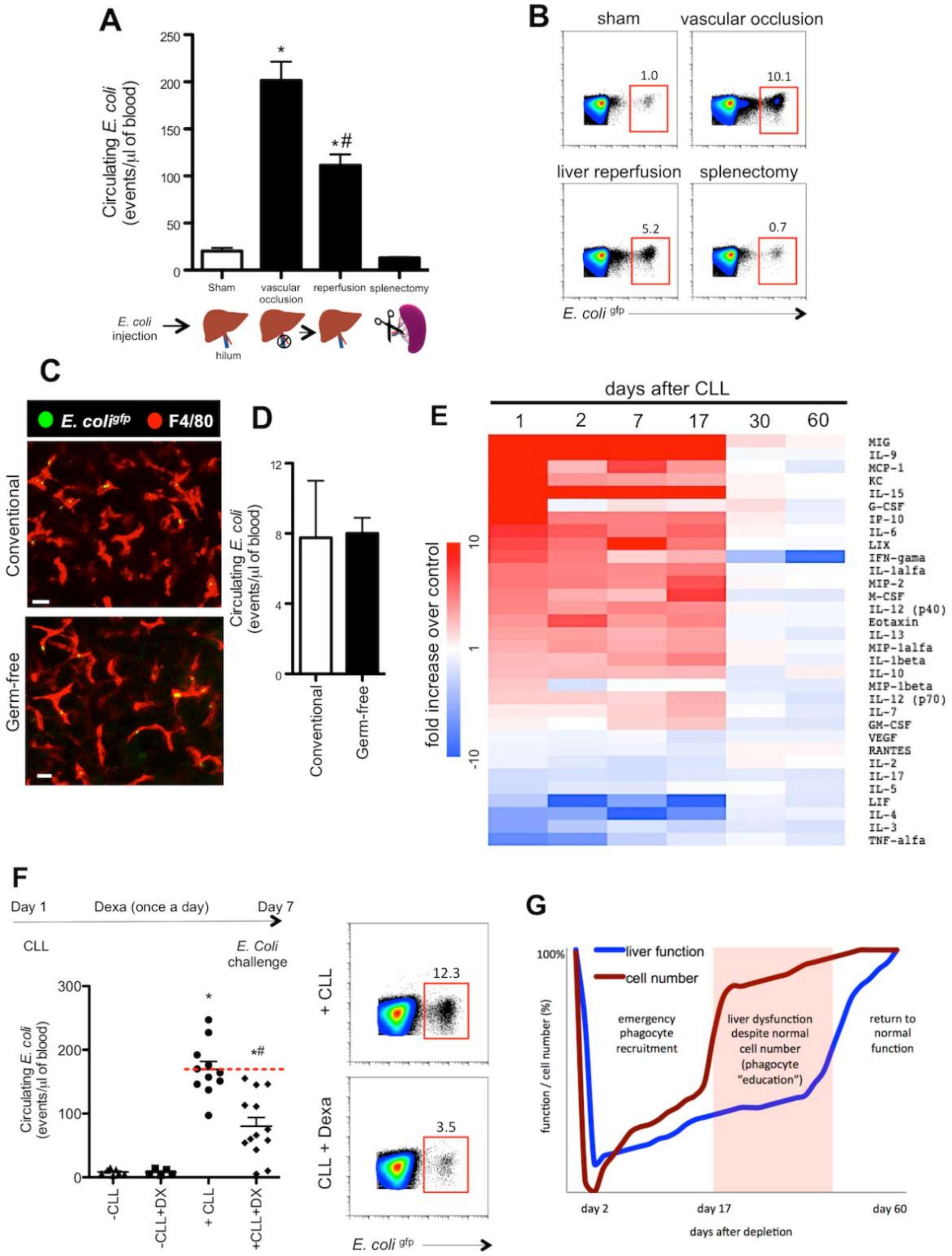

Figure 14: Reestablishment of liver function after phagocyte educational period is dependent on hepatic environment rather than bacterial clues. (**A**) Circulating *E. coli* number in mice submitted to temporary hepatic vascular occlusion (HVO; 5 minutes), reperfused (5 minutes after desoclusion) and splenectomised mice (1 hour before *E. coli* challenge) in comparison to sham-operated group. (**B**) Same as **A**, but analyzed by FACS. Numbers in the gates are GFP^{+} events/µl **(C)** Liver intravital microscopy showing similar phagocytic ability of Kupffer cells from germ-free and conventional mouse. **(D)** Free *E. coli* quantification by FACS in the blood of conventional and germ-free mouse. (**E**) Fold increase of different inflammatory mediators following phagocyte depletion and replenishment in comparison to controls assessed by Luminex. Here, controls were set as fold = 1, therefore have white color code. (**F**) Chronic dexamethasone treatment (5mg/Kg, once a day for 7 days) accelerated liver return to normal bacterial clearance, as shown by flow cytometry. (**G**) Graphical abstract showing our main conclusions regarding the different dynamics of phagocyte repopulation and recovery of liver function. Scale bars, 65 µm. Error bars indicate the mean (± s.e.m.). Scale bars, 16µm. $*P < 0.05$ (unpaired *t*-test) in comparison to sham. $^{\#}P < 0.05$ (one way ANOVA test) in comparison to HVO group. N=5/group.

To explore the consequences of replacement of native phagocytes by BM-derived cells, we challenged mice with acetaminophen at different stages after replenishment. After 17 days of CLL-induced depletion, acetaminophen-treated mice still had worse liver dysfunction in comparison to the non-depleted group (**Fig. 13A**). Moreover, while liver metabolic function was completely restored in non-depleted mice after 3 days of acetaminophen overdose, replenished mice had delayed return of liver function after 17 days of CLL treatment (**Fig. 13A**). Serum transaminase quantification (Jagger *et al.*) and histopathology during APAP-mediated liver injury and recovery confirmed the metabolic function assessed by our ICG clearance protocol (**Fig. 13B and C**). Interestingly, this increased injury was not observed at the earliest time (2 days) after CLL depletion, suggesting the cells must first fully seed the liver at which point they harbor a pro-inflammatory phenotype until at least 17 days. Nevertheless, liver response to injury was completely restored after 60 days of replenishment (**Fig. 13A and B**), demonstrating that despite a transient hyper-responsiveness profile during the initial phases of replenishment, the liver recovers its normal regenerative ability. In line with this, normal KC distribution was also observed after 17-30 days following APAP-induced acute hepatitis (Supplemental Fig. 14B).

4.5. Phagocytic instruction of BM-derived KCs during replenishment

To investigate whether BM-derived phagocytes functioned in the same fashion as yolk sac-derived cells during infection, we assessed phagocytic function at different stages of replenishment following clodronate depletion. For this, GFP-expressing *E. coli* were injected intravenously and bacterial capture was evaluated in real time using intravital microscopy (**Fig. 13D and E**). High magnification imaging revealed that free-flowing *E. coli* were immediately immobilized to the KC membrane at first contact, and no pseudopod formation or major changes in KC morphology seemed to be necessary for initial bacterial arrest (**Supplementary movie 5 and 6**). This highlights that the mechanisms involved in rapid bacterial clearance exerted by KCs under shear may be different from other classic phagocytosis processes. Imaging experiments were complemented by flow cytometry quantification of free bacteria in the blood (**Fig. 13F**). Naïve mice efficiently cleared *E. coli* from circulation (**Fig. 13F and G**); however, increased numbers of circulating *E. coli* were observed in mice that were either depleted (CLL 2 days; **Supplementary movie 6**) or fully replenished (up to 17 days after CLL; **Fig. 13F and 6G** and **Supplementary movie 6**). In fact, intravital imaging showed that KC adhesiveness to *E. coli* was dramatically reduced in immature KCs, and despite brief bacterial interactions with KC membrane, only a few bacteria were arrested and internalized (**Fig. 13D and E, Supplementary movie 5 and 6**). Therefore, despite normal cell density and location, newly arrived KCs have reduced phagocytic capacity for at least 17 days. In agreement, adoptive transfer of bone marrow isolated cells to recently depleted mice caused no detectable improvement in bacterial clearance after at least one week, confirming that even when precursors are delivered in high numerical amounts into the circulation, a period of adaptation within the liver microenvironment is required for KC education (data not shown). Between 30-60 days of replenishment, normal phagocytic activity and clearance of circulating *E. coli* was restored (**Fig. 13F and G** and **Supplementary movie 5**). Since only a few *E. coli* were seen in the extravascular compartment or interacting with DCs, we suggest that KCs are the primary cell population involved in rapid *E. coli* capture within the liver (**Fig. 13H** and **Supplementary Movie 7**), while DCs seems to be involved to further antigen presentation, as shown by gene expression assays.

To investigate if the liver was the main site for systemic *E. coli* removal, we interrupted the hepatic blood flow using a transitory vascular occlusion approach. In fact, higher numbers of circulating *E. coli* were found when the blood was not circulating through the liver, and liver reperfusion significantly restored *E. coli* clearance (**Fig. 14A and B**). Although systemic CLL treatment also depletes splenic resident macrophages that may be involved in bacterial sequestration from the circulation, splenectomised mice had efficient systemic *E. coli* clearance throughout the experiment (**Fig. 14A and B**). Together, these data reveal a window of hepatic phagocytic dysfunction while KC maturation occurs.

A long-term exposure to microbe-associated molecular patterns from the portal tract could be important for maturation of newly recruited precursors. However, in the absence of commensal microbiota (germ-free mice), KCs had normal ability to clear systemic bacteria (**Fig. 14C and D**) despite minor morphological and numeric differences (data not show). Therefore, we hypothesized that intrinsic liver-derived factors shaped KC function during replenishment. To explore this, hepatic inflammatory status was evaluated using a multiplexed cytokine approach. After 1 day of CLL treatment, an increase of several pro-inflammatory cytokines was observed in comparison to non-depleted mice (**Fig. 14E**), including IL-6, IFN-γ, KC/CXCL1 and IL-9. Concomitantly, IL-3, IL-4 and TNF-α were down regulated following depletion (**Fig. 14E**). Other cytokines that have been implicated in support and replenishment of stromal and myeloid cells, such as LIX (LPS-induced CXC chemokine), were highly expressed and sustained up to 17 days post depletion (**Fig. 14E**), entirely consistent with the observed liver dysfunction. Thus, phagocyte depletion and replenishment imprinted a transitory pro-inflammatory signature in the liver, suggesting that such changes in the liver microenvironment could explain the rapid infiltration of phagocyte precursors and also the altered response to bacterial clearance. To dampen liver inflammation triggered by phagocyte depletion, we chronically treated mice with a broad-spectrum anti-inflammatory drug (dexamethasone) during the first week of the replenishment phase. Intriguingly, dexamethasone-treated mice had a significantly faster recovery of *E. coli* extraction from circulation (**Fig. 14F**). Non-depleted mice treated with dexamethasone under the same conditions were not different from controls (**Fig. 14F**). Consistent with this, the liver responded normally to inflammation and bacterial challenge after 60 days of depletion, which was associated with the return of hepatic inflammatory mediators to baseline levels (**Fig. 14E**).

4.6. GEO accession number: GSE81645. Gene expression assessed by Nanostring experiments. Intravascular CX3CR1$^-$ F4/80$^+$ and extravascular CX3CR1$^+$ F4/80$^-$ cells were isolated by sorting (FACS) and immune system-related genes expression was quantified using Nanostring. Statically relevant results consist in *p-value* < 0.05 and a fold change of at least 50% higher or lower. Pathways and functional classification were done by cross association using KEGG Pathways and KEGG Brite databases.

4.7. Legends for Supplementary Movies (CD em anexo)

Supplementary Movie 1 Identification of main hepatic vascular arrangements. Temporal distribution of FITC-albumin (Hanna *et al.*) within the liver (5mg/Kg). Portal spaces were identified as the first vascular region evidenced by fluorescence, and central vein were defined as the secondary draining vessels. Total experimenta time: 1 minute.

Supplementary movie 2 Three-dimensional rendering of liver intravital imaging. Spatial distribution of Kupffer cells. Vessels are in blue (anti-PECAM-1 antibody) and KCs in red (anti-F4/80 antibody). Images were collect from a 3D section of 80-100µm of depth.

Supplementary movie 3 Three-dimensional rendering of liver intravital imaging. Liver dendritic cell (DCs) morphology and distribution in CD11c-EYFP mice. Vessels are in blue (anti-PECAM-1 antibody) and DCs in yellow (EYFP). Images were collect from a 3D section of 80-100µm of depth.

Supplementary movie 4 Three-dimensional rendering of liver intravital imaging. Liver dendritic cell morphology and distribution in CX3CR1-EGFP mice. Vessels are in blue (anti-PECAM-1 antibody) and DCs in green (EGFP). Images were collect from a 3D section of 80-100µm of depth.

Supplementary movie 5: KCs instantaneously trap circulating *E. coli* from the circulation. Merged video comparing *E. coli* arresting by a control KC (non-depleted mouse) versus an immature KC (7 days after CLL). Note that *E. coli* are arrested at the first passage through the liver, while immature KC are unable to proper catch and internalize bacteria. Kupffer cells (KCs) are in red and *E. coli* in green. Total video time: 10 minutes. 10^7 *E.coli* were injected in the beginning of the imaging procedure.

Supplementary movie 6 Circulating *E. coli* capture by Kupffer cells. Merged video showing *E. coli* arresting by control group (non-depleted mouse) and after different timepoints of replenishment period (7, 17, 30 and 60 days). Kupffer cells (KCs) are in red and *E. coli* in green. Due to photobleaching issues, a still frame from KC channel was used as reference during the video. Total video time: 10 minutes each experimental group. 10^7 *E.coli* were injected in the beginning of the imaging procedure

Supplementary movie 7 *E. coli* are exclusively arrested by intravascular cells Three-dimensional rendering of liver confocal intravital microscopy showing GFP expressing E coli inside sinusoids. Sinusoids are in blue (anti-PECAM-1 antibody) and *E. coli*^{gfp} in green. Images were collect from a 3D section of 80-100µm of depth.

5. DISCUSSÃO

Utilizando uma combinação de citometria associada a espectrometria de massa, microscopia confocal intravital e expressão genética, descrevemos com precisão os diferentes fenótipos imunológicos, morfologia, densidade e localização dos fagócitos hepáticos. Mostramos que existe uma vasta população de CDs hepáticas e parte dessas células estão localizadas no espaço subcapsular, e não apenas entre os hepatócitos ou ao redor de grandes vasos, como sugerido anteriormente (HEYMANN & TACKE, 2016). Esta localização estratégica também pode permitir a comunicação inter-compartimentos entre as células do parênquima hepático e os sinusóides, o mesotélio e até mesmo a cavidade peritoneal (WANG & KUBES, 2016). Considerando seu repertório de receptores de superfície e sua expressão gênica, esta população de CDs hepáticas também podem processar e apresentar antígenos como outras subpopulações bem estabelecidas de CDs. Uma vez que as CKs estão intimamente associadas ao endotélio dos capilares sinusóides, é possível que que esses macrófagos interajam com as CDs durante respostas imunes que ocorrem no fígado. Apesar das diferentes origens de CKs e CDs, nós demonstramos usando uma abordagem de imunofenotipagem de alta dimensão que precursores mielóides são capazes de restaurar completamente a densidade celular normal e a localização original após a depleção, e é provável que isso ocorra após o seu recrutamento via intravascular. É importante destacar que a densidade de fagócitos hepáticos também pode ser restabelecida para valores normais, mesmo após um modelo de depleção total, mostrando que a auto-replicação não é inteiramente necessária para um restabelecimento completo dessas populações. Além disso, os progenitores mielóides repõem tanto a população CKs como CDs em dois compartimentos anatômicos diferentes.

Uma vez aderidos ao endotélio dos capilares sinusóides hepáticos, os precursores apresentam dois fenótipos distintos: alguns não se moveram mais ficando retidos no interior dos capilares em contato direto com o sangue circulante, enquanto outros aderem nos mesmos sinusoides, mas, em seguida, migram para fora da vasculatura seguindo um gradiente de CX3CL1 (fractalquina). Nossos dados também sugerem que embora o CCL2 (ligante de CCR2) tenha aumentado durante o período de repovoamento, é improvável que essa qiomiocina desempenhe papel no repovoamento de CKs/CDs no fígado porque os camundongos deficientes para CCR2 não apresentaram qualquer diferença na distribuição e densidade dessas células.

A interacção CX3CR1/CX3CL1 foi fundamental para restabelecer a população de CDs hepática mas não para a população de CKs. Entretanto, o fato de os precursores mielóides que dão origem a ambas as populações expressarem o receptor de CX3CL1, levanta a questão de por que algumas das células permanecem nos sinusóides para se tornar CKs enquanto outras emigraram para o espaço extravascular. Observamos uma diminuição da expressão de GFP associada ao CX3CR1 à medida que as células precursoras tomaram-se residentes nos sinusóides e se diferenciaram em células de Kupffer. Portanto, podemos supor que enquanto os receptores de CX3CR1 podem ser internalizados muito rapidamente, o GFP seria mais lentamente degradado explicando estas observações.

Utilizando o CyTOF, identificamos que sob condições de homeostase, as células hepáticas CD11c$^+$ não são exclusivamente CDs como previamente assumido (CONNOLLY *et al*., 2011) mas sim um subconjunto de células de Kupffer e células dendríticas que expressam este marcador. Além disso, as células CX3CR1$^+$ podem compreender uma população CDs maior do que apenas o subtipo CDs mieloide, que também pode incluir células de Ito (GINHOUX *et al*., 2011; (HEYMANN & TACKE, 2016). Considerando a densidade celular e a morfologia idêntica das células CD11c$^+$ e CX3CR1$^+$ extravasculares, é possível que uma parte substancial das CDs hepáticas expressem constitutivamente ambos os marcadores.

Foi recentemente descrito que novos CKs derivados da medula óssea podem adotar um perfil gênico que pode se assemelhar aos às células originais de origem embrionária (SCOTT *et al*., 2016). Aqui, nós expandimos esses achados mostrando que os precursores intravasculares restauram a densidade e a localização de CKs/CDs após a completa depleção por clodronato ou irradiação, mas por pelo menos 17-30 dias, os fígados repovoados não atingiram os seus níveis tolerogênicos ótimos e sendo mais propensos a danos colaterais. Além disso, acreditamos que as CKs possuem um mecanismo único para prender rapidamente bactérias presentes na sangue que envolve, inicialemente, a adesão "passiva" da bactéria à superfície celular do macrófago e sua posterior internalização. De modo interessante, as "novas" CKs apresentam capacidade de retenção de *E. coli* bastante reduzida, indicando uma exigência de maturação adicional das CKS e uma suposta susceptibilidade aumentada à propagação bacteriana. É razoável sugerir que várias moléculas envolvidas em processos fagocíticos que são expressos por CKs sob condições normais podem estar reduzidas em CKs imaturas e podem atingir níveis de expressão ótimos durante o processo de maturação. Uma vez que os CKs de camundongos *germ free* apresentam captura bacteriana sistêmica totalmente funcional, é provável que a capacidade fagocítica - e talvez também sua disfunção

- não dependam de instruções da microbiota, mas provavelmente de mediadores endógenos que compõem o ambiente hepático (CORBITT *et al.*, 2013).

Embora pensássemos inicialmente que os mediadores inflamatórios pudessem induzir a expressão dos receptores necessários para a captura bacteriana pelas CKs, o oposto foi observado. Quando reduzimos a resposta inflamatória do fígado durante estágios iniciais do repovoamento, a fagocitose realizada pelas CKs foi significativamente maior. Isso sugere que as intervenções terapêuticas destinadas a bloquear a inflamação podem também ajudar os pacientes que sofreram de lesões hepáticas extensas ou foram submetidos a irradiação, condições em que uma parte substancial dos fagócitos do fígado podem ser eliminadas. Após 60 dias de repovoamento, o fígado respondeu normalmente à lesão e readquiriu a função de depuração bacteriana de modo eficiente, o que foi concomitante com o retorno aos níveis basais de citocinas hepáticas. Isto implica que, apesar do número e distribuição normal dos fagócitos em estágios iniciais do repovoamento, um "período educacional" é necessário para a restituição da função normal destas células. Coletivamente, esses achados fornecem uma visão sobre os mecanismos envolvidos em uma maior susceptibilidade à lesão hepática colateral e à infecção sistêmica observada após lesões hepáticas extensas e também em pacientes que foram submetidos a irradiação de corpo inteiro.

6. REFERÊNCIAS BIBLIOGRÁFICAS

ARII, S.; IMAMURA, M. Physiological role of sinusoidal endothelial cells and Kupffer cells and their implication in the pathogenesis of liver injury. **J Hepatobiliary Pancreat Surg,** v. 7, n. 1, p. 40-8, 2000.

ARII, S.; IMAMURA, M. Physiological role of sinusoidal endothelial cells and Kupffer cells and their implication in the pathogenesis of liver injury. **Journal of hepato-biliary-pancreatic surgery,** v. 7, n. 1, p. 40-8, 2000.

AUFFRAY, C.; SIEWEKE, M. H.; GEISSMANN, F. Blood monocytes: development, heterogeneity, and relationship with dendritic cells. **Annu Rev Immunol,** v. 27, p. 669-92, 2009.

BONE-LARSON, C. L. et al. The role of chemokines in the immunopathology of the liver. **Immunol Rev,** v. 177, p. 8-20, Oct 2000.

BOTTCHER, J. P.; KNOLLE, P. A.; STABENOW, D. Mechanisms balancing tolerance and immunity in the liver. **Digestive diseases,** v. 29, n. 4, p. 384-90, 2011.

DAL-SECCO, D. et al. A dynamic spectrum of monocytes arising from the in situ reprogramming of CCR2+ monocytes at a site of sterile injury. **The Journal of experimental medicine,** v. 212, n. 4, p. 447-56, Apr 06 2015.

DAVID, B. A. et al. Combination of Mass Cytometry and Imaging Analysis Reveals Origin, Location, and Functional Repopulation of Liver Myeloid Cells in Mice. **Gastroenterology,** v. 151, n. 6, p. 1176-1191, Dec 2016.

DAVID, B. A. et al. Isolation and high-dimensional phenotyping of gastrointestinal immune cells. **Immunology**, Dec 31 2016.

DECKER, K. The response of liver macrophages to inflammatory stimulation. **Keio J Med,** v. 47, n. 1, p. 1-9, Mar 1998.

DECKER, K. The response of liver macrophages to inflammatory stimulation. **The Keio journal of medicine,** v. 47, n. 1, p. 1-9, Mar 1998.

GAUTIER, E. L. et al. Gene-expression profiles and transcriptional regulatory pathways that underlie the identity and diversity of mouse tissue macrophages. **Nat Immunol,** v. 13, n. 11, p. 1118-28, Nov 2012.

GEISSMANN, F. et al. Development of monocytes, macrophages, and dendritic cells. **Science,** v. 327, n. 5966, p. 656-61, Feb 05 2010.

GINHOUX, F. et al. Fate mapping analysis reveals that adult microglia derive from primitive macrophages. **Science,** v. 330, n. 6005, p. 841-5, Nov 05 2010.

GINHOUX, F.; GUILLIAMS, M. Tissue-Resident Macrophage Ontogeny and Homeostasis. **Immunity,** v. 44, n. 3, p. 439-49, Mar 15 2016.

GINHOUX, F.; JUNG, S. Monocytes and macrophages: developmental pathways and tissue homeostasis. **Nature reviews. Immunology,** v. 14, n. 6, p. 392-404, Jun 2014.

GINHOUX, F.; JUNG, S. Monocytes and macrophages: developmental pathways and tissue homeostasis. **Nat Rev Immunol,** v. 14, n. 6, p. 392-404, Jun 2014.

GINHOUX, F. et al. The origin and development of nonlymphoid tissue CD103+ DCs. **J Exp Med,** v. 206, n. 13, p. 3115-30, Dec 21 2009.

GINHOUX, F. et al. New insights into the multidimensional concept of macrophage ontogeny, activation and function. **Nature immunology,** v. 17, n. 1, p. 34-40, Jan 2016.

GOMEZ PERDIGUERO, E. et al. Tissue-resident macrophages originate from yolk-sac-derived erythro-myeloid progenitors. **Nature,** v. 518, n. 7540, p. 547-51, Feb 26 2015.

GORDON, S. Elie Metchnikoff: father of natural immunity. **European journal of immunology,** v. 38, n. 12, p. 3257-64, Dec 2008.

GORDON, S. Phagocytosis: The Legacy of Metchnikoff. **Cell,** v. 166, n. 5, p. 1065-8, Aug 25 2016.

GREGORY, S. H.; WING, E. J. Neutrophil-Kupffer cell interaction: a critical component of host defenses to systemic bacterial infections. **J Leukoc Biol,** v. 72, n. 2, p. 239-48, Aug 2002.

HANIFFA, M.; COLLIN, M.; GINHOUX, F. Ontogeny and functional specialization of dendritic cells in human and mouse. **Advances in immunology,** v. 120, p. 1-49, 2013.

HANNA, R. N. et al. The transcription factor NR4A1 (Nur77) controls bone marrow differentiation and the survival of Ly6C- monocytes. **Nature immunology,** v. 12, n. 8, p. 778-85, Jul 03 2011.

HASHIMOTO, D.; MILLER, J.; MERAD, M. Dendritic cell and macrophage heterogeneity in vivo. **Immunity,** v. 35, n. 3, p. 323-35, Sep 23 2011.

HEATH, W. R.; CARBONE, F. R. Dendritic cell subsets in primary and secondary T cell responses at body surfaces. **Nat Immunol,** v. 10, n. 12, p. 1237-44, Dec 2009.

HEYMANN, F. et al. Liver inflammation abrogates immunological tolerance induced by Kupffer cells. **Hepatology,** v. 62, n. 1, p. 279-91, Jul 2015.

HEYMANN, F.; TACKE, F. Immunology in the liver--from homeostasis to disease. **Nature reviews. Gastroenterology & hepatology,** v. 13, n. 2, p. 88-110, Feb 2016.

HOEFFEL, G. et al. Adult Langerhans cells derive predominantly from embryonic fetal liver monocytes with a minor contribution of yolk sac-derived macrophages. **J Exp Med,** v. 209, n. 6, p. 1167-81, Jun 4 2012.

HOGABOAM, C. M. et al. Novel CXCR2-dependent liver regenerative qualities of ELR-containing CXC chemokines. **FASEB J,** v. 13, n. 12, p. 1565-74, Sep 1999.

HOGABOAM, C. M. et al. Macrophage inflammatory protein-2 gene therapy attenuates adenovirus- and acetaminophen-mediated hepatic injury. **Gene Ther,** v. 6, n. 4, p. 573-84, Apr 1999.

JAGGER, A. L. et al. FAS/FAS-L dependent killing of activated human monocytes and macrophages by CD4+CD25- responder T cells, but not CD4+CD25+ regulatory T cells. **Journal of autoimmunity,** v. 38, n. 1, p. 29-38, Feb 2012.

JENKINS, S. J. et al. Local macrophage proliferation, rather than recruitment from the blood, is a signature of TH2 inflammation. **Science,** v. 332, n. 6035, p. 1284-8, Jun 10 2011.

JU, C. et al. Protective role of Kupffer cells in acetaminophen-induced hepatic injury in mice. **Chem Res Toxicol,** v. 15, n. 12, p. 1504-13, Dec 2002.

KRAUSGRUBER, T. et al. IRF5 promotes inflammatory macrophage polarization and TH1-TH17 responses. **Nat Immunol,** v. 12, n. 3, p. 231-8, Mar 2011.

LASKIN, D. L.; WEINBERGER, B.; LASKIN, J. D. Functional heterogeneity in liver and lung macrophages. **J Leukoc Biol,** v. 70, n. 2, p. 163-70, Aug 2001.

LEE, W. Y. et al. An intravascular immune response to Borrelia burgdorferi involves Kupffer cells and iNKT cells. **Nature immunology,** v. 11, n. 4, p. 295-302, Apr 2010.

MACPHEE, P. J.; SCHMIDT, E. E.; GROOM, A. C. Evidence for Kupffer cell migration along liver sinusoids, from high-resolution in vivo microscopy. **Am J Physiol,** v. 263, n. 1 Pt 1, p. G17-23, Jul 1992.

MARQUES, P. E. et al. Imaging liver biology in vivo using conventional confocal microscopy. **Nature protocols,** v. 10, n. 2, p. 258-68, Feb 2015.

MELLMAN, I.; STEINMAN, R. M. Dendritic cells: specialized and regulated antigen processing machines. **Cell,** v. 106, n. 3, p. 255-8, Aug 10 2001.

MURRAY, P. J.; WYNN, T. A. Protective and pathogenic functions of macrophage subsets. **Nat Rev Immunol,** v. 11, n. 11, p. 723-37, Nov 2011.

NAITO, M.; HASEGAWA, G.; TAKAHASHI, K. Development, differentiation, and maturation of Kupffer cells. **Microsc Res Tech,** v. 39, n. 4, p. 350-64, Nov 15 1997.

NATHAN, C.; DING, A. Nonresolving inflammation. **Cell,** v. 140, n. 6, p. 871-82, Mar 19 2010.

PERDIGUERO, E. G.; GEISSMANN, F. The development and maintenance of resident macrophages. **Nature immunology,** v. 17, n. 1, p. 2-8, Jan 2016.

SALLUSTO, F.; LANZAVECCHIA, A. Efficient presentation of soluble antigen by cultured human dendritic cells is maintained by granulocyte/macrophage colony-stimulating factor plus interleukin 4 and downregulated by tumor necrosis factor alpha. **J Exp Med,** v. 179, n. 4, p. 1109-18, Apr 1 1994.

SCHULZ, C. et al. A lineage of myeloid cells independent of Myb and hematopoietic stem cells. **Science,** v. 336, n. 6077, p. 86-90, Apr 06 2012.

SEKI, S. et al. The liver as a crucial organ in the first line of host defense: the roles of Kupffer cells, natural killer (NK) cells and NK1.1 Ag+ T cells in T helper 1 immune responses. **Immunol Rev,** v. 174, p. 35-46, Apr 2000.

SEKI, S. et al. The liver as a crucial organ in the first line of host defense: the roles of Kupffer cells, natural killer (NK) cells and NK1.1 Ag+ T cells in T helper 1 immune responses. **Immunological reviews,** v. 174, p. 35-46, Apr 2000.

SIEWEKE, M. H.; ALLEN, J. E. Beyond stem cells: self-renewal of differentiated macrophages. **Science,** v. 342, n. 6161, p. 1242974, Nov 22 2013.

SLEYSTER, E. C.; KNOOK, D. L. Relation between localization and function of rat liver Kupffer cells. **Lab Invest,** v. 47, n. 5, p. 484-90, Nov 1982.

SLEYSTER, E. C.; KNOOK, D. L. Relation between localization and function of rat liver Kupffer cells. **Laboratory investigation; a journal of technical methods and pathology,** v. 47, n. 5, p. 484-90, Nov 1982.

STEINMAN, R. M.; COHN, Z. A. Identification of a novel cell type in peripheral lymphoid organs of mice. I. Morphology, quantitation, tissue distribution. **J Exp Med,** v. 137, n. 5, p. 1142-62, May 1 1973.

SU, G. L. Lipopolysaccharides in liver injury: molecular mechanisms of Kupffer cell activation. **Am J Physiol Gastrointest Liver Physiol,** v. 283, n. 2, p. G256-65, Aug 2002.

THOMSON, A. W.; KNOLLE, P. A. Antigen-presenting cell function in the tolerogenic liver environment. **Nat Rev Immunol,** v. 10, n. 11, p. 753-66, Nov 2010.

TOTH, C. A.; THOMAS, P. Liver endocytosis and Kupffer cells. **Hepatology,** v. 16, n. 1, p. 255-66, Jul 1992.

VAN DE LAAR, L. et al. Yolk Sac Macrophages, Fetal Liver, and Adult Monocytes Can Colonize an Empty Niche and Develop into Functional Tissue-Resident Macrophages. **Immunity,** v. 44, n. 4, p. 755-68, Apr 19 2016.

VILLADANGOS, J. A.; YOUNG, L. Antigen-presentation properties of plasmacytoid dendritic cells. **Immunity,** v. 29, n. 3, p. 352-61, Sep 19 2008.

YONA, S. et al. Fate mapping reveals origins and dynamics of monocytes and tissue macrophages under homeostasis. **Immunity,** v. 38, n. 1, p. 79-91, Jan 24 2013.

YOU, Q. et al. Role of hepatic resident and infiltrating macrophages in liver repair after acute injury. **Biochem Pharmacol,** v. 86, n. 6, p. 836-43, Sep 15 2013.

ZIGMOND, E. et al. Infiltrating monocyte-derived macrophages and resident kupffer cells display different ontogeny and functions in acute liver injury. **J Immunol,** v. 193, n. 1, p. 344-53, Jul 1 2014.

PRODUÇÃO CIENTIFICA

1. DAVID, B. A. *et al*. Combination of Mass Cytometry and Imaging Analysis Reveals Origin, Location, and Functional Repopulation of Liver Myeloid Cells in Mice. **Gastroenterology,** v. 151, n. 6, p. 1176-1191, Dec 2016.

2. SOYSA, R. and CRISPE, I. Subcapsular Hepatic Dendritic Cells: Hiding in Plain Sight. **Gastroenterology,** Oct 2016.

Editorial sobre o artigo: DAVID, B. A. *et al*. Combination of Mass Cytometry and Imaging Analysis Reveals Origin, Location, and Functional Repopulation of Liver Myeloid Cells in Mice. **Gastroenterology,** v. 151, n. 6, p. 1176-1191, Dec 2016.

3. DAVID, B. A. et al. Isolation and high-dimensional phenotyping of gastrointestinal immune cells. **Immunology**, Dec 31 2016.

Gastroenterology 2016;151:1176–1191

Combination of Mass Cytometry and Imaging Analysis Reveals Origin, Location, and Functional Repopulation of Liver Myeloid Cells in Mice

Bruna Araujo David,[1] Rafael Machado Rezende,[2] Maísa Mota Antunes,[1] Mônica Morais Santos,[1] Maria Alice Freitas Lopes,[1] Ariane Barros Diniz,[1] Rafaela Vaz Sousa Pereira,[1] Sarah Cozzer Marchesi,[1] Débora Moreira Alvarenga,[1] Brenda Naemi Nakagaki,[1] Alan Moreira Araújo,[1] Daniela Silva dos Reis,[3] Renata Monti Rocha,[3] Pedro Elias Marques,[3] Woo-Yong Lee,[4] Justin Deniset,[4] Pei Xiong Liew,[4] Stephen Rubino,[2] Laura Cox,[2] Vanessa Pinho,[5] Thiago Mattar Cunha,[6] Gabriel Rocha Fernandes,[7] André Gustavo Oliveira,[1,8] Mauro Martins Teixeira,[3] Paul Kubes,[4] and Gustavo Batista Menezes[1]

[1]Center for Gastrointestinal Biology, Departamento de Morfologia, Instituto de Ciências Biológicas, Universidade Federal de Minas Gerais, Belo Horizonte, Minas Gerais, Brazil; [2]Ann Romney Center for Neurologic Diseases, Brigham and Women's Hospital, Harvard Medical School, Boston, Massachusetts; [3]Departamento de Bioquímica e Imunologia, Instituto de Ciências Biológicas, Universidade Federal de Minas Gerais, Belo Horizonte, Minas Gerais, Brazil; [4]University of Calgary, Alberta, Canada; [5]Resolution of Inflammation Lab, Departamento de Morfologia, Instituto de Ciências Biológicas, Universidade Federal de Minas Gerais, Belo Horizonte, Minas Gerais, Brazil; [6]Faculdade de Medicina de Ribeirão Preto, Universidade de São Paulo, São Paulo, Brazil; [7]Centro de Pesquisas René Rachou, FIOCRUZ, Belo Horizonte, Minas Gerais, Brazil; and [8]Departamento de Fisiologia, Instituto de Ciências Biológicas, Universidade Federal de Minas Gerais, Belo Horizonte, Minas Gerais, Brazil

See editorial on page 1065.

BACKGROUND & AIMS: Resident macrophages are derived from yolk sac precursors and seed the liver during embryogenesis. Native cells may be replaced by bone marrow precursors during extensive injuries, irradiation, and infections. We investigated the liver populations of myeloid immune cells and their location, as well as the dynamics of phagocyte repopulation after full depletion. The effects on liver function due to the substitution of original phagocytes by bone marrow–derived surrogates were also examined. **METHODS:** We collected and analyzed liver tissues from C57BL/6 (control), *LysM-EGFP, B6 ACTb-EGFP, CCR2$^{-/-}$, CD11c-EYFP, CD11c-EYFP-DTR,* germ-free mice, *CX3CR1$^{gfp/gfp}$*, *CX3CR1$^{gpf/wt}$*, and *CX3CR1-DTR-EYFP*. Liver nonparenchymal cells were immunophenotyped using mass cytometry and gene expression analyses. Kupffer and dendritic cells were depleted from mice by administration of clodronate, and their location and phenotype were examined using intravital microscopy and time-of-flight mass cytometry. Mice were given acetaminophen gavage or intravenous injections of fluorescently labeled *Escherichia coli*, blood samples were collected and analyzed, and liver function was evaluated. We assessed cytokine profiles of liver tissues using a multiplexed array. **RESULTS:** Using mass cytometry and gene expression analyses, we identified 2 populations of hepatic macrophages and 2 populations of monocytes. We also identified 4 populations of dendritic cells and 1 population of basophils. After selective depletion of liver phagocytes, intravascular myeloid precursors began to differentiate into macrophages and dendritic cells; dendritic cells migrated out of sinusoids, after a delay, via the chemokine CX3CL1. The cell distribution returned to normal in 2 weeks, but the repopulated livers were unable to fully respond to drug-induced injury or clear bacteria for at least 1 month. This defect was associated with increased levels of inflammatory cytokines, and dexamethasone accelerated the repopulation of liver phagocytes. **CONCLUSIONS:** In studies of hepatic phagocyte depletion in mice, we found that myeloid precursors can differentiate into liver macrophages and dendritic cells, which each localize to distinct tissue compartments. During replenishment, macrophages acquire the ability to respond appropriately to hepatic injury and to remove bacteria from the blood stream.

Keywords: CyTOF; DC; Liver Development; Mouse Model.

The liver is a key organ for immune maturation during embryogenesis[1,2] and also plays an essential role in immune surveillance throughout life. The hepatic environment physiologically harbors a vast population of immune cells, including natural killer (NK)[3] and NK T cells,[4] dendritic cells (DCs),[5] and macrophages (Kupffer cells [KCs]).[6] In order to accomplish critical innate immune functions, phagocytic cells are strategically positioned within hepatic compartments. KCs are located in the

---

Abbreviations used in this paper: **APAP, acetaminophen; BM, bone marrow; CLL, clodronate-loaded liposomes; CyTOF, time-of-flight mass cytometry; DC, dendritic cell; GFP, green fluorescent protein; HSC, hepatic stellate cell; ICG, indocyanine green; IL, interleukin; KC, Kupffer cell; NK, natural killer cell.**

Most current article

© 2016 by the AGA Institute
0016-5085/$36.00
http://dx.doi.org/10.1053/j.gastro.2016.08.024

sinusoidal lumen, where they are constantly surveying blood content, ingesting aging erythrocytes,[7,8] and catching pathogens out of the mainstream of blood.[9,10]

Recent studies have shown that macrophages seed the liver during embryogenesis from yolk sac progenitors, and this resident pool may be maintained in adulthood via both self-renewal of precursors and, to a lesser extent, recruitment of bone marrow (BM)–derived cells. Indeed, there is a growing body of evidence that the KC population is composed mainly of cells related to embryonic precursors rather than hematopoietic cells.[11,12] DCs develop from BM-derived hematopoietic stem cells, but circulating monocyte precursors can also contribute to the resident DC pool.[13] A small population of liver DCs have been described previously[14–16]; however, in vivo studies aiming to define the precise location and actual density of DCs within the liver, as well as their relationship with other hepatic cells are needed. Additionally, despite being described as phagocytes, their ability to engulf and destroy whole pathogens remains debatable.[17]

The resident DC and KC liver populations in adulthood, therefore, are some combination of embryonic-derived precursors and monocyte-derived cells, and it is likely that multiple factors define the extent of the contribution of these 2 sources.[2] However, during *emergency repopulation*—a term we coined for the sudden complete loss of immune cells due to toxins, pathogens (ie, *Listeria*), or trauma—self-replication may not be an option. Here we used a combination of high-throughput analysis with live-imaging approaches to precisely determine phagocytic populations within the liver and the functional consequences of their replenishment by BM cells.

Methods

Experimental Procedures

Animals. C57BL/6 wild type, LysM-EGFP ($\mathit{Lyz2}^{\mathit{tm1.1Graf}}$), B6 ACTb-EGFP (C57BL/$6^{\mathit{Tg(CAG\text{-}EGFP)1Osb/J}}$; chicken beta actin), CCR$2^{-/-}$ (B6.129S4-$\mathit{Ccr2}^{\mathit{tm1Ifc}}$/Jand), CD11c-EYFP (NOD.$^{\mathit{Cg\text{-}Tg(Itgax\text{-}Venus)1Mnz/QtngJ}}$) mice were from Centro de Bioterismo in Universidade Federal de Minas Gerais (CEBIO–UFMG, Brazil). Germ-free Swiss/NIH mice were derived from a germ-free nucleus (Taconic Farms, Hudson, NY). CD11c-EYFP-DTR, CX3CR$1^{\mathrm{gfp/gfp}}$ and CX3CR$1^{\mathrm{gpf/wt}}$ (B6.129P-$^{\mathit{Cx3cr1tm1Litt/J}}$) were from Animal Facility of University of Calgary (Alberta, Canada). CX3CR1-DTR-EYFP (B6.129P$2^{\mathit{(Cg)\text{-}Cx3cr1tm2.1(cre/ERT2)Litt/WganJ}}$) mice were from Animal Facility of Harvard Institutes of Medicine (Boston, MA). Mice that expressed diphtheria toxin receptor received tamoxifen (10 mg/mouse in peanut oil, intraperitoneally) for 5 consecutive days and were treated with diphtheria toxin (500 ng/mouse, in sterile phosphate-buffered saline; intraperitoneally) for 2 consecutive days for selective depletion before experiments. CD11c-DTR mice were treated with diphtheria toxin at the same regimen from CX3CR1-DTR. All animals were housed in a conventional specific pathogen-free facility at the Universidade Federal de Minas Gerais, Harvard Institutes of Medicine and University of Calgary, according to the animal protocol, with the full knowledge and permission of the Standing Committee on Animals at all institutions.

Confocal Microscopy and Immunohistochemistry

Confocal intravital imaging was performed as described previously.[18] Before surgery, mice received a single dose or a mixture of the following antibodies or fluorescent probes: anti-F4/80 phycoerythrin (4 μg, clone BM8, eBiosciences, San Diego, CA), anti-CD31 BV-421 (4 μg, clone MEC 13.3, BD Horizon, San Jose, CA), anti-CX3CL1 phycoerythrin (60 μL per mouse; eBiosciences), 4′,6-diamidino-2-phenylindole (0.1 mL at 1 mM; Sigma, St Louis, MO), and albumin fluorescein isothiocyanate (0.1 mL at 5 mg per mL). Liver fragments were also stained with anti-podoplanin phycoerythrin (1:50 solution; BioLegend, San Diego, CA), anti–green fluorescent protein (GFP) (1:50 solution; Santa Cruz Biotechnology, Santa Cruz, CA), or desmin (1:50; Dako, Carpinteria, CA) for ex vivo images. Alexa Fluor 586–conjugated goat anti-mouse was used as secondary antibody for desmin experiments (1:50, Thermo Fisher Scientific, Logan, UT). Vitamin A autofluorescence was imaged using a 405-nm laser. Mice were imaged using Nikon Eclipse Ti with a C2 confocal. Cell density, location, and 3-dimensional rendering were made using Volocity (6.3) (Perkin Elmer, Waltham, MA).

Liver Nonparenchymal Cells

Liver nonparenchymal cells were isolated as reported previously.[19] Livers were digested in a collagenase solution and cells were differentially separated by centrifugation. For time-of-flight mass cytometry (CyTOF) experiments, 1×10^6 cells were stained with isotope-conjugated antibodies as described.[20] Events were gated for CD45$^+$ cells, and T cells, B cells, red blood cells, and hepatic stellate cells (HSCs) were excluded from analysis. NK cells frequency was investigated by fluorescence-activated cell sorting (CD11c$^+$CD3$^-$NKp46$^+$NK1.1$^+$). Absence of HSCs in these samples was also checked by reverse transcription polymerase chain reaction. A complete list of antibody panels and genes used in reverse transcription polymerase chain reaction (Taqman probes) can be found in Supplementary Table 1. Samples were acquired with a Helios Mass Cytometer (Fluidigm, South San Francisco, CA) and data were plotted using viSNE analysis as described previously. Gates were done as described in Results section.

For Nanostring experiments, liver nonparenchymal cells were isolated from CX3CR$1^{\mathrm{gfp/wt}}$ mice and stained with anti-F4/80 allophycocyanin (1:100, clone BM8; eBiosciences). Samples were acquired using cell sorter FACSAria III and gates were made in F4/80$^+$CX3CR1$^-$ for intravascular cells and F4/80$^-$CX3CR1$^+$ for extravascular cells. Splenic DCs were sorted as CD11c$^+$ F4/80$^-$ cells and peritoneal macrophages were collected by lavage and sorted as F4/80$^+$ cells. Approximately 1×10^5 of each cell type was sorted, and each sample consisted in a pool of 2 mice, and 3 samples were run independently.

Bone Marrow Isolation

BM cells were harvested from mouse femurs and tibia using a needle to remove the cells from the medullary cavity.[21] BM chimeras were performed as described previously.[22] In these experiments, wild-type mice received 10^7 BM cells intravenously from B6 ACTb-EGFP mice and were allowed to recover for 6 weeks before experiments.

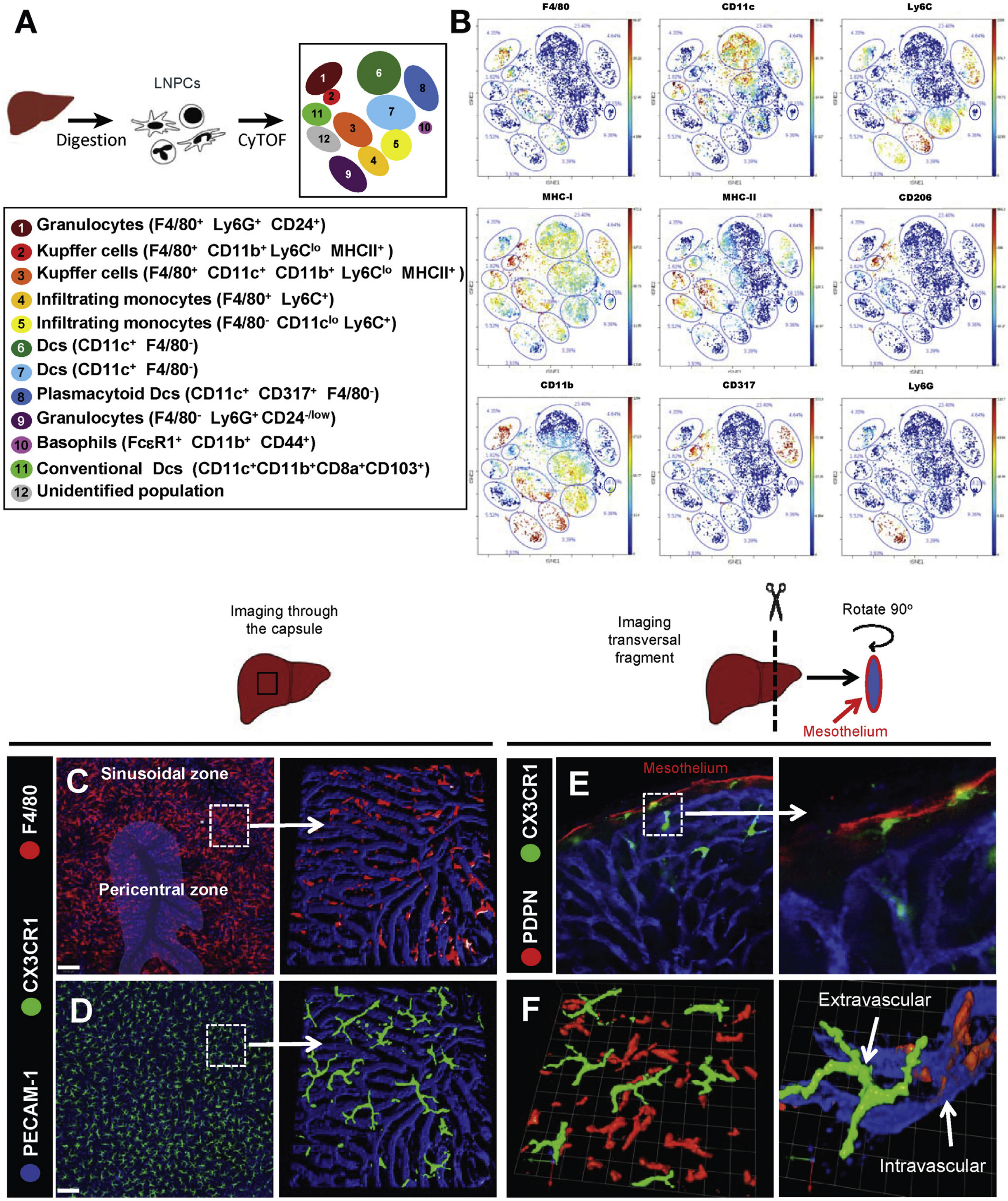
A
LNPCs
Digestion
CyTOF
1 2 3 4 5 6 7 8 9 10 11 12
1 Granulocytes (F4/80⁺ Ly6G⁺ CD24⁺)
2 Kupffer cells (F4/80⁺ CD11b⁺ Ly6Clo MHCII⁺)
3 Kupffer cells (F4/80⁺ CD11c⁺ CD11b⁺ Ly6Clo MHCII⁺)
4 Infiltrating monocytes (F4/80⁺ Ly6C⁺)
5 Infiltrating monocytes (F4/80⁻ CD11clo Ly6C⁺)
6 Dcs (CD11c⁺ F4/80⁻)
7 Dcs (CD11c⁺ F4/80⁻)
8 Plasmacytoid Dcs (CD11c⁺ CD317⁺ F4/80⁻)
9 Granulocytes (F4/80⁻ Ly6G⁺ CD24⁻/low)
10 Basophils (FcεR1⁺ CD11b⁺ CD44⁺)
11 Conventional Dcs (CD11c⁺CD11b⁺CD8a⁺CD103⁺)
12 Unidentified population
B
F4/80
CD11c
Ly6C
MHC-I
MHC-II
CD206
CD11b
CD317
Ly6G
Imaging through the capsule
Imaging transversal fragment
Rotate 90º
Mesothelium
C
Sinusoidal zone
Pericentral zone
D
F4/80
CX3CR1
PECAM-1
E
Mesothelium
CX3CR1
PDPN
F
Extravascular
Intravascular

Figure 1. Identification of liver phagocytes by CyTOF and intravital microscopy. (*A*) Schematic representation of isolation liver nonparenchymal cells (LNPC) and clustering after CyTOF analysis. (*B*) *Dot plot* representation of viSNE analysis showing different clusters and the expression of several different surface markers that enable the distinction of immune populations. (*C*) Liver confocal intravital microscopy imaging through the capsule evidencing the distribution of F4/80$^+$ cells (Kupffer cells; in *red*; anti-F4/80) in different liver regions. (*D*) Same as (*C*) but for CX3CR1$^+$ cells (CX3CR1$^{gfp/wt}$ mice). (*E*) Ex vivo imaging of liver fragment revealed that DCs (CX3CR1$^+$ cells) are mainly located under the mesothelium (stained with anti-podoplanin). (*F*) Three-dimensional rendering of F4/80$^+$ (intravascular) and CX3CR1$^+$ cells (extravascular) showing their different spatial location. *Scale bars* = 120 μm. Error bars indicate the mean ± SEM. *$P < .05$ (unpaired *t* test). n = 5/group.

Drug-Induced Liver Injury Model and Clodronate-Induced Depletion

Acetaminophen (APAP; 600 mg per kg; Sigma) was dissolved in warm saline before gavage and serum alanine aminotransferase was estimated as described.[21] Indocyanine green (ICG; Sigma) clearance by the liver was estimated in serum after injecting a single dose of 20 mg per kg intravenously. Blood was collected 20 minutes after injection and the amount of ICG was determined by spectrophotometry (absorbance in 800 nm). KC/DC depletion was achieved by intravenous injection of 200 μL clodronate liposomes (ClodronateLiposomes.com) 48 hours before experiments. In dexamethasone treatment protocol, mice received a daily intraperitoneal dose of 5 mg/kg of dexa dissolved in corn oil during 7 days.

Systemic Escherichia coli *Injection*

Escherichia coli GFP (ATCC 25922GFP) were cultivated in Luria broth medium (MP Biomedicals, Santa Ana, CA). In flow cytometry experiments, mice intravenously received 10^6 *E coli* and blood was collected after 5 minutes. Blood samples were immediately diluted in phosphate-buffered saline (1:20) and read in cytometer. To in vivo imaging of *E coli* capture, mice received 10^7 *E coli* intravenously and were imaged under confocal microscopy for 5 minutes.

Multiplex Cytokine Array

Liver samples were weighted (50 mg) and homogenized. Cytokine concentration in the supernatant was dosed following manufacture's instruction (Milliplex MCYTOMAG- 0K-32. Mouse Cytokine MAGNETIC Kit).

Expression Data Analysis

Expression abundance was obtained by Nanostring nCounter mouse Immunology Assay. The correlation of gene expression among different cell types were calculated and plotted as heatmap using the R platform. Differentially expressed genes were identified by DESeq2 R Package. Statistically relevant results are considered with $P < .05$ and a fold change of at least 50% higher or lower. Pathways and functional classification were done by cross association using Kyoto Encyclopedia of Genes and Genomes Pathways and Kyoto Encyclopedia of Genes and Genomes Brite databases.

Statistical Analyses

Experimental data analysis was performed with one-way analysis of variance (one-way analysis of variance with Tukey's post-hoc test) and unpaired Student *t* test provided by Prism 5.0 software (GraphPad, La Jolla, CA). All data are given as the mean ± SEM. In vivo experimental groups had at least 5 mice per group. Data shown are representative of at least 2 independent experiments. Differences were considered to be significant at $P < .05$.

Results

High-Dimensional Identification of Liver Phagocytes

To better characterize the resident phagocytic populations, we purified liver nonparenchymal cells (CD45$^+$ liver nonparenchymal cells) and performed CyTOF analysis, which allows for simultaneous staining with multiple combinations of cell markers, and can reveal new immune cell populations that would not be uncovered by conventional flow cytometry. In these experiments, we gated on CD45$^+$ cells and excluded red blood cells, Ito cells, and B and T cells during analysis. Using an unbiased viSNE analysis to map high-dimensional cytometry data, we identified 12 clusters of liver nonparenchymal cells (Figure 1*A*). The majority of cells mapped to either F4/80 (clusters 1–4) or CD11c (clusters 5–8) (Figure 1*A* and *B*). Cluster 1 was defined as mature granulocytes due to intermediate expression level of Ly6G (Figure 1*A* and *B*) and high expression of CD24 (Supplementary Figure 1*A*). Based on the expression of F4/80, MHC-II, and CD11b (Figure 1*A* and *B*), we defined 2 different populations of KCs (clusters 2 and 3). KC cluster 2 expressed CD206, CD317, and CD1d, whereas cluster 3 was negative for CD206, CD317, and CD1d, but expressed CD11c (Figure 1*A* and Supplementary Figure 1*A*). Cluster 4 and 5 were characterized as infiltrating monocytes because they were CD11b$^+$Ly6C$^+$MHC-I^{int}MHC-II^{lo}, but cluster 5 was F4/80$^-$ and CD11c^{lo} (Figure 1*A* and *B*). Clusters 6–8 and 11 were categorized as DCs, because they were CD11c$^+$CD11b$^{int/hi}$F4/80$^-$Ly6G$^-$MHC-I$^+$MHC-II$^{+/lo}$. Cluster 8 was defined as plasmacytoid DCs due to their high expression of the plasmacytoid DC marker CD317 (Figure 1*A* and *B*). Cluster 9 was also defined as granulocytes according to their high expression of Ly6G, CD11b, and Gr1, as well as intermediate expression of CD24 and Ly6C (Figure 1*A* and *B* and Supplementary Figure 1*A*). Finally, cells that expressed the high-affinity IgE receptor (FcεRI), together with CD44 and CD11b, were clustered as basophils (cluster 10) (Figure 1*A* and *B* and Supplementary Figure 1*A*). Cluster 11 may represent a population of conventional DCs due to the expression of CD11c, CD11b, CD8a, and CD103 (Figure 1*A* and *B* and Supplementary Figure 1*A*). CD11c$^+$ NK cells (NK1.1 and NKp46) comprised an insignificant population in this setup (<0.2%) and were not considered during analysis (Supplementary Figure 1*B*). Cluster 12 could not be categorized using the markers chosen for this experiment. A schematic clustering explanation is depicted in Figure 1*A*.

To spatially resolve the location and the relationship between the main F4/80$^+$ and CD11c$^+$ populations, we imaged the liver by confocal intravital microscopy.[18] We first identified the main vascular arrangements that could constitute points of reference for the location of different liver immune cells (Supplementary Figure 2 and Supplementary Movie 1). Based on in vivo blood flow tracking, 2 main vascular regions were defined: the area surrounding a centrilobular vein was termed the *pericentral zone*, and the remaining areas in between were referred to as the sinusoidal zone (Figure 1*C*). In an expanded field of view, we observed that F4/80$^+$ cells were not homogeneously distributed within the liver, as they accumulated preferentially in the sinusoidal zone rather than in pericentral areas (Figure 1*C*). Three-dimensional reconstruction showed that these cells inhabited the intravascular compartment exclusively and specifically (Figure 1*C* and

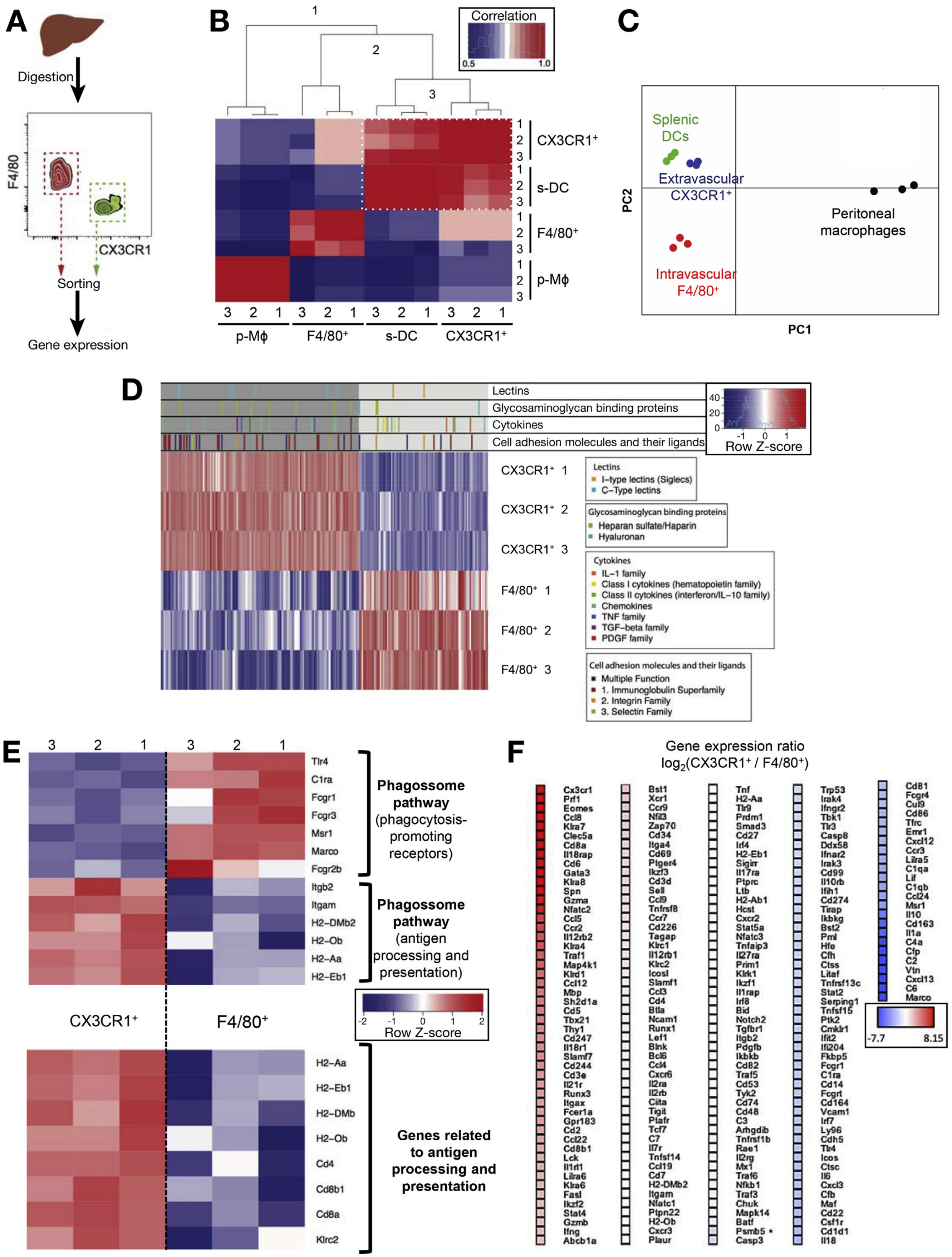
A
Digestion
F4/80
CX3CR1
Sorting
Gene expression
B
1
2
3
Correlation
0.5
1.0
CX3CR1^{+}
s-DC
F4/80^{+}
p-Mϕ
3 2 1 3 2 1 3 2 1 3 2 1
p-Mϕ
F4/80^{+}
s-DC
CX3CR1^{+}
C
Splenic DCs
Extravascular CX3CR1^{+}
Peritoneal macrophages
Intravascular F4/80^{+}
PC2
PC1
D
Lectins
Glycosaminoglycan binding proteins
Cytokines
Cell adhesion molecules and their ligands
40
20
0
-1 0 1
Row Z-score
CX3CR1^{+} 1
CX3CR1^{+} 2
CX3CR1^{+} 3
F4/80^{+} 1
F4/80^{+} 2
F4/80^{+} 3
Lectins
I–type lectins (Siglecs)
C–Type lectins
Glycosaminoglycan binding proteins
Heparan sulfate/Haparin
Hyaluronan
Cytokines
IL–1 family
Class I cytokines (hematopoietin family)
Class II cytokines (interferon/IL–10 family)
Chemokines
TNF family
TGF–beta family
PDGF family
Cell adhesion molecules and their ligands
Multiple Function
1. Immunoglobulin Superfamily
2. Integrin Family
3. Selectin Family
E
3 2 1 3 2 1
Tlr4
C1ra
Fcgr1
Fcgr3
Msr1
Marco
Fcgr2b
Itgb2
Itgam
H2–DMb2
H2–Ob
H2–Aa
H2–Eb1
Phagossome pathway (phagocytosis-promoting receptors)
Phagossome pathway (antigen processing and presentation)
-2 -1 0 1 2
Row Z-score
CX3CR1^{+}
F4/80^{+}
H2–Aa
H2–Eb1
H2–DMb
H2–Ob
Cd4
Cd8b1
Cd8a
Klrc2
Genes related to antigen processing and presentation
F
Gene expression ratio
$\log_2$(CX3CR1^{+} / F4/80^{+})
Cx3cr1
Prf1
Eomes
Ccl8
Klra7
Clec5a
Cd8a
Il18rap
Cd6
Gata3
Klra8
Spn
Gzma
Nfatc2
Ccl5
Ccr2
Il12rb2
Klra4
Traf1
Map4k1
Klrd1
Ccl12
Mbp
Sh2d1a
Cd5
Tbx21
Thy1
Cd247
Il18r1
Slamf7
Cd244
Cd3e
Il21r
Runx3
Itgax
Fcer1a
Gpr183
Cd2
Ccl22
Cd8b1
Lck
Il1rl1
Lilra6
Klra6
Fasl
Ikzf2
Stat4
Gzmb
Ifng
Abcb1a
Bst1
Xcr1
Ccr9
Nfil3
Zap70
Cd34
Itga4
Cd69
Ptger4
Ikzf3
Cd3d
Sell
Ccl9
Tnfrsf8
Ccr7
Cd226
Tagap
Klrc1
Il12rb1
Klrc2
Icosl
Slamf1
Ccl3
Cd4
Btla
Ncam1
Runx1
Lef1
Blnk
Bcl6
Ccl4
Cxcr6
Il2ra
Il2rb
Ciita
Tigit
Ptafr
Tcf7
C7
Il7r
Tnfsf14
Ccl19
Cd7
H2-DMb2
Itgam
Nfatc1
Ptpn22
H2-Ob
Cxcr3
Plaur
Tnf
H2-Aa
Tlr9
Prdm1
Smad3
Cd27
Irf4
H2-Eb1
Sigirr
Il17ra
Ptprc
Ltb
H2-Ab1
Hcst
Cxcr2
Stat5a
Nfatc3
Tnfaip3
Il27ra
Prim1
Klrk1
Ikzf1
Il1rap
Irf8
Bid
Notch2
Tgfbr1
Itgb2
Pdgfb
Ikbkb
Cd82
Traf5
Cd53
Tyk2
Cd74
Cd48
C3
Arhgdib
Tnfrsf1b
Rae1
Il2rg
Mx1
Traf6
Nfkb1
Traf3
Chuk
Mapk14
Batf
Psmb5 *
Casp3
Trp53
Irak4
Ifngr2
Tbk1
Tlr3
Casp8
Ddx58
Ifnar2
Irak3
Cd99
Il10rb
Ifih1
Cd274
Tirap
Ikbkg
Bst2
Pml
Hfe
Cfh
Ctss
Litaf
Tnfrsf13c
Stat2
Serping1
Tnfsf15
Ptk2
Cmklr1
Ifit2
Ifi204
Fkbp5
Fcgr1
C1ra
Cd14
Fcgrt
Cd164
Vcam1
Irf7
Ly96
Cdh5
Tlr4
Icos
Ctsc
Il6
Cxcl3
Cfb
Maf
Cd22
Csf1r
Cd1d1
Il18
Cd81
Fcgr4
Cul9
Cd86
Tfrc
Emr1
Cxcl12
Ccr3
Lilra5
C1qa
Lif
C1qb
Ccl24
Msr1
Il10
Cd163
Il1a
C4a
Cfp
C2
Vtn
Cxcl13
C6
Marco
-7.7
8.15

Supplementary Movie 2). Consistent with this, all F4/80$^+$ cells were also positive for lysozyme M, a marker for macrophages (LysM-EGFP mice; Supplementary Figure 3*A*), confirming that all of these cells were KCs and none were ever seen in the parenchyma.

Intravital imaging also revealed a large hepatic population of CD11c$^+$ cells with differential spatial distribution (CD11c-EYFP reporter mice; Supplementary Figure 3*B*). The CD11c$^+$F4/80$^-$ population was larger in size, displayed numerous dendrites on their surface and inhabited the extravascular space, suggestive of a population of DCs (Supplementary Movie 3). However, as mentioned, CD11c$^+$F4/80$^+$ cells were also observed lining the intravascular area, and resembled KC morphology validating 2 different KC populations from CyTOF (Figure 1*B*, Supplementary Figure 3*B* and Supplementary Movie 3). CD11c expression in both intravascular and extravascular populations was confirmed by CD11c-targeted depletion (CD11c-DTR-EYFP mice), which caused full depletion of extravascular CD11c$^+$ cells and also a significant decrease (approximately 50%) in intravascular CD11c$^+$F4/80$^+$ cells (Supplementary Figure 3*C*).

To image just the extravascular cells, we used CX3CR1$^{gfp/wt}$ reporter mice because CX3CR1 is expressed on DCs,[23] but not on mature KCs under homeostatic conditions.[11] We found an exclusively extravascular population of CX3CR1$^+$ cells (Figure 1*D* and Supplementary Movie 4), which were similar in shape and number to an extravascular CD11c$^+$F4/80$^-$ population (Supplementary Figure 3*B*). Intravital images through the liver surface showed that CX3CR1$^+$ cells are abundant and uniformly distributed in the field of view; however, ex vivo imaging of liver fragments using transversal slices revealed that such spider-like CX3CR1$^+$ cells were found mainly under a thin layer of mesothelium that covers the liver (Figure 1*E*), and were not distributed throughout the sinusoids as KCs. Also, CX3CR1$^+$ cells were CD11c$^+$ (Supplementary Figure 4*A*), but negative for desmin (Supplementary Figure 5*A*), excluding them as a population of HSCs. Of note, CD11c$^+$ cells were also negative for desmin (Supplementary Figure 5*A*). Deeper imaging within the liver showed that some CX3CR1$^+$ cells were also found surrounding larger hepatic vessels (Supplementary Figure 4*B* and *C*). As seen in higher magnification of 3-dimensional reconstructions, there is intimate contact of some F4/80$^+$ intravascular and CX3CR1$^+$ extravascular cells, and the latter emit protrusions to reach the vessel lumen (Figure 1*F*). To confirm that extravascular, and not intravascular, cells specifically expressed CX3CR1, we used a mouse strain that has both DTR and EYFP expression under control of CX3CR1 (CX3CR1 [CreER]-DTR-EYFP). Treatment with diphtheria toxin led to 95% depletion of extravascular CX3CR1$^+$ cells, with no detectable effects on intravascular F4/80$^+$ cells, validating CX3CR1 as a selective marker for extravascular cells under homeostatic conditions (monitored by intravital microscopy; Supplementary Figure 3*D*).

Next, we isolated extravascular CX3CR1$^+$F4/80$^-$ and intravascular CX3CR1$^-$F4/80$^+$ cells by sorting (Figure 2*A*) and dissected their phenotypic identities by measuring gene expression using the Nanostring nCounter mouse immunology assay, a multiplexed messenger RNA hybridization approach. We excluded the presence of HSCs in these samples because, after our isolation procedure, we did not detect the expression of HSCs common genes (Supplementary Figure 5*B*). Also, we did not detect vitamin A granules by either intravital microscopy (Supplementary Figure 5*C*) or fluorescence-activated cell sorting (Supplementary Figure 5*D*). Both liver-isolated populations clustered together when compared with a liver-unrelated cell (activated peritoneal macrophage; Figure 2*B* and *C*). This approach suggests that the extravascular CX3CR1$^+$F4/80$^-$ and intravascular CX3CR1$^-$F4/80$^+$ cells have a similar source and/or environment dictating their clustered genotype.

However, functional category analysis showed that intra- and extravascular cells had a differential expression of genes belonging to C- and I-type lectins, glycosaminoglycan-binding proteins, cytokines, and various other molecules (Figure 2*C* and GEO accession number: GSE81645). Phagocytosis-promoting receptors were significantly enriched on the CX3CR1$^-$F4/80$^+$ population (Figure 2*E*), suggesting an active role in recognition and clearance of bacteria or antigens from the circulation. In line with this, CX3CR1$^-$F4/80$^+$ cells had significantly higher expression of macrophage-related genes, such as *Marco*, *Cd163*, and *Mrs1* (Figure 2*F*). By contrast, CX3CR1$^+$F4/80$^-$ cells had enriched pathways involved in antigen processing and presentation (Figure 2*E*), with higher expression of DC common genes, including *Cx3cr1*, *Prf1*, and *Itgax* (Figure 2*F*). In fact, hierarchical clustering (Figure 2*B*) and principal coordinate analysis (Figure 2*C*) confirmed that the genetic profile of CX3CR1$^+$F4/80$^-$ cells was closely related to a classic DC isolated from the spleen. Taking together the expression of surface markers, cell morphology, and genetic profile, we established that extravascular CX3CR1$^+$F4/80$^-$ cells are a population of liver DCs that are located mainly in the submesothelial space, while intravascular CX3CR1$^-$F4/80$^+$ cells comprised the hepatic resident macrophages, or KCs.

Figure 2. Genetic profiles of different liver phagocytes. (*A*) Schematic representation of isolation and sorting of CX3CR1$^+$ and F4/80$^+$ cells. Total RNA was extracted to further gene analysis. (*B*) Heatmap showing gene expression correlation between liver CX3CR1$^+$ and F4/80$^+$ cells, splenic dendritic cells (s-DC; CD11c$^+$ F4/80$^-$) and peritoneal macrophages (p-Mϕ). *White dotted square* highlights the genetic proximity between liver CX3CR1$^+$ cells and splenic DCs (correlation $\sim$1). (*C*) Principal coordinates analysis (PCoA) of different isolated cells showing how extravascular CX3CR1$^+$ cells genetically correlate with splenic DCs. (*D*) Functional category analysis based on the gene expression ratio between liver CX3CR1$^+$ and F4/80$^+$ cells evidencing their putative different functions within the liver. (*E*) Same as (*D*), but grouped as functional pathways based on gene ontology. (*F*) Statistically different genes ranked as expression ration of CX3CR1$^+$/F4/80$^+$. n = 3/group.

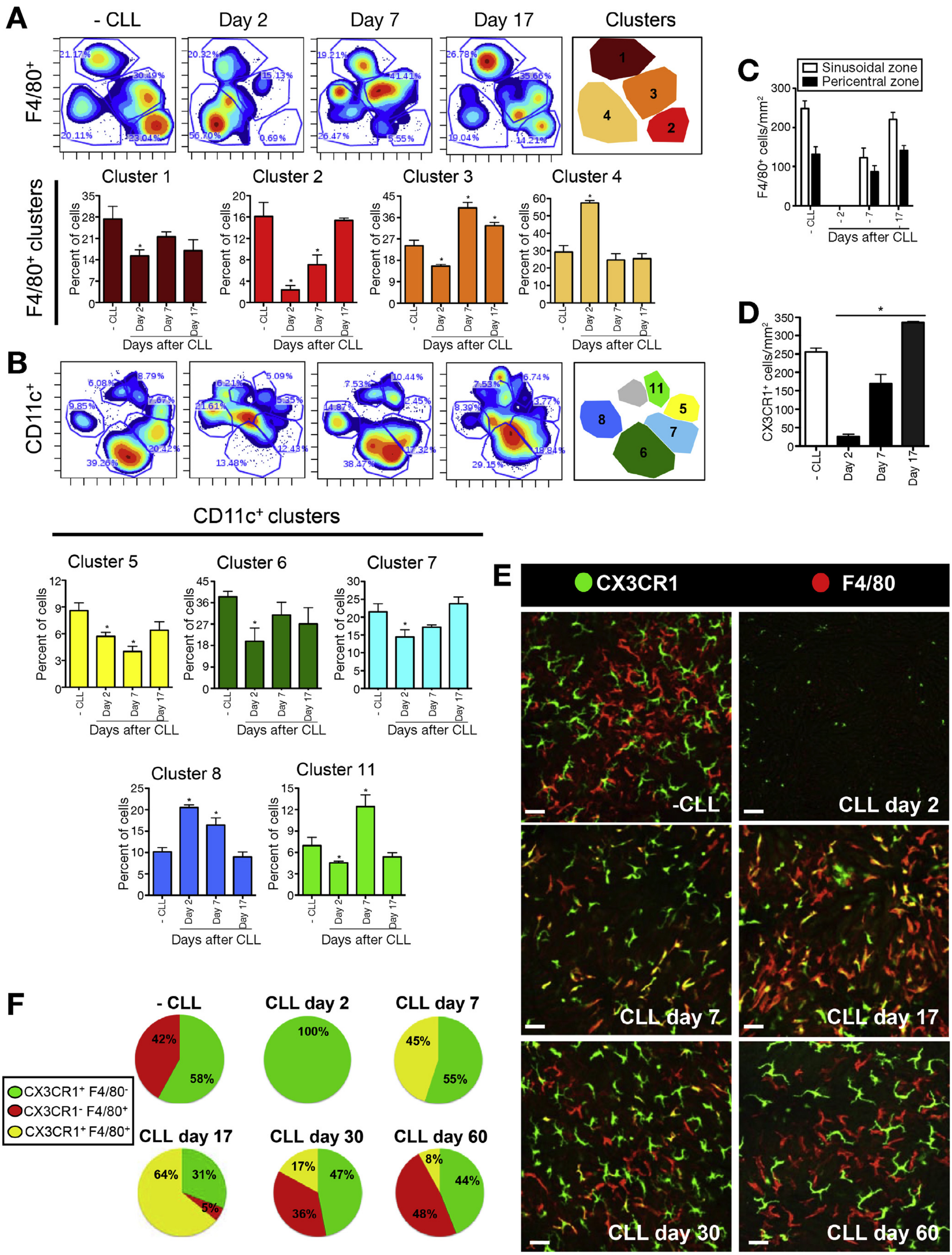
A
- CLL
Day 2
Day 7
Day 17
Clusters
F4/80+
21.17%
30.49%
20.11%
23.04%
20.32%
15.13%
56.70%
0.69%
19.21%
41.41%
26.47%
5.55%
26.78%
35.66%
19.04%
14.21%
1
2
3
4
F4/80+ clusters
Cluster 1
Cluster 2
Cluster 3
Cluster 4
Percent of cells
Days after CLL
- CLL
Day 2
Day 7
Day 17
*
B
CD11c+
6.08%
8.79%
9.85%
7.67%
39.26%
20.42%
6.21%
5.09%
21.61%
5.35%
13.48%
12.43%
7.53%
10.44%
14.87%
2.45%
38.47%
17.32%
7.53%
6.74%
8.39%
3.77%
29.15%
18.84%
5
6
7
8
11
CD11c+ clusters
Cluster 5
Cluster 6
Cluster 7
Cluster 8
Cluster 11
C
Sinusoidal zone
Pericentral zone
F4/80+ cells/mm2
D
CX3CR1+ cells/mm2
E
CX3CR1
F4/80
-CLL
CLL day 2
CLL day 7
CLL day 17
CLL day 30
CLL day 60
F
- CLL
CLL day 2
CLL day 7
CLL day 17
CLL day 30
CLL day 60
CX3CR1+ F4/80-
CX3CR1- F4/80+
CX3CR1+ F4/80+
42%
58%
100%
45%
55%
64%
31%
5%
17%
47%
36%
8%
44%
48%

Emergency Repopulation Dynamics After Sudden Phagocyte Depletion

To better understand how these 2 populations are maintained within the liver, we removed liver phagocytes with clodronate-loaded liposomes (CLL), a commonly used method to deplete tissue macrophages, and monitored their replenishment dynamics. Focusing on F4/80-gated clusters (Figure 3*A*), CyTOF analysis showed that the majority of KCs (clusters 2–3) were depleted 2 days after CLL treatment (Figure 3*A* and Supplementary Figure 1*C*). The frequency of infiltrating monocytes was increased (cluster 4), suggesting that these cells may consist in a source of monocyte-derived macrophages. Gating on CD11c$^+$ events (Figure 3*B*), we observed that DC clusters (6, 7, and 11) were also reduced, demonstrating that CLL treatment depletes not only KCs, but also DCs (Figure 3*B*). Intravital imaging confirmed full depletion of KCs (Figure 3*C*) and approximately 95% reduction in DC numbers (Figure 3*D*) after CLL. Of note, the remaining DCs after CLL treatment were mainly the plasmacytoid DCs (cluster 8), which were not affected by CLL (Figure 3*B*). At this time point, F4/80$^+$Ly6C$^+$ infiltrating monocytes belonging to cluster 4 were highly increased (20.11% in nondepleted group to 56.70% in CLL day 2 group; Figure 3*A*).

One week after depletion, CLL-depleted clusters began to replenish the liver (Figure 3*A* and *B* and Supplementary Figure 6*A*) and infiltrating monocytes (cluster 4) returned to baseline frequency. In vivo imaging showed that the majority of the 2 populations of replenished cells were CX3CR1$^+$ and inhabited the intravascular compartment at the 7th day post depletion (Figure 3*E*). These cells were homogeneously distributed throughout the liver (Figure 3*E*) and F4/80 expression was now (but not at day 2) detected on half of the population of CX3CR1$^+$ cells (Figure 3*F*). Seventeen days after CLL treatment, normal frequencies and numbers of both KC and DC clusters were observed as determined by CyTOF analysis (Figure 3*A* and *B* and Supplementary Figure 6*B*). Almost all cells remained CX3CR1$^+$, whereas F4/80 expression was found on 64% of these cells and a small population of F4/80$^+$ cells (5%) has lost their CX3CR1 expression (Figure 3*E* and *F*). By day 30, 36% of cells were F4/80$^+$CX3CR1$^-$, with only 17% double-positive cells. After 60 days, cells returned to near baseline distribution, with only 8% remaining F4/80$^+$CX3CR1$^+$ (Figure 3*F*). Noteworthy is that at day 7, all of the CX3CR1$^+$ cells (half F4/80-positive half negative) were still inside the vasculature, suggesting that their early differentiation occurs in the sinusoids. KC distribution recovered 80% of the baseline values at day 17 after depletion (Figure 4*A* and *B*), while the DC density was still reduced at the same time point, suggesting that DCs have slower repopulation kinetics in comparison with KCs. Normal cell numbers were observed at day 30 for both cell types (Figure 4*A* and *B*). Normalized absolute event numbers corroborated frequency data from all CyTOF experiments (Supplementary Table 2).

A CXC3CL1 Gradient Drives Extravascular Dendritic Cell Re-establishment

Because CX3CR1 expression was prevalent early in the repopulation period, we hypothesized that a gradient of its ligand, CX3CL1, would guide CX3CR1$^+$ phagocyte precursors initially to the sinusoids and facilitated their differentiation into mature KCs and DCs. In vivo staining revealed that CX3CL1 was constitutively found in the liver microvasculature (Figure 5*A* and *B*) and its expression was increased after depletion and during the first time points of the replenishment phase (2nd and 7th day after CLL; Figure 5*A* and *B*). CX3CL1 was also increased in the extravascular compartment (*arrowheads* on Figure 5*A*) and, after 17 days post-CLL treatment, baseline expression of CX3CL1 was re-established (Figure 5*A*). This suggests that CX3CL1 production precedes DC extravasation to extravascular spaces. To confirm the role of CX3CL1 on both cell recruitment and distribution, we used CX3CR1$^{gfp/gfp}$ (deficient) mice and found approximately 50% less liver DCs under basal conditions in comparison with the heterozygote strain (CX3CR1$^{gfp/wt}$; Figure 5*C* and *D*). This 50% relative reduction in DC density in CX3CR1-deficient mouse was seen throughout the emergency repopulation period (Figure 5*D*). Interestingly, CX3CR1-deficient mice had about 20%–30% more KCs under basal conditions (Figure 5*E* and *F*), and this small density increase was observed throughout the experimental time (Figure 5*F*). This suggests that CX3CR1 was not required for progenitor cell recruitment and KC development, but was crucial for DC extravasation and survival in the extravascular space. Because CCL2/CCR2 interaction mediates monocyte egress from BM and their further recruitment into tissues, we also investigated the contribution of CCR2 to phagocyte seeding within the liver. In sharp contrast to the absence of CX3CR1, CCR2$^{-/-}$ mice have normal KC/DC distribution and density (Supplementary Figure 5*E* and *F*). In addition, CCR2 seems not to contribute to further DC emigration and maturation within the extravascular compartment.

Figure 3. Emergency repopulation dynamics of liver phagocytes. (*A*) Density *dot plot* from CyTOF showing clustered populations based on F4/80 expression during phagocyte replenishment period and percentage of cells in the different F4/80$^+$ clusters during phagocyte replenishment period. Mice were treated with CLL (200 μL) at day 0, and evaluated in different time points. (*B*) Same as (*A*), but for CD11c expression. (*C*) Quantification of F4/80$^+$ cells in different liver zones showing their heterogeneous distribution and their recovery to normal number and location after 17 days. (*D*) Same as (*C*), but for CX3CR1$^+$ cells (CX3CR1$^{gfp/wt}$ mice). (*E*) Liver intravital microscopy throughout phagocyte repopulating period. (*F*) Quantification of CX3CR1$^+$, F4/80$^+$ or double-positive cells from intravital microscopy. Scale bars = 40 μm. Error bars indicate the mean ± SEM. *$P < .05$ (unpaired *t* test), in comparison to –CLL group. n = 5/group.

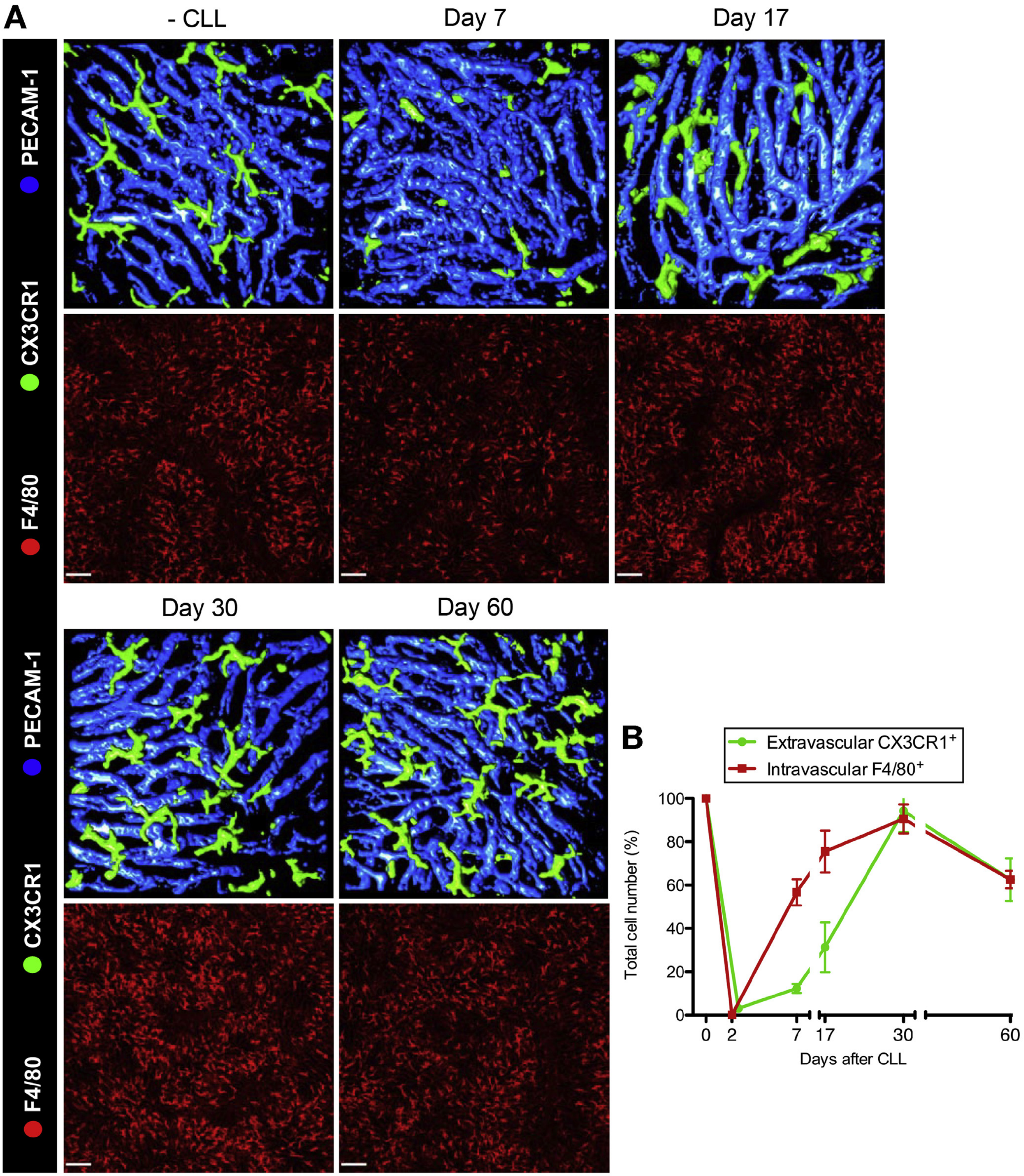
A
- CLL
Day 7
Day 17
● F4/80 ● CX3CR1 ● PECAM-1
Day 30
Day 60
● F4/80 ● CX3CR1 ● PECAM-1
B
Extravascular CX3CR1+
Intravascular F4/80+
Total cell number (%)
100
80
60
40
20
0
0
2
7
17
30
60
Days after CLL

Figure 4. Differential repopulation kinetics of DCs and KCs. (*A*) Liver intravital microscopy images from different time points after clodronate injection. *Upper panel* shows extravascular CX3CR1$^+$ cells (in *green*, 3-dimensional rendering; CX3CR1$^{gfp/wt}$ mice). Sinusoids were evidenced in *blue* (anti–PECAM-1 antibody). KCs (intravascular F4/80$^+$ cells stained with anti-F4/80 antibody) are depicted in *lower panels*. (*B*) Quantification of cell numbers over the repopulation period in comparison to baseline values (adjusted to 100% as control). *Scale bars* = 120 μm.

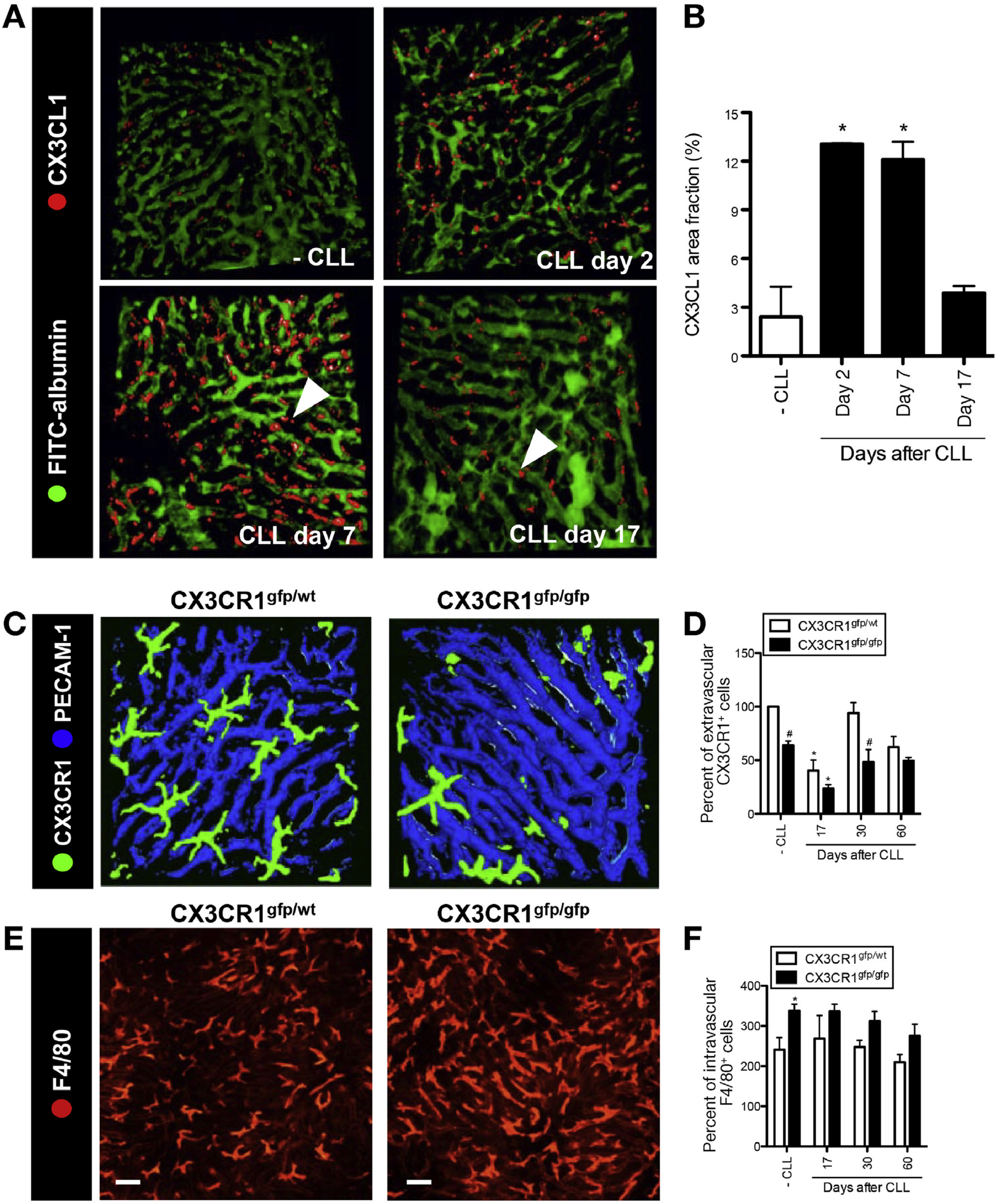
A
● FITC-albumin ● CX3CL1
- CLL
CLL day 2
CLL day 7
CLL day 17
B
CX3CL1 area fraction (%)
15
12
9
6
3
0
*
*
- CLL
Day 2
Day 7
Day 17
Days after CLL
C
CX3CR1gfp/wt
CX3CR1gfp/gfp
● CX3CR1 ● PECAM-1
D
☐ CX3CR1gfp/wt
■ CX3CR1gfp/gfp
Percent of extravascular CX3CR1+ cells
150
100
50
0
#
*
*
#
- CLL
17
30
60
Days after CLL
E
CX3CR1gfp/wt
CX3CR1gfp/gfp
● F4/80
F
☐ CX3CR1gfp/wt
■ CX3CR1gfp/gfp
Percent of intravascular F4/80+ cells
400
300
200
100
0
*
- CLL
17
30
60
Days after CLL

Figure 5. CX3CR1 guides BM precursors to repopulate the liver. (*A*) Liver intravital microscopy showing the expression and distribution of CX3CL1 (in *red*; anti-CX3CL1) and (*B*) digital quantification of CX3CL1 distribution within the liver. Vessels were stained by intravenous injection of fluorescein isothiocyanate albumin (5 mg/kg). (*C*) Liver intravital microscopy from CX3CR1$^{gfp/wt}$ and CX3CR1$^{gfp/gfp}$ (deficient) mice showing the reduced number of extravascular DCs in deficient mice. (*D*) Quantification of extravascular CX3CR1^{+} cells during repopulation period. (*E*) Same as (*C*), but for intravascular F4/80^{+} cells. (*F*) Same as (*D*), but for intravascular F4/80^{+} cells. Scale bars = 40 μm. *$P < .05$, in comparison with vehicle-treated group and $^{\#}P < .05$ in comparison to –CLL group of the respective time point (one-way analysis of variance test). n = 5/group.

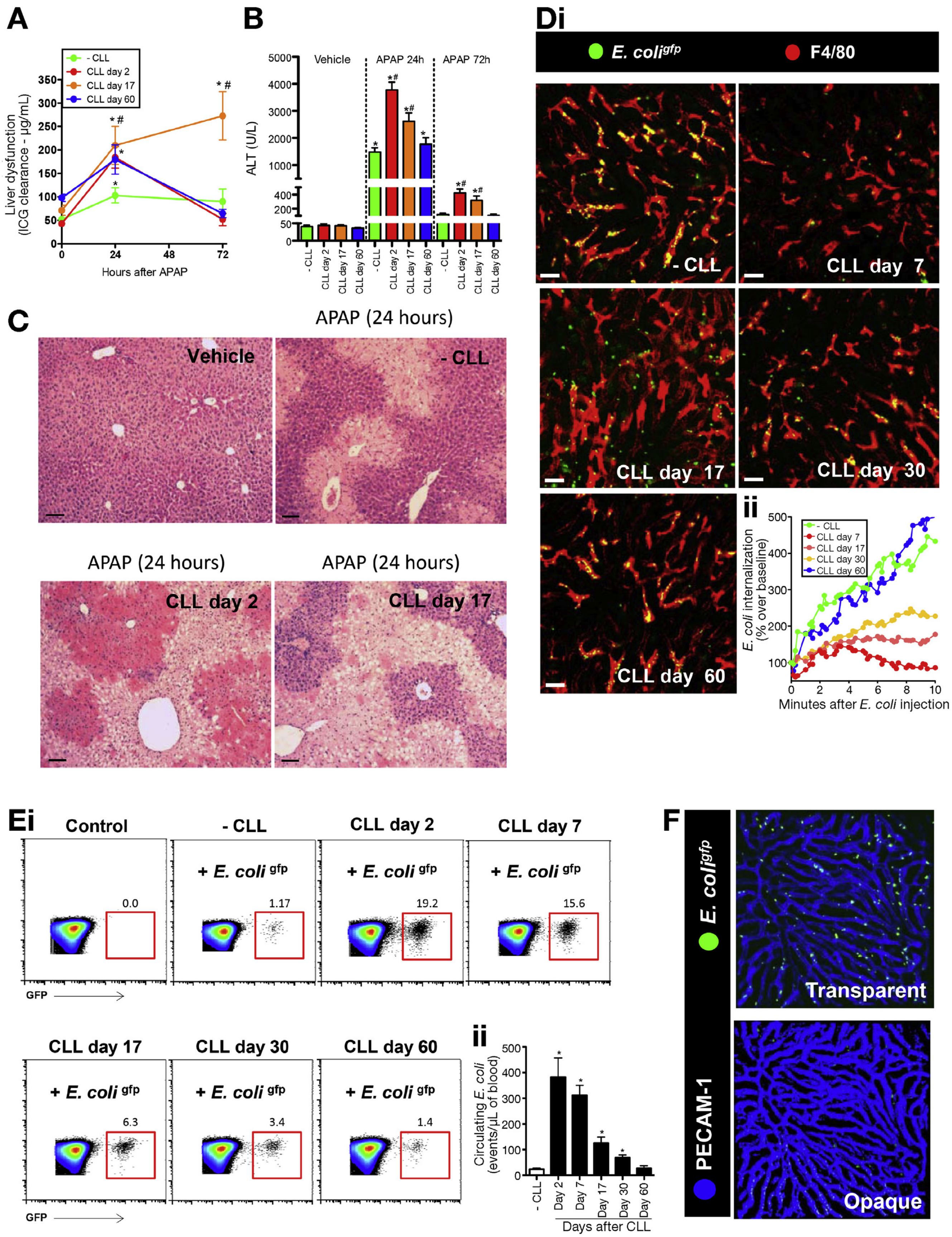
A
- CLL
CLL day 2
CLL day 17
CLL day 60
Liver dysfunction (ICG clearance - μg/mL)
0
50
100
150
200
250
300
350
* #
*
*
* #
0
24
48
72
Hours after APAP
B
ALT (U/L)
5000
4000
3000
2000
1000
400
200
50
0
Vehicle
APAP 24h
APAP 72h
*
*#
*#
*
*#
*#
- CLL
CLL day 2
CLL day 17
CLL day 60
C
APAP (24 hours)
Vehicle
- CLL
APAP (24 hours)
APAP (24 hours)
CLL day 2
CLL day 17
Di
E. coli^gfp
F4/80
- CLL
CLL day 7
CLL day 17
CLL day 30
CLL day 60
ii
E. coli internalization (% over baseline)
500
400
300
200
100
- CLL
CLL day 7
CLL day 17
CLL day 30
CLL day 60
0
2
4
6
8
10
Minutes after E. coli injection
Ei
Control
- CLL
CLL day 2
CLL day 7
+ E. coli gfp
0.0
1.17
19.2
15.6
GFP
CLL day 17
CLL day 30
CLL day 60
+ E. coli gfp
6.3
3.4
1.4
GFP
ii
Circulating E. coli (events/μL of blood)
500
400
300
200
100
0
*
*
*
*
- CLL
Day 2
Day 7
Day 17
Day 30
Day 60
Days after CLL
F
E. coli^gfp
PECAM-1
Transparent
Opaque

To test whether the BM is the major source of intravascular precursors that replenish the liver, we transplanted GFP-expressing BM precursors to gamma ray–irradiated mice. Intravital imaging confirmed that approximately 99% of liver KCs and also extravascular DCs were derived from the BM (Supplementary Figure 7*A*). Altogether, we demonstrated that both KC and DC replenishment occurs initially via myeloid precursors that accumulate within the sinusoids after depletion. Cells that sustain CX3CR1 expression emigrate toward the extravascular compartment by following a CX3CL1 gradient, thus re-establishing the DC population.

Phagocyte depletion and replenishment imprints a temporary altered response to injury

Acute liver failure is a worldwide medical concern, and it is becoming increasingly clear that liver immune cells play a key role in the pathogenesis. In these situations, the local milieu of immune cells is thought to be set toward a regulatory phenotype that minimizes liver injury after toxicity and other pathogenic events. Thus, we investigated the impact of the absence of hepatic phagocytes in a model of APAP-induced sterile liver injury. To better define the clinical impact of our procedures, we directly assessed liver metabolic function by monitoring the hepatic clearance rate of ICG, an excellent index of liver function. Phagocyte depletion by CLL led to overt liver dysfunction after APAP administration in comparison with nondepleted mice (Figure 6*A*). In addition, absence of phagocytes delayed recovery to normal function after APAP challenge (Figure 6*A*). Of note, APAP administration alone also caused significant reduction in KC numbers (approximately 40% reduction; Supplementary Figure 7*B*).

To explore the consequences of replacement of native phagocytes by BM-derived cells, we challenged mice with APAP at different stages after replenishment. After 17 days of CLL-induced depletion, APAP-treated mice still had worse liver dysfunction in comparison with the nondepleted group (Figure 6*A*). In addition, although liver metabolic function was completely restored in nondepleted mice after 3 days of APAP overdose, replenished mice had delayed return of liver function after 17 days of CLL treatment (Figure 6*A*). Serum transaminase quantification (alanine aminotransferase) and histopathology during APAP-mediated liver injury and recovery confirmed the metabolic function assessed by our ICG clearance protocol (Figure 6*B* and *C*). Interestingly, this increased injury was not observed at the earliest time (2 days) after CLL depletion, suggesting that the cells must first fully seed the liver, at which point they harbor a pro-inflammatory phenotype until at least 17 days. Nevertheless, liver response to injury was completely restored after 60 days of replenishment (Figure 6*A* and *B*), demonstrating that despite a transient hyper-responsiveness profile during the initial phases of replenishment, the liver recovers its normal regenerative ability. In line with this, normal KC distribution was also observed 17 to 30 days after APAP-induced acute hepatitis (Supplementary Figure 7*B*).

Phagocytic Instruction of Bone Marrow–Derived Kupffer Cells During Replenishment

To investigate whether BM-derived phagocytes functioned in the same fashion as yolk sac–derived cells during infection, we assessed phagocytic function at different stages of replenishment after clodronate depletion. For this, GFP-expressing *E coli* were injected intravenously and bacterial capture was evaluated in real time using intravital microscopy (Figure 6*Di* and *Dii*). High-magnification imaging revealed that free-flowing *E coli* were immediately immobilized to the KC membrane at first contact, and no pseudopod formation or major changes in KC morphology seemed to be necessary for initial bacterial arrest (Supplementary Movies 5 and 6). This highlights that the mechanisms involved in rapid bacterial clearance exerted by KCs under shear may be different from other classic phagocytosis processes. Imaging experiments were complemented by flow cytometry quantification of free bacteria in the blood (Figure 6*Ei*). Naïve mice efficiently cleared *E coli* from circulation (Figure 6*Ei* and *Eii*); however, increased numbers of circulating *E coli* were observed in mice that were either depleted (CLL 2 days; Supplementary Movie 6) or fully replenished (up to 17 days after CLL; Figure 6*F* and *G* and Supplementary Movie 6). In fact, intravital imaging showed that KC adhesiveness to *E coli* was dramatically reduced in immature KCs, and despite brief bacterial interactions with KC membrane, only a few bacteria were arrested and internalized (Figure 6*Di* and *Dii*, Supplementary Movies 5 and 6). Therefore, despite normal cell density and location, newly arrived KCs have reduced phagocytic capacity for at least 17 days. In agreement,

Figure 6. Substitution of phagocytes imprints a temporary altered response to injury and infection. Assessment of liver function (*A*) and (*B*) injury during different times of repopulation period. Mice received a single dose of ICG (20 mg/kg) and its clearance from the circulation was measured over the time. (*C*) Liver histopathology analysis from mice treated with APAP (500 mg/kg) after different periods of repopulation confirming overt injury in repopulated mice. (*Di*) In vivo imaging of *E coli*^{gfp} capture by KCs (F4/80^{+}) in control mice and at different time points after phagocyte depletion. (*Dii*) Digital quantification of *E coli*^{gfp} accumulation inside KCs expressed as increased over the baseline (set as 100% as the first frame after injection. (*Ei*) Quantification of free-flowing *E coli*^{gfp} by fluorescence-activated cell sorting (FACS) in the blood during repopulation period. *Numbers* in the gates are GFP^{+} events/μL. (*Eii*) Serum *E coli*^{gfp} concentration normalized by blood volume. Data collected from FACS. (*F*) Liver intravital microscopy evidencing the exclusive intravascular location of GFP-expressing *E coli*. *Scale bars* in (*C*) = 100 μm, and in (*Di* and *E*) = 65 μm. Error bars indicate the mean ± SEM. **P* < .05, in comparison with vehicle-treated group and $^{\#}P < .05$ in comparison to –CLL group of the respective time point (one-way analysis of variance test). n = 5/group.

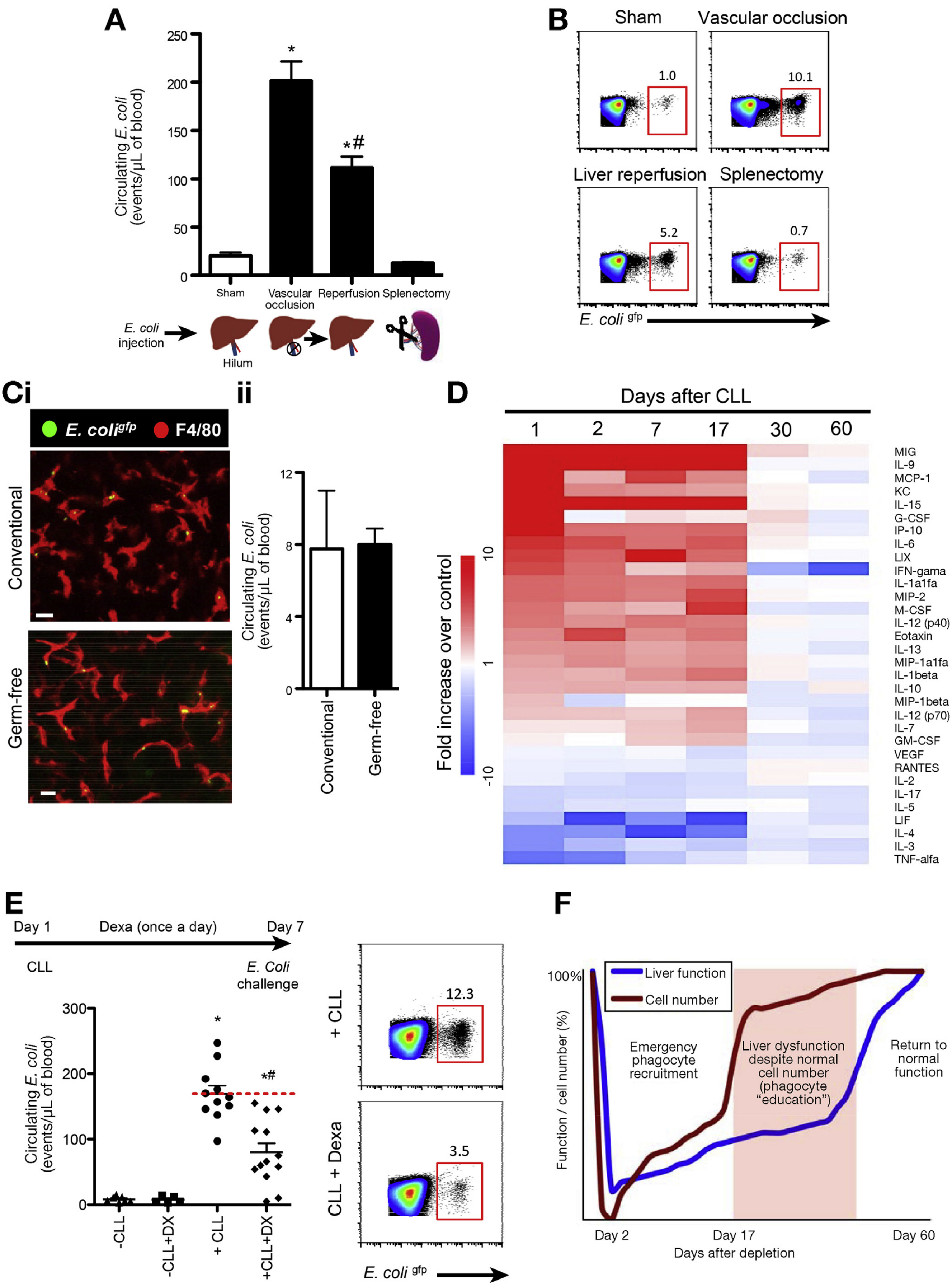
A
Circulating E. coli (events/μL of blood)
250
200
150
100
50
0
*
*#
Sham
Vascular occlusion
Reperfusion
Splenectomy
E. coli injection
Hilum
B
Sham
Vascular occlusion
1.0
10.1
Liver reperfusion
Splenectomy
5.2
0.7
E. coli gfp
Ci
ii
E. coli gfp
F4/80
Conventional
Germ-free
Circulating E. coli (events/μL of blood)
12
8
4
0
Conventional
Germ-free
D
Days after CLL
1
2
7
17
30
60
Fold increase over control
10
1
-10
MIG
IL-9
MCP-1
KC
IL-15
G-CSF
IP-10
IL-6
LIX
IFN-gama
IL-1a1fa
MIP-2
M-CSF
IL-12 (p40)
Eotaxin
IL-13
MIP-1a1fa
IL-1beta
IL-10
MIP-1beta
IL-12 (p70)
IL-7
GM-CSF
VEGF
RANTES
IL-2
IL-17
IL-5
LIF
IL-4
IL-3
TNF-alfa
E
Day 1
Dexa (once a day)
Day 7
CLL
E. Coli challenge
Circulating E. coli (events/μL of blood)
300
200
100
0
*
*#
-CLL
-CLL+DX
+CLL
+CLL+DX
+ CLL
CLL + Dexa
12.3
3.5
E. coli gfp
F
Liver function
Cell number
100%
Function / cell number (%)
Emergency phagocyte recruitment
Liver dysfunction despite normal cell number (phagocyte "education")
Return to normal function
Day 2
Day 17
Day 60
Days after depletion

adoptive transfer of BM isolated cells to recently depleted mice caused no detectable improvement in bacterial clearance after at least 1 week, confirming that even when precursors are delivered in high numbers into the circulation, a period of adaptation within the liver microenvironment is required for KC education (data not shown). Between 30 and 60 days of replenishment, normal phagocytic activity and clearance of circulating *E coli* were restored (Figure 6*Ei* and *Eii* and Supplementary Movie 5). Because only a few *E coli* were seen in the extravascular compartment or interacting with DCs, we suggest that KCs are the primary cell population involved in rapid *E coli* capture within the liver (Figure 6*F* and Supplementary Movie 7), while DCs seems to be involved in further antigen presentation, as shown by gene expression assays.

To investigate whether the liver was the main site for systemic *E coli* removal, we interrupted the hepatic blood flow using a transitory vascular occlusion approach. In fact, higher numbers of circulating *E coli* were found when the blood was not circulating through the liver, and liver reperfusion significantly restored *E coli* clearance (Figure 7*A* and *B*). Although systemic CLL treatment also depletes splenic resident macrophages that may be involved in bacterial sequestration from the circulation, splenectomized mice had efficient systemic *E coli* clearance throughout the experiment (Figure 7*A* and *B*). Together, these data reveal a window of hepatic phagocytic dysfunction while KC maturation occurs.

A long-term exposure to microbe-associated molecular patterns from the portal tract could be important for maturation of newly recruited precursors. However, in the absence of commensal microbiota (germ-free mice), KCs had a normal ability to clear systemic bacteria (Figure 7*Ci* and *Cii*), despite minor morphologic and numeric differences (data not shown). Therefore, we hypothesized that intrinsic liver-derived factors shaped KC function during replenishment. To explore this, hepatic inflammatory status was evaluated using a multiplexed cytokine approach. After 1 day of CLL treatment, an increase of several proinflammatory cytokines was observed in comparison with nondepleted mice (Figure 7*D* and Supplementary Table 3), including interleukin (IL) 6, interferon (IFN) γ, KC/CXCL1, and IL9. Concomitantly, IL3, IL4, and tumor necrosis factor (TNF)$-\alpha$ were down-regulated after depletion (Figure 7*D*). Other cytokines that have been implicated in support and replenishment of stromal and myeloid cells, such as lipopolysaccharide-induced CXC chemokine, were highly expressed and sustained up to 17 days post-depletion (Figure 7*D*), entirely consistent with the observed liver dysfunction. Thus, phagocyte depletion and replenishment imprinted a transitory proinflammatory signature in the liver, suggesting that such changes in the liver microenvironment could explain the rapid infiltration of phagocyte precursors and also the altered response to bacterial clearance. To dampen liver inflammation triggered by phagocyte depletion, we chronically treated mice with a broad-spectrum anti-inflammatory drug (dexamethasone) during the first week of the replenishment phase. Intriguingly, dexamethasone-treated mice had a significantly faster recovery of *E coli* extraction from circulation (Figure 7*E*). Nondepleted mice treated with dexamethasone under the same conditions were not different from controls (Figure 7*E*). Consistent with this, the liver responded normally to inflammation and bacterial challenge after 60 days of depletion, which was associated with the return of hepatic inflammatory mediators to baseline levels (Figure 7*E*).

Discussion

Using a previously unreported combination of mass cytometry, confocal intravital microscopy, and multiplexed gene expression array, we precisely described the different immune phenotypes, morphology, density, and location of liver phagocytes. We show that there is a vast population of liver DCs, and part of these cells are located in the subcapsular space and not just between hepatocytes or in the vasculature, as suggested previously.[24] This strategic localization may also allow for inter-compartment communications among the liver parenchyma and sinusoids, the mesothelium, and perhaps even the peritoneal cavity.[25] Considering their repertoire of cell surface receptors and gene expression, this population of liver DCs might also process and present antigens like a number of the other DC subtypes. Despite the different origins of native KCs and DCs, we demonstrated using a high-dimensional immunophenotyping approach that myeloid precursors were able to fully restore normal cell density and location after depletion, and this is likely to occur after their recruitment via an intravascular route. Importantly, liver phagocyte density can also be re-established to normal values, even after a full depletion methodology using clodronate,

Figure 7. Re-establishment of liver function after phagocyte educational period is dependent on hepatic environment rather than bacterial clues. (*A*) Circulating *E coli* number in mice submitted to temporary hepatic vascular occlusion (HVO; 5 minutes), reperfused (5 minutes after reperfusion), and splenectomized mice (1 hour before *E coli* challenge) in comparison to sham-operated group. (*B*) Same as (*A*), but analyzed by fluorescence-activated cell sorting (FACS). Numbers in the gates are GFP$^+$ events/μL. (*Ci*) Liver intravital microscopy showing similar phagocytic ability of KCs from germ-free and conventional mouse. (*Cii*) Free *E coli* quantification by FACS in the blood of conventional and germ-free mouse. (*D*) Fold increase of different inflammatory mediators after phagocyte depletion and replenishment in comparison with controls assessed by Luminex. Here, controls were set as fold = 1, therefore, have *white color code*. (*E*) Chronic dexamethasone treatment (5 mg/kg, once a day for 7 days) accelerated liver return to normal bacterial clearance, as shown by flow cytometry. (*F*) Graphical abstract showing our main conclusions regarding the different dynamics of phagocyte repopulation and recovery of liver function. *Scale bars* = 65 μm. Error bars indicate the mean ($\pm$SEM). Scale bars = 16 μm. $^*P < .05$ (unpaired *t* test) in comparison with sham. $^\#P < .05$ (one-way analysis of variance test) in comparison with HVO group. n = 5/group.

showing that self-replication is not entirely necessary to a complete re-establishment of phagocytic populations. Also, myeloid progenitors can replenish both the KC and DC population into 2 different anatomic compartments. In fact, the KC and DC precursors adhered within the sinusoids and 2 phenotypes were observed: some moved no further, while others adhered in the same sinusoids and followed a gradient of the ligand for CX3CR1 to emigrate out of the vasculature. CX3CR1/CX3CL1 interaction was critical to re-establish the liver DC, but not the KC population, but because the majority of the intravascular precursors expressed the receptor for CX3CL1, it raises the question why some of the cells remained in the sinusoids to become KCs, while others emigrated into the extravascular parenchymal space.

Using CyTOF, we identified that under baseline conditions, liver CD11c$^+$ cells are not exclusively DCs as previously assumed,[26] but are rather also a subset of KCs that express this marker. It was recently described that new BM-derived KCs can adopt a genetic profile that may resemble their native counterparts.[27] Here we expanded these findings, showing that intravascular precursors restored KC/DC density and location after full depletion by clodronate or irradiation, but for at least 17–30 days, repopulated livers did not reach their optimal tolerogenic levels and were still more prone to collateral damage. Also, KCs may have a unique mechanism to rapidly arrest bacteria under shear that involves initial "passive" bacterial adhesion to the cell surface, and further internalization. Interestingly, newly emigrated KCs had defective *E coli* catching from the circulation, indicating a further maturation requirement of the KCs and a putative enhanced susceptibility to bacterial spread. It is reasonable to suggest that several molecules involved in phagocytic processes that are expressed by KCs under normal conditions may be reduced in immature KCs, and may reach optimal expression levels during the maturation process. Because KCs from germ-free mice had fully functional systemic bacterial catching, it is likely that the phagocytic ability—and perhaps also their dysfunction—are not dependent on instructions from microbiota, but probably from endogenous mediators that compose the hepatic environment.[28]

Although we initially thought that inflammatory mediators might induce the necessary receptors for bacterial catching and tolerance in the maturing KC, the opposite was true. When we dampened liver inflammatory response, proper phagocytosis by KCs was reached at earlier time points. This suggests that therapeutic interventions aimed to block overt inflammation might also help patients that suffered from extensive liver injury or were subjected to irradiation, conditions where a substantial part of liver phagocytes might have been depleted. After 60 days replenishment time, the liver responded normally to injury, and reacquired efficient bacterial clearance function. This implies that despite the normal number and distribution of phagocytes at earlier time points after replenishment, an "educational period" is required for the restitution of normal function of these cells. Thus, it is possible that the liver has a unique secretome signature that maintains tissue-resident populations and that education of precursors requires up to 30–60 days for full maturation. Collectively, these findings provide insight into the mechanisms involved in relatively higher susceptibility to collateral liver injury and systemic infection observed during extensive liver damage and also in patients that were subjected to full body irradiation.

Supplementary Material

Note: To access the supplementary material accompanying this article, visit the online version of *Gastroenterology* at www.gastrojournal.org, and at http://dx.doi.org/10.1053/j.gastro.2016.08.024.

References

1. Epelman S, Lavine KJ, Randolph GJ. Origin and functions of tissue macrophages. Immunity 2014;41:21–35.
2. Ginhoux F, Jung S. Monocytes and macrophages: developmental pathways and tissue homeostasis. Nat Rev Immunol 2014;14:392–404.
3. Wisse E, van't Noordende JM, van der Meulen J, et al. The pit cell: description of a new type of cell occurring in rat liver sinusoids and peripheral blood. Cell Tissue Res 1976;173:423–435.
4. Bendelac A, Savage PB, Teyton L. The biology of NKT cells. Annu Rev Immunol 2007;25:297–336.
5. Thomson AW, O'Connell PJ, Steptoe RJ, et al. Immunobiology of liver dendritic cells. Immunol Cell Biol 2002;80:65–73.
6. Jenne CN, Kubes P. Immune surveillance by the liver. Nat Immunol 2013;14:996–1006.
7. Lee SJ, Park SY, Jung MY, et al. Mechanism for phosphatidylserine-dependent erythrophagocytosis in mouse liver. Blood 2011;117:5215–5223.
8. Terpstra V, van Berkel TJ. Scavenger receptors on liver Kupffer cells mediate the in vivo uptake of oxidatively damaged red blood cells in mice. Blood 2000;95:2157–2163.
9. Balmer ML, Slack E, de Gottardi A, et al. The liver may act as a firewall mediating mutualism between the host and its gut commensal microbiota. Sci Transl Med 2014;6:237ra66.
10. Wong CH, Jenne CN, Petri B, et al. Nucleation of platelets with blood-borne pathogens on Kupffer cells precedes other innate immunity and contributes to bacterial clearance. Nat Immunol 2013;14:785–792.
11. Yona S, Kim KW, Wolf Y, et al. Fate mapping reveals origins and dynamics of monocytes and tissue macrophages under homeostasis. Immunity 2013;38:79–91.
12. Schulz C, Gomez Perdiguero E, Chorro L, et al. A lineage of myeloid cells independent of Myb and hematopoietic stem cells. Science 2012;336:86–90.
13. Liu K, Nussenzweig MC. Origin and development of dendritic cells. Immunol Rev 2010;234:45–54.
14. Matsuno K, Ezaki T, Kudo S, et al. A life stage of particle-laden rat dendritic cells in vivo: their terminal division,

active phagocytosis, and translocation from the liver to the draining lymph. J Exp Med 1996;183:1865–1878.
15. Sato T, Yamamoto H, Sasaki C, et al. Maturation of rat dendritic cells during intrahepatic translocation evaluated using monoclonal antibodies and electron microscopy. Cell Tissue Res 1998;294:503–514.
16. Woo J, Lu L, Rao AS, et al. Isolation, phenotype, and allostimulatory activity of mouse liver dendritic cells. Transplantation 1994;58:484–491.
17. Waite JC, Leiner I, Lauer P, et al. Dynamic imaging of the effector immune response to listeria infection in vivo. PLoS Pathog 2011;7:e1001326.
18. Marques PE, Antunes MM, David BA, et al. Imaging liver biology in vivo using conventional confocal microscopy. Nat Protoc 2015;10:258–268.
19. Lee WY, Moriarty TJ, Wong CH, et al. An intravascular immune response to Borrelia burgdorferi involves Kupffer cells and iNKT cells. Nat Immunol 2010;11:295–302.
20. Becher B, Schlitzer A, Chen J, et al. High-dimensional analysis of the murine myeloid cell system. Nat Immunol 2014;15:1181–1189.
21. Marques PE, Oliveira AG, Pereira RV, et al. Hepatic DNA deposition drives drug-induced liver injury and inflammation in mice. Hepatology 2015;61:348–360.
22. McDonald B, Pittman K, Menezes GB, et al. Intravascular danger signals guide neutrophils to sites of sterile inflammation. Science 2010;330:362–366.
23. Ginhoux F, Liu K, Helft J, et al. The origin and development of nonlymphoid tissue CD103+ DCs. J Exp Med 2009;206:3115–3130.
24. Heymann F, Tacke F. Immunology in the liver—from homeostasis to disease. Nat Rev Gastroenterol Hepatol 2016;13:88–110.
25. Wang J, Kubes P. A reservoir of mature cavity macrophages that can rapidly invade visceral organs to affect tissue repair. Cell 2016;165:668–678.
26. Connolly MK, Ayo D, Malhotra A, et al. Dendritic cell depletion exacerbates acetaminophen hepatotoxicity. Hepatology 2011;54:959–968.
27. Scott CL, Zheng F, De Baetselier P, et al. Bone marrow-derived monocytes give rise to self-renewing and fully differentiated Kupffer cells. Nat Commun 2016;7:10321.
28. Corbitt N, Kimura S, Isse K, et al. Gut bacteria drive Kupffer cell expansion via MAMP-mediated ICAM-1induction on sinusoidal endothelium and influence preservation-reperfusion injury after orthotopic liver transplantation. Am J Pathol 2013;182:180–191.

Received July 14, 2016. Accepted August 21, 2016.

Reprint requests
Address requests for reprints to: Gustavo Batista Menezes, PhD, Center for Gastrointestinal Biology, ICB Room N3-140, Federal University of Minas, Belo Horizonte, Minas Gerais, 31270-901, Brazil. e-mail: menezesgb@ufmg.br; fax: +55 31 3409 2770; or Paul Kubes, PhD, Calvin, Phoebe and Joan Snyder Institute for Chronic Diseases, Department of Physiology and Pharmacology, Cumming School of Medicine, University of Calgary, Alberta, T2N 4N1, Canada. e-mail: pkubes@ucalgary.ca; fax: (403) 270–7516.

Acknowledgments
The authors thank Dr Julio Scharfstein and Dr Clarissa Nascimento for providing CD11c-EYFP mice (UFRJ, Brazil) and Dr Howard Weiner, Dr Shirong Liu (Harvard Medical School, Boston, MA), Giuliana Bertozi (FMRP, Universidade de São Paulo, Brazil), and Dr Flaviano Martins (UFMG, Brazil) for assistance, reagents, and mice strains. We thank Rodrigo Nogueira, Paulo Lutero de Mello e Silva II, and Dr Denise Cara for helping in the generation of scientific divulgation material. Also, we would like to thank the Centro de Aquisição e Processamento de Imagens (CAPI- ICB/UFMG) and the Flow Cytometry facility of Centro de Pesquisas René Rachou (FIOCRUZ-MG).

GEO accession number: GSE81645.

Conflicts of interest
The authors disclose no conflicts.

Funding
This work was supported by FAPESP, FAPEMIG, CAPES (Biocomputacional), and CNPq (Brazil), and Canadian Institutes of Health Research and the Heart and Stroke Foundation of Canada.

Supplementary Fig. 1

A CyTOF – without CLL (- CLL)

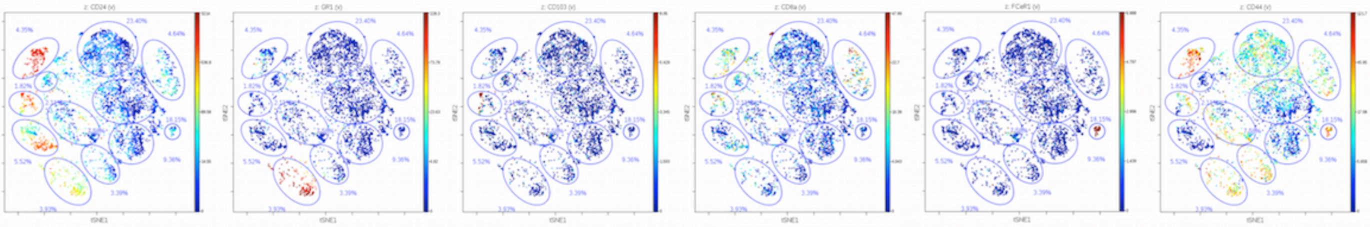

B

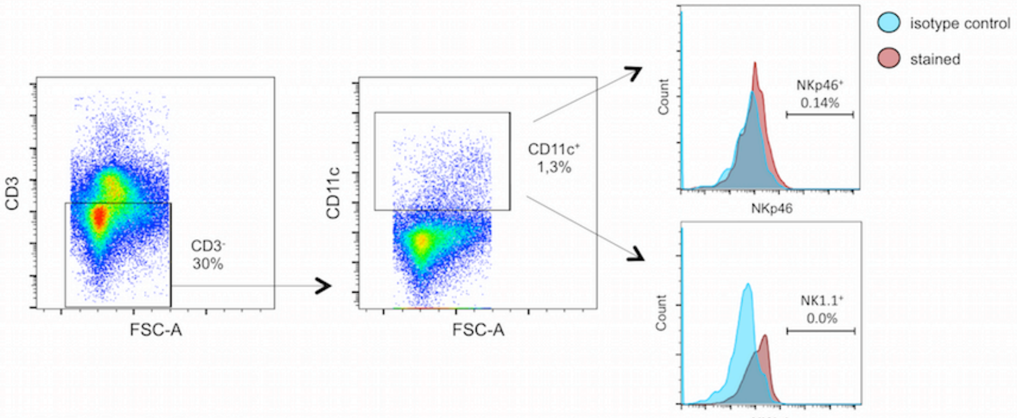

C CyTOF – Day 2 after CLL

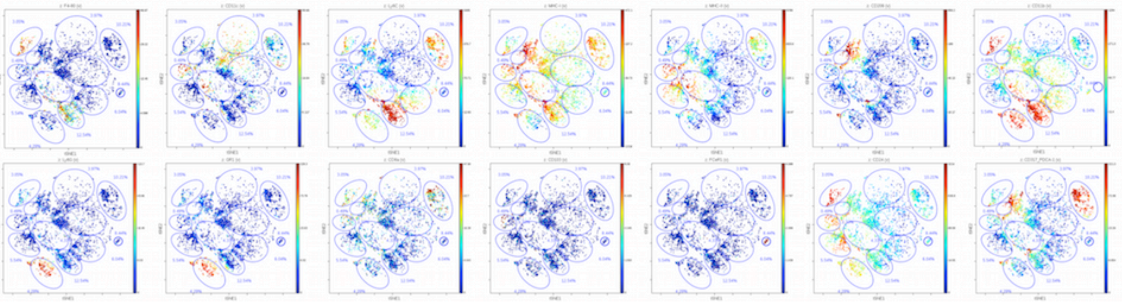

Supplementary Fig. 2

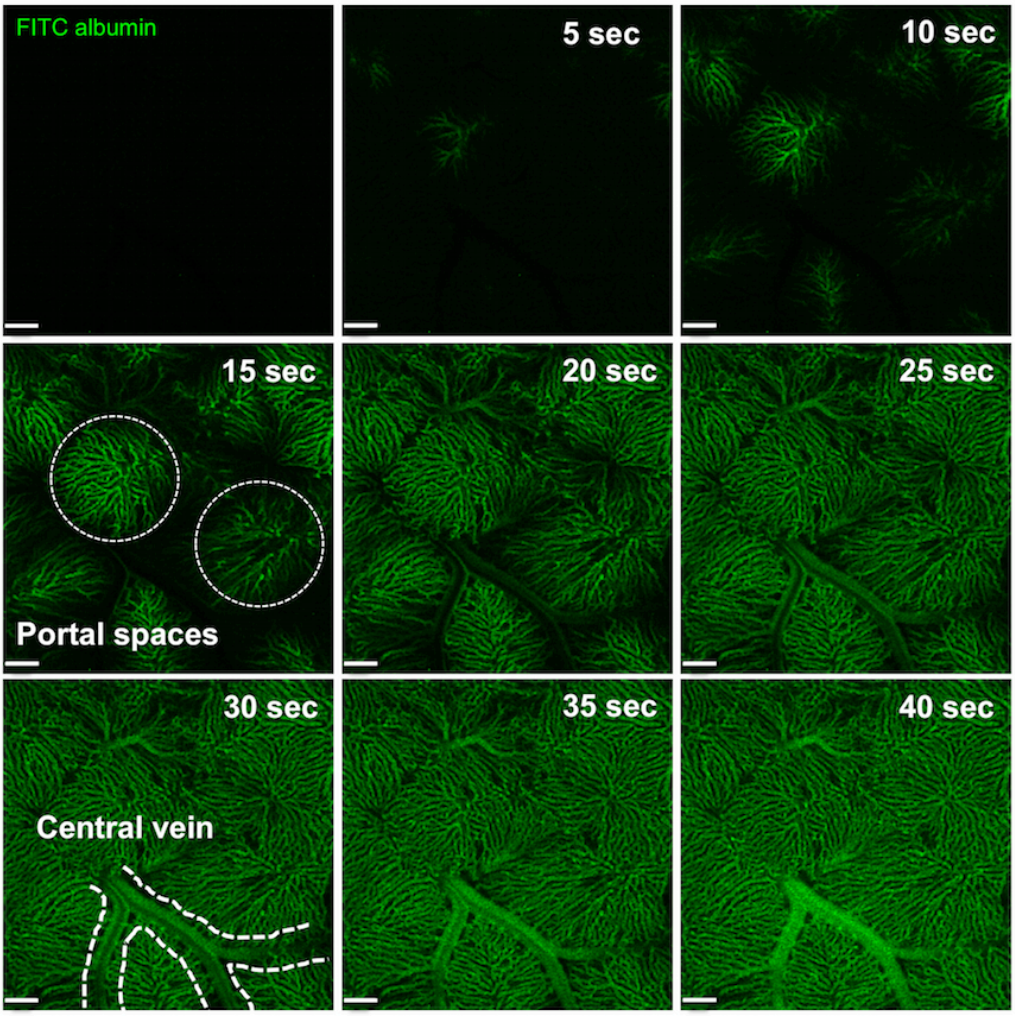
FITC albumin
5 sec
10 sec
15 sec
Portal spaces
20 sec
25 sec
30 sec
Central vein
35 sec
40 sec

Supplementary Fig. 3

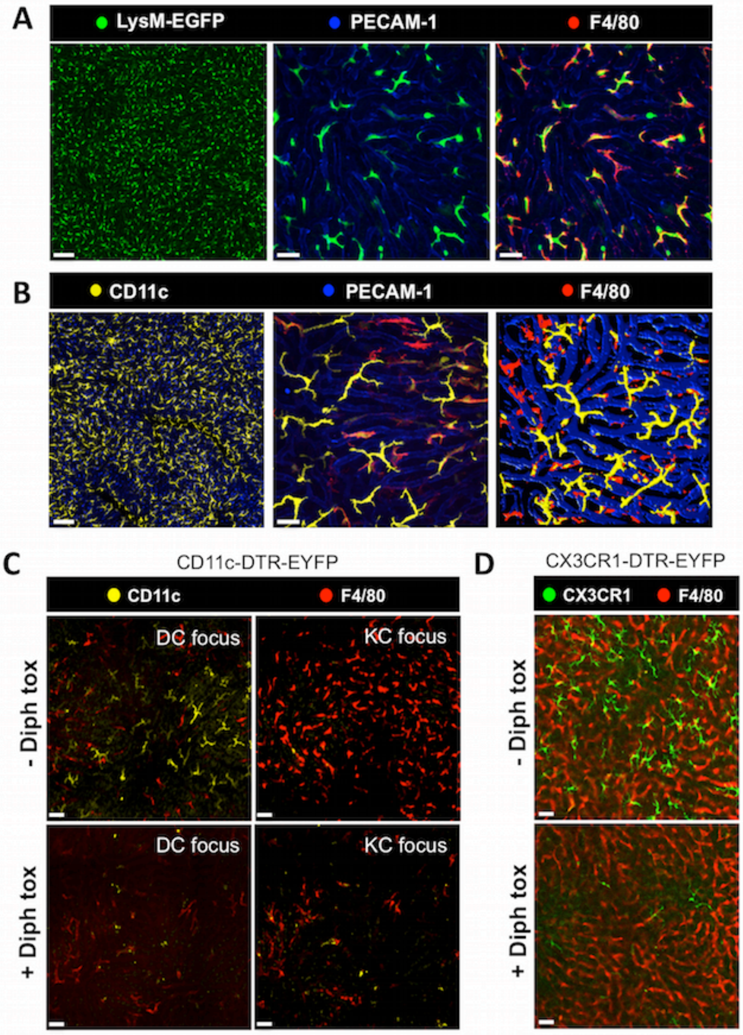
A
LysM-EGFP
PECAM-1
F4/80
B
CD11c
PECAM-1
F4/80
C
CD11c-DTR-EYFP
CD11c
F4/80
- Diph tox
+ Diph tox
DC focus
KC focus
DC focus
KC focus
D
CX3CR1-DTR-EYFP
CX3CR1
F4/80
- Diph tox
+ Diph tox

Supplementary Fig. 4

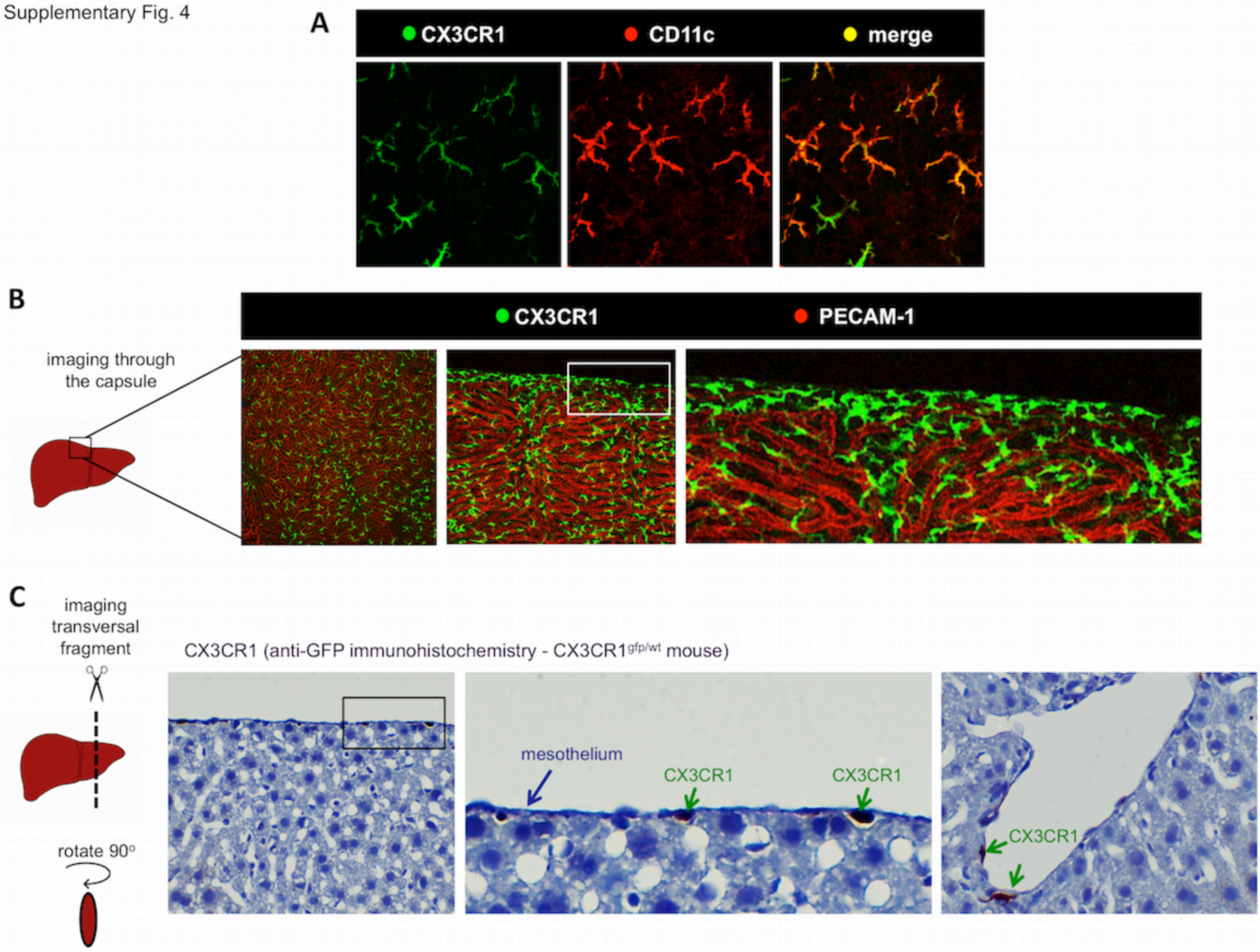
A
● CX3CR1
● CD11c
● merge
B
imaging through the capsule
● CX3CR1
● PECAM-1
C
imaging transversal fragment
rotate 90°
mesothelium
CX3CR1
CX3CR1
CX3CR1

CX3CR1 (anti-GFP immunohistochemistry - CX3CR1$^{gfp/wt}$ mouse)

Supplementary Fig. 5

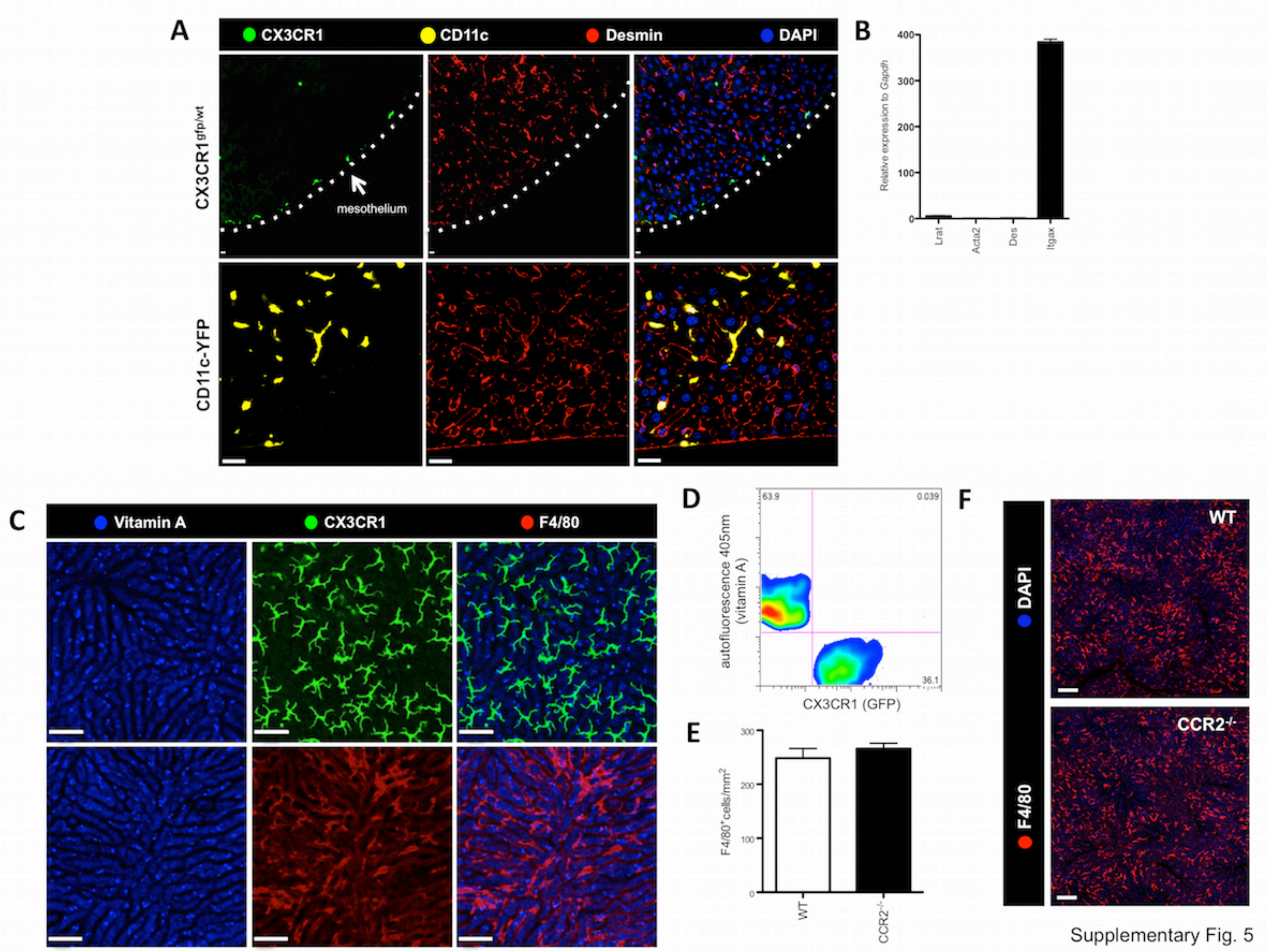
A
CX3CR1
CD11c
Desmin
DAPI
CX3CR1gfp/wt
mesothelium
CD11c-YFP
B
Relative expression to Gapdh
400
300
200
100
0
Lrat
Acta2
Des
Itgax
C
Vitamin A
CX3CR1
F4/80
D
autofluorescence 405nm (vitamin A)
CX3CR1 (GFP)
63.9
0.039
36.1
E
F4/80+ cells/mm2
300
200
100
0
WT
CCR2-/-
F
DAPI
F4/80
WT
CCR2-/-
Supplementary Fig. 5

Supplementary Fig. 6

A CyTOF – Day 7 after CLL

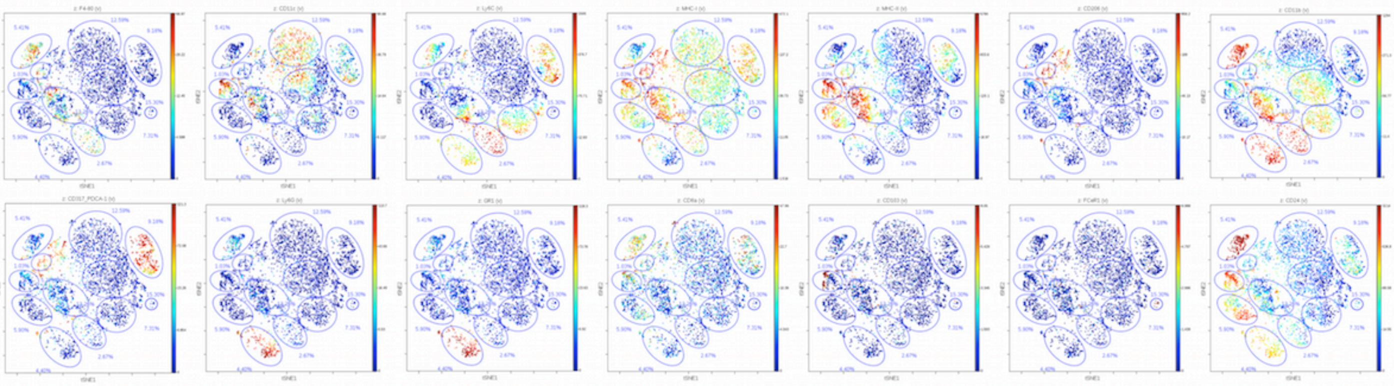

B CyTOF – Day 17 after CLL

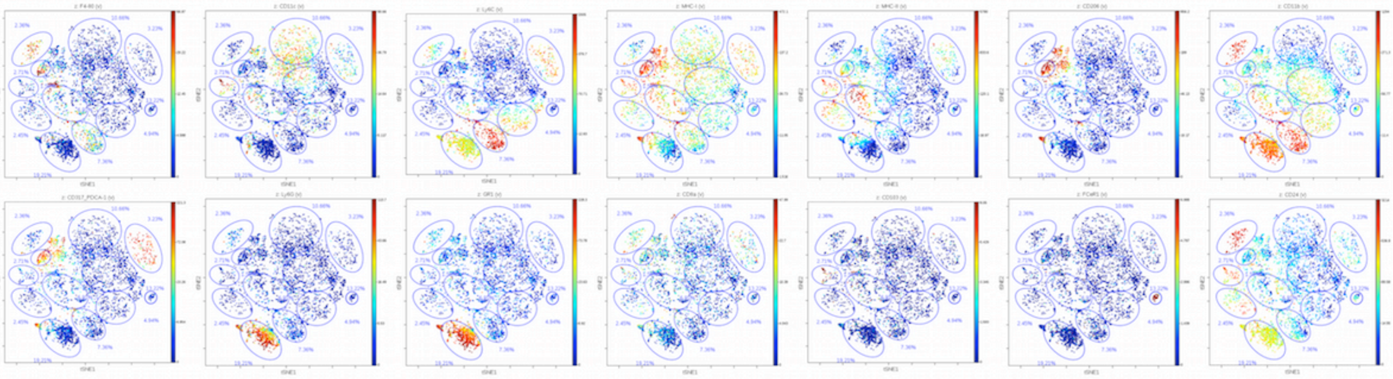

Supplementary Fig. 7

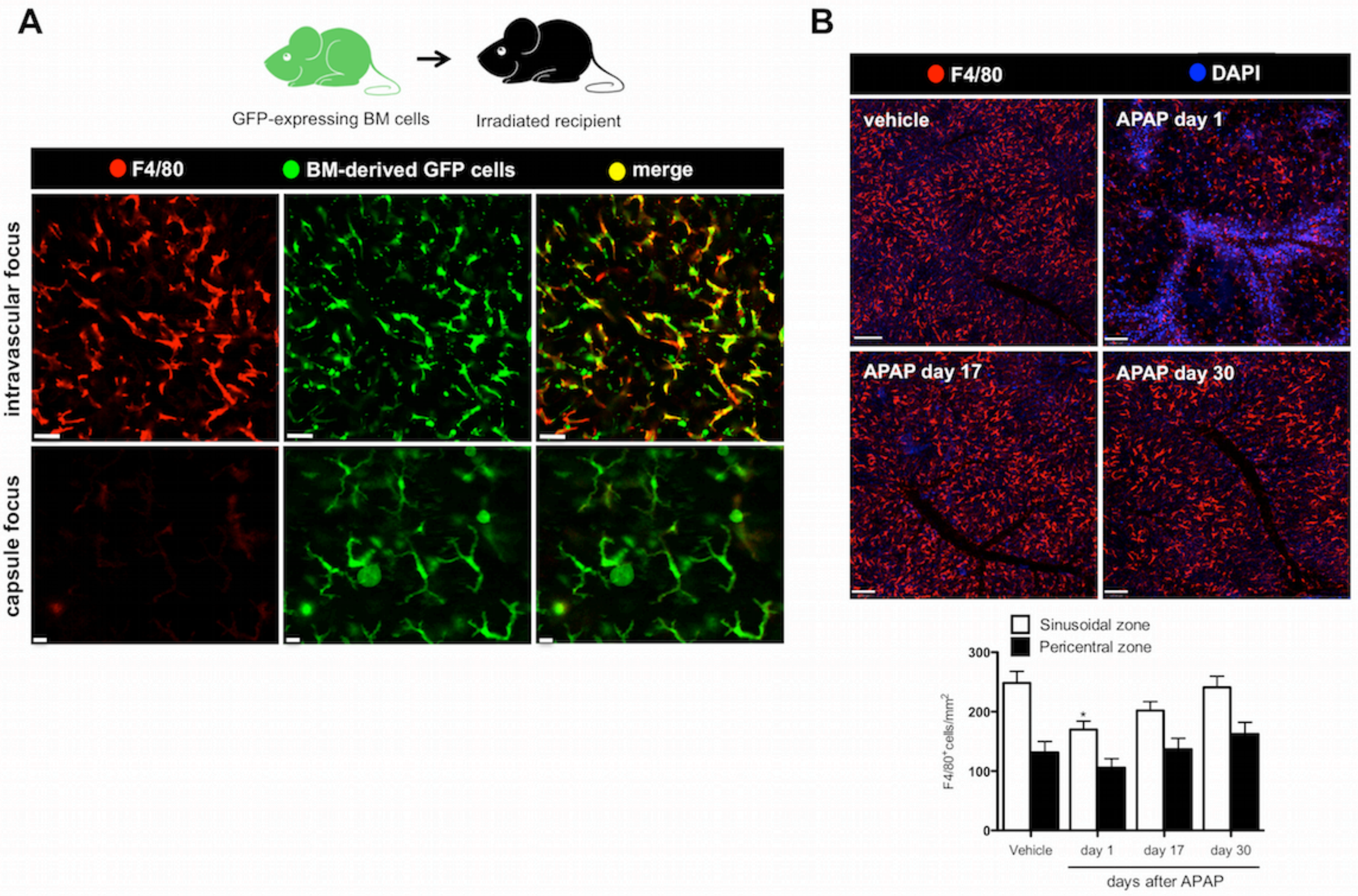
A
GFP-expressing BM cells
Irradiated recipient
F4/80
BM-derived GFP cells
merge
intravascular focus
capsule focus
B
F4/80
DAPI
vehicle
APAP day 1
APAP day 17
APAP day 30
Sinusoidal zone
Pericentral zone
300
200
100
0
F4/80$^+$cells/mm^2
*
Vehicle
day 1
day 17
day 30
days after APAP

Supplemental Figures legends

Supplementary Figure 1 (A) Additional dot plots from CyTOF analysis from untreated group. (**B**) Gating strategy for assessment of CD11c$^+$ NK cells frequency in liver non-parenchymal cells samples. CD11c$^+$ NK cells were defined as CD3$^-$CD11c$^+$NKp46$^+$NK1.1$^+$ events. (**C**) Additional dot plots from CyTOF analysis from mice 2 days after CLL treatment.

Supplementary Figure 2 Identification of main hepatic vascular arrangements. Snapshots of chronological distribution of FITC-albumin within the liver (5mg/Kg). Portal spaces were identified as the first vascular region evidenced by fluorescence, and central vein were defined as the secondary draining vessels. Scale bars, 120 μm.

Supplementary Figure 3 Expression of different cell surface markers in liver phagocytes. (**A**) Liver macrophage expression of lysozyme M (LysM-EGFP mice) and F4/80. (**B**) Same for **A**, but for CD11c (CD11c-EYFP mice). (**C**) Depletion of both intravascular CD11c$^+$F4/80$^+$ and extravascular CD11c$^+$ cells upon diphtheria toxin (DT) treatment in CD11c-DTR-EYFP mice. **(D)** Expression of EYFP and DTR under control of CX3CR1 in liver dendritic cells and selective depletion following diphtheria toxin administration. Note that only CX3CR1+ cells are depleted after DT treatment, with no effect on intravascular F4/80+ cells. Scale bars, 120 μm. Illustrative images from different experiments (N>5).

Supplementary Figure 4 Liver dendritic cells are located in the subcapsular compartment and are CD11c$^+$ **(A)** Liver intravital microscopy of CX3CR1$^{gfp/wt}$ mouse showing the distribution of CD11c$^+$ dendritic (anti-CD11) cells and

(B,C) confirmation of sub-mesothelial location of CX3CR1$^+$ cells by intravital microscopy **(B)** immunohistochemistry **(C).** Illustrative images from different experiments (N>5).

Supplementary Figure 5 Characterization of different cell surface markers and CCR2 role in phagocytes **(A)** Liver *ex vivo* transversal fragment showing that subcapsular neither CX3CR1$^+$ nor CD11c$^+$ cells are positive for desmin (anti-desmin antibody), excluding this population as hepatic stellate cells. **(B)** Real-time PCR from isolated macrophages and dendritic cells showing that hepatic stellate cells (HSCs) did not contaminate samples. The following HSCs genes were measured: lecithin retinol acyltransferase (*Lrat*), desmin (*Des*) and alpha-actin-2 (*Acta2*). Data were normalized by a constitutive gene (*Gapdh*) and *Itgax* (CD11c) was used as positive control. **(C)** Liver intravital microscopy showing that neither CX3CR1$^+$ cells nor F4/80$^+$ have vitamin A granules (auto-fluorescence in 405nm laser). (**D)** Flow cytometry investigation of the absence of vitamin A in CX3CR1$^+$ population (auto-fluorescence in 405nm laser). **(E)** CCR2$^{-/-}$ mouse have normal KC density (anti-F4/80) and **(F)** location. Scale bars in A, 10 μm; B, 65μm and E, 120μm.

Supplementary Figure 6 Additional dot plots from CyTOF analysis from mice 7 and 17 days after phagocyte depletion. Expression of cell surface markers in liver non-parenchymal cells clodronate depleted mice after 7 days **(A)** and after 17 days **(B)**. CyTOF was performed and events were clustered as described in Methods and Results.

Supplementary Figure 7 (A) Replenishment of liver phagocytes is driven by a bone marrow-derived precursor. Different focal planes imaged by intravital confocal microscopy from GFP-expressing bone marrow chimeras showing that all Kupffer cells (F4/80$^+$GFP$^+$ cells in intravascular focus) and dendritic cells (GFP$^+$ cells in capsule focus) were derived from the bone marrow. (**B**) Acetaminophen (APAP) treatment caused a significant depletion of KCs (red; F4/80$^+$ cells) and normal cell density and location were restored after 17-30 days. In blue, DAPI stains for necrosis. Scale bars in KC focus, 35 μm, in DC focus, 20 μm and in APAP-treated group 120 μm. *$P < 0.05$ (unpaired *t*-test) in comparison to vehicle.

Legends for Tables

Table 1 Antibody panel for CyTOF and for genes for Real Time PCR. For PCR, cells were isolated and RNA was extracted with a miRNeasy kit (Qiagen), then was reverse-transcribed with a high capacity cDNA reverse transcription kit and analyzed by quantitative RT-PCR with a Vii 7 Real-time PCR system with Taqman primers. The following HSCs genes were measured: lecithin retinol acyltransferase (*Lrat*), desmin (*Des*) and alpha-actin-2 (*Acta2*). Data were normalized by a constitutive gene (*Gapdh*) and *Itgax* (CD11c) was used as positive control. The comparative threshold cycle method and the internal control Gapdh was used for normalization of the target genes.

Table 2 Absolute cell numbers (events) from time-of-flight flow cytometry (CyTOF) experiments. Liver samples from different groups were collected and processed for CyTOF. Events were normalized in all samples.

Table 3 Quantification of liver cytokine expression by multiplexed Luminex array. Liver samples from different groups were collected and processed for multiplexed cytokine array. Data are displayed as individual samples from different experiments.

GEO accession number: GSE81645. Gene expression assessed by Nanostring experiments. Intravascular CX3CR1$^-$ F4/80$^+$ and extravascular CX3CR1$^+$ F4/80$^-$ cells were isolated by sorting (FACS) and immune system-related genes expression was quantified using Nanostring. Statically relevant results consist in *p-value* < 0.05 and a fold change of at least 50% higher or lower. Pathways and functional classification were done by cross association using KEGG Pathways and KEGG Brite databases.

Legends for Supplementary Movies

Supplementary Movie 1 Identification of main hepatic vascular arrangements. Temporal distribution of FITC-albumin (green) within the liver (5mg/Kg). Portal spaces were identified as the first vascular region evidenced by fluorescence, and central vein were defined as the secondary draining vessels. Total experimenta time: 1 minute.

Supplementary movie 2 Three-dimensional rendering of liver intravital imaging. Spatial distribution of Kupffer cells. Vessels are in blue (anti-PECAM-1 antibody) and KCs in red (anti-F4/80 antibody). Images were collect from a 3D section of 80-100μm of depth.

Supplementary movie 3 Three-dimensional rendering of liver intravital imaging. Liver dendritic cell (DCs) morphology and distribution in CD11c-EYFP mice. Vessels are in blue (anti-PECAM-1 antibody) and DCs in yellow (EYFP). Images were collect from a 3D section of 80-100μm of depth.

Supplementary movie 4 Three-dimensional rendering of liver intravital imaging. Liver dendritic cell morphology and distribution in CX3CR1-EGFP mice. Vessels are in blue (anti-PECAM-1 antibody) and DCs in green (EGFP). Images were collect from a 3D section of 80-100μm of depth.

Supplementary movie 5: KCs instantaneously trap circulating *E. coli* from the circulation. Merged video comparing *E. coli* arresting by a control KC (non-depleted mouse) versus an immature KC (7 days after CLL). Note that *E. coli* are arrested at the first passage through the liver, while immature KC are unable to proper catch and internalize bacteria. Kupffer cells (KCs) are in red and *E. coli* in green. Total video time: 10 minutes. 10^7 *E.coli* were injected in the beginning of the imaging procedure.

Supplementary movie 6 Circulating *E. coli* capture by Kupffer cells. Merged video showing *E. coli* arresting by control group (non-depleted mouse) and after different timepoints of replenishment period (7, 17, 30 and 60 days). Kupffer cells (KCs) are in red and *E. coli* in green. Due to photobleaching issues, a still frame from KC channel was used as reference during the video. Total video time: 10 minutes each experimental group. 10^7 *E.coli* were injected in the beginning of the imaging procedure

Supplementary movie 7 *E. coli* are exclusively arrested by intravascular cells Three-dimensional rendering of liver confocal intravital microscopy showing GFP expressing E coli inside sinusoids. Sinusoids are in blue (anti-PECAM-1 antibody) and *E. coli*^{gfp} in green. Images were collect from a 3D section of 80-100μm of depth.

ANTIGEN	CLONE	METAL-CONJUGATE
GR1	**RB6-8C5**	**139La**
CD44	**IM7**	**141Pr**
CD115	**AFS98**	**142Nd**
TER-119	**TER-119**	**143Nd**
CD1d	**K253**	**144Nd**
CD4	**RM4-5**	**145Nd**
CD11c	**N418**	**146Nd**
CD317/PDCA-1	**927**	**148Nd**
CD274 (PDL-1)	**10F.9G2**	**149Sm**
TCRb	**H57-597**	**150Nd**
Ly6C	**HK1.4**	**151Eu**
CD3	**145-2C11**	**152Sm**
CD172a/SIRPa	**P84**	**153Eu**
CD103	**2,00E+07**	**154Sm**
CD106/VCAM-1	**429**	**155Gd**
CD19	**6D5**	**156Gd**
Ly6G	**1A8**	**158Gd**
CD11b	**M1/70**	**160Gd**
CD54/ICAM-1	**YN1/1.7.4**	**161Dy**
CD24	**M1/69**	**162Dy**
CD8a	**53-6.7**	**164Dy**
CD45	**30-F11**	**165Ho**
CD86/B7-2	**GL-1**	**166Er**
CD25/IL-2Ra	**3C7**	**167Er**
FCeR1	**MAR*1**	**169Tm**
CD80	**mar/23**	**170Er**
CD206	**C068C2**	**172Yb**
H-2L^{d}/H-2D^{b} (MHC I)	**28-14-8**	**173Yb**
I-A/I-E (MHC II)	**M5/114.15.2**	**174Yb**
F4/80	**BM8**	**175Lu**

Genes for RT-PCR (Taqman Probes)
Lrat - Mm00469972_m1
Acta2 - Mm01546133_m1
Des - Mm00802455_m1
Itgax - Mm00498701_m1
Gapdh (Mm99999915-g1)

F4/80+

Cluster 1	**mouse 1**	**mouse 2**	**mouse 3**	**mouse 4**	**AVERAGE**
without CLL	1700	2030	1300	1520	1637,5
day 2	1110	1730	1620	1370	1457,5
day 7	1950	1440	1300	1220	1477,5
day 17	990	1890	800	1900	1395

Cluster 2	**mouse 1**	**mouse 2**	**mouse 3**	**mouse 4**	**AVERAGE**
without CLL	1090	370	990	670	780
day 2	90	180	50	80	100
day 7	670	870	1660	910	1027,5
day 17	600	570	720	640	680

Cluster 3	**mouse 1**	**mouse 2**	**mouse 3**	**mouse 4**	**AVERAGE**
without CLL	1710	1460	1790	2230	1797,5
day 2	1670	1230	1510	1690	1525
day 7	4960	4160	3290	2530	3735
day 17	1500	2180	2110	2070	1965

Cluster 4	**mouse 1**	**mouse 2**	**mouse 3**	**mouse 4**	**AVERAGE**
without CLL	1420	1650	1780	1390	1560
day 2	6420	6380	6700	6670	6542,5
day 7	1610	2300	1910	1220	1760
day 17	4280	3680	3730	1660	3337,5

CD11c+

Cluster 5	**mouse 1**	**mouse 2**	**mouse 3**	**mouse 4**	**AVERAGE**
without CLL	2640	2470	2250	2270	2407,5
day 2	1650	1810	1720	1600	1695
day 7	1590	2610	1340	1330	1717,5
day 17	2890	3670	2570	2200	2832,5

Cluster 6	**mouse 1**	**mouse 2**	**mouse 3**	**mouse 4**	**AVERAGE**
without CLL	10270	9090	9720	8300	9345
day 2	6400	7350	2780	1860	4597,5
day 7	6370	4390	9010	10040	7452,5
day 17	2780	880	7020	8590	7805

Cluster 7	**mouse 1**	**mouse 2**	**mouse 3**	**mouse 4**	**AVERAGE**
without CLL	4170	6330	4720	4490	4927,5
day 2	3680	4800	2600	1910	3247,5
day 7	3820	3150	4210	4450	3907,5
day 17	5370	5680	4350	4960	5090

Cluster 8	**mouse 1**	**mouse 2**	**mouse 3**	**mouse 4**	**AVERAGE**
without CLL	1410	1950	1810	2190	1840
day 2	3960	3720	3900	4090	3917,5
day 7	3340	4250	3010	2560	3290
day 17	1850	1540	1380	2510	1820

Cluster 11	**mouse 1**	**mouse 2**	**mouse 3**	**mouse 4**	**AVERAGE**
without CLL	900	620	1200	1700	1105
day 2	1120	730	1250	1360	1115
day 7	2030	2220	1460	1050	1690
day 17	550	1050	1280	670	887,5

Luminex Assay					
Analyte Sample	G-CSF	Eotaxin	GM-CSF	IFN-gama	IL-1alfa
	pg/ml	pg/ml	pg/ml	pg/ml	pg/ml
Samples experiment 1					
Control 1	41,6	288,46	81,01	119,63	192,9
Control 2	65,42	343,98	82,04	216,02	248,06
Control 3	52,17	208,02	74,19	90,72	235,89
CLL day 1 - 1	514,37	311,06	81,01	241,9	395
CLL day 1 - 2	613,37	188,11	63,8	554,67	274,31
CLL day 1- 3	527,47	197,82	60,67	370,93	235,89
CLL day 1 - 4	713,27	161,77	30,77	251,2	230,03
CLL day 2 - 1	62,21	583,29	79	213,32	205,42
CLL day 2 - 2	34,45	318,98	41,6	202,85	335,44
CLL day 2 - 3	52,17	213,32	40,57	453,59	260,85
CLL day 2 - 4	52,17	339,68	54,86	213,32	232,94
CLL day 7 - 1	71,44	292,11	83,08	95,4	295,8
CLL day 7 - 2	70,55	202,85	119,63	84,13	192,9
CLL day 7 - 3	68,8	178,89	118,13	82,04	260,85
CLL day 7 - 4	55,56	146,29	60,67	132,29	208,02
CLL dia 17 - 1	97,83	311,06	122,67	129	295,8
CLL dia 17 - 2	57,69	241,9	118,13	102,87	254,38
CLL dia 17 - 3	82,04	284,85	122,67	303,34	327,11
Samples experiment 2					
Control 1	47,2	987,5	62,9	110,5	1756,7
Control 2	35	1002,4	35,1	170,1	2476,6
Control 3	31,6	1131	51,8	56,2	6673,3
Control 4	83,2	1631,6	75,2	3134,7	2241,7
Control 5	37,7	1061,1	53	3413,4	6335,6
CLL day 30 - 1	41,4	973,2	36,6	167,3	4614,5
CLL day 30 - 2	96,1	1047,1	46,2	859	8063,2
CLL day 30 - 3	150,1	1056,5	44,9	2687,3	1734,9
CLL day 30 - 4	72,6	1179,8	40,9	3556,6	1296,7
CLL day 30 - 5	62,1	1275	46,8	127,7	9527,5
CLL day 30 - 6	60,7	1077,2	44,9	158,8	1715,1
CLL day 60 - 1	33,6	876,6	33,6	4966,8	15816,8
CLL day 60 - 2	29,6	1232,1	36,6	83,6	1266,7
CLL day 60 - 3	28,9	726,4	28,7	825,4	9123,6
CLL day 60 - 4	43,4	1036,9	42,2	94,4	1813,8
CLL day 60 - 5	30,9	1395	42,2	115,4	5848,1
CLL day 60 - 6	49,5	978,8	43,6	109,5	2223,1

IL-1beta	IL-2	IL-4	IL-3	IL-5	IL-6	IL-7
pg/ml	pg/ml	pg/ml	pg/ml	pg/ml	pg/ml	pg/ml
127,39	32,35	6,38	10,01	27,47	254,38	74,19
185,76	31,95	8,9	19,57	27,13	318,98	113,76
157,75	31,95	6,29	14,43	30	318,98	90,72
176,65	54,86	12,94	17,69	32,35	514,37	102,87
132,29	36,69	8,39	9,58	30,77	410,19	76,08
139,11	32,76	7,47	14,05	25,8	390,07	68,8
70,55	43,2	8,64	4,59	14,43	370,93	41,6
157,75	31,95	9,44	25,8	63,8	318,98	84,13
79	40,57	11,08	10,76	30	361,72	52,17
140,87	40,06	7,69	14,43	27,82	380,38	76,08
110,93	33,6	10,01	15,2	44,86	318,98	68,8
157,75	26,79	7,05	23,93	34,89	303,34	113,76
238,88	23,33	4,09	30	32,35	218,75	95,4
257,59	21,64	5,95	27,82	43,2	267,5	115,2
132,29	29,63	5,07	44,86	32,35	274,31	86,27
303,34	32,76	9,44	22,19	68,8	335,44	150,01
241,9	29,63	6,29	12,76	47,18	281,29	129
390,07	34,45	8,52	40,57	54,86	343,98	183,44
120,9	522,9	14	7,7	3,2	235,3	161,9
86,9	427,8	11,9	5,2	3,6	187,4	123,7
97	366,5	10,6	5	2,9	152,9	130,3
177,7	648,9	20,8	11,3	6,8	286,5	280,7
123,3	634,2	15,1	5,4	2,9	281	183,5
125,6	650,4	14,1	3,9	3,5	289,9	192
113,6	545,3	12	4,4	3,6	316,1	159,2
143,7	475,2	13,6	6,5	4,7	215,3	145,6
151,6	531,7	14,4	4,7	3,3	254	182,4
116,6	457	13,2	4,9	4,4	186,4	143,1
160	610,4	13,6	6	4,9	282,3	191,7
108,6	675,5	13,3	2,9	3,5	279,4	166,1
86,2	492	11,3	4,3	2,6	196,7	130,1
101,6	679,2	14,7	2,9	2,2	245,1	148,5
99,7	485,8	13,5	4,4	3,1	207,3	132,8
129,2	532,1	14,3	4,4	2,4	247,5	161,5
106,7	491,7	12,8	4,4	3,2	187,2	129,5

IL-9	IL-10	IL-12 (p40)	IL-12 (p70)	LIF	IL-13	LIX
pg/ml	pg/ml	pg/ml	pg/ml	pg/ml	pg/ml	pg/ml
1517	142,65	165,89	122,67	1,72	184,03	343,98
1656	165,89	208,02	110,93	4,09	219,45	425,95
1406	142,65	213,32	102,87	3,13	193,52	274,31
1878	213,32	331,25	202,85	13,67	282,19	489,14
1498	122,67	254,38	150,01	21,1	179,46	425,95
1389	108,18	241,9	119,63	15,6	175	284,85
1555	113,76	188,11	50,88	14,81	144,92	335,44
1517	121,14	208,02	116,66	4,48	179,46	235,89
1517	178,89	157,75	53,5	10,01	222,22	352,74
1720	161,77	224,32	100,32	2,45	216,7	235,89
1720	144,46	224,32	139,11	3,39	193,52	339,68
1831	135,66	284,85	88,47	18,61	156,28	1150
1225	110,93	260,85	97,83	15,8	150,49	628,99
1389	190,49	274,31	86,27	12,59	184,03	808,83
1272	125,8	200,32	81,01	4	143,11	213,32
1720	165,89	251,2	197,82	6,12	214	277,78
1288	142,65	218,75	165,89	5,63	175	299,55
1720	176,65	299,55	218,75	5,34	225,04	303,34
1164,6	698,2	410,6	72,2	3,6	1705,1	950,1
1019,7	716,7	334,8	44,9	3,9	1336,2	807,3
862	300,1	322,1	60	3,4	1400,2	621,3
1580,2	1047,8	624,2	126,8	7,9	2616,4	1263,3
1259,6	172,5	479,8	69,8	2,8	1603,5	1104,2
1170,1	789,1	522,5	46,6	2,8	1501,2	1201,5
1088,2	120,7	446,3	171,3	3,5	1428,3	1074,8
1101,7	378,3	409,9	66,5	4,7	1542,2	881,5
1259,6	493,3	451,2	55,9	4,1	1743,8	923,4
1017,5	242,3	390,5	58,3	4	1454,5	784,5
1247,5	786,2	522,5	101,5	4,3	1921,2	1030,3
1295,4	1411,9	458,5	64,1	2,9	1385,1	1154
901,8	379,8	409,9	47,5	3	1138,4	929
1458,4	1152,9	453,2	32,9	2	1594,2	1143,2
1104,5	657,4	380,9	48,3	3,4	1321	910,4
1134	481,3	428,4	44,9	2,3	1572	935,5
1048,8	684,9	349,8	38,9	3,6	1233,9	837,5

IL-15	IL-17	IP-10	KC	MCP-1	MIP-1alfa	MIP-1beta
pg/ml	pg/ml	pg/ml	pg/ml	pg/ml	pg/ml	pg/ml
514,37	25,48	248,06	465,15	125,8	96,61	125,8
769,16	34,45	343,98	224,32	192,9	178,89	59,16
598,14	28,53	352,74	170,11	161,77	90,72	41,6
808,83	36,69	769,16	940,56	1809	216,02	142,65
645,01	30,38	583,29	695,55	1461	195,34	99,07
514,37	23,93	527,47	527,47	1014	197,82	161,77
410,19	15,2	361,72	311,06	621,13	64,6	60,67
613,37	33,18	238,88	183,44	202,85	257,59	41,6
628,99	20,84	442,33	241,9	79	153,83	25,16
645,01	28,53	174,44	235,89	170,11	159,75	26,46
628,99	27,13	208,02	218,75	146,29	267,5	23,93
628,99	25,8	235,89	964,52	590,67	99,07	29,26
645,01	27,47	307,17	235,89	299,55	178,89	50,88
808,83	28,53	260,85	216,02	311,06	218,75	44,86
568,8	22,75	248,06	150,01	323,02	190,49	197,82
1014	42,66	274,31	183,44	251,2	299,55	62,21
695,55	42,66	241,9	150,01	221,52	254,38	50,88
1150	51,52	281,29	202,85	288,46	135,66	74,19
1597,6	29,3	402,6	247,1	110,9	177,2	134,3
1211,9	24,9	375,3	202,5	88,1	151,4	118,9
1094,8	24	361,9	200,9	88,1	147,7	128,2
2213,7	42,8	558,4	383,7	141,7	203,9	191,3
1488	27	520,5	306,7	93,1	168,5	122,4
2243,5	20,9	515	338,2	86,5	181,7	114,8
1309,8	17,7	471	254,3	102,6	145	117,1
1323,2	25,9	388,1	300,6	114,5	167,9	119,7
1908	26,1	667,7	311,8	112,3	228,7	117,1
1543	22,8	470,1	247,2	91,5	237,2	117,4
2362	26,9	500,6	316,4	125,7	210,6	120,2
2286,6	20,8	402,8	293,2	81,2	199,8	110,7
1488	18,8	434,3	225,6	74,8	152,7	113,5
1366,5	13,6	303,5	309,7	68	156,9	106
1269,5	22,5	398,9	224,7	83,9	156,2	119,2
1777,8	25,5	530,3	328,2	83	174,4	118,7
1941,7	18,9	321	236,5	81,2	152,4	111,8

M-CSF	MIP-2	MIG	RANTES	VEGF	TNF-alfa
pg/ml	pg/ml	pg/ml	pg/ml	pg/ml	pg/ml
113,76	216,02	1855	50,88	20,06	5,79
183,44	267,5	3292	48,38	34,02	24,53
174,44	238,88	3106	48,38	24,53	11,56
380,38	327,11	32860	54,86	79	17,69
311,06	311,06	22334	52,17	47,78	13,3
224,32	295,8	18695	41,6	36,23	13,67
135,66	192,9	29531	30,77	43,75	2,73
213,32	307,17	2405	35,78	43,75	19,57
60,67	216,02	2341	62,21	62,21	3,29
142,65	284,85	1902	32,35	35,78	19,57
161,77	251,2	2615	35,33	42,66	9,17
105,49	205,42	8832	34,89	70,55	15,2
132,29	230,03	9737	39,56	67,09	27,82
170,11	270,88	3925	39,07	27,82	27,82
105,49	227,16	3197	53,5	24,53	11,56
489,14	420,63	1926	38,58	25,16	40,57
335,44	352,74	1636	41,6	27,13	30
390,07	436,8	4945	52,17	33,18	41,6
64,2	488,7	1011,5	245	47	22,9
56,3	495,4	961,8	205	33,3	16,3
78,9	513,2	1121,3	202,8	39,5	15,1
123,1	634,6	1239,4	311,7	89,1	33,2
64,2	502	1704,7	265,9	55,6	15,5
57,3	527,2	2307,7	306	47,3	16,3
61,2	474,9	2234,4	248,7	51,6	21,6
72	522,6	1342,5	209,4	46,1	20,4
65,6	573,3	2647,9	283,3	52,4	15,5
64,2	530,2	1424,8	206	40,1	18,8
72	578,7	1307	266,3	62,9	21,8
56,3	604,9	1393,7	264,1	57,8	15,1
55,3	460,6	1543	261,8	47,9	13,5
45,9	433,8	1274,3	310,8	51,4	11,6
59,7	570,5	1114,6	228,5	43,4	15,1
66,6	581,4	2061,5	250,2	45,3	14,3
57,3	490,4	874,9	194,7	46,1	17,1

EDITORIAL

Subcapsular Hepatic Dendritic Cells: Hiding in Plain Sight

See "Combination of mass cytometry and imaging analysis reveals origin, location, and functional repopulation of liver myeloid cells in mice," by David BA, Rezende RM, Antunes MN, et al, on page 000.

UNCORRECTED PROOF

The consensus view of resident hepatic myeloid cells envisages many Kupffer cells, together with smaller populations of granulocytes, monocytes and several kinds of dendritic cells.[1–4] These conclusions derive from the integration of data from immunohistology and multiparameter flow cytometry. Even using a few parameters, the data obtained from immunohistology and from flow cytometry do not always add up.[5] In this issue of *Gastroenterology*, an international group of investigators reports use of multiparameter mass cytometry (CyTOF) in tandem with intravital microscopy to look more closely at the liver's resident myeloid cells.[6] Their startling result is that an abundant population of myeloid dendritic cells is present in normal mouse liver. These cells have been hiding in plain sight, but are now revealed (Figure 1*A*).

These combined CyTOF and intravital imaging studies documented an abundant population of cells with dendritic morphology that express the dendritic cell marker CD11c, but lack the mature macrophage marker F4/80. These cells were extravascular, and located mainly in the subendothelial space close to the peritoneal surface of the liver. In contrast to these dendritic cells, 2 populations of F4/80$^+$ Kupffer cells were identified, both located in the sinusoids, one expressing CD11c and the other without; however, the extravascular dendritic cells were the most abundant of these cell populations.

Intravital imaging using a reporter of the CX3CR1 chemokine receptor also revealed extravascular dendritic cells, but transverse sections of liver tissue showed these cells most abundantly close to the liver's capsule, whereas deeper in the liver tissue they were located mostly around blood vessels. In view of the dendritic shape of the cells, it was important to consider that they might be a subset of hepatic stellate cells. Indeed, the paper defining the immunologic functions of hepatic stellate cells also revealed a substantial CD11c-low population.[7] However, the cells described here were unlikely to be stellate cells for 3 reasons: they did not express desmin, they contained no vitamin A granules, and upon cell sorting they did not express known stellate cell genes.

The location of these CD11c$^+$ CX3CR1$^+$ dendritic cells in the subcapsular region of the liver is highly provocative. This tissue zone abuts the peritoneal cavity, an immunologically active compartment that is rich in macrophages and B cells and that can be a source for the repopulation of Kupffer cells.[8] However, repopulation of the subcapsular dendritic cells after depletion using clodronate liposomes seemed to be from blood monocytes, which flooded the liver at 2 days after clodronate treatment. This phase was followed by repopulation of both the intravascular Kupffer cells and the extravascular CX3CR1$^+$ dendritic cells, apparently from a common pool of CX3CR1$^+$ macrophage-like cells, of which one-half acquired F4/80 to become CX3CR1$^+$F4/80$^+$, and then lost CX3CR1 to become Kupffer cells. The other CX3CR1$^+$ cells slowly migrated into the extravascular space, likely in response to CX3CL1 chemokine, to become the dendritic cells (Figure 1B). Their capacity to limit hepatic injury was restored over time, and the Kupffer cells also slowly acquired phagocytic activity.

The repopulation of both the Kupffer cells and the subcapsular dendritic cells from monocytes via a CX3CR1$^+$ intermediate raises the question of how these cells are related to long-lived resident Kupffer cells of yolk sac origin. Lineage-tracing experiments using an inducible, CX3CR1-driven Cre recombinase to mark cells early in embryonic development have revealed that many adult Kupffer cells in a pathogen-free mouse have early origins, when hematopoiesis is focused in the yolk sac.[9,10] In addition, at an early neonatal stage the growing liver is seeded by bone marrow derived monocytes that become long-lived self-renewing Kupffer cells.[11] Microglia in the central nervous system also originate from yolk sac progenitors,[12] and share with Kupffer cells a relatively radiation-resistant subset.[13]

Thus, a question of great interest is whether the abundant subcapsular dendritic cells of the normal liver are also a self-renewing population seeded in the embryo. Other possible sources include a population that migrates from the peritoneum, or cells that seed in early neonatal life; or the cells could be maintained by bone marrow-derived dendritic cell precursors during normal homeostasis.

How has this abundant population of liver dendritic cells been hiding so effectively until now? It is partly because the identification of liver cells by flow cytometry depends on details of the cell isolation technique. It is partly because the specific combination of stains that resolve these cells (CD45, F4/80, CX3CR1, and CD11c) may not have been used together in such a systematic way. And partly, perhaps, it is because the dendritic cells inhabit a subendothelial space not clearly distinct from the space of Disse, the home of hepatic stellate cells, which are also morphologically dendritic, so that in the absence of optimized markers, the cells might be difficult to distinguish. A major strength of the study by David et al[6] is that they used tissue dissociation to identify specific cell types of interest, and then carried the results back into intact, living tissue. In so doing, they have revealed an abundant population of subcapsular hepatic dendritic cells that, until now, were hiding in plain sight.

An urgent question is whether a similar population of subcapsular dendritic cells exists in the human liver that exhibit both immunogenic and tolerance-promoting properties.[14] The surface area of the mouse liver is much

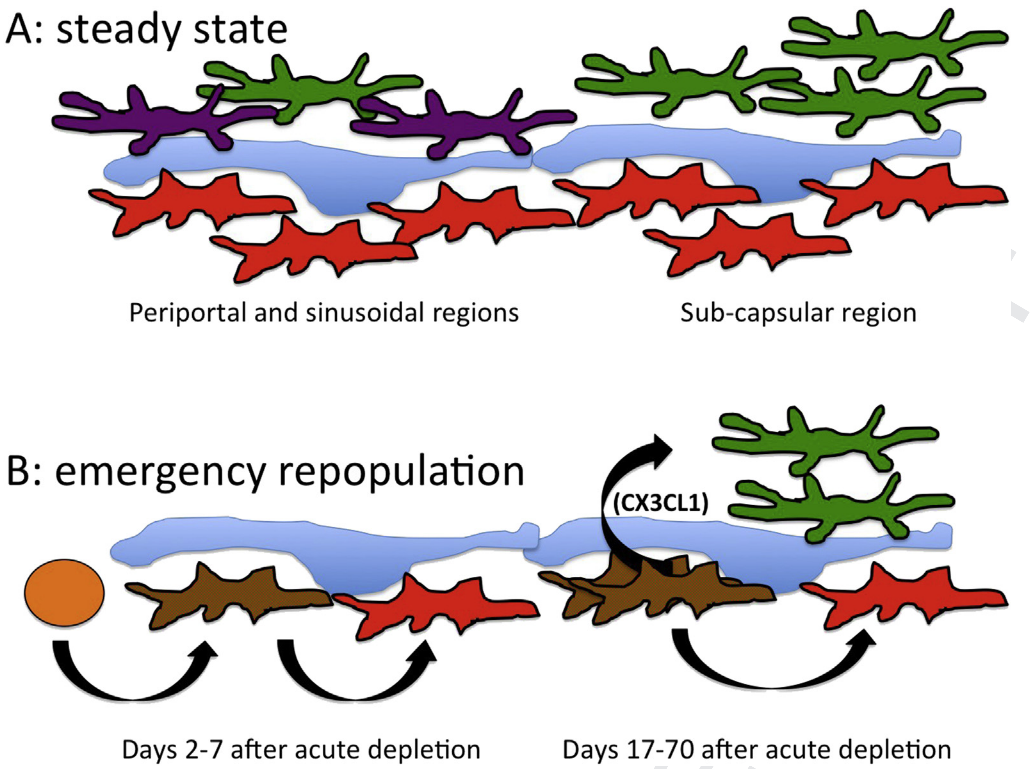
A: steady state
Periportal and sinusoidal regions
Sub-capsular region
B: emergency repopulation
(CX3CL1)
Days 2-7 after acute depletion
Days 17-70 after acute depletion

print & web 4C/FPO

Figure 1. ■■■ Q4

greater in proportion to its volume than is the case in humans, so if these cells exist only at the peritoneal surface of the organ, they will likely form a much smaller fraction of human liver dendritic cells. However, the human liver has a more complex anatomy than the mouse liver, and additional niches may exist that allow these cells their prominent place. The paper by David et al[6] already suggests that they are equipped to present antigen to T cells, but the T cells they engage, the consequences for T-cell function versus tolerance, and their role in human disease all remain issues for the future.

Q5 *D. RADIKA SOYSA*
IAN N. CRISPE
Department of Pathology
University of Washington
Seattle, Washington

UNCORRECTE

References

1. Crispe IN. The liver as a lymphoid organ. Annu Rev Immunol 2009;27:147–163.
2. Ezzelarab M, Thomson AW. Tolerogenic dendritic cells and their role in transplantation. Semin Immunol 2011;23:252–263.
3. Crispe IN. Immune tolerance in liver disease. Hepatology 2014;60:2109–2117.
4. Heymann F, Tacke F. Immunology in the liver–from homeostasis to disease. Nat Rev Gastroenterol Hepatol 2016;13:88–110.
5. Klein I, Cornejo JC, Polakos NK, et al. Kupffer cell heterogeneity: functional properties of bone marrow derived and sessile hepatic macrophages. Blood 2007;110:4077–4085.
6. David BA, Rezende RM, Antunes MN, et al. Combination of mass cytometry and imaging analysis reveals origin, location, and functional repopulation of liver myeloid cells in mice. Gastroenterology 2016. 00:000–000. Q3
7. Winau F, Hegasy G, Weiskirchen R, et al. Ito cells are liver-resident antigen-presenting cells for activating T cell responses. Immunity 2007;26:117–129.
8. Wang J, Kubes P. A reservoir of mature cavity macrophages that can rapidly invade visceral organs to affect tissue repair. Cell 2016;165:668–678.
9. Hagemeyer N, Kierdorf K, Frenzel K, et al. Transcriptome-based profiling of yolk sac-derived macrophages reveals a role for Irf8 in macrophage maturation. EMBO J 2016;35:1730–1744.
10. Yona S, Kim KW, Wolf Y, et al. Fate mapping reveals origins and dynamics of monocytes and tissue macrophages under homeostasis. Immunity 2013;38:79–91.
11. Scott CL, Zheng F, De Baetselier P, et al. Bone marrow-derived monocytes give rise to self-renewing and fully differentiated Kupffer cells. Nat Commun 2016;7:10321.
12. Lavin Y, Mortha A, Rahman A, et al. Regulation of macrophage development and function in peripheral tissues. Nat Rev Immunol 2015;15:731–744.
13. Kennedy DW, Abkowitz JL. Kinetics of central nervous system microglial and macrophage engraftment: analysis using a transgenic bone marrow transplantation model. Blood 1997;90:986–993.

14. Ibrahim J, Nguyen AH, Rehman A, et al. Dendritic cell populations with different concentrations of lipid regulate tolerance and immunity in mouse and human liver. Gastroenterology 2012;143:1061–1072.

Reprint requests
Address requests for reprints to: D. Radika Soysa, Department of Pathology, University of Washington 1959 NE Pacific Street, Seattle, WA 980195. e-mail: soysar@uw.edu.

Conflicts of interest
The authors disclose no conflicts. Q1

© 2016 by the AGA Institute

0016-5085/$36.00
http://dx.doi.org/10.1053/j.gastro.2016.10.030

UNCORRECTED PROOF

IMMUNOLOGY ORIGINAL ARTICLE

Isolation and high-dimensional phenotyping of gastrointestinal immune cells

Bruna A. David,[1,†] Stephen Rubino,[2,†] Thais G. Moreira,[3] Maria A. F. Lopes,[1] Alan M. de Araújo,[1] Nicole E. Paul,[4] Rafael M. Rezende[2,‡] and Gustavo B. Menezes[1,‡]

[1] *Departamento de Morfologia, Centre for Gastrointestinal Biology, Instituto de Ciências Biológicas, Universidade Federal de Minas Gerais, Belo Horizonte, Minas Gerais, Brazil,* [2] *Ann Romney Center for Neurologic Diseases, Brigham and Women's Hospital, Harvard Medical School, Boston, MA, USA,* [3] *Departamento de Bioquímica e Imunologia, Instituto de Ciências Biológicas, Universidade Federal de Minas Gerais, Belo Horizonte, Minas Gerais, Brazil and* [4] *Dana-Farber Cancer Institute, Harvard Medical School, Boston, MA, USA*

doi:10.1111/imm.12706

Received 23 November 2016; revised 21 December 2016; accepted 24 December 2016.

[†] These authors contributed equally to this study.

[‡] These authors jointly supervised this study.

Correspondence: Gustavo Batista Menezes, Instituto de Ciências Biológicas, Universidade Federal Minas Gerais, Av Antônio Carlos 6627 – Belo Horizonte, Minas Gerais 31270-901, Brazil. Email: menezesgb@ufmg.br

Senior author: Xxxxxxx

Summary

The gastrointestinal immune system plays a pivotal role in the host relationship with food antigens, the homeostatic microbiome and enteric pathogens. Here, we describe how to collect and process liver and intestinal samples to efficiently isolate and analyse resident immune cells. Furthermore, we describe a step-by-step methodology showing how to high-dimensionally immunophenotype resident leucocytes using cytometry by time-of-flight, providing a well-characterized antibody platform that allows the identification of every leucocyte subset simultaneously. This protocol also includes instructions to purify and cultivate primary murine hepatocytes, a powerful tool to assess basic cell biology and toxicology assays. Gut and liver samples from the same mouse can be collected, processed and stained in less than 6 hr. This protocol enables the recovery of several populations of purified and viable immune cells from solid and fibrous organs, preventing unwanted loss of adherent cells during isolation.

Keywords: cell isolation; cytometry by time of flight; lamina propria; liver; mass cytometry.

UNCORRECTED PROOF

Introduction

The gastrointestinal immune system (GIS), which includes the gastrointestinal tract, liver and associated lymphoid organs such as mesenteric lymph nodes, appendix (caecal patch in mice) and Peyer's patches, harbours one of the most complex populations of immune cells in our body.[1,2] Indeed, all leucocyte subsets can be found under homeostatic conditions within the intestines[1,3] or the liver.[4,5] These resident immune cells play a crucial role for tissue homeostasis from embryonic phase and throughout adulthood. GIS cells are involved in tissue remodelling and repair,[6] immune tolerance to food antigens[7,8] and they sustain a healthy relationship with our commensal microbiota.[9] For this, an exquisite network of immune cells organizes an efficient firewall against dissemination of gut-derived bacteria, viruses and other pathogens within circulation. Notably, disruption of gastrointestinal homeostasis due to gut and liver diseases is associated with several infectious and inflammatory diseases, including sepsis,[10–12] and autoimmune[13,14] and auto-inflammatory diseases.[13,15] Therefore, it is becoming increasingly clear that expanding our knowledge on the immunobiology of the GIS may guide future clinical

CE: Prakash A
PE: Amul S.
Dispatch: 25.1.17
No. of pages: 15
WILEY
12706
Manuscript No.
I M M
Journal Code

interventions and diagnoses, and also add to the development of more precise immune-based therapies.

The gastrointestinal tract is composed of a unique vascular and parenchymal architecture that comprises a diverse array of tissue-resident immune cells to mediate homeostatic functions of the organs. Taking into account that these cells are usually part of an intricate tissue network, their isolation for *ex vivo* studies can be challenging. Indeed, improper tissue processing will lead to inefficient recovery of leucocyte subtypes, which will not reflect the actual pool of resident cells. Moreover, cells with larger protrusions (i.e. macrophages or dendritic cells) or cells within the connective tissue that are firmly adhered to the extracellular matrix will be inadvertently discarded during the isolation procedure.[16] Hence, reliable and efficient cell isolation procedures specifically designed for solid and fibrous organs are of broad interest.

Efforts to characterize the tissue-resident immune cell populations in the GIS have to date mostly relied on flow cytometry-based analysis, which has proven to be an invaluable tool to identify and assess the role of GIS-resident immune cells in homeostasis and disease pathogenesis.[17,18] However, traditional flow cytometry has limitations that can make data interpretation difficult, these limitations include: a relatively small number of markers per panel and spectral overlap of fluorescent markers leading to compensation artefacts. These limitations are particularly evident in the characterizations of non-lymphoid cell populations, (monocytes, macrophages, dendritic cells and granulocytes) in the liver and small intestine lamina propria, which harbour numerous unique tissue-resident subsets that require several specific markers to study.

To overcome some of the limitations of flow cytometry, cytometry by time-of-flight (CyTOF), mass cytometry (Fig. 1) was recently developed and its use has become more widespread.[19–24] This technique uses a mass spectrometer to characterize single cells labelled with antibodies conjugated to metal isotopes instead of the fluorophores used in traditional flow cytometry. Currently, over 40 isotope-conjugated markers can be analysed in a single panel without the need to compensate different isotope channels. The high-dimensional data that are generated from using this many markers can be analysed straightforwardly using widely available algorithms on CYTOBANK, these include viSNE,[25] CITRUS[26] and SPADE.[27] One of the drawbacks of CyTOF is that the sample must comprise a purified cell population because the cells are vaporized during the run and gating for cells is based on DNA content, which will be compromised by samples with a high density of debris. This is an important consideration for the study of immune cells from the GIS, where the digestion of tissues such as the intestine and liver leads to loss of cell viability and generates a large amount of residual debris.

Here, we describe a robust and simple protocol for the isolation, staining and CyTOF analysis of purified and viable leucocytes from the intestinal lamina propria and the liver that generates high-quality and reproducible high-dimensional immunophenotyping data of the GIS. Additionally, using the same protocol, we also describe the procedures to isolate leucocytes from the mesenteric lymph nodes, and how to cultivate primary mouse hepatocytes. This may be of interest to groups studying liver biology and toxicology.

The integrated protocol, encompassing cell isolation to analysis of gastrointestinal immune cells, described here will expedite discoveries in uncovering the role of the GIS in health and disease. Indeed, high-dimensional analysis can offer a more detailed characterization of the dynamic changes in resident cell populations during the disease courses of models of chronic inflammation (e.g. inflammatory bowel disease, hepatitis) or gastrointestinal cancers, and after perturbation to GIS homeostasis (e.g. changes in diet, microbiome). For example, we recently used viSNE to characterize the distinct temporal changes of novel myeloid cell clusters during the repopulation and seeding of liver phagocytes after depletion.[23] Another emerging application of CyTOF analysis is the discovery of novel single cell-based biomarkers, where the high-dimensional nature of CyTOF data permits more rapid screening of targets than would be possible using traditional flow cytometry.[21]

Taking into account that this protocol deals with challenging solid and fibrous tissues, and the immunophenotyping methodology proposed here covers the majority of the leucocyte subsets, minimal modifications would allow the processing and analysis of different organs other than the gastrointestinal tract, which may include brain, lung, spleen and others.

One of the current limitations of CyTOF is the low sample acquisition rate of the mass cytometer (200–600 events per second) compared with a traditional flow cytometer (i.e. BD FACS Aria; BD, Franklin Lakes, NJ; up 4
to 20 000 events per second). To circumvent this low acquisition rate, individual samples can be bar-coded and pooled together for a single run. However, the low acquisition rate will still make it difficult to analyse very rare populations, as it would take 20–100 times longer than flow cytometry to collect enough events for proper statistical testing. One solution for analysing very rare populations by mass cytometry is to first enrich for these populations using bead or flow-sorting-based techniques before staining and running on the mass cytometer.

Materials and methods 5

Reagents

Common use of reagents.

Mice: 18–25 g C57BL/6. Other mouse backgrounds are acceptable. All experiments involving animals must

UNCORRECTED PROOF

LOW RESOLUTION FIG

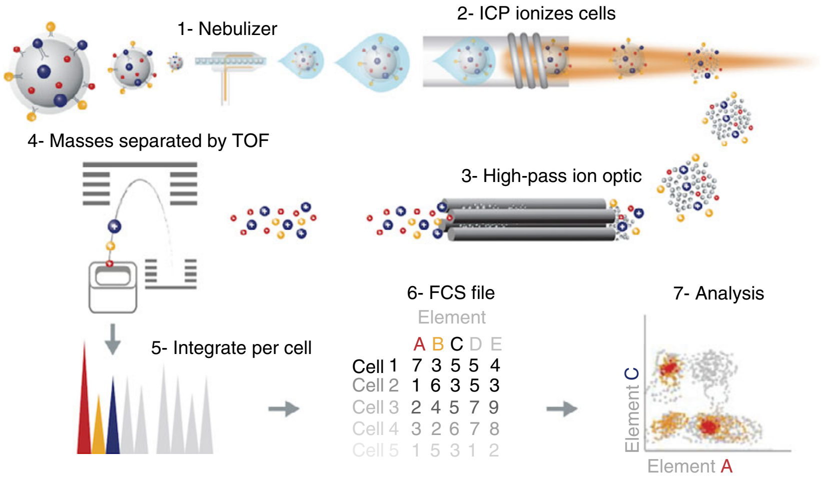

Colour online, B&W in print

[25] **Figure 1.** Schematic representation of basic principles of cytometry by time-of-flight (CyTOF). Cells are labelled with a panel of heavy-metal-conjugated probes using methods very similar to flow cytometry staining protocols. The single-cell suspension is introduced into the nebulizer where it is aerosolized (step 1). It is critical to remove as much water as possible from the sample so that it can be efficiently ionized in the plasma. This is achieved first by aerosolizing the sample in the nebulizer followed by delivery to the plasma through the heated spray chamber. The single-cell aerosol droplets that exit the spray chamber are transmitted to the inductively coupled plasma (ICP) source where they are vaporized, atomized and ionized in the plasma for subsequent mass analysis (step 2). This results in the formation of an ion cloud containing the ions derived from metal-conjugated probes, endogenous cell components and argon. The ion cloud then passes through the plasma–vacuum interface. The purpose of the vacuum interface is to efficiently transport ions from the plasma at atmospheric pressure to the chambers that house the ion optics at less than 10^{-3} Torr (step 3). Mass cytometers use a three-cone interface to transport the ion beam into a low-pressure vacuum: sampler, skimmer and reducer. Low-mass ions, non-ionized particles and photons are removed in the high-pass ion optics, resulting in a cloud of ions enriched for the probe isotopes. The ion clouds that exit the high-pass ion optic consist of a mixture of high-molecular-weight probes in a randomly distributed array. These ions are sent to the TOF mass analyser, which separates the ions on the basis of their mass-to-charge ratio (step 4). The ion clouds, now enriched for high mass ions, enter through the entrance slit into the accelerator chamber of the TOF analyser. At 13-microsecond intervals, or pushes (frequency of 76·8 kHz), a pulse is applied to the push-out plate, accelerating the accumulated packet of ions orthogonally toward the reflector, which redirects the ions toward the detector. The electric fields in the accelerator and reflector are configured to focus ions into tight time-resolved bands regardless of initial position or energy. Each packet of ions resolves into a series of bands, with the lightest probes reaching the detector first and each successively heavier mass reaching the detector at a later time. Each time-resolved band of ions of mass M is separated from its $M \pm 1$ neighbour by 20–25 ns. After the first packet of ions is pushed out and detected, a second pulse pushes out the next packet of ions for detection and the cycle repeats until data acquisition is complete. Data for each 13-microsecond push are digitized sequentially and integrated to obtain ion counts for the channels selected for analysis (steps 5 and 6). The resulting record is processed according to cell event selection criteria set by the user. These criteria include a minimum signal threshold and a range for event duration consistent with single-cell events. As a result, the data acquired contain the integrated number of total ion counts for each selected analyte on a per-cell basis. These data are saved as text (.txt) and flow cytometry standard (.fcs) 3.0 format for data analysis in compatible software programs (step 7).

Uncor

conform to all relevant governmental and institutional regulations.
Ethanol, 70% [volume/volume (vol/vol)] in distilled water
Commercial ethyl alcohol absolute 99·5% (Merk Millipore, Billerica, MA, cat. no. 100990) [6]
Sterile saline solution, 0·9% [weight (wt)/vol] (NaCl)
Fetal bovine serum (FBS; Gibco, Grand Island, NY, ref.12657-029) [7]
Anaesthetic solution (see Reagent set-up)

Reagents for liver cells isolation.

Hydrochloric acid 1 M (Synth – cod. SC 1002-1) [8]
Penicillin–streptomycin (Sigma-Aldrich, St Louis, MO, P4333) [9]
Collagenase from *Clostriduim histolyticum* (Sigma-Aldrich, C2139-1G)
Milli-Q water
Type I collagen from rat tail (Sigma-Aldrich, C3867)
Trypan Blue Solution 0·4% (Thermo Fisher Scientific, Waltham, MA, cat. number 15250061 [10]
Sodium chloride – NaCl (Synth, cod. 01C1060·01.AH)
Potassium chloride – KCl (Synth, cod. 01C1058·01.AH)
Potassium dihydrogen phosphate – KH_2PO_4 (Synth, cod. 01F2002·01.AG)
Sodium phosphate dibasic anhydrous – Na_2HPO_4 (Sigma-Aldrich, cod. V000317)
Sodium bicarbonate – $NaHCO_3$ (Synth, cod. 01B20007·01.AG)

UNCORRECTED PROOF

Magnesium sulphate heptahydrate – $MgSO_4·7H_2O$ (Dinâmica Química Contemporânea, Sao Paulo, Brazil, cod. 1159) 11
Magnesium chloride hexahydrate – $MgCl_2·6H_2O$ (Dinâmica Química Contemporânea, cod. 1055)
Calcium chloride dihydrate – $CaCl_2·2H_2O$ (Synth, cod. 01C2013·01.AH)
Sodium hydroxide – NaOH (Sigma-Aldrich, S5881)
12 RPMI-1640 medium (Cultilab, cod. 0010 – see Reagent set-up)
Williams' E medium (Sigma-Aldrich, W4125 – see Reagent set-up)
Hanks' Medium A (see Reagent set-up)
Hanks' Medium B (see Reagent set-up)
PBS 10 × (see Reagent set-up)
PBS 1 × (see Reagent set-up)

Reagents for lamina propria cells isolation.

X-VIVO™ 15 chemically defined, serum-free haematopoietic cell medium (Lonza, Basel, Switzerland 04-418Q) 13
Iscove's modified Dulbecco's medium (GlutaMAX™; Gibco, cat. no. 31980-030)
Liberase TL (Roche Molecular Biochemicals, Basel, Switzerland, 05401020001) 14
Deoxyribonuclease I from bovine pancreas (Sigma-Aldrich, D5025)
EDTA (Sigma-Aldrich, E6758)
1,4-Dithiothreitol (Sigma-Aldrich, D9760)
Bovine serum albumin – (Sigma-Aldrich, A5123)
Lamina propria buffer A (Reagent set-up)
Lamina propria buffer B (Reagent set-up)
Lamina propria Buffer C (Reagent set-up)
Lamina propria buffer D (Reagent set-up)
MACS buffer (Reagent set-up)
HEPES (Sigma-Aldrich, 7365-45-9)
EDTA stock solution – 0·5 M (Reagent set-up)

CyTOF staining reagents.

CD45 MicroBeads, mouse (Miltenyi Biotec, Bergisch Gladbach, Germany, 130-052-301) 15
CyTOF-PBS (Low-barium PBS): PBS Ca^{2+}- and Mg^{2+}-free (Gibco, cat. no. 10010-023).
Bovine serum albumin, protease-free (Sigma-Aldrich, A3059)
Sodium azide (Sigma-Aldrish, 71289)
MaxPar® Fix and Perm Buffer (Fluidigm/DVS Sciences, South San Francisco, CA, cat. no. 201067) 16
MaxPar® Intercalator Ir 500 μM (Fluidigm/DVS Sciences, cat. no. 201192B)
Cell-ID™Cisplatin – Natural Abundance Platinum (Fluidigm/DVS Sciences, cat. no. 201064)
EQ™ Four-Element Calibration Beads (Fluidigm/DVS Sciences, cat. no. 201078)
Cell staining buffer – CSB (see Reagent set-up)
Intercalator solution (see Reagent set-up)
MaxPar® Multi-Metal Labelling Kit (Fluidigm/DVS Sciences)

Reagent set-up

Anaesthetics. Anaesthetic solution: Mix 10% (wt/vol) ketamine solution (2·5 ml) with 2% (wt/vol) xylazine solution (2·0 ml) and 1 × PBS (5·5 ml). Inject 50 μl intraperitoneally per 10 g of body weight (ketamine: 60–80 mg/kg and xylazine: 8–15 mg/kg). Anaesthetic solution should be freshly made.

Solutions for liver cell isolation – non-parenchymal cells. RPMI-1640 medium: In a beaker, dilute the contents of a sachet of RPMI-1640 in 800 ml of distilled water. Add 2·2 g of sodium bicarbonate and 10 ml of penicillin–streptomycin (100 ×). Complete up to a final volume of 1000 ml, keeping the solution under constant stirring with a magnetic stirrer.

Digestion solution 1 – liver non-parenchymal cell isolation: Dilute 10 mg of collagenase (1 mg/ml) in 9 ml of RPMI-1640 medium supplemented with 1 ml of FBS (10% vol/vol).

Solutions for liver cell isolation – hepatocytes. Williams' medium E: In a beaker, dilute the contents of a sachet of RPMI-1640 in 800 ml of distilled water. Add 2·2 g of sodium bicarbonate and 10 ml (1/100 vol/vol) of Pen strep (100 ×). Complete for a final volume of 1000 ml keeping the solution under constant stirring with a magnetic stirrer. Measure the pH, filter into sterile receptacle and store at 4°.

Stock solutions to prepare Hanks' A and B (for hepatocytes isolation): Solution 1: In a beaker, dilute 35·1 g of sodium chloride (NaCl – 1·2 M), 1·9 g of potassium chloride (KCl – 50 mM), 0·27 g of potassium dihydrogen phosphate (KH_2PO_4 – 4 mM) and 0·14 g of disodium phosphate (Na_2HPO_4 – 2 mM) in 400 ml of distilled water keeping the solution under constant stirring with a magnetic stirrer. Complete for a final volume of 500 ml, filter and store at 4°.

Solution 2: In a beaker, dilute 26·25 g of sodium bicarbonate ($NaHCO_3$ – 625 mM) in 400 ml of distilled water keeping the solution under constant stirring with a magnetic stirrer. Complete for a final volume of 500 ml, filter and store at 4°.

Solution 3: In a beaker, dilute 1·23 g of magnesium sulphate heptahydrate ($MgSO_4·7H_2O$ – 10 mM), 1·27 g of magnesium chloride hexahydrate ($MgCl_2·6H_2O$ – 12·5 mM) and 5·51 g of calcium chloride dihydrate ($CaCl_2·2H_2O$ – 75 mM) in 400 ml of distilled water keeping the solution under constant stirring with a magnetic stirrer. Complete to a final volume of 500 ml, filter and store at 4°.

Hanks' A solution: In a beaker, dilute 0·5 g of D-glucose (0·1% wt/vol), 0·095 g of EGTA (0·5 mM), 50 ml of the stock solution 1, 50 ml of the stock solution 2 and 10 ml of penicillin–streptomycin (100 ×) in 400 ml of distilled water keeping the solution under constant stirring with a magnetic stirrer. Complete for a final volume of 500 ml, set pH to 7–7·4, filter and store at 4°.

Hanks' B solution: In a beaker, dilute 0·5 g of D-glucose (0·1% wt/vol), 50 ml of the stock solution 1, 20 ml of the stock solution 2, 20 ml of the stock solution 3 and 10 ml of penicillin–streptomycin (100 ×) in 400 ml of distilled water keeping the solution under constant stirring with a magnetic stirrer. Complete for a final volume of 500 ml, set pH to 7–7·4, filter and store at 4°.

Digestion solution 2 – hepatocyte isolation: Dissolve 20 mg of collagenase in 25 ml of Hanks' B to obtains a 0·8 mg/ml collagenase solution.

Sodium hypochlorite solution: Dilute 10 ml of sodium hypochlorite in 90 ml of distilled water.

Solutions for lamina propria cell isolation. EDTA stock solution: Dissolve 116·9 g of EDTA in H_2O to obtain a 0·5 M stock solution. Stir vigorously on a magnetic stirrer. Adjust the pH to 8·0 with NaOH. Dispense into aliquots and sterilize by autoclaving.

Lamina propria buffer A: Mix 25 ml of FBS and 12·5 ml of HEPES (1 M) in 462·5 ml of Hanks' balanced salt solution (HBSS). Sterilize the solution by filtration using a 0·22-μm syringe filter, and store it for up to 1 month at 4°.

Lamina propria buffer B: Mix 2 ml of EDTA stock solution (0·5 M) and 12·5 ml of HEPES (1 M) in 485·5 ml of

PROOF

LOW RESOLUTION FIG

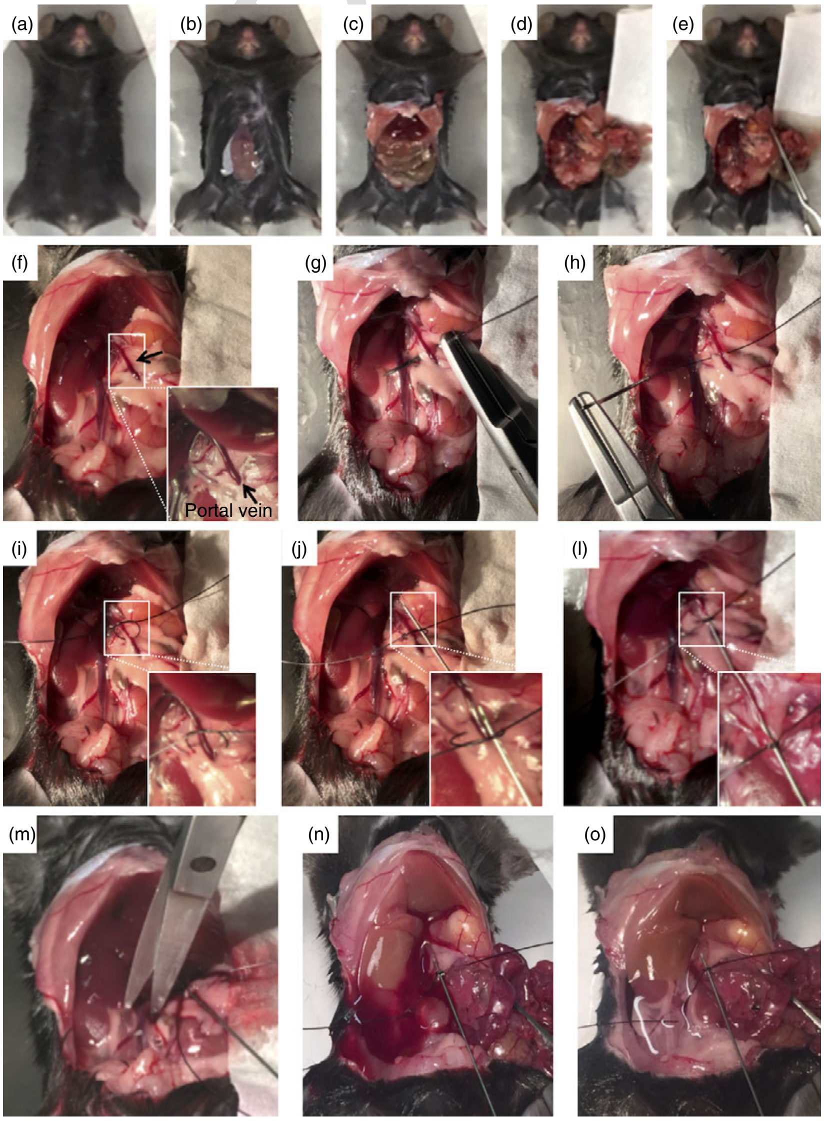

Colour online, B&W in print

26 **Figure 2.** Surgical procedures for portal vein cannulation and liver perfusion. (a–e) Midline laparotomy and viscera dislocation to visualize the branch of portal vein. (f) Higher magnification imaging showing the anatomical location of the portal vein. (g, h) A suture wire is trespassed under the portal vein in the median portion, perforating the associated adipose tissue and mesentery, without lacerating the portal vein. (i, j) A loose knot will receive the cannulation catheter (j) that after portal vein perforation will firmly retain the catheter in a stable position. (m–o) After confirmation of cannulation patency, the vena cava is cut to allow liver perfusion. Note that liver colour changes from wine red to brown after perfusion. 18

Colour online, B&W in print

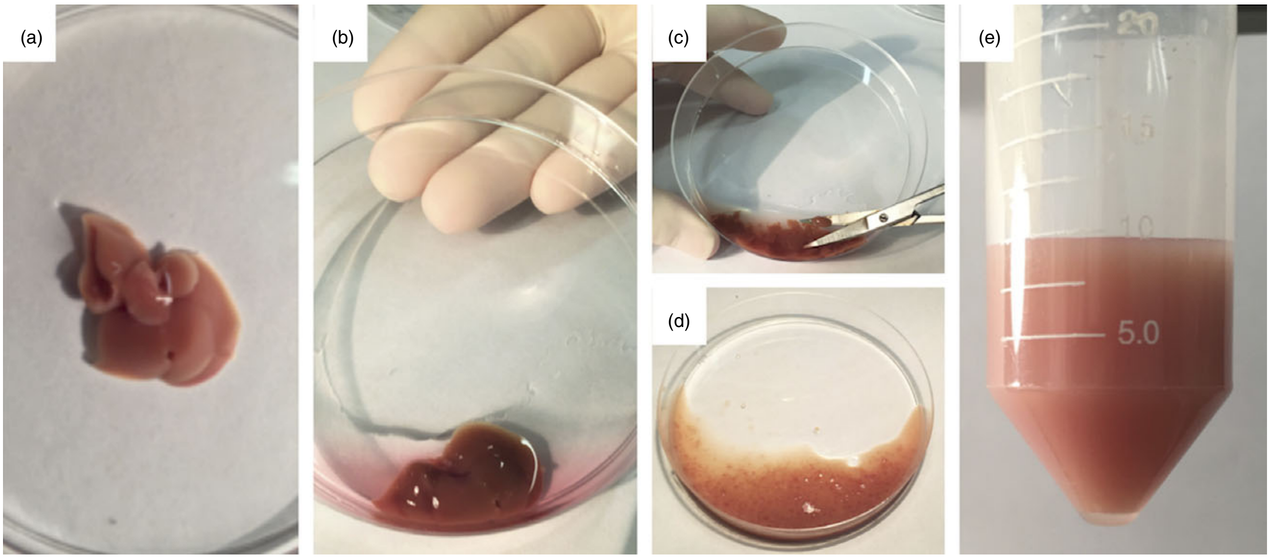

Figure 3. Liver processing for isolation of non-parenchymal cells. (a) Liver aspect after perfusion *in vivo*. (b) Initial digestion in a Petri dish using collagenase-based solution. (c, d) Liver is minced to very small fragments using scissors to enhance digestion by collagenase. (e) Final aspect after digestion protocol.

UNCORRECTED

HBSS. Sterilize the solution by filtration using a 0·22-μm syringe filter, and store it for up to 1 month at 4°.

Lamina propria buffer C: Mix 5 ml of EDTA stock solution (0·5 M), 50 ml of FBS and 0·5 ml of HEPES (1 M) in 437·5 ml HBSS and then dissolve 0·77 g of dithiothreitol to obtain a 1 mM solution. Sterilize the solution by filtration using a 0·22-μm syringe filter, and store it for up to 1 month at 4°.

Lamina propria buffer D: Dissolve 5 mg of liberase TL and 450 μl of DNAse stock solution in 30 ml of Iscove's or X-Vivo medium.

DNAse stock solution: Dissolve 20 mg of DNAse in 10 ml of sterile saline solution, 0·9% (wt/vol) to obtain a 2 mg/ml (4000 U/ml) stock solution. Store the solution in 1 ml aliquots at −20° for up to 1 month.

MACS buffer: Dissolve 50 g of BSA (0·5% – wt/vol) in 100 ml of PBS 1 × and store up to 1 week at 4°.

Solutions for CyTOF staining. Cell staining buffer – CSB: Dissolve 2·5 g of BSA and 100 mg of sodium azide in 500 ml low-barium PBS. Store in a Nalgene polypropylene bottle that has never been washed with detergent. Prepare up to 1 month in advance and store at 4°.

Intercalator solution: MaxPar Intercalator-Ir 500 μM 1 : 4000 dilution in MaxPar Fix and Perm Buffer.

Procedures for hepatocyte culture. The culture of hepatocytes is performed in 6-well and 24-well plates with or without cover slip, depending on the purpose of the experiment.

Preparation of the cover slips: Using a small forceps, wash each cover slip individually, according to the following sequence: distilled water (five times), absolute ethanol (five times), hydrochloric acid (HCl, 1 M) for 1 hr, distilled water 17 (five times), absolute ethanol (five times). Place it to dry in the laminar flow on a sterile filter paper for approximately 30 min, keeping the UV light on. Subsequently, turn the cover slips so that they stay under UV light for over 30 min. Place one coverslip inside each well.

Preparation of the plates: 1 day before the hepatocytes isolation experiment, treat the plates and the cover slips with type I collagen (see Reagent set-up) to enhance cell adhesion. Prepare the solution of type I collagen at a concentration of 5 μg/cm^2 and pipette it into the wells. In wells with cover slip, pipette slowly and carefully, so that the solution can form a big drop just on the surface of the cover slip without draining to the bottom of the wells. Let it dry overnight in laminar flow under UV light. The plates and cover slips treated with type I collagen can be sealed and stored at 4° for a week. Before use, hydrate collagen with Williams' E medium for 30 min. Remove medium before adding the required amount of cell suspension.

Required amount of type I collagen depending on the plate design:

Surface	Area (cm^2)	Type I collagen – stock solution (μl) (5 mg/ml)
Six-well plates	9·6	1200
Cover slip for six-well plates (22 × 22 mm)	4·9	600
24-well plates	1·9	200
Coverslip for 24-well plates (13 mm diameter)	1·33	150

Procedure

Cannulation of the portal vein timing: ~ 1 hr.

1 Clean the perfusion catheter with sodium hypochlorite solution (see Reagent set-up) for 5 min at fast flow.
2 Wash the perfusion catheter with distilled water for 10 min at fast flow.
3 Calibrate the water bath to 37° to preheat the solutions before perfusion. The liver should be perfused with Hanks' A and Hanks' B for hepatocyte isolation, and with PBS 1 × for hepatic non-parenchymal cell isolation.
4 Calibrate the perfusion pump to medium flow of 12·5 ml/min.
5 Anaesthetize the mouse by intraperitoneal injection (see Reagent set-up for dose). Wait about 10 min until mouse is under deep anaesthesia.
6 Position the mouse on a surgical stage with the abdomen facing up, taping the animal by the limbs (Fig. 2a).
7 Apply 70% ethanol on the chest and abdominal skin of the mouse. This will avoid small pieces of fur entering the peritoneal cavity. Perform the midline incision in the abdomen from the pubis to the xiphoid process (Fig. 2b).
8 Dissociate the abdominal musculature from the skin to allow the visualization of blood vessels and to prevent disruption and possible bleeding. Perform lateral incisions in the skin and, subsequently, in the abdominal muscles along the costal margin to the mid axillary line (Fig. 2c).
9 Slide abdominal viscera to the right side using a cotton swab (Fig. 2d).
10 Stabilize abdominal viscera with self-closing forceps to visualize the portal vein (Fig. 2e).
11 Locate the hepatic portal vein (white arrow), and move the forceps and the organs until the portal vein remains straight to be cannulated (Fig. 2f).

LOW RESOLUTION FIG

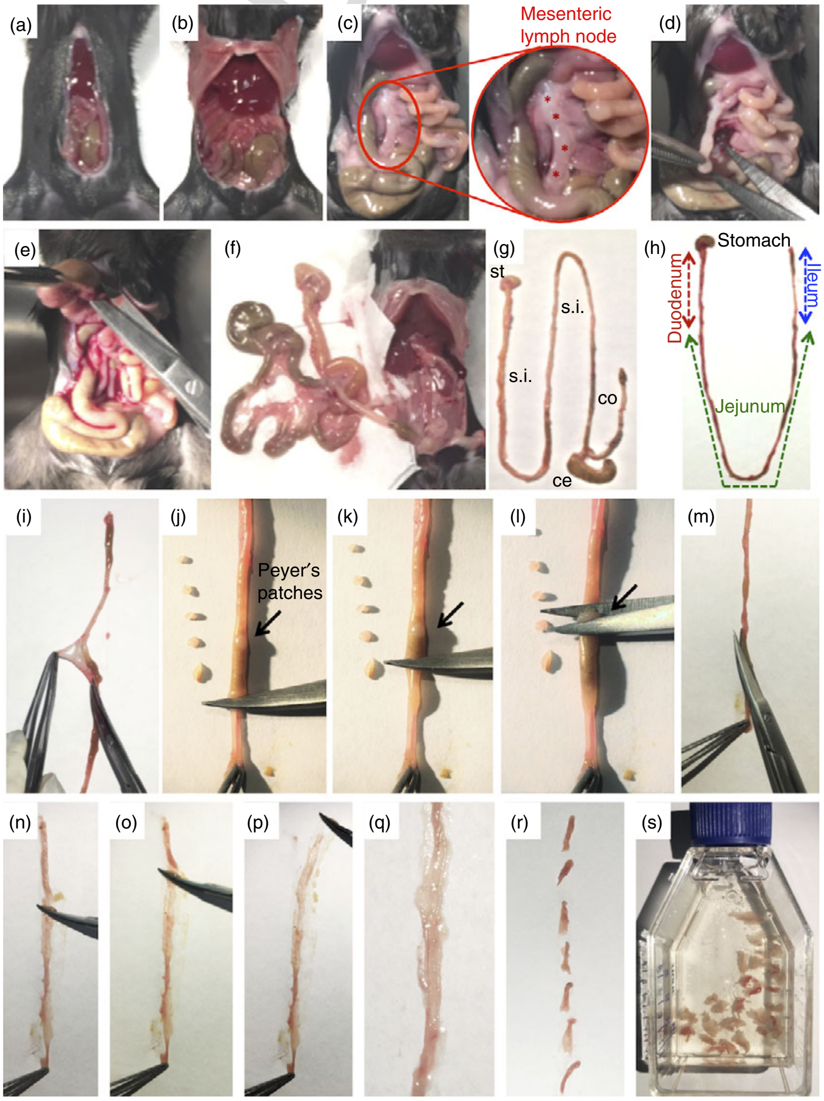

Colour online, B&W in print

Figure 4. Experimental procedures to remove and process different portions of gastrointestinal tract. (a,b) Midline laparotomy and surgical approach to visualize visceral organs. (c) Four mesenteric lymph nodes (indicated by red stars) can be visualized and (d) removed for further analysis. (e) Stomach is carefully detached from the liver and adjacent organs and (f) all the viscera are removed from the peritoneal cavity. (g) Final aspect of stomach (st), small intestine (s.i.), caecum (ce) and colon (co). (h) Schematic representation of different portions of small intestine. (i–l) Removal of visceral adipose tissue, mesentery and Peyer's patches. (m) Longitudinal incision to expose intestinal lumen. (n–p) Removal all intestinal contents. (r) Intestine is minced into smaller pieces. (s) Initial cleaning/digestion procedures.

12 Using a Mayo–Hegar needle holder with a 20 mm needle and 5-0-nylon filament, trespass the suture under (dorsally) the hepatic portal vein (Fig. 2g,h).

13 Make a loose knot with the nylon filament around the hepatic portal vein without tying the blood vessel (Fig. 2i).

14 Insert the catheter inside the loose knot made with the suture thread so that, after cannulating the hepatic portal vein the knot will hold the catheter and keep it immobilized during perfusion (Fig. 2j).

15 Carefully and with the bevel of the catheter facing up, cannulate the hepatic portal vein at the middle portion of its exposed part. To do this, position the catheter parallel to the hepatic portal vein and with a small angle (~ 5°) insert the needle approximately 5 mm into the vein.

16 After cannulating, require the help of a second person to tight the knot around the portal vein and the catheter (Fig. 2l). Keep the catheter immobilized until the knot is tight. Release the catheter with extreme caution to prevent rupture of the blood vessel or untie the knot.

17 Start the perfusion for 1–2 seconds to check whether the vein was properly cannulated and then stop perfusion, the liver should change its colour to pale/beige and no leakage should occur.

18 Cut inferior vena cava using a scissor to release the blood and start the perfusion immediately (Fig. 2m).

19 The liver changes rapidly to its original colour after the blood is washed by the perfusion solution (Fig. 2n,o).

20 Wait until the perfusion is over and then carefully remove the liver. Follow with cell isolation protocols.

Isolation of liver non-parenchymal cells timing: ~ 1 hr 30 min.

21 After cannulation (Fig. 2), perfuse the liver with 50 ml of PBS 1 × (see Reagent set-up) previously warmed at 37°. Keep the solution in the water bath during perfusion.

22 Carefully remove the liver from the peritoneal cavity and wash it in a Petri dish containing PBS once (Fig. 3a). This will remove blood and clots from liver surface.

23 Transfer to another Petri dish with 3 ml of the digestion solution 1 (see Reagent set-up) for hepatic non-parenchymal cell isolation (Fig. 3b).

24 Mince the liver into small pieces (Fig. 3c,d) using scissors.

25 Transfer the minced liver to a 50-ml tube. Collect all the small liver pieces with the rest of digestion solution (~ 7 ml).

26 Incubate for 30 min at 37° under constant stirring.

27 Filter the homogenate (Fig. 2e) using a 70 µm cell strainer and transfer the filtrate to a 50-ml tube.

28 Complete the tube with cold RPMI medium 10% FBS (vol/vol) to a final volume of 50 ml.

29 Centrifuge at 4° for 5 min at 300 ***g***. This step will retrieve all cells in suspension.

30 Discard the supernatant and resuspend the pellet in 15 ml of cold RPMI medium 10% FBS (vol/vol).

31 Transfer the samples to 15-ml tubes and centrifuge at 4° for 3 min at 60 ***g***. This step will eliminate hepatocytes and possible lumps.

32 Collect the supernatant and transfer it to a 15-ml tube. Centrifuge at 4° for 3 min at 60 ***g***. This step will eliminate hepatocytes.

33 Collect the supernatant; transfer it to a 15 ml tube. Centrifuge at 4° for 5 min at 300 ***g***. This step will recover all the cells in suspension, with the exception of hepatocytes.

34 Discard supernatant.

35 Resuspend the pellet in 200 µl of cold RPMI medium 10% FBS (vol/vol). Count the cells (Boxes 1–3). 19

Procedures for CyTOF analysis timing: ~ 3–7 hr. Cell-surface CyTOF staining protocol:

1 Prepare single cell suspensions. In general, try to start with $1{\cdot}5 \times 10^6$ to 3×10^6 cells in 100 µl. Mouse liver (in 5 ml complete Media) used 100–200 µl suspension; mouse lamina propria (in 1 ml complete media) used 100–200 µl.

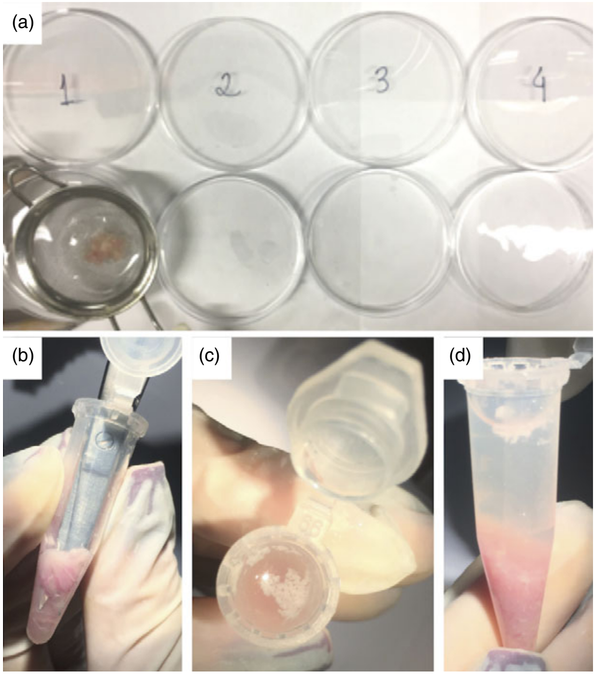

Figure 5. Digestion of intestinal fragments. (a) Initial washing procedures. (b) Intestinal fragments are minced inside a centrifuge tube to enhance digestion. (c, d) Note that all visceral fat in the supernatant should be discarded. 28

LOW RESOLUTION FIG
Colour online, B&W in print

UNCORRECTED PROOF

© 2017 John Wiley & Sons Ltd, *Immunology*

2 Pipette cells into 96-well polypropylene plates and centrifuge cells for 3 min at 500 ***g***.
3 Wash once with 200 µl CyTOF CSB, spin 3 min at 500 ***g***.
4 Cell Viability Step: Add 20 µl of cisplatin solution (cisplatin diluted 1 : 1000 in CSB) to wells. Incubate for 5 min at room temperature. Add 200 µl of CSB to solution to dilute out cisplatin. Centrifuge cells for 3 min at 500 ***g***.
5 Wash cells with 200 µl CSB, spin 3 min at 500 ***g***. For many samples there can be a residue left in the wells from the culture medium and/or viability stain. To

Box 1: Hepatocyte isolation timing: ~ 3 hr 30 min

1 Perfuse (see Fig. 2) the liver with 50 ml of Hanks' A (see Reagent set-up) previously warmed at 37°. Keep the solution in the water bath at 37° during perfusion.
2 Perfuse the liver with the digestion solution 2 for hepatocyte isolation (see Reagent set-up). Keep the solution in the water bath at 37° during the entire process. *Critical*: it is not necessary to stop the perfusion to change tubes containing different solutions, simply pour digestion solution 1 into the tube when Hanks' solution is almost over.
3 When the digestion solution 1 ends, carefully remove the catheter from the hepatic portal vein.
4 Carefully remove the liver and transport it to the laminar flow in a covered Petri dish with cold William's E medium supplemented with 10% FBS (vol/vol).
5 In the laminar flow, open the Petri dish and tear liver's capsule using two forceps to release the cells. Gently shake the liver to help spread its contents on the Petri dish. Repeat this until there are no large pieces left.
6 Use a previously autoclaved mesh to filter all supernatant from the Petri dish. Use a sterile beaker to collect all supernatant. Gently squeeze the mesh against the beaker wall to help with filtration process.
7 Transfer the filtrate to a 50-ml tube and complete to a final volume of 50 ml with cold William's E medium supplemented with 10% FBS (vol/vol). *Critical*: Use the medium to wash the Petri dish before filtration and the beaker after filtration.
8 Centrifuge the tube at 60 ***g*** for 3 min at 4°.
9 Discard the supernatant and resuspend the pellet in 50 ml cold William's E medium supplemented with 10% FBS.
10 Centrifuge the tube at 60 ***g*** for 3 min at 4°.
11 Remove the supernatant and resuspend the pellet in 10 ml of cold William's E medium supplemented with 10% FBS (vol/vol).
12 Mix 10 µl of cells with 10 µl of Trypan Blue and count the cells in a Neubauer chamber (see Reagent set-up).
13 Add the appropriate volume of cells in each well and complete to 2 ml with William's E medium supplemented with 10% FBS (vol/vol).
14 Incubate the cells at 37° with 5% CO_2 for 2 hr to initial adherence. *Critical*: Cells will remain viable for 6–8 hr (Fig. B1).

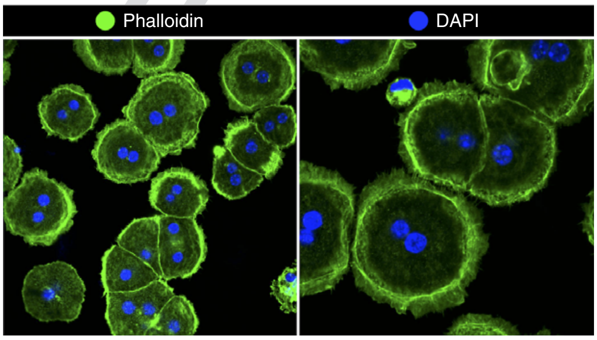

Figure B1. Hepatocyte isolation protocol. Representative image of primary murine hepatocytes stained with Alexa-fluor 488 conjugated phalloidin (in green) and DAPI.

Suggested hepatocyte density for different plates.

Surface	Number of cells	Final volume (ml)
Six-well plates	5×10^5	2
Cover slip for six-well plates (22 × 22 mm)	3×10^5	2
24-well plates	2×10^5	1
Coverslip for 24-well plates (13 mm diameter)	1×10^5	1

UNCORRECTED PROOF

UNCORRECTED PROOF

Box 2: Lamina propria cell isolation timing: ~ 3 hr 10 min

1. Anaesthetize the mouse by intraperitoneal injection (see Reagent set-up for dose). Wait about 10 min until mouse is under deep anaesthesia. Alternatively, these procedures can be run with a killed mouse.
2. Position the mouse on a surgical slate with the abdomen facing up, trapping the animal by the limbs using masking tape.
3. Apply 70% ethanol on the chest and abdomen skin of the mouse to keep the hair out of the way during surgery. Then, perform the midline incision in the abdomen from the pubis to the xiphoid process (Fig. 4a).
4. Dissociate the abdominal musculature from the skin to allow the visualization of blood vessels and to prevent disruption and possible bleeding. Perform lateral incisions in the skin and, subsequently, in the abdominal muscles along the costal margin to the mid axillary line (Fig. 4b).
5. Slide the abdominal viscera to the right side with the aid of a cotton swab (Fig. 4c).
6. Localize and remove mesenteric lymph nodes by finding the caecum localization (if desired) (Fig. 4c,d).
7. Localize stomach and separate it from oesophagus (Fig. 4e).
8. Bring stomach in a vertical direction all the way up from the mouse to detach the small intestine, caecum and large intestine (Fig. 4e,f).
9. Remove as much fat and mesothelium as possible and position the organs in order to separate the caecum and large intestine (Fig. 4g).
10. Place the small intestine on a paper in a ‘U’ shape. Identify the small intestine compartments and separate them accordingly (Fig. 4h).
11. Remove stomach.
12. Remove faeces from the small intestine squeezing the segment with scissors. This will help to identify Peyer’s patches for further removal (Fig. 4j–l)
13. Transfer the collected intestine compartments into Petri dish in Buffer A to wash and remove mucus.
14. Place intestine compartments on a paper towel.
15. Clean out the faeces and mucus by opening up the intestines and shaking them in the buffer (Fig. 4m–p).
16. Place the intestines on a paper towel; re-open them using forceps and scissors (Fig. 4q).
17. Cut the intestine into 1–2 cm pieces and transfer them to a 50 ml tube or T25 flasks containing 20 ml of Buffer B (Fig. 4r,s).
18. Shake or vortex once and discard the supernatant using metal strainer (pour Falcon tube content into a metal cell strainer placed in a beaker). Repeat this procedure until a clean supernatant is obtained.
19. Collect the pieces withheld on the cell strainer and transfer them into 50-ml Falcon tubes containing 10 ml pre-warmed Buffer C at 37°. Shake (200 rpm) for 20–30 min for epithelial removal.
20. Following incubation shake up and down using hands and vortex.
21. Remove the supernatant using metal strainer placed in a beaker.
22. Transfer the metal cell strainer to 1, 2, 3, 4 Petri dishes containing Buffer A (quick dry it in between washes using paper towel) (Fig. 5a).
23. Transfer the small pieces of intestine withheld on the metal strainer to a 50-ml Falcon tube, fill up with 20 ml Buffer A, vortex and pour into the metal strainer. Repeat this at least twice (until supernatant is clean).
24. Transfer all tissue pieces to a 1·5-ml Eppendorf tube, fill it up with Buffer A.
25. Spin 300 ***g*** for 30 seconds to 1 min (to pellet).
26. Remove supernatant.
27. Using microsurgery-curved scissors, mince the intestine (Fig. 5b).
28. Fill it up with Buffer B.
29. Spin 300 ***g*** for 30 seconds to 1 min (to pellet)
30. Remove supernatant (Fig. 5c,d).
31. Add 1 ml of Buffer D solution containing DNAse and liberase TL into the tube containing minced intestine. Vortex to detach the pellet.
32. Pour into a six-well plate or 50-ml tube.
33. Wash the tube with Buffer D to collect all small pieces and transfer to the plate well.
34. Shake plates or tubes on a 37° shaker with Buffer C for 1 hr.
35. Vortex (twice) after every 20 min.
36. After incubation period carefully open plates or tubes.
37. Using a Pasteur pipette, transfer digested intestine into a 50-ml Falcon tube containing Buffer A.
38. Centrifuge for 7 min 500 ***g*** and discard supernatant.
39. Fill tube with 10 ml Buffer A and vortex to detach pellet.
40. Pour Tube content into a new Falcon tube containing 100-μm cell strainer
41. Use the back of 1-ml syringe to gently help the content to pass through cell strainer, wash with Buffer A. Collect the filtrate.
42. Spin for 300 ***g*** for 7 min and remove the supernatant. Resuspend the pellet in Buffer B.
43. Pass tube content through 40-μm cell strainer. Collect the filtrate.
44. Spin and remove the supernatant.
45. Make single cell suspension by re-suspending the pellet in 450 μl of MACS beads solution. Transfer to a 15-ml tube.

UNCORRECTED PROOF

Box 2: Continued

46 Add 50 μl of CD45 microbeads (up to five mice pooled). Use regular inversion to mix the cell suspension (do not vortex). For single sample use 25 μl of beads and 75 μl of MACS solution.
47 Incubate the cell suspension for 20 min at 4° (on ice).
48 Fill Tube with 9·5 ml of MACS solution.
49 Centrifuge for 7 min at 300 ***g***.
50 Prepare a MACS column of appropriate size (see manufacturer's instructions). Columns for positive selection are ready to use [pre-treat columns and cell strainer with 1 ml MACS solution (twice) while cells is centrifuging].
51 Resuspend pellet in 1 ml MACS solution.
52 Pass the content to the beads column. Allow unlabelled cells to flow through the column.
53 Rinse column twice with 2 ml MACS solution.
54 Remove column from racks (magnetic field).
55 Fill the column with 5 ml buffer and elute the positive cells outside the magnetic field using the supplied plunger. Repeat this step twice.
56 Spin at 300 ***g*** for 7 min at 4° and discard the supernatant.
57 Resuspend pellet according to labelling protocols.

Note. Step 30: floating fat can be present on the supernatant and should be removed.

improve cell pelleting, move all samples to fresh wells during this CSB washing step.
6 Add 20 μl Fc-Block antibodies (rat-anti mouse CD16/32, BD clone 2.4G2) per well (1 : 100 in CSB); incubate for 10 min at room temperature.
7 Add 20 μl of metal-coupled surface antibody cocktail to each well (1 : 100 dilution of each surface antibody in CSB). Incubate at room temperature for minimum of 30 min. Note: Staining antibodies used (see Supplementary material, Table S1 and S2) were coupled to selected lanthanide metals using the MaxPar® Multi-Metal Labeling Kit according to the manufacturer's protocol.
8 Wash twice with 200 μl CSB, spin with 500 ***g*** for 3 min.
9 Resuspend cells in 200 μl of Intercalator solution.
10 Incubate at room temperature for 1 hr OR leave overnight at 4°.
11 Centrifuge cells during 3 min at 500 ***g***.
12 Wash twice with 200 μl CSB, centrifuge cells during 3 min at 500 ***g***.
13 Wash twice with 200 μl MilliQ water (low barium); centrifuge cells during 3 min at 500 ***g***.
14 Resuspend cells in 200 μl MilliQ water containing 1 : 10 dilution of EQ beads (for normalization).
15 Count cells using a haemocytometer to get a final cell count of 5×10^5 cells/ml.
16 Transfer cell suspension to 5-ml filter cap tubes.
17 Add additional EQ Bead MilliQ water to get final volume to ~ 500 μl.
18 Samples are ready for run.

Running CyTOF on HELIOS *platform*:

19 Acquire samples on a CyTOF2 (Fluidigm, Inc.) mass cytometer operating on the HELIOS platform (software version 6.5.358) using dual count detection.
20 Calibrate the instrument daily, no more than 8 hr before acquisition with the automated full tuning protocol and validate with 4-element EQ-beads run at stock concentration.
21 Deliver the filtered samples to the DFCI CyTOF Core diluted in water with 1 : 10 4-element EQ beads at a concentration at or below 5×10^5 cells/ml and process at a flow rate of 30 μl/min, event rate of 200–600 events per second, and software

Box 3: Isolation of immune cells from mesenteric or intestinal lymph nodes timing: ~ 3 hr 30 min

1 Position the mouse on a surgical slate with the abdomen facing up, trapping the animal by the limbs using masking tape.
2 Apply 70% ethanol on the skin of chest and abdomen to prevent hair from contaminating the surgery. Perform a midline incision in the abdomen from the pubis to the xiphoid process (Fig. 4a).
3 Dissociate the abdominal musculature from the skin to allow the visualization of blood vessels and to prevent disruption and possible bleeding. Perform lateral incisions in the skin and, subsequently, in the abdominal muscles along the costal margin to the mid axillary line (Fig. 4b).
4 Slide the abdominal viscera to the right side with the aid of a cotton swab (Fig. 4c).
5 Localize and remove mesenteric lymph nodes by finding the caecum localization (if desired) (Fig. 4c,d).
6 Carefully remove fat tissue from the mesenteric lymph node.
7 Place mesenteric lymph nodes on six-well plates containing 70-μm cell strainers and filled with 7 ml of complete media. The media will allow the organ to be constantly bathed, which may result in better cell survival.
8 Mash mesenteric lymph nodes using a 1-ml syringe plunger.
9 Remove the cell strainers and transfer the media containing single cell suspension to a 15-ml Falcon tube.
10 Centrifuge at 400 ***g*** for 5 min at 4°.
11 Discard the supernatant and resuspend the pellet with 500 μl of complete medium.

LOW RESOLUTION FIG

Colour online, B&W in print

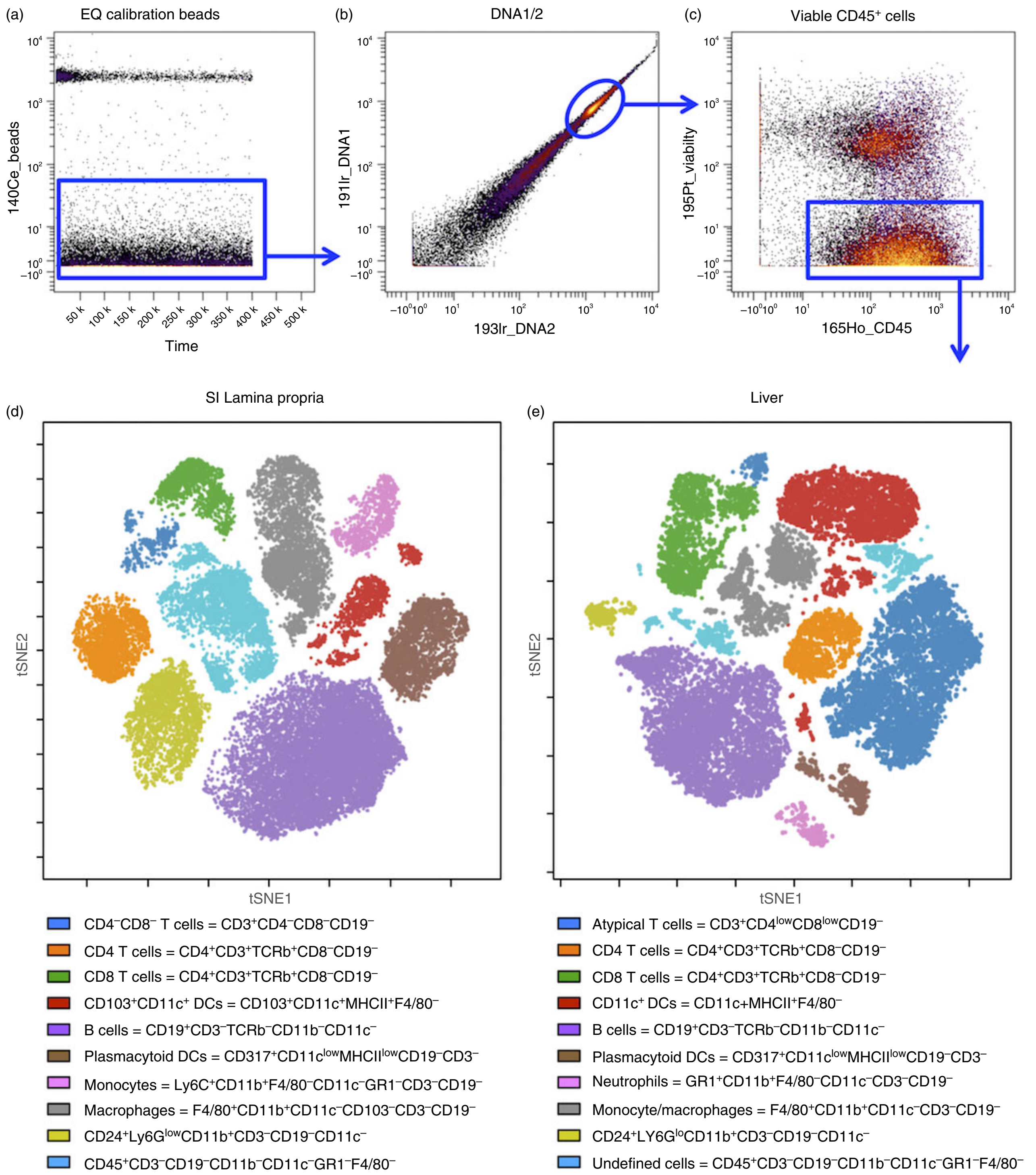

29

Figure 6. ViSNE analysis of small intestine lamina propria and liver CD45$^+$ immune cells. (a) Dot plot of EQ calibration beads (*y*-axis) versus time (*x*-axis); (b) Dot plot of 191Ir_DNA1 (*y*-axis) versus 193Ir_DNA2 (*x*-axis) on gated bead-excluded cells. (c) Dot plot of 195P-Viability (*y*-axis) and 165Ho-CD45 (*x*-axis) gated on DNA1/2 double-positive cells. (d, e) Dot plots depict tSNE1 (*y*-axis) versus tSNE2 (*x*-axis) of clustering after viSNE analysis for a representative sample from (d) small intestine lamina propria and (e) liver. Undefined cells in liver may include natural killer cells, innate lymphoid cells and others.

default settings for threshold and event duration. The length of acquisition is dependent on the final sample volume.

22 After acquisition, normalize samples to the bead signal with the HELIOS software normalizer. Perform normalization in 100-second intervals with a minimum

LOW RESOLUTION FIG
Colour online, B&W in print

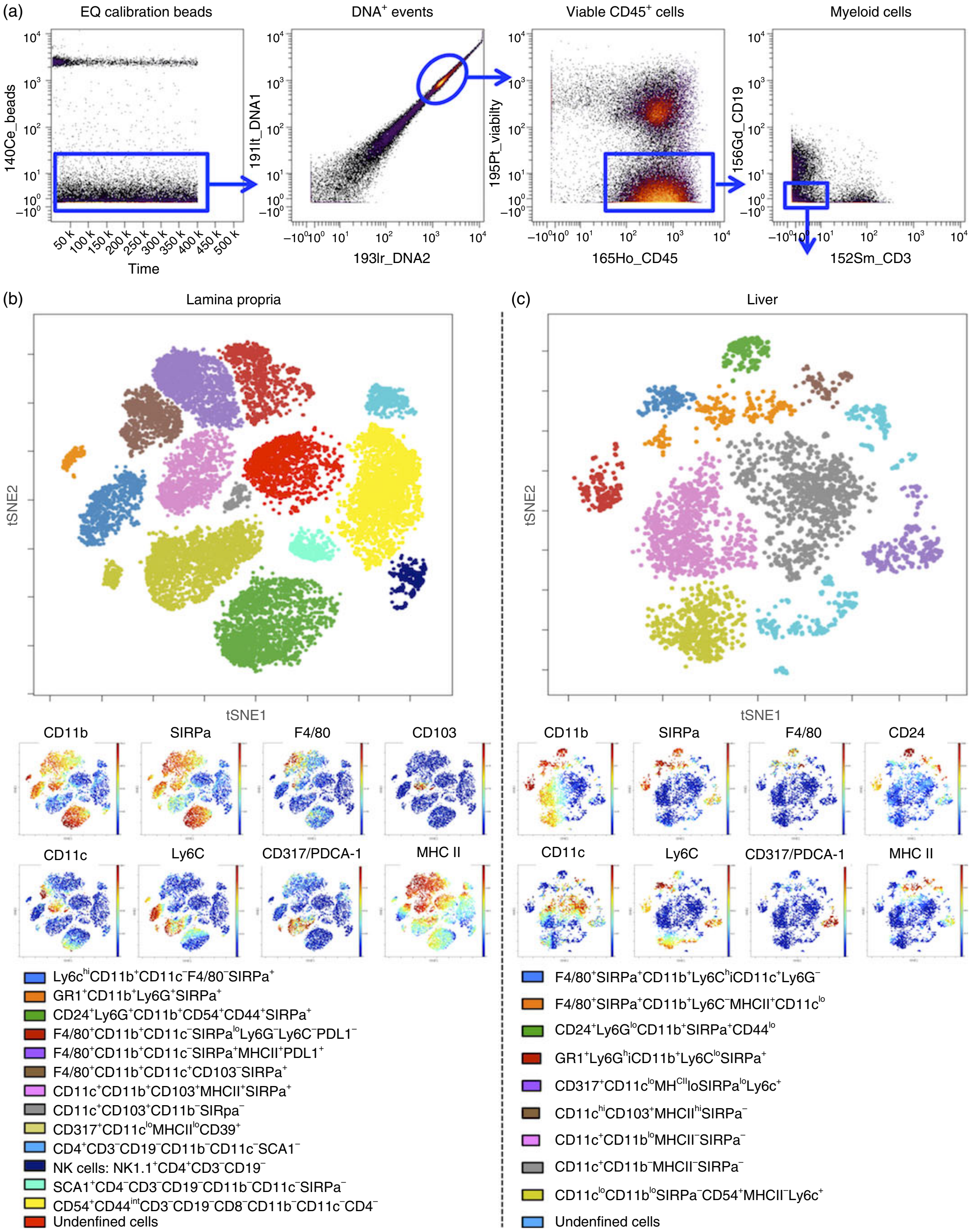

30 **Figure 7.** ViSNE analysis of small intestine lamina propria and liver myeloid cells. (a) Dot plot of EQ calibration beads (*y*-axis) versus time (*x*-axis). (b) Dot plot of 191lr_DNA1 (*y*-axis) versus 193lr_DNA2 (*x*-axis) on gated bead-excluded cells. (c) Dot plot of 195P-Viability (*y*-axis) and 165Ho-CD45 (*x*-axis) gated on DNA1/2 double-positive cells. (d) Gating strategy to obtain live CD45^{+} CD3^{-} CD19^{-} myeloid cells for viSNE analysis. (e) Dot plot depicts tSNE1 (*y*-axis) versus tSNE2 (*x*-axis) of clustering after viSNE analysis for a representative sample from small intestine (SI) lamina propria with major myeloid populations labelled according to lineage marker expression (see key). Dot plots depict expression levels (red = high expression, blue = low expression) selected markers: CD11b, CD11c, SIRPa (CD172), Ly6C, F4/80, CD317/PDCA-1, CD103 and MHC class II. (f) Dot plot depicts tSNE1 (*y*-axis) versus tSNE2 (*x*-axis) of clustering after viSNE analysis for a representative liver sample with major myeloid populations labelled according to lineage marker expression. Dot plots depict expression levels (red = high expression, blue = low expression) selected markers: CD11b, CD11c, SIRPa (CD172), Ly6C, F4/80, CD317/PDCA-1, CD24 and MHC class II.

UNCORRECTED PROOF

of 50 beads per interval. Exclude intervals with fewer than 50 beads from the data.

23 Export normalized data as flow cytometry standard (.fcs) files.

Analysis of CyTOF data using cytobank:

24 Import normalized data .fcs files for liver and lamina propria samples into a new experiment file in CYTOBANK.

25 Gating Strategy: first, exclude normalization beads (Fig. 6a), then gate samples on DNA1 and DNA2 double-positive cells to exclude debris and select for cells with appropriate DNA content levels (Fig. 6b). From the DNA1/2 double-positive gate, gate live immune cells as Cisplatin-negative (195P_Viability *y*-axis, Fig. 6a) and CD45-positive (165Ho_CD45 *x*-axis, Fig. 6c). Myeloid cells were gated on $CD45^+$ $CD3^-$ $CD19^-$ cells (Fig. 7d).

26 ViSNE Analysis: analyse gated $CD45^+$ (Fig. 6d,e) live cells and $CD45^+$ $CD3^-$ $CD19^-$ myeloid cells (Fig. 7e,f) from the liver and lamina propria using the viSNE algorithm in CYTOBANK. Analyse a minimum of 10 000 cells for liver and lamina propria control samples using every marker in the panel for clustering (se Supplementary materials, Tables S1 and S2, for the panels used for the liver and lamina propria).

27 After viSNE analysis, manually define clusters of different cell populations in tSNE1 and tSNE2 dot plots for total $CD45^+$ live cells (Fig. 6d,e) and $CD45^+$ $CD3^-$ $CD19^-$ myeloid cells (Fig. 7e,f) from lamina propria and liver samples according to surface marker expression. Assign demarcating colours to each population using overlaid visualization in the CYTOBANK. See Fig. 7(e,f) for detailed marker expression levels of myeloid subsets in the liver and lamina propria.

Anticipated results (Results and discussion)

The number of cells recovered during this protocol will vary according to the mouse strain, age, gender, and mainly due to experimental model. For example, models for inflammatory diseases usually allow for a higher number of leucocytes. However, under certain conditions (i.e. irradiation, chemical ablation or immunosuppression protocols), mouse leucocyte populations can be dramatically reduced throughout the body. Also, any experimental conditions that induce liver injury (drugs, chemicals, infections, hepatectomy) will decrease the number of viable hepatocytes recovered using this protocol. Under these circumstances, polling samples to achieve sufficient cell density to further staining and analysis may be necessary. Under baseline conditions, an adult mouse (8–12 weeks old, weighing around 20–25 g) yields up to 1×10^7 to 5×10^7 liver non-parenchymal cells, 1×10^7 to 3×10^7 hepatocytes, 5×10^5 to 10×10^5 lamina propria leucocytes and 1×10^7 to 2×10^7 mesenteric lymph node cells (pool of four lymph nodes). Cell viability after these procedures is usually > 90%. Regarding the identification and immunophenotyping of leucocyte populations, different antibody panels will allow for a high variable number of cell clusters. In this protocol, and based on previous studies,[24,28] we could identify 20 populations of leucocytes within the liver and lamina propria (Fig. 6). Further gating on myeloid cells ($CD45^+$ $CD3^-$ $CD19^-$ events) revealed at least 10 different populations in each organ (Fig. 7).

It is worth mentioning that the proposed protocol might be applied not only in a plethora of immune cell characterization under homeostasis,[22,24] but also during inflammatory processes.[23,29] In fact, using the same isolation protocol and CyTOF analysis, we recently showed that during massive liver macrophage depletion by clodronate injection (CLL), an overt inflammatory response was observed. Using a multiplexed cytokine array, we demonstrated that several different cytokines, including MIG, interleukin-9, CXCL1, and others were significantly increased after macrophage depletion. Concomitantly, CyTOF analysis revealed that 2 days after CLL injection, all the clusters defined as liver macrophages and dendritic cells were significantly reduced. Interestingly, CyTOF was also useful to monitor their replenishment dynamics over time.[23] In addition, due to changes in the expression of the surface of intracellular markers used for CyTOF staining throughout the experimental protocol, minor or major changes in clustering position may be observed, which may require a deeper and more complex analysis.

Acknowledgements

The authors would like to thank Dr Michelle Poulin and Dr Gary Impey (Fluidigm) for their help in the preparation of CyTOF figures and description. Also, we would like to thank CAPES, FAPEMIG and CNPq (Brazil) for financial support.

Disclosures

The authors declare that there are no conflicts of interest.

References

1 Mowat AM, Agace WW. Regional specialization within the intestinal immune system. *Nat Rev Immunol* 2014; **14**:667–85.

2 Perez-Lopez A, Behnsen J, Nuccio SP, Raffatellu M. Mucosal immunity to pathogenic intestinal bacteria. *Nat Rev Immunol* 2016; **16**:135–48.

3 Herbrand H, Bernhardt G, Forster R, Pabst O. Dynamics and function of solitary intestinal lymphoid tissue. *Crit Rev Immunol* 2008; **28**:1–13.

4 Geissmann F, Cameron TO, Sidobre S, Manlongat N, Kronenberg M, Briskin MJ *et al.* Intravascular immune surveillance by $CXCR6^+$ NKT cells patrolling liver sinusoids. *PLoS Biol* 2005; **3**:e113.

5 Jenne CN, Kubes P. Immune surveillance by the liver. *Nat Immunol* 2013; **14**:996–1006.

6 Bain CC, Mowat AM. Macrophages in intestinal homeostasis and inflammation. *Immunol Rev* 2014; **260**:102–17.

7 Pabst O, Mowat AM. Oral tolerance to food protein. *Mucosal Immunol* 2012; **5**:232–9.

8 Faria AM, Weiner HL. Oral tolerance: therapeutic implications for autoimmune diseases. *Clin Dev Immunol* 2006; **13**:143–57.

9 Rooks MG, Garrett WS. Gut microbiota, metabolites and host immunity. *Nat Rev Immunol* 2016; **16**:341–52.

10 McDonald B, Kubes P. Neutrophils and intravascular immunity in the liver during infection and sterile inflammation. *Toxicol Pathol* 2012; **40**:157–65.

11 Nesseler N, Launey Y, Aninat C, Morel F, Malledant Y, Seguin P. Clinical review: the liver in sepsis. *Crit Care* 2012; **16**:235.

12 Bernal W, Wendon J. Acute liver failure. *N Engl J Med* 2013; **369**:2525–34.

13 Targan SR, Karp LC. Defects in mucosal immunity leading to ulcerative colitis. *Immunol Rev* 2005; **206**:296–305.

14 Round JL, Mazmanian SK. The gut microbiota shapes intestinal immune responses during health and disease. *Nat Rev Immunol* 2009; **9**:313–23.

15 Podolsky DK. The current future understanding of inflammatory bowel disease. *Best Pract Res Clin Gastroenterol* 2002; **16**:933–43.

16 Mederacke I, Dapito DH, Affo S, Uchinami H, Schwabe RF. High-yield and high-purity isolation of hepatic stellate cells from normal and fibrotic mouse livers. *Nat Protoc* 2015; **10**:305–15.

17 Breton G, Lee J, Liu K, Nussenzweig MC. Defining human dendritic cell progenitors by multiparametric flow cytometry. *Nat Protoc* 2015; **10**:1407–22.

18 Lian ZX, Okada T, He XS, Kita H, Liu YJ, Ansari AA *et al.* Heterogeneity of dendritic cells in the mouse liver: identification and characterization of four distinct populations. *J Immunol* 2003; **170**:2323–30.

19 Yao Y, Liu R, Shin MS, Trentalange M, Allore H, Nassar A *et al.* CyTOF supports efficient detection of immune cell subsets from small samples. *J Immunol Methods* 2014; **415**:1–5.

20 van Unen V, Li N, Molendijk I, Temurhan M, Hollt T, van der Meulen-de Jong AE *et al.* Mass cytometry of the human mucosal immune system identifies tissue-and disease-associated immune subsets. *Immunity* 2016; **44**:1227–39.

21 Bendall SC, Simonds EF, Qiu P, el Amir AD, Krutzik PO, Finck R *et al.* Single-cell mass cytometry of differential immune and drug responses across a human hematopoietic continuum. *Science* 2011; **332**:687–96.

22 Guilliams M, Dutertre CA, Scott CL, McGovern N, Sichien D, Chakarov S *et al.* Unsupervised high-dimensional analysis aligns dendritic cells across tissues and species. *Immunity* 2016; **45**:669–84.

23 David BA, Rezende RM, Antunes MM, Santos MM, Freitas Lopes MA, Diniz AB *et al.* Combination of mass cytometry and imaging analysis reveals origin, location, and functional repopulation of liver myeloid cells in mice. *Gastroenterology* 2016; **???**:???–???.

24 Becher B, Schlitzer A, Chen J, Mair F, Sumatoh HR, Teng KW *et al.* High-dimensional analysis of the murine myeloid cell system. *Nat Immunol* 2014; **15**:1181–9.

25 el Amir AD, Davis KL, Tadmor MD, Simonds EF, Levine JH, Bendall SC *et al.* viSNE enables visualization of high dimensional single-cell data and reveals phenotypic heterogeneity of leukemia. *Nat Biotechnol* 2013; **31**:545–52.

26 Bruggner RV, Bodenmiller B, Dill DL, Tibshirani RJ, Nolan GP. Automated identification of stratifying signatures in cellular subpopulations. *Proc Natl Acad Sci U S A* 2014; **111**:E2770–7.

27 Qiu P, Simonds EF, Bendall SC, Gibbs KD Jr, Bruggner RV, Linderman MD *et al.* Extracting a cellular hierarchy from high-dimensional cytometry data with SPADE. *Nat Biotechnol* 2011; **29**:886–91.

28 Spits H, Artis D, Colonna M, Diefenbach A, Di Santo JP, Eberl G *et al.* Innate lymphoid cells – a proposal for uniform nomenclature. *Nat Rev Immunol* 2013; **13**:145–9.

29 Lutz C, Mozaffari M, Tosevski V, Caj M, Cippa P, McRae BL *et al.* Increased lymphocyte apoptosis in mouse models of colitis upon ABT-737 treatment is dependent upon BIM expression. *Clin Exp Immunol* 2015; **181**:343–56.

Supporting Information

Additional Supporting Information may be found in the online version of this article:

Table S1. List of monoclonal antibodies used in this study – liver non-parenchymal cells

Table S2. List of monoclonal antibodies used in this study – small intestine lamina propria

UNCORRECTED PROOF

Graphical Abstract

The contents of this page will be used as part of the graphical abstract of html only. It will not be published as part of main article.

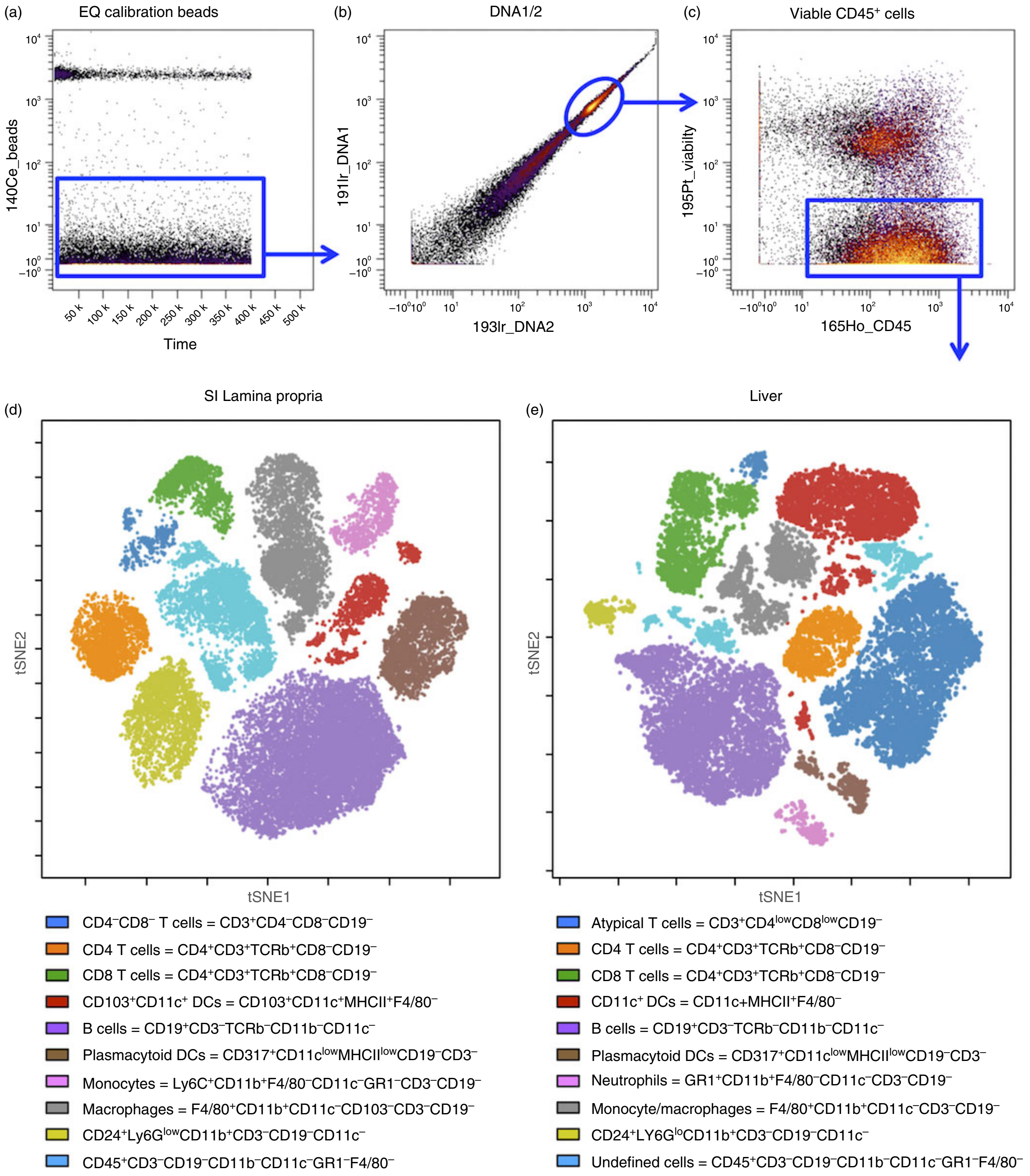

A protocol to isolate viable immune cells from gut lamina propria and liver, and a high-dimensional analysis of cell immunophenotyping using mass cytomety (CyTOF) are described.

DIVULGAÇÃO CIENTIFICA

1. Divulgação do trabalho *Combination of Mass Cytometry and Imaging Analysis Reveals Origin, Location, and Functional Repopulation of Liver Myeloid Cells in Mice* no Boletim UFMG (impresso e *online*) em setembro de 2016.

2. Divulgação do trabalho *Combination of Mass Cytometry and Imaging Analysis Reveals Origin, Location, and Functional Repopulation of Liver Myeloid Cells in Mice* no site da Sociedade Brasileira de Imunologia em outubro de 2016 (*online*).

3. *Vídeo abstract* do trabalho *Combination of Mass Cytometry and Imaging Analysis Reveals Origin, Location, and Functional Repopulation of Liver Myeloid Cells in Mice* divulgado pela *American Gastroenterological Association* no link https://www.youtube.com/watch?v=rx1B9-7jqbg&index=3&list=PL1DE0E0B4378B4525 e no CD em anexo.

UFMG

BOLETIM

Nº 1957 - Ano 42
19.09.2016

Janela de suscetibilidade

Pesquisa constata vulnerabilidade funcional do fígado durante processo de regeneração

Ana Rita Araújo

Foca Lisboa/UFMG

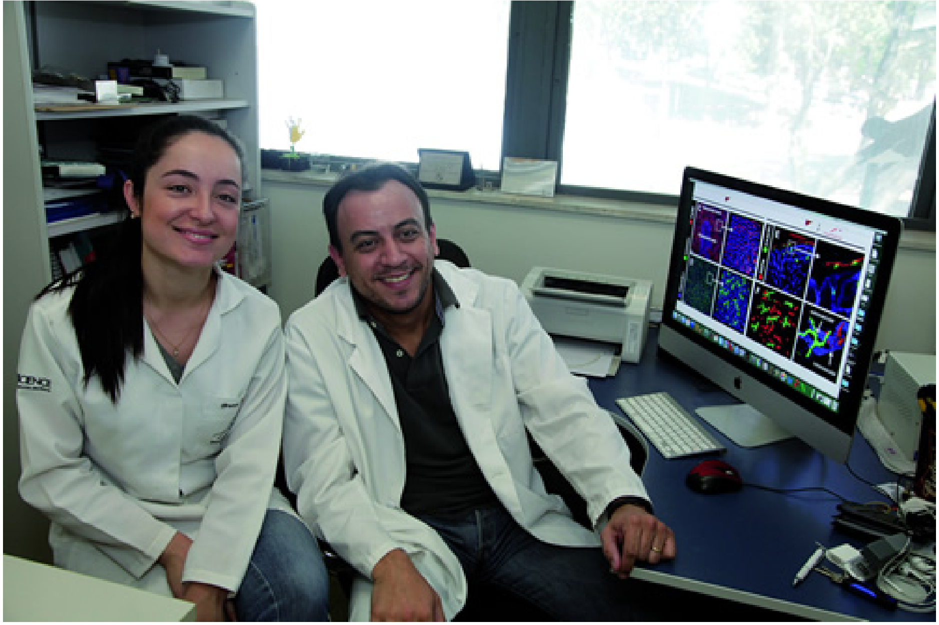

Bruna e Gustavo: combinação de sequenciamento gênico, citometria de fluxo e imagem in vivo

Embora aparentemente recuperado, o fígado permanece disfuncional após processos inflamatórios, o que pode tornar o indivíduo vulnerável a infecções por cerca de duas semanas. Isso parece decorrer da imaturidade das novas células, que ainda não "aprenderam" a exercer sua função. A descoberta é um dos destaques de artigo produzido no Instituto de Ciências Biológicas (ICB) e publicado no fim de agosto no periódico Gastroenterology.

O trabalho, que tem como primeira autora a doutoranda Bruna Araújo David e como líder seu orientador, Gustavo Menezes, também caracterizou uma nova população de células dendríticas, cuja existência no fígado não era bem estabelecida. Realizado em colaboração com pesquisadores das universidades de Harvard (EUA) e de Calgary (Canadá), o estudo sugere a necessidade de tratamentos com anti-inflamatórios para acelerar a regeneração funcional do órgão.

Segundo Gustavo Menezes, a janela de suscetibilidade que o fígado enfrenta quando está se regenerando caracteriza-se não por número menor de células, mas pela qualidade delas. "Se um profissional comparasse uma lâmina de biópsia de fígado no período de disfunção com a de um paciente saudável, elas seriam indistinguíveis. Porém, o primeiro ainda está doente, e o segundo não", assegura o pesquisador, que é professor do Departamento de Morfologia do ICB. "A capacidade de funcionamento em ambas é completamente diferente. Nem acreditamos a princípio, repetimos os testes várias vezes", enfatiza.

O principal achado da pesquisa foi a revelação de que, nesse período, as células hepáticas ganham aspecto de normalidade apenas visualmente, enquanto o órgão permanece disfuncional, por exemplo, para responder a processos inflamatórios e especialmente para exercer a função de eliminar bactérias que caem na corrente sanguínea. O trabalho usou combinação de técnicas para mostrar a localização e a função de todas as populações celulares do fígado. "Procuramos entender o órgão saudável e observar como ele muda e como volta ao normal", explica o orientador.

Maturidade

Acervo pesquisa

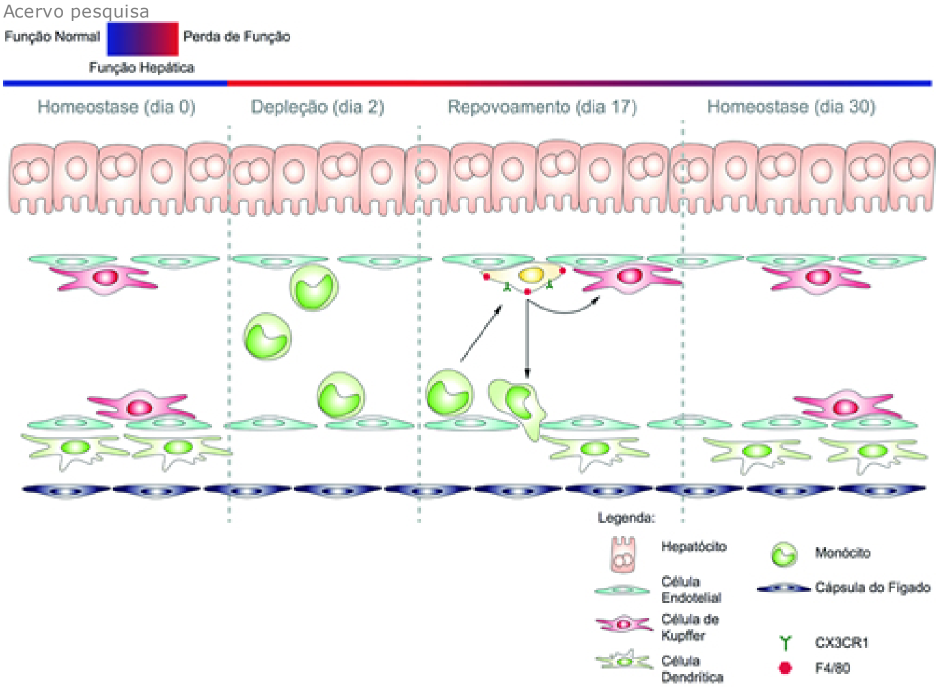

Dinâmica de repovoamento e restabelecimento de função hepática. Representação esquemática do ambiente hepático na homeostase (dia zero) com função, quantidade e localização de células em estado normal. No período pós-depleção (dia 2), os fagócitos hepáticos são eliminados do tecido, e há produção de grande quantidade de citocinas pró-inflamatórias e recrutamento de monócitos originados na medula óssea. Em conjunto, esses fatores comprometem o funcionamento normal do órgão. Os monócitos recrutados dão origem aos novos macrófagos e células dendríticas (dia 17). Os macrófagos se diferenciam e permanecem no interior dos capilares sanguíneos, enquanto as células dendríticas migram para o espaço subcapsular fora das capilares. Após 30 dias, o órgão reassume o perfil original, e as células restabelecem suas funções.

Quase todos os órgãos do corpo têm células chamadas macrófagos residentes, que moram no tecido e ajudam em seu funcionamento normal, como defesa contra infecções e reparos em casos de lesão. Doenças infecciosas, abuso de medicamentos, procedimentos do tipo irradiação e quimioterapia matam todos os macrófagos residentes no fígado – ou parte deles –, forçando o organismo a repor essas células.

Em seu trabalho, Bruna David acompanhou programa do próprio fígado, que transporta células da medula óssea, pela circulação sanguínea, para substituir as antigas, exatamente no mesmo número e na mesma forma anterior, processo que se completa em apenas duas semanas. Observou, contudo, que esse período não é suficiente para que elas aprendam a funcionar como macrófagos hepáticos. Por estarem imaturas, precisam de aproximadamente 30 dias para "entender o ambiente" e tornar o fígado funcional.

"Esse processo é comum em vários órgãos. Pulmão e cérebro, por exemplo, muitas vezes recebem os mesmos precursores que poderiam, inclusive, tornar-se macrófagos do fígado", explica Gustavo Menezes, destacando que cada órgão instrui a célula precursora a falar a sua língua. "São os mediadores inflamatórios do fígado que ensinam células da medula óssea a se tornarem células hepáticas", completa.

Depois que o corpo vence o processo inflamatório que matou abruptamente grande quantidade de células, segue-se delicado período em que ocorre o desbalanço nos mediadores inflamatórios do fígado, tornando-o temporariamente incapaz de ensinar as novas células a exercer suas funções. O trabalho desenvolvido sob a orientação de Gustavo Menezes mostrou que, quando o processo inflamatório é controlado, as novas células assumem sua função muito mais rapidamente – em pelo menos metade do tempo.

Segundo o pesquisador, embora antibióticos utilizados em tratamentos possam eliminar microrganismos que estejam lesando o fígado, nem sempre se dá a devida importância ao combate do processo inflamatório causado pela infecção. "Há muitos casos em que o paciente reage tão mal à infecção que entra numa síndrome inflamatória e morre. Controlar a inflamação é, portanto, necessário para que o órgão retome suas funções mais rapidamente", reforça Menezes. Ele lembra que há duas causas principais de mortalidade por doença hepática: falência por doença do próprio órgão e perda da capacidade do fígado de remover bactérias em circulação, o que predispõe o paciente a infecção sistêmica. E comenta que é fundamental entender como o fígado educa as células, para acelerar esse processo em pacientes em regeneração hepática. "Saber que existe essa janela de suscetibilidade é importante, por exemplo, em tratamentos de câncer", afirma.

Lacunas preenchidas

Acervo pesquisa

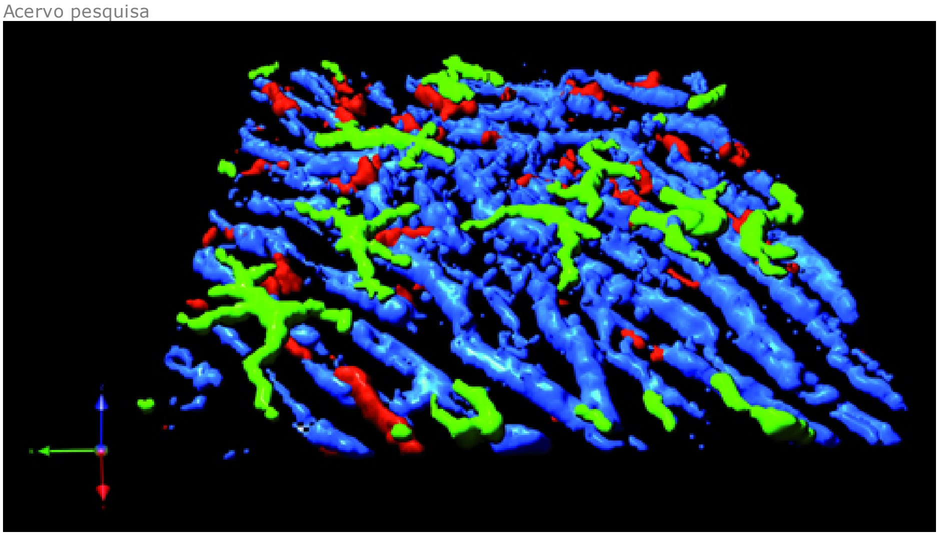

Reconstrução em 3D de microscopia intravital de fígado de camundongos. Macrófagos hepáticos (em vermelho) no interior dos capilares sinusóides (azul), em contato direto com a circulação sanguínea. No espaço extravascular, encontram-se as células dendríticas hepáticas (verde).

De acordo com o orientador, o trabalho de Bruna David preenche várias lacunas que foram sugeridas por outras pesquisas. "Achados desse estudo vão ajudar muita gente a entender até processos com os quais nossa equipe não trabalha", reforça. O trabalho combinou pelo menos nove linhagens diferentes de animais e utilizou técnicas que não existem no Brasil. Alguns testes foram realizados em colaboração com pesquisadores de Harvard e de Calgary.

Para exemplificar a dimensão e o nível de rigor da pesquisa, Gustavo Menezes explica que normalmente são usados até 12 marcadores de superfície para fazer caracterização de uma célula. No trabalho, foram empregados cerca de 30 marcadores simultaneamente, ampliando a chance de localizar populações celulares muito especializadas. "Além disso, enquanto estudos de expressão gênica trabalham normalmente com um número de dezenas a algumas centenas de genes, nesta pesquisa usamos mais de 570."

Para mostrar pela primeira vez a população de células dendríticas no fígado, a pesquisa usou combinação de sequenciamento gênico, citometria de fluxo e imagem *in vivo*. Bruna David explica que os marcadores geralmente usados para identificar macrófagos e células dendríticas mudam de um órgão para outro. "Havia o entendimento de que essas células eram uma subpopulação de macrófagos, mas mostramos que não. Trata-se de células primas, muito próximas, sendo bastante difícil discriminá-las nos tecidos, e conseguimos fazer isso claramente", diz a doutoranda. "Agora que sabemos que célula é essa, vamos procurar entender o quanto ela se relaciona com as outras populações celulares do fígado. Acreditamos que ela pode ter papel importante em infecções virais, por exemplo", sugere o orientador.

Depois de identificar, em microscópio, a célula no animal vivo, a equipe estudou diversos genes do sistema imunológico. "Comparamos esses genes com os de células já bem estabelecidas e mostramos que elas são muito próximas geneticamente de outras células dendríticas do corpo e diferentes de outras células imunológicas", explica Gustavo Menezes.

O pesquisador pondera que a colaboração com universidades estrangeiras para a realização dos testes não diminui a autonomia da UFMG e mostra que a pesquisa tem de ser feita globalmente. Segundo ele, é improvável que um único instituto detenha todos os métodos que a velocidade da ciência pede na atualidade. "Vários grandes trabalhos são feitos em colaboração, sem fronteiras. São multicêntricos e envolvem continentes diferentes; é disso que a ciência precisa: um esforço global pelo bem da humanidade", argumenta Menezes.

> **Artigo:** *Combination of mass cytometry and imaging analysis reveals origin, location, and functional repopulation of liver myeloid cells in mice*
> **Autores:** Bruna Araujo David, Rafael Machado Rezende, Maísa Mota Antunes, Mônica Morais Santos, Maria Alice Freitas Lopes, Ariane Barros Diniz, Rafaela Vaz Sousa Pereira, Sarah Cozzer Marchesi, Débora Moreira Alvarenga, Brenda Naemi Nakagaki, Alan Moreira Araújo, Daniela Silva dos Reis, Renata Monti Rocha, Pedro Elias Marques, Woo-Yong Lee, Justin Deniset, Pei Xiong Liew, Stephen Rubino, Laura Cox, Vanessa Pinho, Thiago Mattar Cunha, Gabriel Rocha Fernandes, André Gustavo Oliveira, Mauro Martins Teixeira, Paul Kubes e
> Gustavo Batista Menezes.
> **Publicação:** Gastroenterology

(http://sbi.org.br)

VOLTAR

(http://www.lfb.com.br/atualidades/nova-imunoglobulina-intravenosa-liquida-do-grupo-lfb-tegeline-newy/)
COMPROMISSO COM A VIDA
AQUI E SAIBA MAIS
LFB COMPROMISSO COM A VIDA

31 agosto, 2016

Enviado por *Comunicação*

PESQUISA

Educando as células após a lesão hepática

Estudo brasileiro publicado na Gastroenterology investiga populações celulares hepáticas e descreve o processo inédito de recuperação após lesão no fígado

Por Paula Vinhas, repórter SBI/NcgCE

Na Imunologia é usualmente adotado que duas semanas após uma lesão hepática, as células mielóides enviadas pela medula óssea para repor as danificadas já aparentam ter trazido o fígado para seu estado normal. Entretanto, um estudo realizado no Centro de Biologia Gastrointestinal, da Universidade Federal de Minas Gerais, mostrou que essa constatação é apenas visual. Apesar das populações de células já terem sido reconstituídas, estas recém-chegadas ainda se encontram imaturas, tornando o fígado disfuncional e suscetível a novas infecções.

O trabalho foi publicado na revista Gastroenterology (http://www.gastrojournal.org/article/S0016-5085(16)34966-6/fulltext), uma colaboração entre pesquisadores brasileiros e norteamericanos. E faz parte da tese da doutoranda Bruna David, sob orientação do professor e imunologista Gustavo Menezes.

Os pesquisadores utilizaram as técnicas de microscopia intravital, sequenciamento génico e CyTOF (um procedimento que mescla a citometria de fluxo e a espectrometria de massa), para identificar as células presentes no fígado. O resultado inédito apontou a presença de duas populações de macrófagos hepáticos e outras duas de monócitos, além de quatro populações de células dendríticas e uma de basófilos, e abre indicação para novas formas de tratamento.

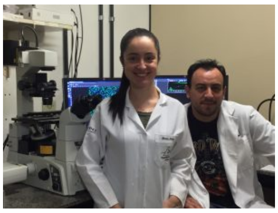

– A doutoranda Bruna David e o professor Gustavo Menezes

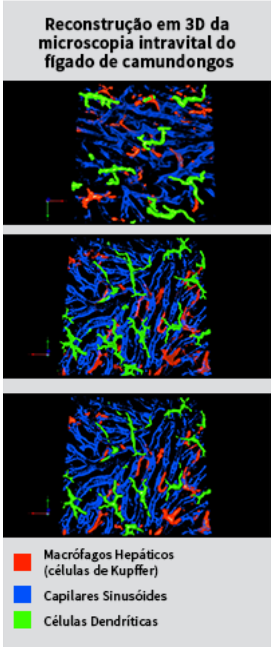
Reconstrução em 3D da microscopia intravital do fígado de camundongos
🟥 Macrófagos Hepáticos (células de Kupffer)
🟦 Capilares Sinusóides
🟩 Células Dendríticas

Após a primeira fase, Menezes e sua equipe utilizaram um modelo quimioterápico em camundongos para induzir a perda de células imunes hepáticas, foi aí que surgiu a primeira surpresa. "Geralmente em duas semanas após uma lesão, a população de células já se recompôs no fígado. O que nós observamos é que apesar das células estarem presentes, elas estão em um estado imaturo, incapazes de defender o fígado, o que gera uma janela de susceptibilidades a infecções. O fígado ainda precisará de duas a três semanas para educar as novas unidades", explica o professor.

Em dias normais o fígado perde células por morte celular, que são repostas da mesma maneira. A diferença entre a morte celular comum e a lesão hepática é o número de células a serem reconstituídas. Na morte celular, a nova célula chega ao fígado já havendo outras que conhecem suas funções, tornando seu amadurecimento mais rápido, enquanto na lesão hepática, o fígado está vazio e inflamado, o que acaba resultando em um tempo maior para que as novas células se adaptem a sua função.

O estudo pode trazer mudanças para os tratamentos de recuperação do fígado. "Hoje, se um paciente está em processo de recuperação de uma lesão hepática, pode ser administrado um antibiótico para tratar a infecção. Mas com este estudo demonstramos que é indicado um tratamento com anti-inflamatórios, que podem diminuir este período disfuncional e acelerar a educação das novas células no fígado", conclui Menezes.

PRÊMIOS

1. Grande prêmio Conceição Ribeiro Machado na XXV semana de Iniciação Científica, promovida pela Pró-Reitoria de Pesquisa da UFMG, 2016. Prêmio ganho pela minha Maria Alice de Freitas Lopes co-orientada por mim.

2. Menção honrosa no prêmio Thereza Kipnis do XLI Congresso da Sociedade Brasileira de Imunologia, 2016.

Semana Conhecimento | UFMG 2016

Cultivar Vidas: Ciência e Sociedade

90 ANOS UFMG 1927 - 2017

CERTIFICADO

CERTIFICAMOS QUE O TRABALHO INTITULADO "CARACTERIZAÇÃO ESPACIAL E MIGRAÇÃO DE CÉLULAS DENDRÍTICAS HEPÁTICAS ", RECEBEU O GRANDE PRÊMIO CONCEIÇÃO RIBEIRO MACHADO NA XXV SEMANA DE INICIAÇÃO CIENTÍFICA , PROMOVIDA PELA PRÓ-REITORIA DE PESQUISA, NO PERÍODO DE 17-10-2016 A 21-10-2016.

AUTOR(A): MARIA ALICE DE FREITAS LOPES

ORIENTADOR(A): GUSTAVO BATISTA DE MENEZES DO(A) INSTITUTO DE CIÊNCIAS BIOLÓGICAS.

CO-AUTORES: ANDRÉ GUSTAVO DE OLIVEIRA, ALAN MOREIRA DE ARAÚJO, DÉBORA MOREIRA ALVARENGA DE CARVALHO, MAÍSA MOTA ANTUNES, BRENDA NAEMI LANZA NAKAGAKI, ARIANE BARROS DINIZ, MÔNICA MORAIS SANTOS, BRUNA ARAÚJO DAVID

SEMANA NACIONAL DE CIÊNCIA E TECNOLOGIA 2016
CIÊNCIA ALIMENTANDO O BRASIL

realização UFMG

IMMUNO 2016
CAMPOS DO JORDÃO
XLI Congress of the
Brazilian Society of Immunology
IX ESCI - Extra Section of Clinical Immunology

October 29 - November 2
Campos do Jordão Convention Center • São Paulo

Organization
SBI
Sociedade Brasileira de Imunologia

Certificate

BRUNA DAVID

received the **"Honorable Mention – Thereza Kipnis Award"**

Title: "COMBINING MASS CYTOMETRY AND IMAGING REVEAL ORIGIN, LOCATION AND FUNCTIONAL REPOPULATION OF LIVER MYELOID CELLS IN MICE"

at the **XLI Congress of the Brazilian Society of Immunology 2016** held on October 29 – November 2, 2016.

Campos do Jordão, November 2nd, 2016.

Gustavo P. Amarante-Mendes
SBI President

ORIENTAÇÕES

Co-orientação da aluna de Iniciação Científica Maria Alice de Freitas Lopes no período de janeiro de 2015 a dezembro de 2016.

center for
gastrointestinal
biology

Belo Horizonte, 16 de janeiro de 2017.

Declaro para os devidos fins que a aluna Bruna Araújo David co-orientou o trabalho de iniciação científica intitulado CARACTERIZAÇÃO ESPACIAL E MIGRAÇÃO DE CÉLULAS DENDRÍTICAS HEPÁTICAS da aluna Maria Alice de Freitas Lopes, número de matrícula 2014005537, no período de janeiro de 2015 a dezembro de 2016 em meu laboratório e sob minha orientação.

Gustavo Batista Menezes, Ph.D.
Professor Adjunto

Av Antonio Carlos, 6627 • UFMG • ICB • Depto Morfologia • N3-140
Belo Horizonte • Minas Gerais • Brasil • 31270-901

ATIVIDADE EXTRA-CURRICULAR

Representante discente do Programa de Pós-Graduação em Biologia Celular do Instituto de Ciências Biológicas - UFMG, no período de fevereiro de 2015 a novembro de 2016.

Universidade Federal de Minas Gerais
Instituto de Ciências Biológicas
Programa de Pós-Graduação em Biologia Celular
Belo Horizonte, MG - BRASIL

UFMG

Belo Horizonte, 5 de dezembro de 2016

Prezado Sr.(a)

Declaro para os devidos fins que Bruna Araújo Davi, ex-aluna de doutorado do Programa de Pós-graduação em Biologia Celular (PPG BioCel) da UFMG, participou, enquanto aluna do Programa, do Colegiado do PPG BioCel, como membro suplente de 10/02/2015 a 25/09/2015 e como membro titular de 16/02/2016 a 25/11/2016.

Coloco-me à disposição para quaisquer esclarecimentos adicionais que se fizerem necessários.

Atenciosamente,

Profa. Luciana de Oliveira Andrade
Coordenadora
Programa de Pós-graduação em Biologia Celular
ICB – UFMG